CLUSTER MULTI-POINT OBSERVATIONS OF THE MAGNETOTAIL PLASMA SHEET

Paul David Henderson

Mullard Space Science Laboratory

Department of Space and Climate Physics

University College London

A thesis submitted to the University of London

for the degree of Doctor of Philosophy

July 30, 2007

I, Paul David Henderson, confirm that the work presented in this thesis is my own. Where information has been derived from other sources, I confirm that this has been indicated in the thesis.

Abstract

This thesis presents observations of the terrestrial magnetotail plasma sheet made by the European Space Agency Cluster mission. The Cluster mission is composed of four identical spacecraft, the first such multi-spacecraft mission, and enables, for the first time, the disambiguation of time versus space phenomena. Using the data from 2003, when the spacecraft were at their smallest average separation to date, many small-scale processes, both microphysical and macrophysical, are investigated.

In the first study presented, two small flux ropes, a possible signature of multiple X-line reconnection, are investigated. By the development and utilisation of various multi-spacecraft methods, the currents and magnetic forces internal and external to the flux ropes, as well as the internal structure of the flux ropes, are investigated. In addition, a theory of their early evolution is suggested.

In the second study presented, various terms of the generalised Ohm's law for a plasma are determined, including, for the first time, the divergence of the full electron pressure tensor, during the passage past the spacecraft of an active reconnection X-line. It is found that the electric field contribution from the divergence of the electron pressure tensor is anti-correlated with the contribution from the Hall term in the direction normal to the neutral sheet. In addition, further signatures of reconnection are quantified, such as parallel electric field generation and Hall quadrupolar magnetic field and current systems.

In the final study presented, the anti-correlation between the divergence of the electron pressure tensor and Hall terms is investigated further. It is found that the anti-correlation is general, appearing in the direction normal to the neutral sheet

because of a cross tail current. In a simple magnetohydrostatic treatment, a force balance argument leads to the conclusion that the gradient of the anti-correlation is a function of the ratio of the electron to ion temperatures, as well as providing information regarding the spatial scales of the pressure tensors.

Acknowledgements

I must first thank my supervisors, Dr Chris Owen and Dr Andrew Fazakerley, for all their guidance over the past three years.

I would like to thank the PEACE operations team, and especially Andrew Lahiff for the generation and individual calibration of many sets of moments from the PEACE instruments.

My co-workers, Ilya Alexeev, Andrew Walsh, Gethyn Lewis, Robert Fear, Jason Dewhurst, Yasir Soobiah, Yulia Bogdanova, Claire Foullon, Andrew Lahiff, Kimberley Steed, Jonathan Eastwood, Jim Slavin, Lin Yin, Henry Reme and Elizabeth Lucek, have been enormously helpful in the work that has contributed to this thesis.

I would like to thank my wife, Bryony, for the emotional support throughout the three years of my research.

Finally, I would like to acknowledge the financial support the Particle Physics and Astronomy Research Council (PPARC) for studentship funding over the past three years.

Table of Contents

List of Figures

List of Tables

Chapter 1

Introduction

1.1 Basic concept

1.1.1 Quasi-neutrality

A plasma is a collection of positively and negatively charged particles, interacting through electromagnetic forces. If a charge imbalance occurs, the imbalance will attract a neutralising charge due to an electrostatic restoring force. As the electrons are lighter than the ions it is the electrons that will move the most. Due to the electron overshooting the ion and therefore feeling an opposite restoring force, the electrons will oscillate around the ion. The natural frequency of these oscillations is called the plasma frequency, ω_{pe}.

$$\omega_{pe} = \left(\frac{n_e e^2}{m_e \epsilon_0} \right)^{\frac{1}{2}} \tag{1.1}$$

Due to any relatively small charge imbalances being transient, the plasma is said to be quasi-neutral. For quasi-neutrality to hold, the electric Coulomb potential ϕ from each charge q at a distance r must be sufficiently shielded by other charges:

$$\phi = \frac{q}{4\pi\epsilon_0 r} \tag{1.2}$$

where ϵ_0 is the permittivity of the vacuum. The shielded potential takes the form of the Debye potential:

$$\phi = \frac{q}{4\pi\epsilon_0 r} \exp\left(-\frac{r}{\lambda_D}\right) \tag{1.3}$$

Thus, for a plasma to be considered quasi-neutral, the characteristic length scale of the system, l, must be large when compared to λ_D, the Debye Length;

$$\lambda_D = \left(\frac{\epsilon_0 k T_e}{n e^2}\right)^{1/2} \tag{1.4}$$

where k is Boltzmann's constant, T_e is the electron temperature, n is density (assuming $n_e \sim n_i$) and e is the charge of the electron.

1.2 Single particle motion

1.2.1 Larmor orbits

The simplest way in which plasma physics can be approached is by the analysis of the motion of single particles. In this regime particle interactions are ignored and only the effect on a single particle by electric and magnetic fields is considered. The equation of motion, where m, $\mathbf{v}$ and q are the particle mass, velocity, charge and $\mathbf{E}$ and $\mathbf{B}$ are the electric and magnetic field, is:

$$m\frac{d\mathbf{v}}{dt} = q(\mathbf{E} + \mathbf{v} \times \mathbf{B}) \tag{1.5}$$

If we assume the electric field is zero and there exists a constant magnetic field, by differentiating Eqn. 1.5 with respect to time, the following may be obtained:

$$\frac{d^2\mathbf{v}}{dt^2} = \left(\frac{-qB}{m}\right)^2 \mathbf{v} \tag{1.6}$$

This is recognisable as an equation of simple harmonic motion with a frequency

of:

$$\omega_L = \frac{qB}{m} \tag{1.7}$$

This frequency, ω_L, is known as the Larmor frequency (or the gyro frequency). Associated with the Larmor frequency is the Larmor (or gyro) radius:

$$r_L = \frac{mv_\perp}{qB} \tag{1.8}$$

Therefore, in the presence of a magnetic field particles will gyrate around a 'guiding centre' with frequency ω_L and at a radius of r_L. These two quantities are magnetic field and charge dependent. It is noted that the velocity parallel to the magnetic field is unaffected by this motion. Thus, if the particle initially has parallel velocity, the effect of this interaction is to cause the guiding centre of the particle to move along the magnetic field. The motion of the particle will therefore be helical around the magnetic field line (Fig 1.1).

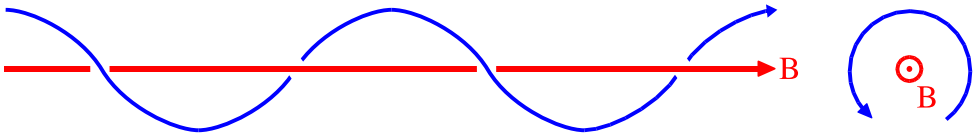

Figure 1.1: The motion of an electron (blue) around a magnetic field line (red). The guiding centre moves parallel to the magnetic field line. An ion would have a larger gyroradius and rotate in the opposite sense.

The angle which the magnetic field makes to the velocity is defined as the pitch angle, θ:

$$\theta = \arctan\left(\frac{v_\perp}{v_\parallel}\right) \tag{1.9}$$

If θ is 0° or 180° then the particles are moving parallel or anti-parallel to the magnetic field respectively. Other values of θ mean that the particle has some gyro-motion around magnetic field lines.

1.2.2 Drift motion

E × B drift

If a steady state electric field is introduced perpendicular to the magnetic field, differentiating Eqn. 1.5 with respect to time leads to:

$$\frac{d^2\mathbf{v}}{dt^2} = -{\omega_L}^2 \left(\mathbf{v} - \frac{\mathbf{E}\times\mathbf{B}}{B^2}\right) \tag{1.10}$$

A more intuitive solution can be shown by writing:

$$\frac{d^2\mathbf{v}}{dt^2} = -{\omega_L}^2 \left(\mathbf{v} - \mathbf{v}_d\right) \tag{1.11}$$

where $\mathbf{v}_d$ in this equation is defined as:

$$\mathbf{v}_d = \frac{\mathbf{E}\times\mathbf{B}}{B^2} \tag{1.12}$$

This is a transformation to a frame in which the velocity of the particle is a sum of its gyromotion (Eqn. 1.6) plus a drift $\mathbf{v}_d$. In effect, the particle gyrates around the guiding centre whilst the guiding centre itself drifts across the magnetic field lines due to the electric field. The electric field will accelerate the particle on one half of the gyration and decelerate the particle on the other half. Ions, with larger mass, gyrate slower with large r_L, and electrons gyrate quicker with small r_L. In this way the $\mathbf{E}\times\mathbf{B}$ drift is charge and mass independent (Fig. 1.2).

1.2.3 Generalised drift

The concept of drift can be generalised by noting in the above case that the force $\mathbf{F} = q\mathbf{E}$ and writing the generalised drift equation:

$$\mathbf{V}_f = \frac{\mathbf{F}\times\mathbf{B}}{qB^2} \tag{1.13}$$

In general, it can be seen that charge independent forces will produce a charge

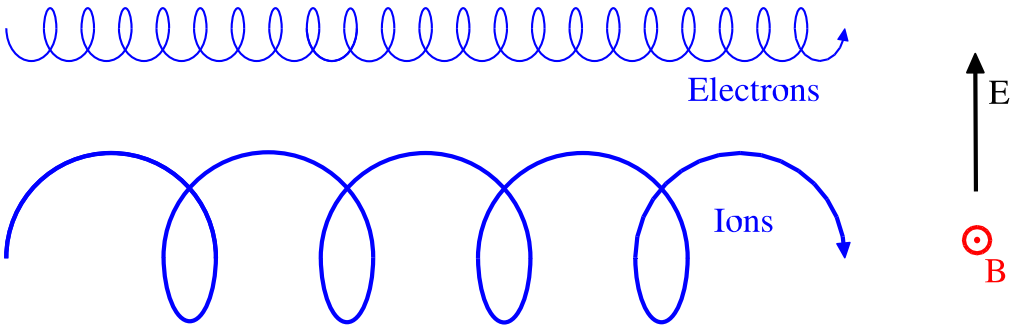

Figure 1.2: Electron and ion drift under $\mathbf{E} \times \mathbf{B}$ drift. With the electric (black) and magnetic (red) fields shown, the both species drift to the right of the page. The larger, slower orbits of the ions are matched by the faster, smaller orbits of the electrons.

dependent drift motion where electrons and ions drift in opposite directions, i.e. a current. Two common examples of drifts that produce flow perpendicular to the magnetic field are drifts caused by gradients in the magnetic field and curvature of the magnetic field.

1.3 Magnetohydrodynamics

1.3.1 Concept

To determine fully the behaviour of a plasma, one must consider the full particle distribution in phase space. Particle distributions will be briefly mentioned in the next section and in the description of the instruments used in this thesis. However, in many cases it is not necessary to know fully the particle distribution at the microscopic level. To satisfactorily describe the plasma in certain circumstances, all that is required is a simpler macroscopic description of the plasma (the moments of the distribution, such quantities as temperature, density and velocity). Ideas such as density, temperature and velocity are well known from fluid dynamics. The combination of the theory of fluid dynamics and the fact that the plasma fluids are electrically conducting and are subject to internal and external electromagnetic fields, gives rise to the theory (Alfvén, 1942) known as magnetohydrodynamics (MHD).

MHD is essentially a simplified set of fluid and electrodynamic equations and can describe most plasma behaviour. In this discussion of MHD, quasi-neutrality is assumed, therefore $n_i \approx n_e \equiv n$. As discussed above quasi-neutrality is valid when the length scales are larger than λ_D. The approximation that is MHD is valid for length scales larger than a gyroradius, and for frequencies smaller than the gyrofrequency.

For electron and ion masses of m and M the mass density is defined as:

$$\rho = n_i M + n_e m \approx nM \tag{1.14}$$

The local charge density σ, as:

$$\sigma = (n_i - n_e)\, e \tag{1.15}$$

The current density **j**, thus;

$$\mathbf{j} = e\left(n_i \mathbf{v}_i - n_e \mathbf{v}_e\right) \approx ne\left(\mathbf{v}_i - \mathbf{v}_e\right) \tag{1.16}$$

where $\mathbf{v}_i$ and $\mathbf{v}_e$ denote the ion and electron bulk velocity respectively.

The continuity equation for species s is:

$$\frac{\partial n_s}{\partial t} + \nabla\cdot\left(n_s \mathbf{v}_s\right) = 0 \tag{1.17}$$

which describes the conservation of number density (as well as mass and charge). The simplest equation of state is often assumed, $p \propto n^\gamma$ with $\gamma = 5/3$.

With these equations, an equation of motion can be derived for species s;

$$n_s \frac{\mathrm{d}\mathbf{v}_s}{\mathrm{d}t} = \frac{n_s q_s}{m_s}\left(\mathbf{E} + \mathbf{v}_s \times \mathbf{B}\right) - \frac{1}{m_s}\nabla.\,\mathsf{P}_s \tag{1.18}$$

where P is the pressure tensor and $\mathrm{d}/\mathrm{d}t$ specifies a total derivative. After linearising the velocity and the inclusion of a simplified collisional term that leads to the

resistivity η, the generalised Ohm's law can be derived by subtracting the equation of motion for ions from that of electrons:

$$\mathbf{E} = -\mathbf{v}_i \times \mathbf{B} + \frac{1}{en_e}\left(\mathbf{j} \times \mathbf{B} - \nabla . \mathsf{P}_e\right) + \eta \mathbf{j} - \frac{m_e}{e}\frac{d\mathbf{v}_e}{dt} \tag{1.19}$$

Note that the electron pressure P_e is generally a non-isotropic tensor. This equation is very important in plasma physics and will be discussed in detail later in this thesis. In the magnetosphere, it is generally sufficient to neglect all terms apart from the $-\mathbf{v}_i \times \mathbf{B}$ term. As will be discussed further, in certain circumstances the other terms can, and sometimes do, become important.

The Maxwell equations complete the set;

$$\nabla \times \mathbf{B} = \mu_0 \mathbf{j} + \frac{1}{c^2}\frac{\partial \mathbf{E}}{\partial t} \tag{1.20}$$

the second term in Eqn. 1.20 is neglected in the MHD approximation;

$$\nabla \times \mathbf{E} = -\frac{\partial \mathbf{B}}{\partial t} \tag{1.21}$$

$$\nabla . \mathbf{B} = 0 \tag{1.22}$$

$$\nabla . \mathbf{E} = \frac{\sigma}{\epsilon_0} \tag{1.23}$$

where c is the speed of light in free space. These are the basic equations of MHD. Many interesting results arise from the manipulation of these equations. For example, combining Eqn. 1.21 with the simplified version of Eqn. 1.19 gives rise to the magnetic induction equation:

$$\frac{\partial \mathbf{B}}{\partial t} = \nabla \times (\mathbf{v}_i \times \mathbf{B}) + \eta \nabla^2 \mathbf{B} \tag{1.24}$$

The first term on the right hand side of Eqn. 1.24 is the change in the magnetic

field over time associated with plasma motion, the second is associated with the diffusion of magnetic field lines through plasma. The ratio of the first to the second term is called the magnetic Reynolds number, R_m. When R_m is much larger than unity the diffusion term is negligible and no diffusion of magnetic field lines through plasma can occur. This is commonly known as the 'frozen flux' approximation (Alfvén, 1942). In the frozen flux approximation, the plasma and magnetic field are frozen together and the amount of flux through any surface convecting in the plasma remains constant. This means that if the plasma moves the magnetic field must move with it and visa versa. This concept is important in the discussion of the behaviour of planetary magnetic fields. If R_m is much larger than unity then the electric field, as discussed above, is given only by $-\mathbf{v}_i \times \mathbf{B}$.

1.3.2 Magnetic forces

The magnetic force density is expressed in the $\mathbf{j} \times \mathbf{B}$ terms in Eqns. 1.18 and 1.19. By substituting the current density with Eqn. 1.20 the magnetic force density term can be resolved into quantities known as magnetic tension and pressure

$$\mathbf{j} \times \mathbf{B} \equiv \frac{(\nabla \times \mathbf{B}) \times \mathbf{B}}{\mu_0} = -\nabla \left(\frac{B^2}{2\mu_0} \right) + \frac{1}{\mu_0} (\mathbf{B}.\nabla)\mathbf{B} \tag{1.25}$$

The first term on the RHS of this equation is the magnetic pressure, the second being the magnetic tension. In this interpretation of magnetic force, the two terms arise from an over or under-density of magnetic flux relative to surroundings and curved magnetic field lines respectively.

These forces describe the way in which the magnetic field behaves. Therefore kinked magnetic field lines will have a $\mathbf{j} \times \mathbf{B}$ such directed as to straighten them (Fig. 1.3), inversely proportional to the radius of curvature, and a high magnetic flux density will have a $\mathbf{j} \times \mathbf{B}$ directed down the pressure gradient (Fig. 1.4).

The magnetic pressure can be directly compared to the plasma pressure in the concept of plasma β, the ratio of the plasma pressure to the magnetic pressure.

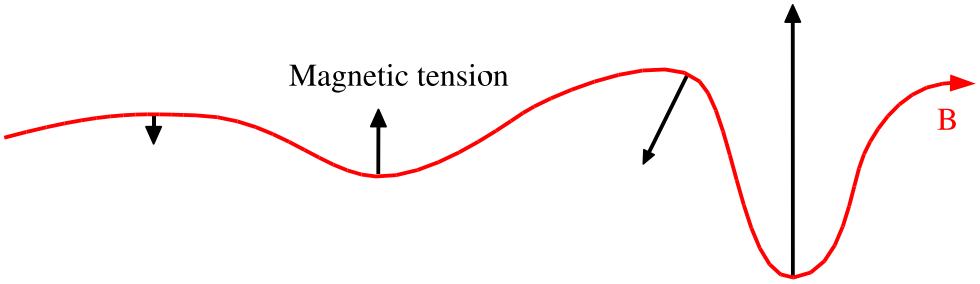

Figure 1.3: Magnetic tension force density (black) arising from a curved magnetic field line. The amount of tension is inversely proportional to the local radius of curvature of the magnetic field line.

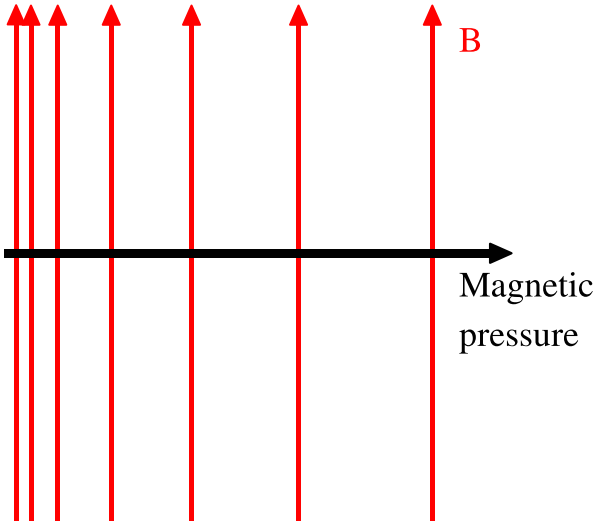

Figure 1.4: Magnetic pressure force density (black) arising from an over density of magnetic field (red).

$$\beta = \frac{(n_e k T_e + n_i k T_i)}{|\mathbf{B}|^2 / 2\mu_0} \tag{1.26}$$

This quantity determines which forces dominate the plasma-magnetic field system. If β is low the magnetic forces are dominant, whereas when β is large the plasma forces are dominant.

1.4 Plasma physics in the solar system

1.4.1 The Solar Wind

The Sun is a star with intermediate luminosity and size and is the primary energy source for the entire solar system. The upper solar atmosphere, the hot, tenuous and topologically complex corona (see Aschwanden, 2005), extends a number of solar radii out into space. A large plasma pressure difference exists between the solar corona and interplanetary space, leading to solar magnetic field and plasma being driven from the Sun. R_m is of the order of 10^{17} and suggests that the magnetic field and plasma are frozen together. Therefore, ideal MHD should be sufficient in the study of the solar wind.

At 1 AU, the solar wind, composed mainly of protons and electrons with a smaller proportion (4%) of alpha particles, is supersonic (Parker, 1958), and can be classed into two sub-types; slow and fast solar wind (McComas et al., 1995). Slow solar wind originates above, or close to, closed magnetic field loops on the Sun with velocity $\sim$ 300 - 500 kms^{-1}. The fast wind originates in the cooler regions of the solar corona where the magnetic field is open. The velocity of fast solar wind is typically $\sim$ 600 - 900 kms^{-1}.

The magnetic field in the solar wind is weak, being many orders of magnitude smaller than that at the surface of the Earth. Table 1.1 lists some average properties of the solar wind at Earth distances, however, these quantities can vary significantly. The solar wind exerts a large influence on the terrestrial magnetic field as will be discussed in this introduction.

Flow speed	400 kms^{-1}
Plasma density	7 cm^{-3}
Plasma temperature	0.1 MK
Magnetic field	5 nT

Table 1.1: Average solar wind parameters at 1 AU from Kivelson and Russell (1995).

As the magnetic field and plasma are frozen together, the solar magnetic field

follows the radial plasma streamlines away from the Sun. As the Sun spins the magnetic field is twisted into an Archimedean or Parker spiral (see Figure 1.5, Parker, 1958), making an angle of $\sim 45°$ to the Earth-Sun line at Earth distances.

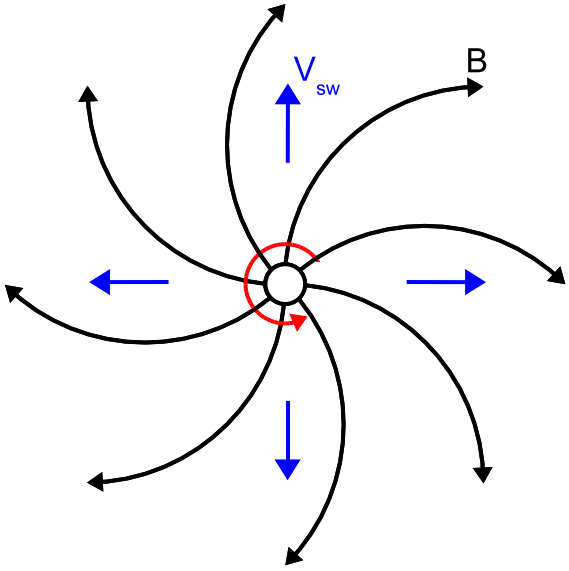

Figure 1.5: The magnetic field (black), frozen into the plasma, flows along the plasma streamlines (blue). As the sun spins (red), the magnetic field forms a spiral shape, the Parker spiral (Parker, 1958).

1.4.2 The Magnetosphere

Due to the frozen in flux approximation, the solar wind magnetic field and plasma cannot mix with the terrestrial magnetic field and plasma. The terrestrial magnetic field therefore presents an obstacle to the solar wind flow which must be diverted around it. A cavity is formed from a total pressure balance between these two systems, called the magnetosphere. The 'nose' of the magnetosphere is approximately 10 Earth radii (R_E) from the Earth, but this distance, the 'stand-off' distance, as well as the overall size and shape of the magnetosphere, is dependent on the solar wind conditions.

The undisturbed terrestrial magnetic field, in the absence of the solar wind, would be almost dipolar, and tilted approximately 11° to the rotation axis.

A coordinate system often used in the magnetosphere is the Geocentric Solar Ecliptic (GSE) system (see Hapgood, 1992). In this system the X axis points from the Earth towards the Sun. The Z axis is aligned to the ecliptic north pole of the Earth, with the Y axis completing the right hand set (and therefore pointing towards dusk). The zero point of these axes are defined at the centre of the Earth. Therefore, locations in the nightside of the magnetosphere have negative X coordinates.

A variant of this coordinate system is introduced by the tilt of the Earth's dipole. In the Geocentric Solar Magnetospheric (GSM) coordinate system, the X axis points again from the Earth towards the Sun, but the Z axis is defined as the projection of the Earth's magnetic field dipole tilt onto the GSE YZ plane. The Y axis completes the set and again points towards dusk.

The magnetosphere consists of various regions that will be discussed in the remaining parts of section 1.4, and are shown in Fig. 1.6. Briefly, they are the dayside magnetosphere where the dipole-like terrestrial field lines are compressed by the solar wind, the cusps at the Earth's magnetic poles, the inner magnetosphere close to the Earth where the radiation belts lie and the nightside magnetosphere where the terrestrial magnetic field lines are stretched away from the sun.

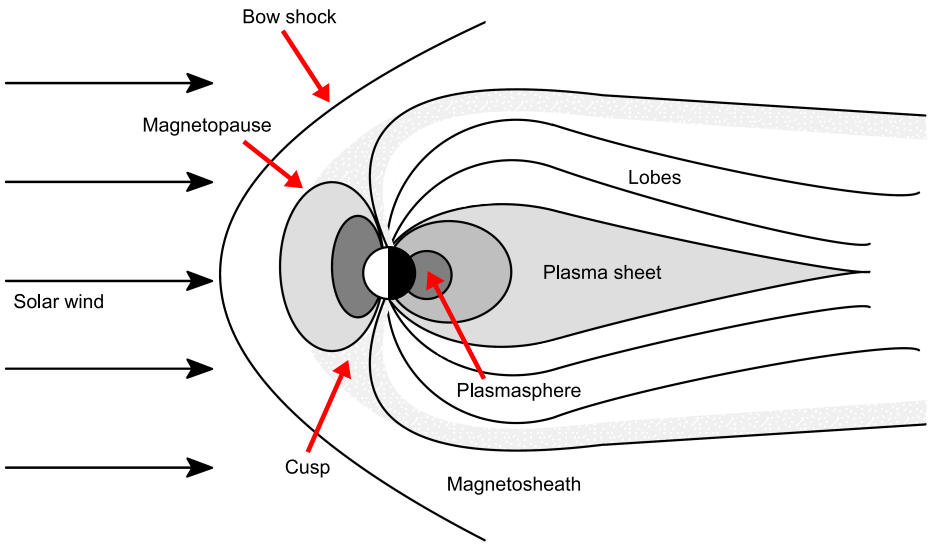

Figure 1.6: The magnetosphere of Earth. Various important magnetospheric regions are marked and will be discussed in this introduction.

1.4.3 Bow shock and dayside

The solar wind upstream of the magnetosphere is supersonic (i.e. the speed of the solar wind is faster than the speed of any pressure wave that could act to divert the flow around the obstacle presented by the magnetosphere). A shock wave standing in the flow is therefore formed in order to slow the solar wind down to subsonic speeds, the shocked solar wind then flows around the magnetosphere. The kinetic energy of the solar wind plasma is converted to thermal energy at this bow shock. This region of slowed solar wind located between the shock and the outer boundary of the magnetosphere is known as the magnetosheath.

The boundary between the magnetosheath and the magnetosphere is called the magnetopause. This boundary is a thin current sheet acting to separate these two topologically different regions (Chapman and Ferraro, 1931; Dungey, 1961).

The ionosphere is important in the study of the magnetosphere as it is the location of closure of different current systems. As will be discussed later, observations of the aurora, or particles coming from other parts of the magnetosphere (i.e. the plasma sheet) colliding with neutrals in the ionosphere, can be used as a diagnostic of magnetospheric activity.

The ionosphere is created by the ionisation of the upper atmosphere by solar radiation. Particles in the ionosphere that have enough energy to escape the attraction of gravity form the plasmasphere. The plasma in the plasmasphere is cool (~ 1 eV) and dense ($\sim 10^3$ cm^{-3}).

The radiation belts (van Allen, 1981) consist of energetic, trapped, field aligned populations that can cause damage to spacecraft. The radiation belts are more dense at the equator as interactions with the neutral atmosphere removes particles at lower latitudes. The outer belt consists of energetic electrons (~ 1 MeV), with a small amount of protons. The inner radiation belt consists mainly of high energy protons, to ~ 100s of MeV.

1.4.4 Nightside

The nightside magnetosphere, also called the magnetotail or simply the tail, extends many hundreds of R_E from the Earth and is, in its most simplified form, cylindrical (see Fig. 1.6). The two parts of the magnetotail, defined by the opposing directions of the magnetic field, are separated by a current that flows across the magnetotail (Ness, 1965). This cross tail current flows from dawn to dusk (+Y in the GSM coordinate system). At the centre of the current sheet where the magnetic field reverses the magnetic field can become negligibly small (if the system is two dimensional, the magnetic field is zero by definition at this point). This region is known as the neutral sheet. Figure 1.7 is a schematic of the magnetotail, indicating some of the different plasma regions that exist, the magnetic field and the neutral sheet.

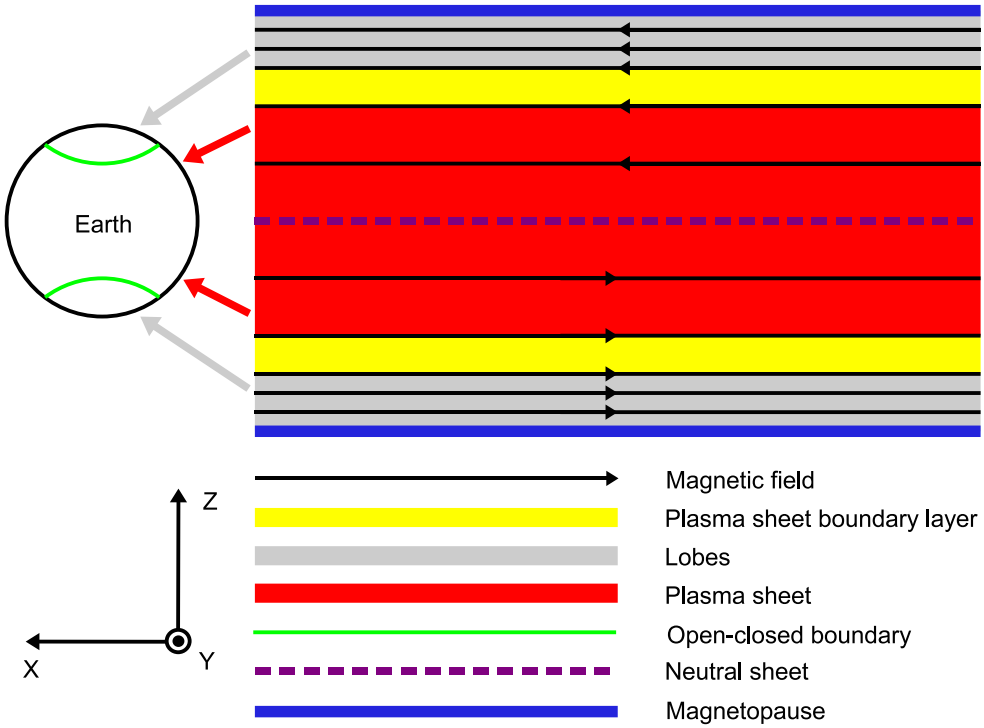

Figure 1.7: Schematic view of the magnetotail of the Earth (not to scale). The magnetic field topology, and different regions of the magnetotail are marked. The polar region to which open (plasma sheet) and closed (lobes) magnetic field map are indicated on a cartoon Earth. The GSM coordinate system is indicated. Note that the lobes are generally much larger in spatial extent than the plasma sheet.

Above the neutral sheet the magnetic field lines point towards the Earth and

map to the northern polar ionosphere. The magnetic field points away from the Earth below the neutral sheet, being connected to the Earth through the southern polar ionosphere. A number of distinct regions in the magnetotail exist, defined by their proximity to the neutral sheet and by their connectivity (Fig. 1.7).

Above and below the neutral sheet, magnetic field lines in the 'lobes' are connected to the northern or southern polar ionosphere only, and are open to the Interplanetary Magnetic Field (IMF). The lobes that contain these 'open' magnetic field lines are characterised by low to negligible plasma density and large magnetic field strengths ($\sim$ 50 nT at X = -20 R_E).

'Plasma sheet'magnetic field lines are, connected to both the northern and southern polar ionospheres and are termed 'magnetically closed'. Closed magnetic field lines reverse in the magnetotail through the neutral sheet (not shown in Fig. 1.7). This is the region in which most of the magnetotail plasma is located. This area is characterised by relatively high plasma density ($\sim$ 1 cm^{-3}) and low magnetic field strengths (0 to 10 nT). During active times in the magnetosphere, the proportion of heavier ionospheric ions can become large (Shelley et al., 1972). In this thesis, a working definition of the plasma sheet is assumed to be where $\beta \gtrsim 0.3$ (Eastman et al., 1984; Baumjohann et al., 1989). In the polar ionospheres, the boundary between open (lobes) and closed (plasma sheet) magnetic field lines is called the 'Open-Closed Boundary' (OCB).

Topologically, the location and orientation of the plasma sheet and lobes can vary significantly, but in a simplified magnetosphere the plasma sheet surrounds and encompasses the neutral sheet, above and below which are the magnetic lobes. A boundary layer exists between the plasma sheet and lobes (Eastman et al., 1984) called the plasma sheet boundary layer (PSBL). Strong field aligned beams of particles are often observed in this layer (e.g. Eastman et al., 1984; Eastman et al., 1985; Parks et al., 1998; Henderson et al., 2006b).

1.4.5 Magnetospheric current systems

Currents in the magnetosphere arise to separate regions across which the magnetic field strength or direction changes (by Ampère's law, Eqn. 1.20), such as at the magnetotail neutral sheet and the magnetopause (see Fig. 1.8). The dayside magnetopause or Chapman-Ferraro (Chapman and Ferraro, 1931) currents flow in a duskward direction, as does the magnetotail neutral sheet current in the centre of the plasma sheet. The magnetopause tail current, flowing on the outer boundary of the tail, flows in the dawnward direction. Due to the differential drift of the ions and electrons (due in turn to the different directions of drift for gradient and curvature drift) in the radiation belts, a westward ring current is set up (Frank, 1967). Currents flowing in the polar ionosphere are connected to those in the magnetosphere via field aligned, or Birkeland currents (Birkeland, 1908).

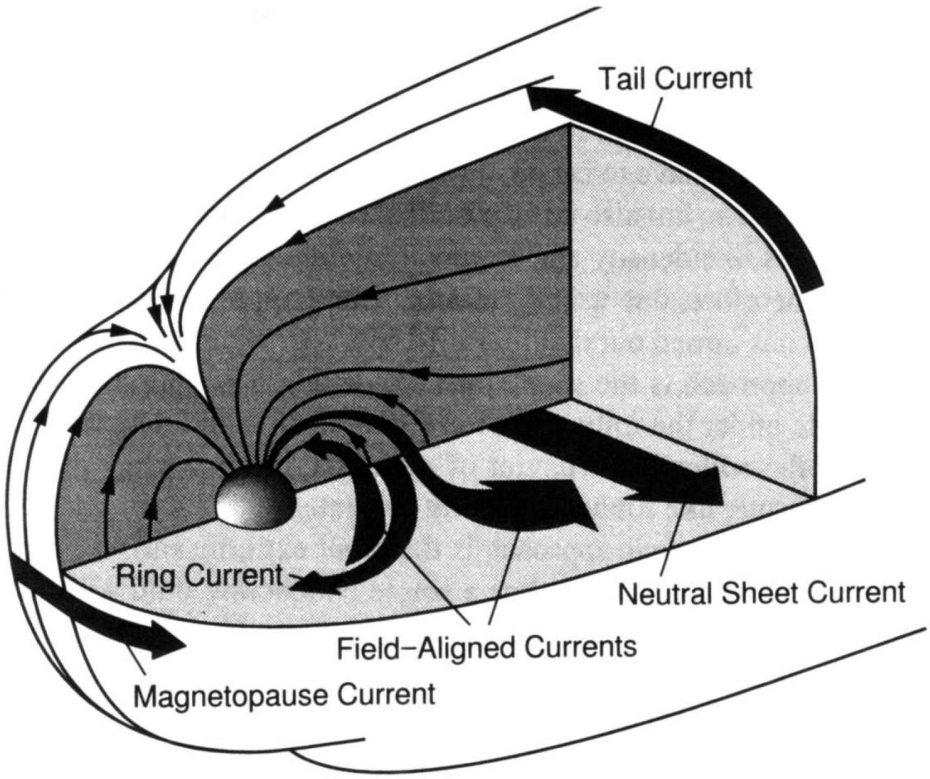

Figure 1.8: The magnetospheric current systems, from Baumjohann and Treumann (1996). The tail magnetopause current is shown by the arrow at the right hand edge of the plot.

1.5 Reconnection

1.5.1 Motivation: The Dungey cycle

The solar wind does not simply flow around the magnetosphere. There is some intermixing of solar wind into the magnetosphere made possible by the so-called reconnection process. For example, if two anti-parallel magnetic field lines come into contact it is possible that they may reconnect to achieve a lower total energy state. A magnetic X-point will therefore be formed (Parker, 1957; Petschek, 1964; Vasyliunas, 1979).

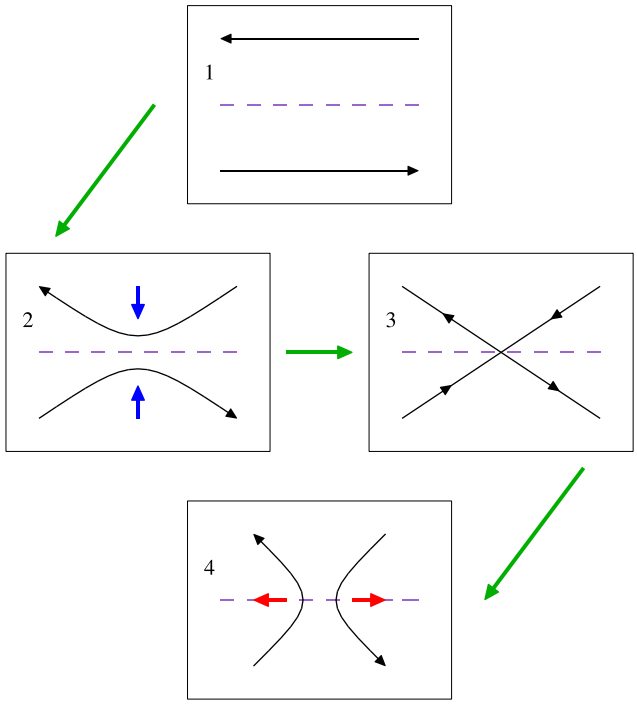

Figure 1.9: Two anti-parallel magnetic field lines (1) come together (2), they then reconnect through the current sheet (3) which changes the magnetic topology. The magnetic field lines begin to move apart (4) under magnetic tension. The current sheets that exist to separate two topologically different regions are marked in purple.

In Fig. 1.9 a schematic outline of the magnetic reconnection process is given. In 1, two oppositely directed magnetic field lines are drawn. A current sheet will exist to separate these two regions (purple). In 2, the two magnetic field lines are drawn approaching a central point (note that in general, the magnetic field in the horizontal

component of Fig. 1.9 is significantly larger than that in the vertical component). At this central point, 3, the magnetic field lines can disconnect and reconnect across the current sheet. The $\mathbf{j} \times \mathbf{B}$ force, or more specifically the magnetic tension force, will then force the magnetic field lines to move apart and straighten, 4.

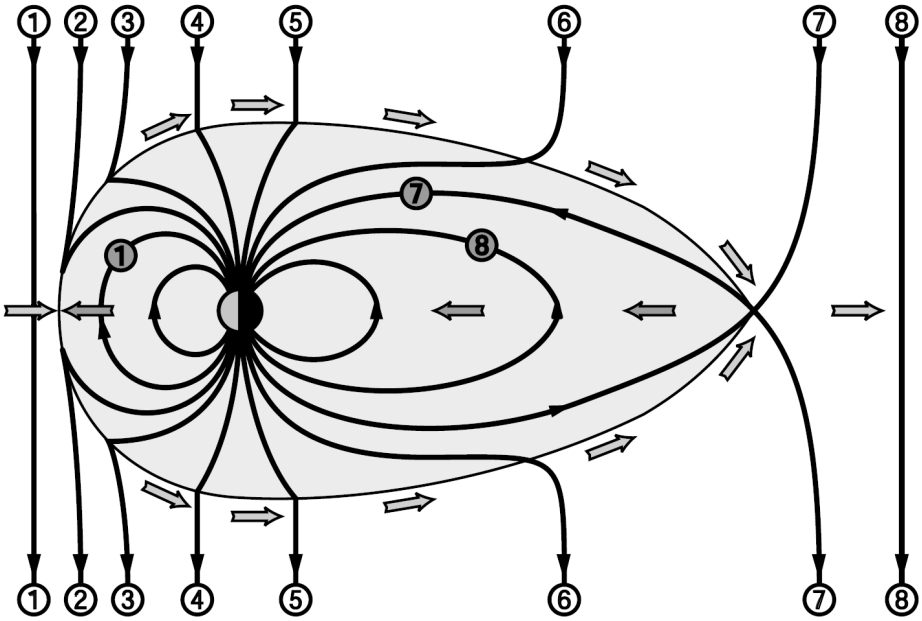

Figure 1.10: The Dungey cycle. In this schematic, two magnetic field lines from the solar wind and Earth (1) connect at the magnetopause. After reconnection (2), they move around the magnetosphere embedded in the solar wind flow (2-6), being connected to the IMF at one end and the Earth at the other. The magnetic field lines reconnect at the Distant Neutral Line (DNL, 7), creating two new magnetic field lines (8), one moving back towards the Earth in the magnetotail wholly connected to the Earth and one in the solar wind wholly connected to the IFM. Figure adapted from Baumjohann and Treumann (1996).

Figure 1.10 shows a schematic of the Dungey cycle (Dungey, 1961). The magnetic field lines marked by the numbers 1 to 8 will now be discussed. The magnetic field of the Earth and Sun meet at the subsolar point (1) and can reconnect in a way such that magnetic field lines (and associated plasma) move away from the X-point under magnetic tension (2), the dayside magnetosphere is eroded (Aubry et al., 1970). These magnetic field lines will then be connected to the Earth at one end and open into the IMF at the other. The magnetic field and plasma will therefore convect with the magnetosheath flow (3-6) and move around the Earth, moving into

the magnetosphere and then the magnetotail (Cowley, 1980). This process therefore moves flux into the magnetosphere across the magnetopause. In order to maintain a steady state this flux must be removed from the magnetosphere in some process. This happens in the magnetotail where an X-point in formed (7), the Distant Neutral Line (DNL) approximately $\sim$ 100 R_E downtail (Slavin et al., 1985). Magnetic flux and plasma that is tailward of this point will not be connected to the Earth and will be ejected from the tail. After DNL reconnection, two new magnetic field lines will be created (8), one moving back towards the Earth in the magnetotail wholly connected to the Earth and one in the solar wind wholly connected to the IMF. In this way a steady state may be achieved, where the reconnection process cycles the solar wind plasma and magnetic field through the magnetosphere. Reconnection is therefore a process which can result in the entire magnetospheric magnetic field being reconfigured.

1.5.2 The applicability of MHD to reconnection theory

In the magnetosphere, a global electric field, the convection electric field or 'reconnection electric field'(E_R), exists across the magnetotail. It is this electric field that causes an $\mathbf{E} \times \mathbf{B}$ drift of material towards the reconnecting region, the X-line, from both above and below the current sheet.

On a global scale the reconnection electric field can be supported by MHD. However, at the current sheet, when the length scale is reduced to a certain point, the ions start to diffuse across the magnetic field lines and no longer move with the magnetic field. This 'ion diffusion region '(Sonnerup, 1979) has a scale size of the ion inertial length, where the inertial length of species s, λ_s, is given by:

$$\lambda_s = \left(\frac{\epsilon_0 m_s c^2}{n_s e^2} \right)^{\frac{1}{2}} \tag{1.27}$$

In the magnetotail, the ion diffusion region is on the order of a few hundred km at X = -20 R_E. In addition, the same process occurs for the electrons at the electron

inertial length, λ_e, in the electron diffusion region. In the magnetotail this region is on the order of a few km at X = -20 R_E. The cause of the diffusion could be due to non-ideal MHD (i.e. anomalous resistivity, Labelle and Treumann, 1988; Watt et al., 2002; Petkaki et al., 2003; Petkaki et al., 2006) or other additional effects outside ideal MHD such as the divergence of the electron pressure (Hesse et al., 1999; Kuznetsova et al., 2001; Yin et al., 2001). It is within these diffusion regions that MHD breaks down and electrons and ions diffuse across the magnetic field lines.

The diffusion of the plasma across the magnetic field allows the breaking and reconnection of the magnetic field lines as seen in Panels 2 to 4 in Fig. 1.9. After the reconnection, the highly kinked magnetic field lines will move away from the X-line under magnetic tension.

1.5.3 Reconnection Theory

The first steady state model of reconnection was the Sweet-Parker model (Parker, 1957). In this MHD model, the magnetic field is reconnected in a long and narrow diffusion region (Fig. 1.11).

The efficiency of the reconnection process, also known as the reconnection rate, $\mathcal{R}_{SP}$, defined by the ratio of the outflow velocity to the inflow velocity:

$$\mathcal{R}_{SP} = R_m^{-1/2} \tag{1.28}$$

As discussed in Section 1.3.1, R_m in space plasmas is generally very high and is usually considered high enough for these plasmas to be considered collisionless. In the Sweet-Parker model reconnection is very slow; the model effectively predicting that reconnection is not an important process in the magnetosphere. There is a large body of evidence in the scientific literature (including this thesis) that suggests reconnection is an important process. A model was developed by Petschek (1964) where the diffusion region is shrunk to a much smaller size. In the Sweet-

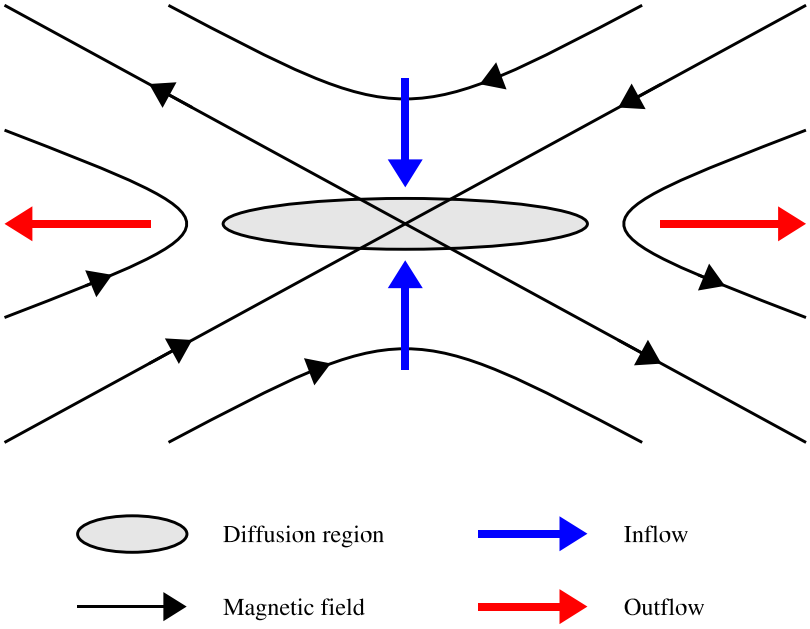

Figure 1.11: The magnetic field topology around an X-line in the Sweet-Parker model.

Parker model all the reconnecting material must pass through the diffusion regions, whereas in the Petschek model only a small fraction of the reconnecting material must do this. The diffusion region can therefore become much smaller. Most of the material abruptly changes direction from inflow to outflow at shocks (Fig. 1.12).

In this way the physics inside the small diffusion region in which the reconnection happens is not important, the solution can be constructed by analysing the MHD shocks away from the central X-point. For large Reynolds numbers, the Petschek reconnection rate is given by:

$$\mathcal{R}_P = \frac{\pi}{8} ln R_m \tag{1.29}$$

For a given magnetic Reynolds number, Petschek reconnection is a vastly more efficient process in which to merge magnetic field lines.

The first improvement on ideal or resistive MHD is to relax the neglect of the Hall term in Ohm's law (Lighthill, 1960). This allows the diffusion of the magnetic field from the ion fluid, but not the electron fluid, in the ion diffusion region. This

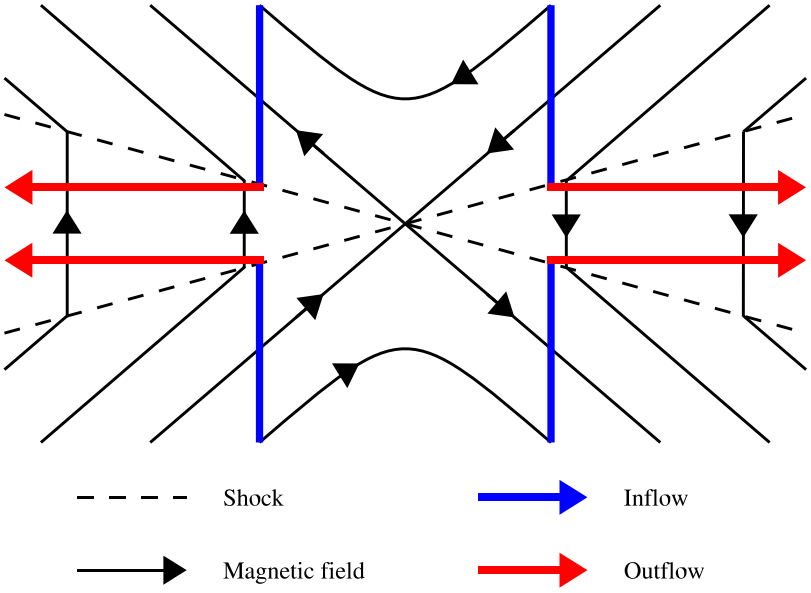

Figure 1.12: The magnetic field topology around an X-line in the Petschek model. A small diffusion region exists at the centre of the picture.

theory is known as Hall-MHD (Witalis, 1986) and has often been used in simulations (e.g. Yin et al., 2001).

1.6 Substorms

The substorm is a very important process in studies of space plasma physics in the magnetotail. The substorm process (Akasofu, 1964; Akasofu, 1968; McPherron, 1970) can be separated into three distinct phases, with the magnetotail dynamics being shown in Fig. 1.13.

Initially, the magnetosphere is in equilibrium. The first phase (panel 1), the growth phase, is where the magnetic flux stored in the tail lobes increases. This is usually associated with southward IMF B_Z and dayside reconnection (not shown in this figure). In fact, all that is required for a substorm growth phase is that more magnetic flux be added to the system on the dayside than is removed on the nightside. The increased amount of flux in the tail leads to a flaring of the tail lobes, which in turn leads to the pressure building across the magnetotail. Flux is added to

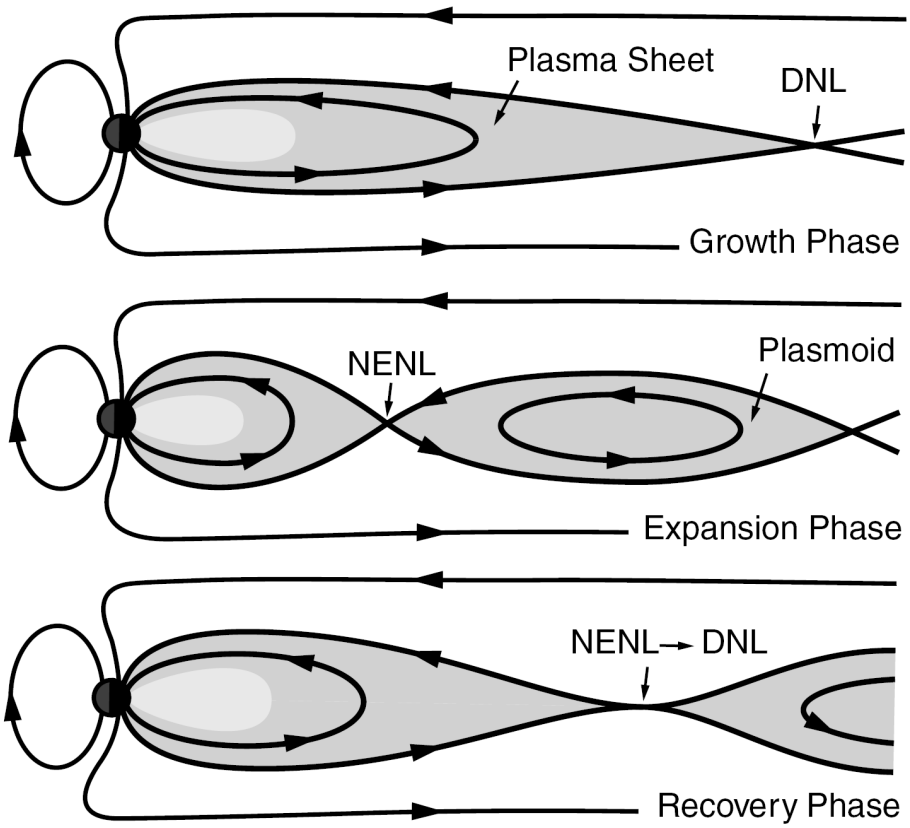

Figure 1.13: The evolution of a substorm. From equilibrium growth (panel 1), expansion (panel 2) and relaxation phases (panel 3). From Baumjohann and Treumann (1996).

the polar cap, which expands equatorwards (Russell, 1972; Cowley and Lockwood, 1992; Chisham and Freeman, 2003). The additional pressure exerted on the magnetotail is transferred to the plasma sheet and causes it to thin (e.g. Hones et al., 1967, Hones et al., 1984, Dewhurst et al., 2004).

This thinning of the plasma sheet leads to the formation of a Near Earth Neutral Line (NENL), an X-line with the same topology as Fig. 1.9, to form, generally considered to be located in the region of X = -20 to -30 R_E (Baker et al., 1996; Nagai et al., 1997). Associated with this NENL formation is the diversion of part of the current inside the plasma sheet via field aligned currents through the ionosphere (McPherron et al., 1973b), the Substorm Current Wedge (SCW). A large increase in the AE index, derived from the horizontal component of the magnetic field at the surface of the Earth and a measure of auroral current activity, is observed. In this

phase (panel 2), the expansion phase, the energy stored in the magnetotail is explosively released in reconnection at the NENL. Flux is removed from the polar cap, which contracts polewards. The aurora (Akasofu, 1964; Akasofu, 1968) and particle beams observed in the PSBL (Eastman et al., 1984; Eastman et al., 1985; Parks et al., 1998) at this time may be explained by acceleration at a reconnection X-line. In the NENL model (McPherron et al., 1973b; Baker et al., 1996), one or more X-lines will be formed due to a global reconnection electric field (see section 1.5.2). When the reconnection propagates out to the lobe magnetic field lines all the material tailwards of the X-line will move away from the Earth in the anti-sunward direction, often in the form of a large bubble of plasma and magnetic field, a plasmoid (Schindler, 1974). All the material Earthwards of the X-line will move towards the Earth, in a Bursty Bulk Flow (BBF) (Baumjohann et al., 1990a; Angelopoulos et al., 1992; Angelopoulos et al., 1994; Schödel et al., 2001). Observations by Slavin et al. (2002) revealed a close temporal correlation between Earthward BBFs and tailward plasmoid ejection using two spacecraft in the tail, suggesting that these phenomena where the result of the outflow from reconnection events. Dipolarisations of the magnetic field may be observed (Fairfield and Ness, 1970; McPherron et al., 1973a), associated with the reduction in the cross tail current caused by the SCW, where the field moves from a highly stretched Earthwards-tailwards configuration to a more dipolar-like configuration due to the reconnection further down tail and the propagation of material Earthwards.

The NENL then retreats down the tail with the solar wind flow to become the DNL in the final, or recovery, stage (panel 3). Plasma flows, of many hundreds of kms^{-1} are often observed (Angelopoulos et al., 1994) as the NENL passes the observing spacecraft. Other manifestations of this phase of the substorm are known, such as the flapping motions (Sergeev et al., 2006) associated with the energisation of the plasma sheet as well as a thickening of the plasma sheet (Bame et al., 1967).

Alternative substorm models exist, where the cause and effect discussed above

is different, the most popular being the Current Disruption model (see the review by Lui, 1996). In this model, a disruption of the cross-tail current, usually by some instability, causes the dipolarisation of the magnetic field close to the Earth via the SCW. This then propagates down the tail and causes an X-line to form. Unfortunately, the time resolution needed to confirm either (or both) model is smaller than the time resolution currently available (usually the resolution of imaging cameras to image the substorm onset time from images of the ionosphere). In the near future missions such as Double Star (Liu et al., 2005) or THEMIS, that use multiple spacecraft to achieve global magnetospheric coverage, should be able to add to this debate.

1.6.1 Flux ropes

As mentioned above, there is no reason why only one magnetospheric X-line may form in the tail. If the magnetic field lines in the magnetotail become close to anti-parallel over a large distance, many X-lines may form (Lee, 1995) in a process called Multiple X-point Reconnection (MXR). In this way the magnetic field between each X-line can form flux ropes (Elphic et al., 1986; Hughes and Sibeck, 1987; Slavin et al., 2003b), coiled ropes of magnetic field. These flux ropes will then be embedded in the outflow from the X-line. These flux ropes can cause bulges in the plasma sheet, Travelling Compression Regions (TCRs), observed as a transient plasma sheet excursion or distortions of the lobe magnetic field (Slavin et al., 1992; Slavin et al., 2003c; Owen et al., 2005). Flux ropes and TCRs are thus interpreted as evidence for reconnection in the magnetotail.

Chapter 2

Instrumentation and techniques

2.1 The Cluster mission and its experiments

The original Cluster I satellites were destroyed after the launch failure of Ariane 5 in 1996. A mission utilising the Cluster I flight spare, Phoenix, was proposed but it was decided that the aims of the original Cluster mission could not be achieved with one spacecraft. The decision was made in 1997 to rebuild the Cluster I mission, Cluster II.

The Cluster II (now generally referred to simply as 'Cluster') spacecraft were launched on the 16thJuly and the 9thAugust 2000 from the Russian cosmodrome in Baikonour, Kazakhstan. They were launched on two Soyuz rockets, each carrying two Cluster satellites. The spacecraft reached the first of their many tetrahedral constellations by the end of August, the mission being declared operational on 1stFebruary 2001 after commissioning.

Cluster is in a polar orbit with apogee and perigee at 19.6 and 4 R_E respectively. The plane of the orbit is fixed in inertial space. As the year evolves, the Earth sweeps through the fixed plane allowing full coverage of the magnetosphere. The orbits of each spacecraft are designed such that an optimised tetrahedron is formed for multi-spacecraft methods in different parts of the magnetosphere at certain points of the year. For example, the 'tail season' occurs between approximately

June and November, where the apogee is in the magnetotail. During this time the spacecraft cross the neutral sheet from the north to the south, and can spend many hours in the plasma sheet. However, apogee is not necessarily at the neutral sheet crossing location. As the plasma sheet is dynamic, the neutral sheet can in fact pass over the spacecraft more than once in one orbit, leading to multiple observations of the neutral sheet. The 'dayside season' occurs between approximately November and June, the tetrahedron being optimised for observations of the magnetopause, bow shock and cusp. At perigee the spacecraft follow each other on approximately the same trajectory, leading to the term 'string of pearls' configuration. This configuration can be used to perform temporal variation analysis, but is however not utilised in this thesis.

The separation of the individual Cluster spacecraft within the tetrahedron has changed throughout the mission. The periods studied in this thesis occurred during the 2003 tail season, during which the average separation between spacecraft was approximately 200 km in the plasma sheet.

The multi-spacecraft nature of Cluster can be used to provide a three dimensional viewpoint of plasma physics processes in various regions of the magnetosphere. Each spacecraft carries identical instrumentation making inter-spacecraft comparison of physical parameters at high time resolution theoretically simple, however this can become difficult in practice. The instrumental complement of each Cluster spacecraft is outlined in Table 2.1. Note that the DWP, EFW, STAFF, WBD and WHISPER form the wave experiment consortium.

This thesis utilises data from the PEACE, FGM, CIS and EFW instruments. As well as the electric field, the spacecraft potential can be measured by EFW and is sometimes used in the calculation of moments from the PEACE instrument (see section 2.2.5). These instruments are described in this chapter.

Instrument	Purpose
ASPOC	Spacecraft potential control
CIS	Ion velocity distributions
EDI	Electric field drift velocity
FGM	Magnetometer
PEACE	Electron velocity distributions
RAPID	High energy electron and ion velocity distributions
DWP	Wave processor
EFW	Electric field and waves
STAFF	Magnetic and electric fluctuations
WBD	Electric field and wave forms
WHISPER	Electron density and waves

Table 2.1: The instrumental complement of each Cluster spacecraft (after Escoubet et al., 2001).

2.2 PEACE

The Plasma Electron And Current Experiment (PEACE) detectors aboard Cluster (Johnstone et al., 1997; Fazakerley et al., 2007[1]) measure the full three dimensional electron velocity distribution function. In fact, each PEACE instrument consists of two 'top hat' sensors mounted on opposite sides of each Cluster spacecraft, as well as a Data Processing Unit (DPU). Both sensors can measure the distribution from 0.6 eV to 26 keV. The sensitivity of one sensor, the Low Energy Electron Analyser (LEEA), is lower that the other, the High Energy Electron Analyser (HEEA), in order to measure the higher fluxes generally seen at lower energies.

2.2.1 Top hat analysers

A top hat analyser consists of two nested hemispherical surfaces called deflection plates (see Fig. 2.1). If an electric field is set up between the two plates an electron (or in principle, an ion) with the appropriate energy will be able to pass around the gap. Electrons with other energies will hit the hemispherical surface and not be detected. In this way, by selecting the applied electric field, a top hat analyser can be 'tuned' to detect certain energies of electrons from the full 360° distribution. The

[1]Manuscript in preparation.

detection of a single electron is difficult, therefore two semi-annular Micro-Channel Plates (MCPs, grey rectangle in Fig. 2.1) are arranged such that an incoming electron will cause a cascade of secondary electrons, therefore amplifying the signal. With large enough gain, this cascade can be detected on a position sensitive read-out. The polar angle of the initial electron arrival direction will be measured from the position that the cascade is recorded on the read-out.

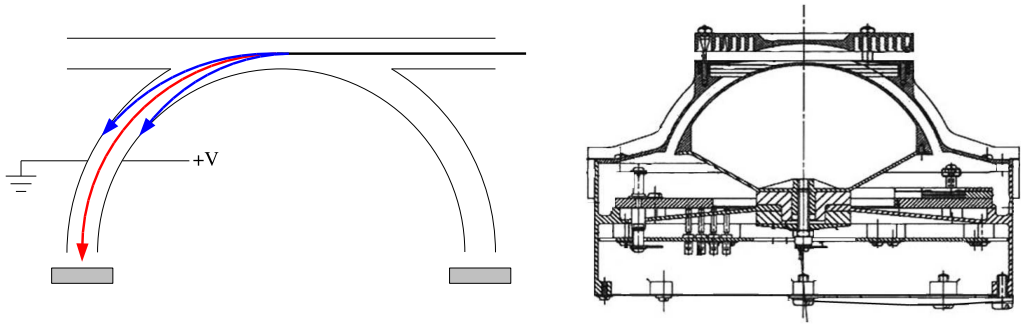

Figure 2.1: Cross-sectional schematic of top hat detector operation and a cross-section of one of the PEACE detectors (reproduced from Fazakerley et al., 2007). In the first figure, electrons with the 'correct' energy pass through the detector (trajectory marked red) and hit the semi-annular MCP (grey rectangle). Electrons at other energies strike the hemispheres and are not detected (trajectories marked blue). The hemispheres and annular MCP can be seen in the right hand figure.

LEEA has a lower Geometric Factor (GF) suitable for the higher fluxes typically seen at lower energy ranges. Physically, this is achieved by limiting the size of the input aperture. As the fluxes of higher energy electrons are (usually) smaller than that of lower energy electrons, the HEEA detector is constructed to have a larger GF (larger than that of LEEA by a factor of approximately 4).

Each top hat detector is mounted on the side of the spacecraft (Figure. 2.2) and can therefore only see 180° at any one time. As the spacecraft spins HEEA and LEEA combined can sample the full 3D distribution of electrons in a certain energy range every half-spin if the detectors measure the same energy range, or every single spin if the detectors measure different energy ranges.

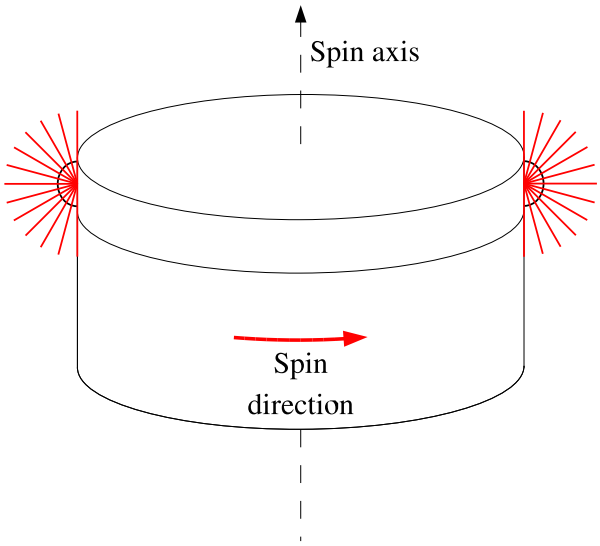

Figure 2.2: Detail of the location of the PEACE detectors. The detectors are marked as black semicircles, with their polar range and resolution (12 equally spaced bins) marked in red.

2.2.2 Resolution

The energy range of the sensors is from 0.6 eV to 26 keV in 88 levels. Between 0.6 and 10 eV there are 16 linear levels. The other 72 levels are logarithmically spaced by a factor of ~ 1.2. Each detector can sweep a maximum number of 60 levels at a time. The time during which the voltage is being increased to its starting voltage is known as the 'flyback period'. The point at which the spin 'starts' is controlled by specifying a delay from the Sun pulse, the sweep rate being synchronised to the spin rate to ensure that an integer number of sweeps is made per spin. Moreover, each sweep consists of an integer number of accumulation bins, of which there are 1024 per spin. The semi-annular detector ring is separated into 12 equal parts, meaning a 15° polar resolution.

Each sensor has four modes of operation: Low Angular Resolution (LAR), Medium Angular Resolution (MAR, the standard mode), High Angular Resolution (HAR) and Fixed Energy (FE). In FE mode the detectors can be set a constant energy level up to 1.8 keV. This mode is generally for operations use and thus will not be discussed here.

LAR

In LAR mode the full 4 π angular coverage is composed of a grid of 12 polar bins by 16 azimuthal bins. 60 energy samples are recorded in each sweep.

MAR

MAR is the standard mode of operation. The azimuthal angular resolution is higher, 12 polar bins by 32 azimuthal bins, whilst the time of the energy sweep is halved, 30 energy samples are recorded. Note that 60 energy levels are covered (as in LAR), but two of these levels are combined into one energy sample.

HAR

The angular resolution is again higher, 12 polar bins by 64 azimuthal bins, with the sweep time again halved, only 15 energy samples are recorded. Note that only 30 levels are covered, with two levels combined into one energy sample (similarly to MAR).

Table 2.2 and Fig. 2.3 detail the energy and angular resolution.

Mode	Energy			Angular resolution	
	coverage (levels)	resolution (levels bin^{-1})	samples (bins)	azimuthal (degrees)	polar (degrees)
LAR	60	1	60	22.500°	15°
MAR	60	2	30	11.250°	15°
HAR	30	2	15	5.625°	15°

Table 2.2: PEACE modes

In addition, each PEACE detector can be set to cover a different energy range. Fig. 2.4 shows some of these ranges. As discussed above, if the detectors cover the same energy range (b), products covering this energy range can be returned each half spin, although it can be seen in this case that the full energy range is not covered.

Each detector can be in different modes at different times. It is common in the magnetotail for HEEA to be in MAR mode covering high energies (34 eV to 26

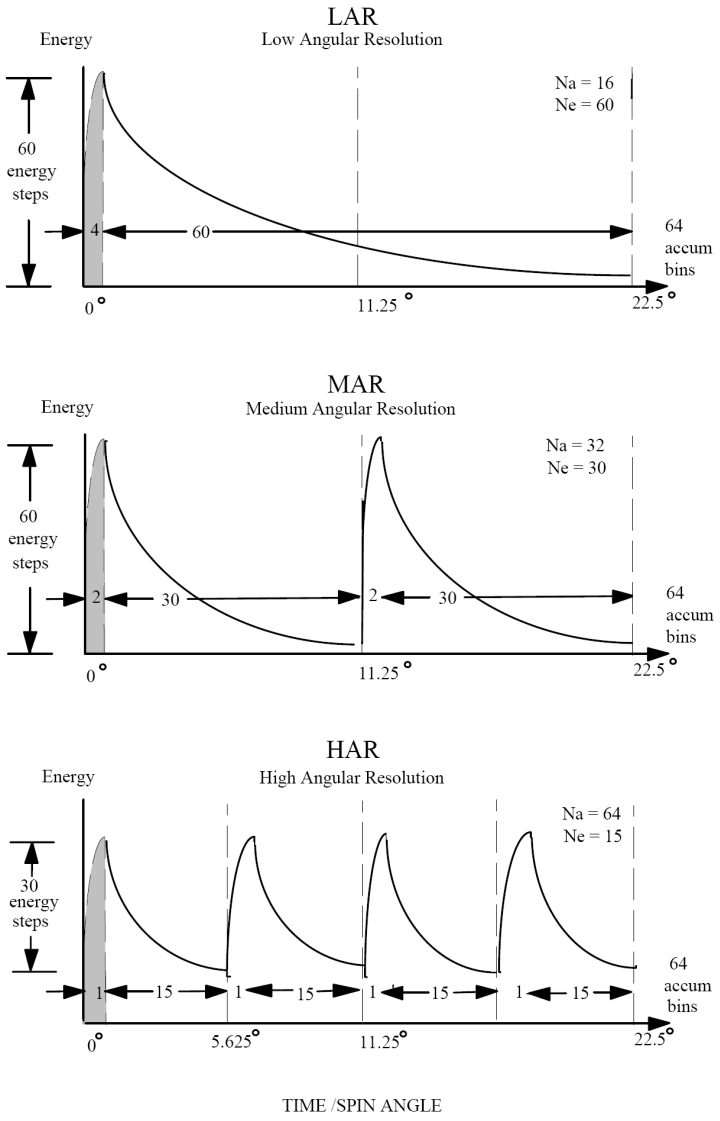

Figure 2.3: PEACE angular resolution modes from Johnstone et al. (1997)

keV, the top, overlap and bottom ranges indicated in Fig. 2.4) with LEEA in HAR mode covering an intermediate range (83 eV to 2.3 keV, the overlap range indicated in Fig. 2.4). In this way HEEA completely overlaps LEEA.

2.2.3 Telemetry

There are six different science telemetry output rates allocated to PEACE, known (also) as modes (Table 2.3).

In nominal operation, Cluster operates in normal mode (NM1), however there

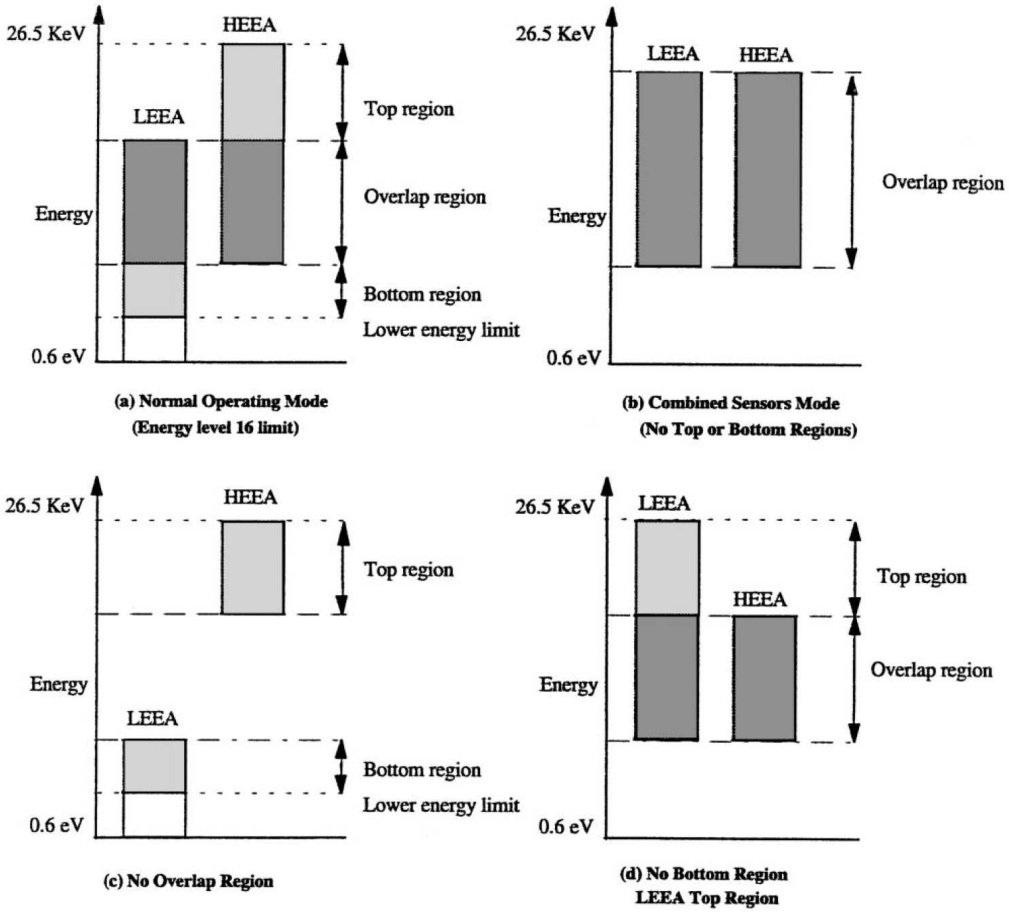

Figure 2.4: The different energy ranges that may be observed by the PEACE instrument. Adapted from Johnstone et al. (1997).

Mode	Bits telemetered per second
Normal mode 1	2515.42
Normal mode 2	1521.67
Normal mode 3	3540.22
Burst mode 1	15980.68
Burst mode 2	3658.23
Burst mode 3	1926.00

Table 2.3: Cluster mode operations

are infrequent burst mode (BM1) times designed to observe specific regions of the magnetosphere.

2.2.4 Other electron sources

When spacecraft are subject to solar ultraviolet radiation, photoelectrons can be emitted from the spacecraft via the photoelectric effect. This effect leads to the spacecraft having a positive potential (Pedersen, 1995; Szita et al., 2001; Torkar et al., 2001). Those electrons that have an energy larger than this potential are able to escape. However, electrons that are at a lower energy than this potential will be attracted back to the spacecraft or trapped in the vicinity of the spacecraft. These electrons can then enter the instruments and be detected. Note also that higher energy electrons that do not exit the spacecraft surface along the normal may enter straight into the detectors.

The spacecraft potential will be determined by the requirement to balance the current arriving at the spacecraft (electrons leaving via the photoelectric effect, depending on the level of light) with the current leaving the spacecraft (electrons being attracted by the positive spacecraft potential, dependent on this potential and the number density of electrons).

In the plasma sheet, the main concern of this thesis, the spacecraft potential is kept low by the high plasma density. In other areas of the magnetosphere, for example the magnetotail lobes, the spacecraft potential can become high due to the low plasma density.

If the spacecraft potential is non-zero, the electron velocity distributions measured by the PEACE detectors will be modified. This modification is a difference between the velocity distribution in the accelerated region near the spacecraft (the one that is measured) and the velocity distribution outside this region (the 'correct' distribution).

Depending on where the PEACE energy ranges are set, the energy of the space-

craft potential, and therefore the photoelectrons, is often, especially in the magnetotail plasma sheet, below the bottom of the energies measured by PEACE. In the calculation of ground moments (see section 2.2.5), the spacecraft potential, however small, is still taken into account due to the fact that it modifies the electron population. On-board moments do not have a spacecraft potential correction, but do exclude all electrons below 10 eV.

The PEACE instruments may also detect secondary electrons caused by the collision of high energy electrons with the insides of the instrument that may not have been deflected sufficiently by the electric field. If these secondary electrons have the appropriate energy to deflected correctly by the electric field then they will be detected. In addition, if solar ultraviolet enters the instrument, photoelectrons may be generated inside the instrument. These effects are minimised by the use of baffles, consisting of a series of plates inside the aperture (see right hand part of Fig. 2.1) as well as the use of a diffusely reflecting, absorbant coating on all internal surfaces. It is noted that LEEA has a smaller aperture which also reduces these factors.

The expected effect of both internal secondary electrons and photoelectrons is shown in Fig. 2.5. In the generation of ground moments, the spacecraft potential of 4 eV would be subtracted, whereas with on-board moments, all electrons with energies less that 10 eV (i.e. all those shown) are ignored.

2.2.5 Data products

If one is interested only in the macrophysical physical quantities (the moments), the most efficient use of telemetry would be to perform all calculation on-board the spacecraft and telemeter the produced macroscopic values. However, due to underlying physical reasons (such as multiple populations, non-zero spacecraft potential, photoelectrons) this is not always the most accurate method. To be of most advantage, the raw data must be telemetered to the ground and processed. As the PEACE instrument collects data at a rate of over 3 Mbits s^{-1} a significant amount of com-

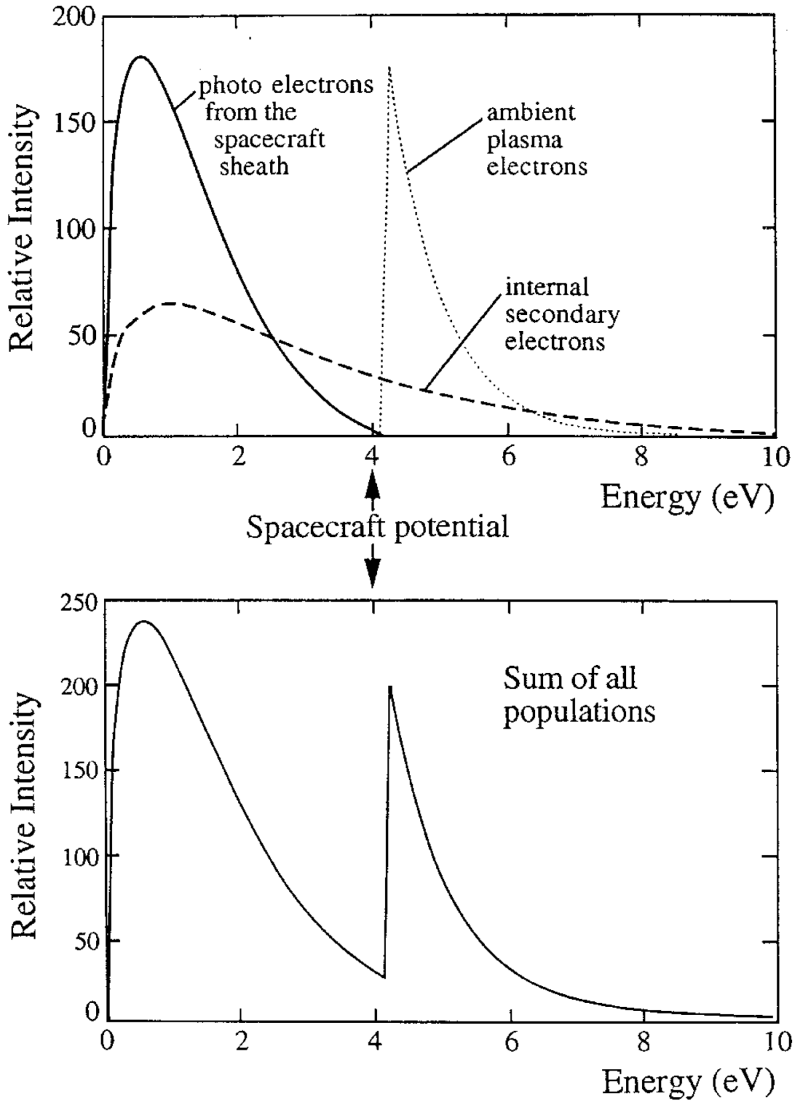

Figure 2.5: The different electron populations that may be observed by the PEACE instrument (from Johnstone et al., 1997). These effects must be considered when calculating moments of the distribution.

pression of the data must take place. A hierarchy of data products is therefore used, with different products being given different ranks to reflect their importance (Table 2.4).

Product	Size (bytes per spin)	Abbreviation
Moments (CORE)	168	MOM
s/c potential (estimated, CORE)	7	SCP
Pitch angle distribution	780	PAD
Low-energy reduced	192	LER
3D reduced resolution	2880	3DR
3D single sensor	variable	3DX
3D full resolution	23040	3DF

Table 2.4: PEACE data products

Moment calculations

If one can measure a 3D velocity distribution of particles, one can use a set of equations to derive macroscopic measurable quantities, such as density and bulk velocity (Baumjohann and Treumann, 1996; Paschmann et al., 1998). The distribution is a function of electron velocity, position and time. As the macroscopic quantities are a function of position and time only, they can be calculated by integrating over velocity. This integration is called taking moments. The ith moment has the form:

$$M_i(\mathbf{x}, t) = \int_0^\infty f(\mathbf{v}, \mathbf{x}, t)\, \mathbf{v}^i dv \tag{2.1}$$

Only the first few moments of the distribution are of scientific interest.

The zeroth order moment can be identified with the number density:

$$n = \int_0^\infty f(\mathbf{v})\, dv \tag{2.2}$$

The bulk flow velocity $\mathbf{v}_b$ is related to the first order moment:

$$\mathbf{v}_b = \frac{1}{n} \int_0^\infty \mathbf{v} f(\mathbf{v})\, dv \tag{2.3}$$

This flow is an average of the flow velocity of the particle species under consideration (i.e. electrons, protons). It is not an individual particle velocity (**v**) and therefore can be unrepresentative of the plasma if the distribution contains multiple populations.

The second order moment gives rise to the pressure (a tensor):

$$\mathsf{P} = m \int_0^\infty (\mathbf{v} - \mathbf{v}_b)(\mathbf{v} - \mathbf{v}_b) f(\mathbf{v}) dv \tag{2.4}$$

The heat flux vector (**q**) describes a flow of heat in a direction that may or may not be the direction of the main flow. It is the trace of the third moment (a dyad):

$$\mathbf{q} = \frac{m}{2} \int_0^\infty (\mathbf{v} - \mathbf{v}_b) \cdot (\mathbf{v} - \mathbf{v}_b)(\mathbf{v} - \mathbf{v}_b) f(\mathbf{v}) dv \tag{2.5}$$

Of course, for these products to be computed, the bulk velocity must first be computed. Therefore, the standard moments (Eqns. 2.6 to 2.9), which do not contain the bulk velocity, are computed first.

Density:

$$n = \int_0^\infty f(\mathbf{v}) dv \tag{2.6}$$

Particle flux:

$$n\mathbf{v}_b = \int_0^\infty \mathbf{v} f(\mathbf{v}) dv \tag{2.7}$$

Stress tensor:

$$\mathsf{P}' = m \int_0^\infty \mathbf{v}\mathbf{v} f(\mathbf{v}) dv \tag{2.8}$$

Generalised heat flux:

$$\mathbf{q}' = \frac{m}{2} \int_0^\infty (\mathbf{v})^2 \mathbf{v} f(\mathbf{v}) dv \tag{2.9}$$

The relative moments (Eqns. 2.2 to 2.5) are then computed from these standard moments via Eqns. 2.10 to 2.13 (Gowen and Birdseye, 1988):

$$n = n \tag{2.10}$$

$$\mathbf{v}_b = \mathbf{v}_b \tag{2.11}$$

$$\mathsf{P} = \mathsf{P}' - mn\mathbf{v}_b\mathbf{v}_b \tag{2.12}$$

$$\mathbf{q} = \mathbf{q}' - \mathbf{v}_b\left(\frac{Tr\mathsf{P}'}{2}\right) - \mathbf{v}_b \cdot \mathsf{P}' + mnv^2\mathbf{v}_b \tag{2.13}$$

CORE

Moment calculations are performed on-board the spacecraft, but, as mentioned above, may be inaccurate. These on-board moments are then telemetered as part of CORE. CORE is always telemetered and has been designed such that it can be transmitted in the mode with least PEACE assigned telemetry. As discussed previously, the on-board method does not take into account the spacecraft potential and simply discards the energy levels below 10 eV. This is sometimes enough to discard any photoelectrons, but also some useful data in some cases. If the spacecraft potential rises above this level the moments can become contaminated with photoelectrons. This process is automated and cannot be controlled from the ground. If the onboard moments have been calculated using out-of-date calibrations they cannot be re-calculated using improved calibrations (which can be uploaded to the spacecraft).

PAD

When the magnetic field is in the azimuthal view of HEEA or LEEA, the minimum required data to construct a 2D distribution are recorded, called PAD. PEACE is sent the magnetic field data via the inter-experiment link one spin later. To record data from the appropriate zones for the construction of the PAD data product, PEACE must therefore assume that the magnetic field does not vary significantly from one spin to the next. If the magnetic field does change significantly PAD can give misleading results. However, with high resolution magnetic field data, this product, and indeed any 2D or 3D product, can be reconstructed on the ground to produce an unambiguous 2D distribution. In this reconstruction however, not necessarily all pitch angles will be recovered.

LER

The Low Energy Range (LER) consists of the linear regime at the lower end of the energy scale measured by PEACE (0.6 eV $<$ Energy $<$ 10 eV). The spacecraft potential, if smaller than 10 eV, can be estimated from LER by finding the energy bin at which the gradient between neighbouring points in the energy spectra (starting from the highest energy) turns positive (see Fig. 2.5). The algorithm then continues down the energy spectrum and finds the energy bin with the lowest count. This energy level is identified with the spacecraft potential. It is this estimate that is telemetered by CORE. However, the spacecraft potential measured by EFW (section 2.5) is normally used in preference to this method.

3D distributions

3DF is the full resolution 3D velocity distribution. Owing to the large product size required to contain the high energy and angular resolution it is rarely telemetered. A reduced version (3DR) is produced where each dimension is reduced in resolution. For example, in MAR mode each dimension is reduced by half, leading to a

data product one eighth the size. In NM1 even 3DR is not telemetered every spin. Indeed, larger data products, such as the 3D data products, can be broken up and telemetered in several segments before being reassembled on the ground. These 3D distributions telemetered over a number of spins in normal mode are useful for checking on-board moment calculations. Due to the extra telemetry available because of an inactive CIS instrument (see section 2.4) on Cluster 2, 3DR is available every spin in normal mode. The EDI instrument is also inactive on Cluster 4 which means that PEACE is able to telemeter 3DR at higher resolution than Clusters 1 and 3, but still not at spin resolution. This is possible due to the flexible nature of the PEACE telemetry mode structure. Other instruments would be unable to modify their telemetry methods to use additional telemetry.

In burst mode it is possible to telemeter 3DR or 3DX every spin. 3DX is a product that can be modified to fit the available remaining telemetry and is the full 3DF distribution summed over polar (3DXP) or energy (3DXE) bins.

In the magnetotail in burst mode it is normal for all spacecraft to telemeter 3DX from all HEEA sensors. For the LEEA sensors, Clusters 2 and 4 to telemeter 3DX whereas Clusters 1 and 3 telemeter 3DR. In this way the moment calculations can be repeated on the ground. These calculations can be done at a later stage with knowledge of the spacecraft potential from EFW, as well as having improved calibrations. The proper calibration of 3D distributions is vital for the use of novel multi-spacecraft techniques.

2.2.6 The V_Z problem

When the moments from PEACE are compared with other instruments aboard the Cluster spacecraft, a number of inconsistencies have been noted. The number density of electrons from PEACE compared to WHISPER is sometimes different (this problem is due to GF calibration errors) in situations where they should be similar. In addition, a difference in Z directed velocity (in GSE) between CIS and PEACE

can sometimes be significant (this problem is due to inter-anode calibration errors). It is noted that these inconsistencies may be due to errors in the calibrations of the PEACE, CIS or WHISPER instruments.

The spacecraft spin plane is close to the XY GSE plane. In the calculation of the velocity in the X direction for example, the velocity of electrons in the +X direction is compared to that in the -X direction. These two measurements are taken with the same anode in the PEACE detector. Essentially, the velocity moment is calculated by the summation of these velocities. Any small constant calibration error is eliminated in the differencing. This process is similar for the entire XY (GSE) plane. However, as the Z direction is out-of-plane, the summation in the Z direction is performed with different anodes. Therefore, any small relative calibration error between the anodes will be important, giving a V_Z offset. This problem, the so-called 'V_Z problem' is spacecraft, sensor, energy and MCP gain dependent, being more pronounced at higher energies. Figure 2.6 shows a plot of electron velocity from PEACE and proton velocity from CIS-CODIF. A large difference can be seen in the Z component of the velocity. In some circumstances the velocities of electrons and ions are unequal (i.e. current), but a difference on this scale is probably an unphysical artifact due to the V_Z problem. Indeed, even if a difference between proton and electron velocities is physical, the PEACE detectors should approximately agree if they are in the same physical region (as in this example, where the spacecraft are in the plasma sheet with small separation). For this reason, intervals where agreement are expected are chosen in the calibration of data.

A large amount of effort has been put into the proper calibration of moments by the PEACE team. Initially, a least-squares fit was used in order to determine certain 'correction factors'that, when multiplied by the phase space density, made the PEACE density agree with the CIS or WHISPER density and the PEACE velocity agree with the CIS velocity. These correction factors were calculated for each anode from each sensor, and were gain and energy dependent. However, due to the

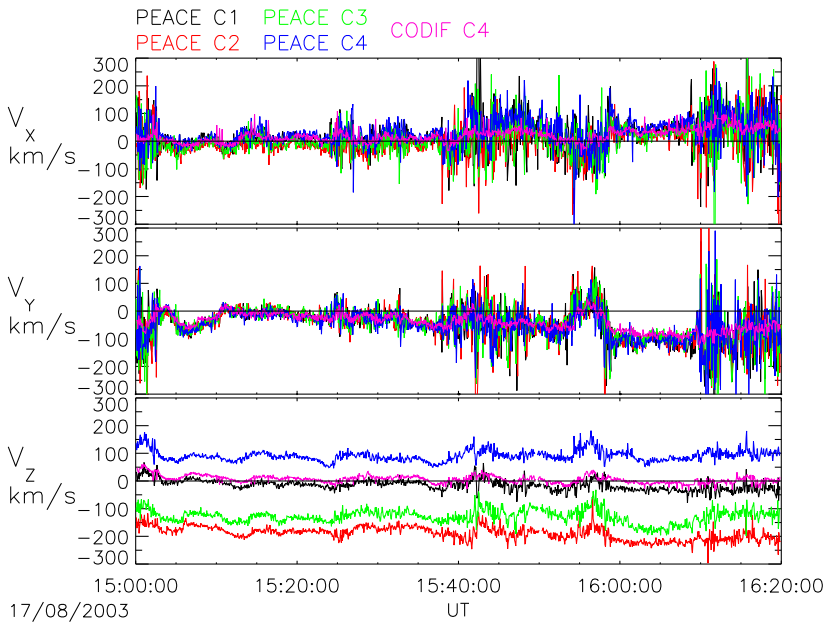

Figure 2.6: PEACE and CIS velocity before V_Z correction.

irreproducibility of the results, a new method has recently been implemented.

In this new method, the inter-anode calibration is improved without the need to fit PEACE velocities to CIS velocities. Intervals are chosen where the isotropy (or anisotropy) of the plasma is approximately constant, and a parabola is used to fit the differential energy flux versus pitch angle profile. Correction factors can be derived by realising that each anode should give the same profile. Producing histograms of velocity (not shown) with this method shows that the velocities are centred close to zero, having been significantly offset from zero previously. These correction factors are energy and gain dependent. PEACE is still compared to WHISPER in order to improve the density.

Figure 2.7 shows the same quantities as shown in Fig. 2.6 after the PEACE team has applied various improved calibrations. It is noted that the electron velocities are more variable than the ion velocities. This is due to the fact that the thermal velocity of electrons is generally much higher than the bulk velocity, whereas it is comparable for ions. As will be discussed below, many of the methods in this thesis rely on differencing techniques from spacecraft to spacecraft, therefore an accurate

determination of electron moments from each spacecraft is necessary.

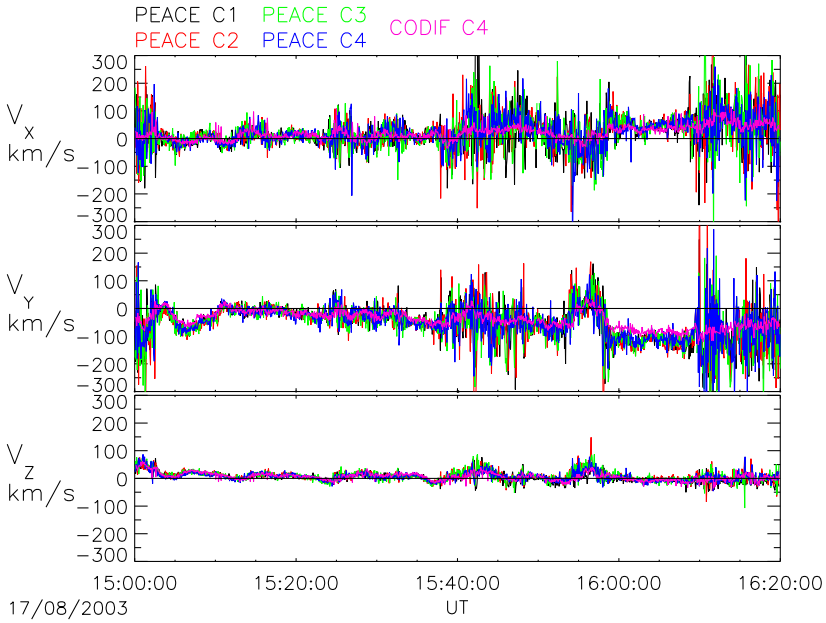

Figure 2.7: PEACE and CIS velocity after V_Z correction.

2.3 The Fluxgate Magnetometer (FGM)

Each Cluster spacecraft carries an identical FGM instrument (Balogh et al., 2001). The instrument consists of two tri-axial fluxgate magnetic field sensors located on one of the two radial booms of the spacecraft and a Data Processing Unit (DPU) located on the main instrument platform of the spacecraft. The outboard sensor, located at the end of the 5 m boom, is designated as the primary sensor in normal circumstances, but either sensor can be designated the primary should one fail.

There are four magnetic field internal ranges of operation of the instruments, detailed in Table 2.5. In addition, one extra mode exists, a low resolution and high range mode that was used in calibration on the ground where the magnetic field is $\sim$30 000 nT, but is not used aboard Cluster

The primary sensor samples the magnetic field vector at a rate of 201.793 vectors sec^{-1}. Unfortunately, this full rate cannot be telemetered to the ground due to the available telemetry rate. The 201.793 vectors sec^{-1} is therefore re-sampled at a

Range No.	Range	Resolution
2	-64 nT to + 63.97 nT	7.8×10^{-3} nT
3	-256 nT to + 255.87 nT	3.1×10^{-2} nT
4	-1024 nT to + 1023.5 nT	0.125 nT
5	-4096 nT to + 4094 nT	0.5 nT

Table 2.5: FGM operation ranges (adapted from Balogh et al., 2001).

lower rate in order for it to be telemetered, the most common lower rates are 22.417 (full time resolution divided by nine) and 67.25 vectors $\sec^{-1}$ (full time resolution divided by three). These are telemetered to the ground in NM1 and BM1 respectively. The Microstructure Analyser (MSA) was planned to be used for storing short periods of high resolution data and also to store, during periods of no telemetry acquisition (such as in the early stages of the Cluster mission where only 50% of data per orbit was telemetered to Earth), data at spin resolution from the primary sensor. An additional 27 hours of data can be stored in this way. This data can be telemetered during burst mode 3 soon after the signal is regained.

The magnetic field vectors are converted from a spinning reference frame to a despun frame in geophysical coordinates, such as GSE or GSM, and scientific units (nT), on the ground using simple algorithms (note that there is a B_Z problem, analogous to the PEACE V_Z problem, with the magnetometers).

2.4 The Cluster Ion Spectrometry Experiment (CIS)

CIS is capable of measuring three dimensional ion distributions at spin resolution and mass per charge resolution (Reme et al., 2001). It consists of two top hat based detectors, the Hot Ion Analyser (HIA, very similar to PEACE) and the time-of-flight COmposition and DIstribution Function analyser (CODIF) in addition to a Data Processing System (DPS).

2.4.1 HIA

HIA has two 180° sections, which look in a plane parallel to the spin axis, known as high and low sensitivity ('high G' and 'low g' respectively). These sections are different in the polar resolution that they provide, but have the same azimuthal resolution of 5.625°. The azimuthal resolution arises because a two dimensional distribution can be recorded every 62.5 ms (the high voltage sweep rate) as the spacecraft spins. In this way, a full three dimensional distribution can be measured every spin. The energy range is from 5 eV q^{-1} to 32 keV q^{-1}, with no differentiation between ions of different mass/charge ratio.

In high G section the 180° polar range is divided into 16 equal sections of 11.25°, whereas the low g section has 8 central 5.625° sections, surrounded by 8 sections of 11.25°. This leaves two blank sections towards the spin axis with no coverage. In reality, ground calibration work revealed that these angles were 5.1° and 9.7°. High G is meant for hot plasmas, whereas the low g is meant for the solar wind.

2.4.2 CODIF

CODIF consists of a top hat analyser to measure the energy per charge and a time of flight section that provides information about the mass/charge ratio. CODIF, like HIA, is split into two sections with different sensitivities to cover the large dynamic range required to observe ions both in the magnetotail lobes and the plasma sheet or magnetosheath. The sensitivity is different by a factor of approximately 100. One section will therefore have a statistically meaningful number of counts at any given time. Each section consists of 8 polar sections, giving a polar angular resolution of 22.5°. Typically, the instrument records the velocity space distributions of H^+, He^+, He^{2+} and O^+ in an energy range of 15 and 38 keV q^{-1}.

CODIF incorporates a Retarding Potential Analyser (RPA) in the aperture in order to extend the range of the instrument to below 15 eV q^{-1}, down to the spacecraft

potential. The RPA consists of a pre-acceleration region to accelerate low energy ions to energies where they can be measured by the main sensors. When the RPA is used, only data from this range are recorded by CODIF. This mode is rarely used.

2.4.3 Moments

The transmission of three dimensional distributions is not always possible at spin resolution. Therefore, like PEACE, some data processing is done on-board to produce moments that can be telemetered at spin resolution. CIS telemeters the following moments from HIA and CODIF (for four masses); particle density, three components of the velocity, six unique components of the momentum flux tensor and the ion heat flux tensor. From this the full ion pressure tensor can be derived (see section 2.2.5 for further details of this process). The limiting factor for the CIS on-board moments, like PEACE, is the finite energy and angular resolution, the limited energy range and problems with counting statistics.

Tables 5 and 6 in Reme et al. (2001) detail the many different telemetry products, consisting of on-board moments, one, two and three dimensional distribution and pitch angle distributions. Much flexibility exists in the selection of which products to telemeter. The products to be telemetered are selected according to the spacecraft telemetry mode (which may be different on different spacecraft), bit-rate sharing between HIA and CODIF, and the plasma environment (for example energy, angle and time resolutions can be optimised to extract the maximum amount of useful data from a time period). It is noted that the plasma environment is predicted by various models and can sometimes lead to inappropriate products being telemetered.

If in burst mode, spin resolution three dimensional distributions can be telemetered. This allows the production of ground calculated moments that use improved calibrations. These ground moments are generally better than on-board moments (however, many different caveats to this statement exist and depend on the period of interest). If the spacecraft is in normal mode a three dimensional distribution

will be telemetered at a lower rate than the spin rate. These distributions can also be used to produce ground moments and can act as a check on the validity of the on-board moments.

The functioning CIS instruments in 2003 (the season investigated in this thesis) are: Cluster 1, HIA and CODIF; Cluster 3, HIA; Cluster 4, CODIF.

2.5 The Electric Fields and Waves instrument (EFW)

Each Cluster spacecraft carries an identical EFW instrument. Each instrument consists of four 8 cm spherical sensors deployed on 45.2 m cables in the spin plane. In addition, there are four deployment units (a rotating reel for the cable and a motor) and a separate electronic unit. The EFW instrument can be used in two ways, to measure voltage and current.

A measurement of the electric field is made by measuring the potential drop from one sensor to the another. The individual probe potentials are sampled at 5 s^{-1} and, depending on the telemetry mode, the potential difference between selected probe pairs at 25 s^{-1} (NM1) or 450 s^{-1} (BM1). One probe failed on Cluster 1 (28thDecember 2001) and on Cluster 3 (29thJuly 2002) which meant that until a 'work-around'was implemented on the 29thSeptember 2003 no high time resolution data was recorded on these spacecraft. However, as this only affected one probe, spin resolution is generally available. As the probes are in the spin plane, the electric field measured by EFW is 2D. Corrections and assumptions must therefore be made to construct this into GSE or GSM, such as correcting for the fact that the spin plane differs by a few degrees to GSE (to avoid shadowing of the probes) and subtracting the spacecraft-motion-induced electric field ($-\mathbf{v}_{sc} \times \mathbf{B}$).

In addition, if it can be assumed that there is no parallel electric field, i.e. $\mathbf{E}.\mathbf{B} = 0$, then the third component (out of the plane, E_Z) can be reconstructed:

$$E_Z = -\left(\frac{B_X}{B_Z}\right) E_X - \left(\frac{B_Y}{B_Z}\right) E_Y \tag{2.14}$$

If B_X/B_Z or B_Y/B_Z is large then small errors in E_X or E_Y will be amplified, leading to an inaccurate E_Z. Therefore, care must be taken when the magnetic field is close to the spin plane (i.e. B_Z is small).

The spacecraft potential can also be measured by the EFW instrument. The spacecraft potential measured by EFW is in fact the potential difference between the probe and the spacecraft. In most situations this is approximately equal to the potential difference between the plasma and the spacecraft, the real spacecraft potential. This can be sampled at the rate 5 s^{-1}.

By voltage biasing the probes, and by stepping this bias, the current-voltage characteristics of the plasma can be measured to calculate the electron temperature and density. A positively biased probe collects an electron current in proportion to the plasma density, assuming that the electron temperature is constant. Variations in this density can be observed as variations in the current collected. Again, problems exist with photoelectrons, therefore this mode is mainly useful in dense plasma environments (e.g. the plasmasphere, magnetosheath) where the spacecraft potential is low.

2.6 Multi-Spacecraft Methods

As mentioned earlier, Cluster is a multi-spacecraft mission. This aspect of the mission allows the use of a novel set of techniques and methods to, for the first time, untangle space versus time ambiguities. Much of the work detailed below (and other novel techniques) uses methods described in Paschmann and Daly (1998).

2.6.1 Timing

By noting certain corresponding 'events' in the four Cluster spacecraft data sets occurring at different times, it is possible to derive the velocity of a postulated surface through the tetrahedron. The particular analysis outlined here is valid when the separation of the spacecraft is small enough that the surface being investigated can be assumed to be planar and moving at a constant velocity. Other possible assumptions lead to further methods, for details see Paschmann and Daly (1998).

Perhaps the simplest method of doing this is the method described in Harvey (1998). In this methodology it is assumed that a discontinuity lies in a plane defined by its normal, $\boldsymbol{n}$, and that the discontinuity is moving in the direction $\boldsymbol{n}$ with velocity $\boldsymbol{V}$. The discontinuity is observed at spacecraft α at time t_α which is located at position $\boldsymbol{r}_\alpha$.

If spacecraft 3 is arbitrarily defined as the reference spacecraft, during time $(t_\alpha - t_3)$ the discontinuity moves the distance $\boldsymbol{V}(t_\alpha - t_3)$ along the normal direction. This is equal to the projection of the separation distance $(\boldsymbol{r}_\alpha - \boldsymbol{r}_3)$ onto $\hat{\boldsymbol{n}}$. Therefore:

$$(\boldsymbol{r}_\alpha - \boldsymbol{r}_3)\hat{\boldsymbol{n}} = \boldsymbol{V}(t_\alpha - t_3) \tag{2.15}$$

The above is generalised after considering all four spacecraft:

$$\mathsf{D}\frac{\hat{\boldsymbol{n}}}{\boldsymbol{V}} = \boldsymbol{T} \tag{2.16}$$

Here D and $\boldsymbol{T}$ are the matrix and vector:

$$\mathsf{D} = (\boldsymbol{r}_1 - \boldsymbol{r}_3,\ \boldsymbol{r}_2 - \boldsymbol{r}_3,\ \boldsymbol{r}_4 - \boldsymbol{r}_3) \tag{2.17}$$

$$\boldsymbol{T} = \begin{pmatrix} t_1 - t_3 \\ t_2 - t_3 \\ t_4 - t_3 \end{pmatrix} \tag{2.18}$$

If the spacecraft are not co-planar then the set of equations is solved by finding the inverse of D:

$$\frac{\hat{\boldsymbol{n}}}{\boldsymbol{V}} = \mathsf{D}^{-1}\boldsymbol{T} \tag{2.19}$$

2.6.2 Spatial gradients

By using a least squares fit, a linear approximation to the spatial gradients inside the spacecraft tetrahedral volume (Harvey, 1998) can be made.

Let $\boldsymbol{k}$ be the spatial gradient of x so that:

$$k_l = \frac{\partial x}{\partial r_l} \tag{2.20}$$

where α is the spacecraft number; $1 \leq \alpha \leq N$. The criterion for optimising the value of $\boldsymbol{k}$ is that:

$$S = \sum_{\alpha=1}^{N}\sum_{\beta=1}^{N} = \left[\boldsymbol{k}\cdot(\boldsymbol{r}_\alpha - \boldsymbol{r}_\beta) - (x_\alpha - x_\beta)\right]^2 \tag{2.21}$$

be minimised.

The least squares value of the gradient is therefore obtained from;

$$k_l = \frac{1}{N^2}\left[\sum_{\alpha\neq\beta}(x_\alpha - x_\beta)(r_{\alpha k} - r_{\beta k})\right]\mathsf{R}_{kl}^{-1} \tag{2.22}$$

where the symbol $\sum_{\alpha\neq\beta}$ indicates the summation over all $N(N-1)/2$ independent terms with $\alpha \neq \beta$

R_{kl} is known as the volumetric tensor:

$$\mathsf{R}_{kl} = \frac{1}{N}\sum_{\alpha=1}^{N} r_{\alpha j} r_{\alpha k} \tag{2.23}$$

In the remainder of Section 2.6.2 a number of applications of equation 2.22 will be discussed.

Application: The Curlometer

Perhaps the most widely used multi-spacecraft technique in the Cluster community is the Curlometer (Robert et al., 1998; Dunlop et al., 2002).

This technique estimates the current (**j**) from a knowledge of the magnetic field (**B**) via the simplified Ampere's Law (1.20):

$$\nabla \times \mathbf{B} = \mu_0 \mathbf{j} \tag{2.24}$$

Or in full:

$$\mathbf{j} = \frac{1}{\mu_0}\left[\left(\frac{\partial B_Z}{\partial Y} - \frac{\partial B_Y}{\partial Z}\right)\hat{\mathbf{i}},\ \left(\frac{\partial B_X}{\partial Z} - \frac{\partial B_Z}{\partial X}\right)\hat{\mathbf{j}},\ \left(\frac{\partial B_Y}{\partial X} - \frac{\partial B_X}{\partial Y}\right)\hat{\mathbf{k}}\right] \tag{2.25}$$

where $\hat{\mathbf{i}}, \hat{\mathbf{j}}$ and $\hat{\mathbf{k}}$ are unit vectors along the X, Y and Z directions.

Each of these terms are in the form Eqn. 2.20 and can be solved by Eqn. 2.22.

The central assumption in the Curlometer technique is that there exists a linear field gradient between the spacecraft, implying that over the spacecraft tetrahedron the current is constant. The accuracy of the derived current can only be determined by noting the deviation of the measured current from a model current. However, with no *a priori* knowledge of the field to be observed, the quality of the result must be determined in other ways. As the divergence of the field should be zero, the calculated divergence of the magnetic field is a good quality indicator to use in place of the error. There is no direct one-to-one correlation between the error and the divergence of the magnetic field but it can be used in place of the error for simple current structures such as flux ropes. Many caveats to this statement exist and are detailed in Robert et al. (1998) and Dunlop et al. (2002). The error in the Curlometer current is mainly dependent on the spatial gradients of the current structure and the spatial sampling of the spacecraft. The assumption that the current is constant over the tetrahedron is most likely to be valid when the spacecraft separation is small, as

in the 2003 tail season.

The best spatial sampling comes when the Cluster spacecraft are in a regular tetrahedral formation. The spatial sampling is characterised with the use of the elongation (E) and planarity (P) parameters. These parameters, ranging from 0 to 1, define a suite of spacecraft configurations. The optimum configuration for most multi-spacecraft techniques is the 'pseudo-sphere', characterised by $\sqrt{E^2 + P^2}$ below ~ 0.4. Robert et al. (1998) and Dunlop et al. (2002) conclude that, if the spacecraft separation is small compared to the current structure being observed and the tetrahedron is regular (taken here as $\sqrt{E^2 + P^2}$ being small), the divergence is a good indicator of the quality of the result in place of the error. By dividing the divergence by the curl of the magnetic field a quantity is produced that is here identified with the relative error, χ, in the Curlometer result:

$$\chi = \frac{|\nabla . \mathbf{B}|}{|\nabla \times \mathbf{B}|} \tag{2.26}$$

Application: Tensor Divergence

The above method may be extended to include other calculations. For example, in Ohm's law (Eqn. 1.19) one term consists of the divergence of the electron pressure tensor ($\nabla . \mathsf{P}_e$).

In Cartesian coordinates, the divergence of a tensor, T, takes the form of:

$$\begin{aligned}
(\nabla . \mathsf{T})_X &= \frac{\partial T_{XX}}{\partial X} + \frac{\partial T_{YX}}{\partial Y} + \frac{\partial T_{ZX}}{\partial Z} \\
(\nabla . \mathsf{T})_Y &= \frac{\partial T_{XY}}{\partial X} + \frac{\partial T_{YY}}{\partial Y} + \frac{\partial T_{ZY}}{\partial Z} \\
(\nabla . \mathsf{T})_Z &= \frac{\partial T_{XZ}}{\partial X} + \frac{\partial T_{YZ}}{\partial Y} + \frac{\partial T_{ZZ}}{\partial Z}
\end{aligned} \tag{2.27}$$

Again, each of these terms are in the form Eqn. 2.20 and can be solved by Eqn. 2.22, subject to similar linear variation assumptions as the Curlometer. In Vogt and

Paschmann (1998) the accuracy of plasma moment derivatives are discussed. Inaccuracies come from two factors; the error in the spacecraft position, and the error in the moments themselves (i.e imperfect calibration of the instruments). These authors found that the errors in the moments were the dominating factor. If spatial gradients of plasma quantities are to be calculated, the quality of the calibrations is paramount.

Therefore, spin resolution 3D distributions must be telemetered to the ground so that the highest quality spin resolution moments can be generated. This situation exists only when the spacecraft are in burst mode. A small separation between the spacecraft is also required for the assumptions of the linear estimator method (i.e. a linear gradient between the spacecraft) to be valid. Therefore, the most appropriate moments to use in the calculation of the $\nabla . \mathsf{P}_e$ term are those from burst mode periods in 2003, where the spacecraft are at their smallest average separation to date. Unfortunately, this limits the size of the available database.

Chapter 3

Flux ropes in the magnetotail

3.1 Introduction

Flux ropes have been interpreted as evidence for multiple X-line reconnection (MXR) in the near-tail associated with substorms (e.g. Elphic et al., 1986; Slavin et al., 2003a; Slavin et al., 2003b; Deng et al., 2004). The study of the formation and evolution of flux ropes, and therefore MXR, is important in learning more about the development of the current sheet during the substorm process.

In MXR, instead of creating one single X line in the tail, the conditions required for reconnection can be satisfied in numerous places, creating a number of X lines (Fig. 3.1).

Given an IMF B_Y component which penetrates into the tail (Hughes and Sibeck, 1987), flux ropes can be created between such X lines. As Schindler (1974) first noted, one X line will generally reconnect plasma sheet field lines more rapidly than others. Reconnection at this X line will be first to propagate out to open field lines in the lobe, thus becoming the single dominant magnetotail X line. This X-line then produces Alfvénic jets in the Earthward and tailward directions. The newly-formed flux ropes between the remaining X lines will be embedded in these flows and thus move away from the point at which they were created.

In this simplest picture, the cores of the flux ropes are nominally directed across

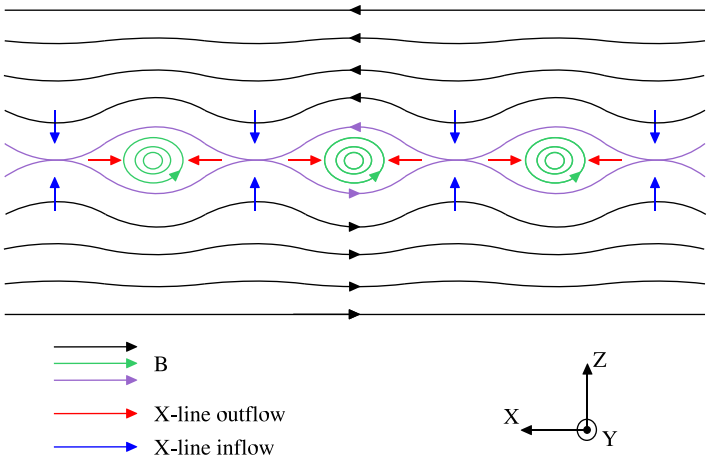

Figure 3.1: Magnetic topology and X-line in/outflow in multiple X-line reconnection (MXR). Plasma sheet magnetic field lines, currently reconnecting magnetic field lines and reconnected magnetic field lines are marked in black, purple and green respectively. The inflow of magnetic field and plasma is in the direction of the blue arrows, with the outflow of the X-line being in the direction of the red arrows. Given an IMF B_Y component which penetrates into the tail (Hughes and Sibeck, 1987), the green magnetic field lines become helices and are known as flux ropes.

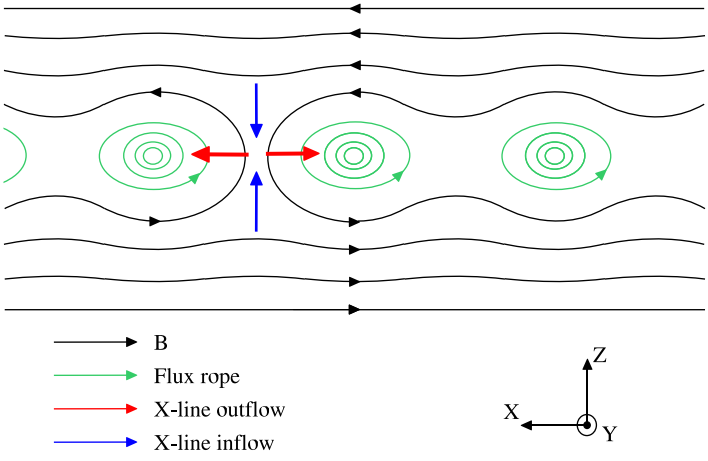

Figure 3.2: One X-line reconnects plasma sheet field lines quicker and becomes the dominant magnetotail X line. This X-line then produces Alfvénic jets in the Earthward and tailward directions.

the tail (i.e. mainly in the GSM Y direction) and the flux ropes travel towards or away from the Earth (i.e. mainly in the GSM X direction), depending on which side of the dominant X line they are located.

The gross, large scale properties of magnetotail flux ropes have been studied with the use of single spacecraft techniques (Elphic et al., 1986; Moldwin and Hughes, 1991; Slavin et al., 1995; Slavin et al., 2003a), but only recently have their small-scale properties been investigated with Cluster (Slavin et al., 2003b; Zong et al., 2004; Eastwood et al., 2005; Walsh et al., 2007; Lui et al., 2007). Observations of these flux ropes are characterised by a bipolar B_Z signature, caused by the magnetic structure moving past the spacecraft, and often show a large increase in the magnitude of **B** caused by a strong core field. Events with a south-then-north (north-then-south) signature are seen to move Earthward (tailward), and are indeed usually embedded in fast plasma flows (Slavin et al., 2003a).

The simplest magnetic flux rope model is the 'force-free' flux rope. This model represents the minimum energy state for helical magnetic field lines, and could therefore represent the cores of well developed, fully evolved flux ropes observed in the deep tail (e.g. Moldwin and Hughes, 1991; Slavin et al., 1995). A popular mathematical representation of a force-free flux rope is known as the 'constant α' solution (e.g. Lepping et al., 1990). In this class of force-free flux rope, $\mathbf{j} = \alpha\mathbf{B}$, where **j** is the current density vector and α is a constant. The topology of the magnetic field is a nested set of helical magnetic field lines ranging from a relatively weak tangential field on the outer boundary of the flux rope to a strong core axial field in the centre. This magnetic field topology is represented schematically in Fig. 3.3. At all places in the flux rope the magnetic force, $\mathbf{j} \times \mathbf{B} = 0$, since the current vector is everywhere parallel to the magnetic field vector. In this model, as $|\mathbf{j}|$ is proportional to $|\mathbf{B}|$, the current in the centre of the flux rope is mainly axial and strongly peaked.

Surveys of flux ropes in the tail have been performed previously (Elphic et al.,

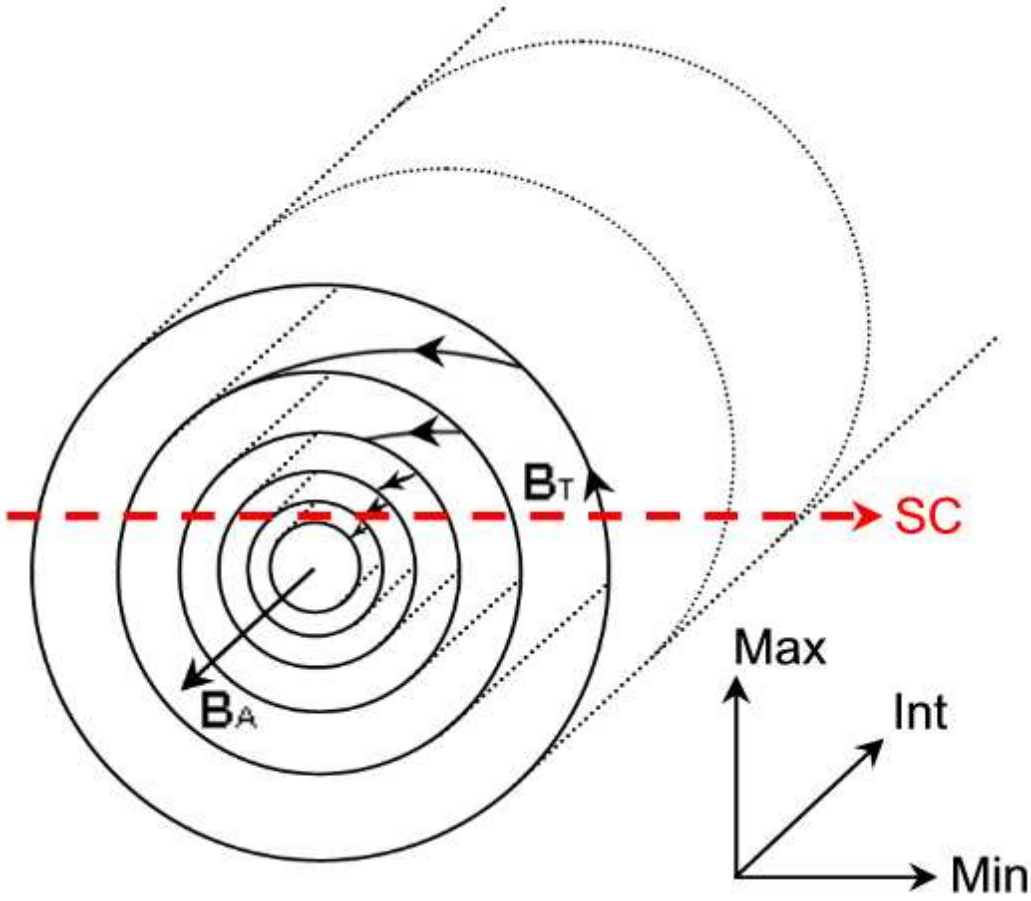

Figure 3.3: The topology of a force-free helical flux rope. The strong axial magnetic field and tangential magnetic field direction are marked. In the centre of the flux rope B_T is zero, increasing to a maximum at the edge, whilst B_A is maximal at the centre, falling to a minimum at the edge of the flux rope. A cartoon spacecraft trajectory is marked, along with the variance coordinate system that would arise from a constant α force-free flux rope.

1986; Slavin et al., 1995; Slavin et al., 2003a). Slavin et al. (1995) reported evidence for the existence of tailward moving plasmoids with force-free flux rope topologies in the distant tail (X $\sim$ -230 R_E). The observations of a strong core field or HFR (High Field Region) with typical scale sizes of $\sim$ 5 to 10 R_E led the authors to suggest that a force-free core was embedded in a non force-free plasmoid. A survey of Geotail data (Slavin et al., 2003a) reported many $\sim$ 2 to 5 R_E diameter flux ropes between 15 and 30 R_E down the tail. A large proportion of these flux ropes was found to fit well with the model outlined above and to be fairly cylindrical in shape. This led to the conclusion that the $\mathbf{j} \times \mathbf{B}$ forces were small, i.e. many

of these flux ropes were in a force-free configuration. This paper reported that a similar proportion of flux ropes were observed moving tailwards as Earthwards. Furthermore, Cluster observations of travelling compression regions (Slavin et al., 2005), a probable signature of the passage of flux ropes in the lobes (Owen et al., 2005; Walsh et al., 2007), show that at very near-tail distances (i.e. X $>\sim$ -20 R_E) 80% of flux ropes are travelling Earthward. Slavin et al. (2003b) reported on a flux rope observed by Cluster in the 2001 tail season, where all four spacecraft sampled the structure directly. This was unexpected as the separation of the Cluster spacecraft was almost comparable to the size of the flux rope ($\sim$ 1 R_E). Slavin et al. (2003b) concluded that this flux rope was not in a force-free configuration as the perpendicular currents were larger than the parallel currents for the first half of the flux rope encounter, although they noted a good agreement with the magnetic field topology of the type illustrated in Fig. 1.

Walsh et al. (2007) reported a series of bipolar signatures observed at different points in the magnetotail. The authors concluded that the signatures had to be a series of separate flux ropes from the same reconnection event, and therefore supporting the MXR theory, rather than one flux rope of complex structure, based on the velocities and orientations of the structures.

Lui et al. (2007) reported the observations of a 2 R_E diameter flux rope that was not force free, indeed having a very complex internal core magnetic field with a complex magnetic field configuration in the outer sections.

In this chapter, the results of which were first detailed in Henderson et al. (2006a), data from the Cluster mission is used along with applications of multi-spacecraft analysis methods to investigate flux ropes in the near-tail region of the magnetosphere of Earth. Multi-spacecraft timing and the calculation of an average curl of the magnetometer data is used in order to probe the internal structure of two such flux ropes. For the first time the magnetic forces are computed throughout flux ropes.

The analysis techniques used in this chapter are described in the next section. Flux ropes in the 2003 Cluster tail season are discussed in section 3. Two case studies of flux ropes observed by Cluster are detailed in section 4 and 5. The results of the case studies and their implications are discussed in section 6.

3.2 Analysis techniques

Previous single spacecraft studies of flux ropes have used minimum variance analysis (Sonnerup and Cahill, 1967; Sonnerup and Scheible, 1998) in an attempt to determine the orientation of the structures (Elphic et al., 1986; Slavin et al., 2003a; Slavin et al., 2003b; Xiao et al., 2004; Walsh et al., 2007; Lui et al., 2007). Minimum variance analysis is frequently used as a means to define a natural flux rope coordinate system. For the constant α force-free model, it can be shown that a variance analysis on the magnetic field components will give an intermediate variance direction which corresponds to the axis of the flux rope (Xiao et al., 2004). Moreover, analysis of magnetic field data from a spacecraft following a trajectory directly through the middle of a constant α force-free flux rope which is invariant along its axis will find the minimum variance direction to be along the spacecraft trajectory. The magnetic field in this direction will be zero, and will therefore have zero variance, of this field. The maximum variance direction is directed along a tangent to the cylindrical outer magnetic field line and the magnetic field in this direction will exhibit the bipolar signature seen in the study of flux ropes. In Fig. 3.3 a coordinate system is sketched that would arise from a minimum variance analysis of the magnetic field data from a spacecraft following the marked trajectory (dashed line) through the structure. In this structure, the magnetic field along the intermediate variance direction will peak at closest approach to the centre of the flux rope and at the zero crossing of the bipolar signature in the maximum variance direction. For trajectories that do not pass directly through the middle of the flux rope, the magnetic field in the intermediate and maximum variance directions will

have smaller amplitude, while the magnetic field along the minimum variance direction will have non-zero variance. It can therefore be seen that, as the trajectory moves away from the centre of the flux rope, the magnetic field in the intermediate and minimum variance directions begin to look similar. A good separation between all three of the eigenvalues of the minimum variance analysis is therefore needed to accurately determine the flux rope orientation using this method. It is important to note, however, that these variance analysis results may also arise from other flux rope models (both force-free and non-force-free). Indeed, more complicated structures may return different orientations of the variance analysis system with respect to the flux rope axis. For example, the intermediate variance direction may not necessarily correspond to the axis in a non-force-free flux rope if there exists a very strong core field. Thus the minimum variance analysis may not always accurately determine a 'flux rope frame' (Moldwin and Hughes, 1991; Slavin et al., 2003b). Further diagnostics are thus needed if to establish accurately the structure of such flux ropes.

As discussed in section 2.6, the typical separation of the Cluster spacecraft was only 200 km in 2003, a separation useful for the determination of the properties of small-scale structures in the near-tail region. A unique set of tools and techniques is made possible with the multi-spacecraft nature of Cluster. By simultaneously measuring the magnetic field at four different spacecraft, the average current through the tetrahedron can be calculated.

With knowledge of the curl of the magnetic field and the gradient of the magnitude of the magnetic field, the magnetic forces inside the flux ropes can be investigated (Eqn. 1.25).

The four spacecraft nature of Cluster can also used for multi-spacecraft timing, also known as four spacecraft timing (4SCT, section 2.6.1). In this study of flux ropes, the time at which each spacecraft observes a particular value of $|\mathbf{B}|$ (constant flux surface) near or shortly after (before) the time of the first (second) inflection

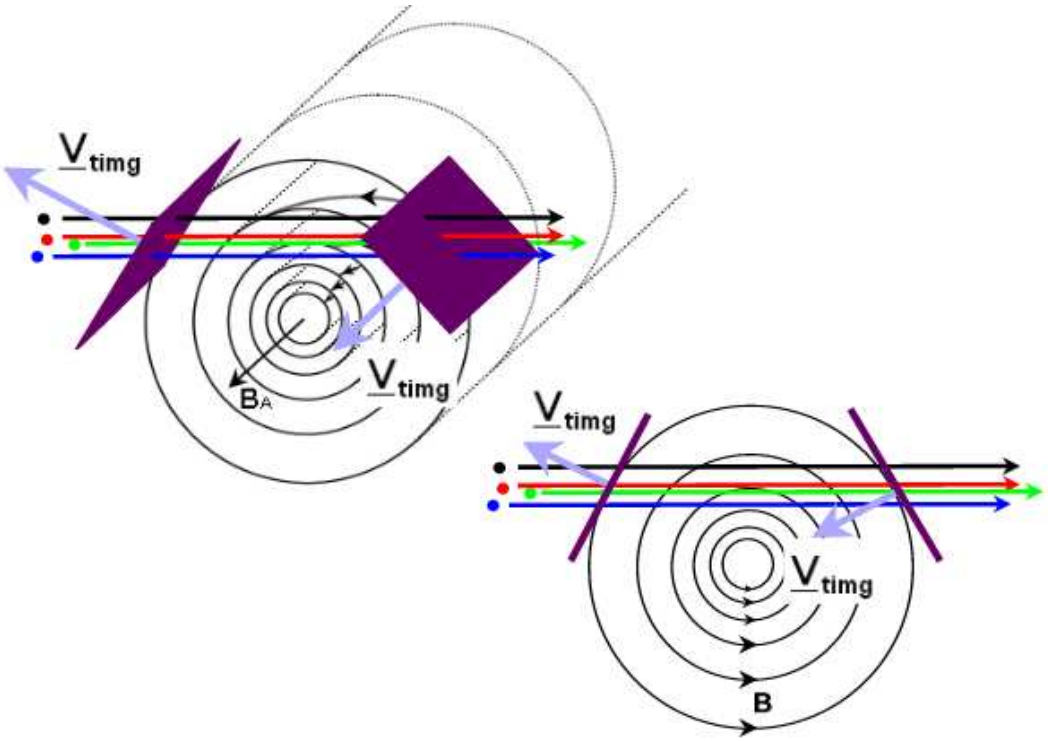

Figure 3.4: Cartoon of constant flux surfaces. By measuring the time lag between observations of constant flux surfaces at each Cluster spacecraft, the marked surfaces and velocities can be constructed.

point of the bipolar signature is noted. These instances are associated with the times at which each Cluster spacecraft observes the outer boundary of the flux rope. Fig. 3.4 shows a cartoon of the two surfaces that would be resolved if this method was applied to a force-free flux rope. A planar surface can be constructed to locally approximate the curved flux rope surface. The velocity of the constructed surface along its normal, $\mathbf{V}_{\text{timg}}$, can be computed. Levels of constant $|\mathbf{B}|$, as opposed to B_Z or the magnetic field in any variance direction, are frame independent and remove any uncertainty arising from the choice of frame. For an axially invariant flux rope, the cross product of the inbound and outbound $\boldsymbol{V}_{\text{timg}}$ vectors can be used to define a plane whose normal represents the axis of the flux rope, i.e.

$$\hat{\boldsymbol{V}}_{\text{timg}}{}^{1} \times \hat{\boldsymbol{V}}_{\text{timg}}{}^{2} \sim \hat{\boldsymbol{e}}_{\text{axis}} \tag{3.1}$$

Where $\hat{\boldsymbol{e}}_{\text{axis}}$ is a unit vector along the axis (note that this methodology has since

been formalised in Zhou et al., 2006). If the flux rope is in a force-free configuration, the intermediate variance direction should correspond with the axis determined from 4SCT (Xiao et al., 2004).

$$\hat{\boldsymbol{e}}_{\text{axis}} \sim \hat{\boldsymbol{e}}_{\text{intermediate}} \tag{3.2}$$

Where $\hat{\mathbf{e}}_{\text{intermediate}}$ is the unit vector along the intermediate variance direction. Consequently, if the structure is close to cylindrical, Eqn. 3.1 gives an independent estimate of the axis of the structure, regardless of whether the structure is in a force-free configuration or not, and can act as an independent test of the applicability of the minimum variance analysis. If minimum variance fails to give a framework in which the structure of a flux rope may be easily determined, as could happen in a non-force-free flux rope, this method could be used to find an axial direction. This method can be used for flux ropes observed in the 2003 tail season, provided the scale size of the flux rope is significantly larger than the spacecraft separation, 200 km (0.03 R_E).

3.3 Flux ropes in the 2003 Cluster tail season

An investigation of the 2003 Cluster small separation tail season has been undertaken in an attempt to find flux ropes in the plasma sheet using the Cluster Fluxgate Magnetometer (FGM; Balogh et al., 2001) and the Plasma Electron And Current Experiment (PEACE; Johnstone et al., 1997; Fazakerley et al., 2007[1]) instruments. Periods when Cluster was close to apogee in the tail between early August and late October were investigated. Spin averaged data ($\sim$ 4 second resolution) were used in the initial stages of the investigation, with high resolution magnetic field data being employed to study events in further detail. An upper threshold on $|\mathbf{B}|$ (30 nT) and a clear signature of plasma sheet electrons in PEACE was used to ensure that only the

[1]Manuscript in preparation.

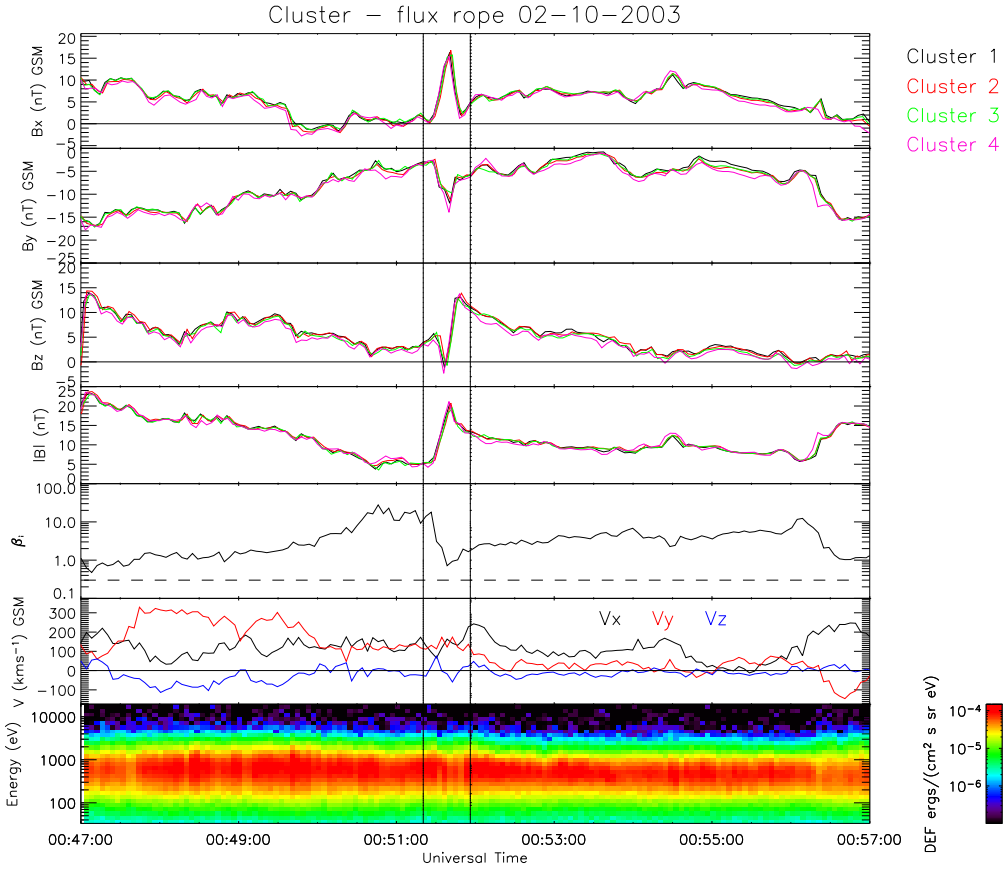

Figure 3.5: Cluster observations of 2nd October 2003. Panels 1 to 4 show components of **B** and |**B**| from each spacecraft (Cluster 1 - black, Cluster 2 - red, Cluster 3 - green, Cluster 4 - magenta). Panel 5 shows plasma β_i, derived from Cluster 1 ion (HIA) moments. β_i = 0.3 is marked, a value of β_i above this is indicative of plasma sheet conditions. Panel 6 shows velocities from CIS (Cluster 1, V_X black, V_Y red, V_Z blue). Panel 7 contains a spectrogram of the direction-averaged differential energy flux for electrons in the energy range 30 eV - 26KeV recorded by the PEACE instrument on Cluster 4. The flux rope event is marked between two black lines.

times when Cluster was in the plasma sheet were investigated. The periods that satisfied these tests were then manually surveyed. The criterion for the identification of a flux rope was a clear north-then-south or south-then-north bipolar signature (i.e. a rotation of the magnetic field component between two points) associated with a clear increase in |**B**| (to eliminate magnetic loop events, which generally exhibit a bipolar signature with no, or little increase in |**B**|).

Ten flux rope candidates were found in the data that satisfied all of the above criteria. However, two such events will be presented in this chapter. These events were selected due to their clear core fields and bipolar signatures.

3.4 Case study one - 2nd October 2003 (A)

On the 2nd October 2003 at approximately 01:00 UT, the Cluster spacecraft were located $\sim$ (-17, 8, -3) R_E (GSM coordinates will be used throughout this chapter unless otherwise stated). Fig. 3.5 shows three components of the magnetic field from all spacecraft (Cluster 1 - black, Cluster 2 - red, Cluster 3 - green, Cluster 4 - magenta) and their magnitudes for the period 00:47 to 00:57 UT. Panel 5 shows the ion plasma beta (β_i) from the Cluster Ion Spectrometry (CIS HIA) experiment on Cluster 1, with β_i = 0.3 marked by a dotted line. Values of β_i above this value are indicative of plasma sheet conditions.

A difference is noted in the ion density determined from on-board moments and ground moments. The density generated from ground moments (12s time resolution) is here higher than that generated from on-board moments (4s time resolution). In order to generate confidence in the plasma pressure measurements, the plasma pressure was 'calibrated' by assuming that total pressure was constant across the tail for the period close to the flux rope encounter. This process assumed that all plasma pressure measurements were modified by a constant multiplicative factor. For ground moments this factor was close to 1.0, giving confidence in the ground moments. For on-board moments this factor was close to 1.35. After taking this factor into account it was found that the plasma pressure determined from on-board moments and ground moments agree well (not shown). These 'corrected' ion pressure on-board moments (4s time resolution) are used throughout this study and are used here in the calculation of β_i.

Panel 6 shows the components of plasma velocity from CIS (V_X black, V_Y red, V_Z blue) on Cluster 1. These velocity moments are determined on board the spacecraft and agree well with lower time-resolution velocity moments determined by ground analysis (not shown) and are therefore not modified. The bottom panel contains a spectrogram of the direction-averaged differential energy flux for electrons in the energy range 30 eV - 26 keV recorded by the PEACE instrument on Cluster

4.

The PEACE energy spectrogram shows a large differential energy flux of $\sim$ 1 keV electrons. Together with magnetic field observations showing B_X ($\sim$ 0 nT), $|\mathbf{B}|$ ($\sim$ 5 nT) and β_i ranging between $\sim$ 1 to 10, this confirms that the Cluster spacecraft were in the plasma sheet throughout the period shown. At approximately 00:52 UT a large enhancement in $|\mathbf{B}|$ can be seen (to $\sim$ 20 nT), along with a sharp increase in B_X (to $\sim$ 15 nT) and B_Y (from $\sim$ -5 nT to $\sim$ -15 nT). A bipolar south-then-north B_Z signature is also evident. The AE index for this time (not shown) indicates that the magnetosphere was in the recovery phase of a large substorm. The south-then-north bipolar signature suggests that this object was a flux rope moving in the Earthward direction. CIS ion velocity shows that this flux rope was embedded in a fast flow in the +X ($\sim$ 150 kms^{-1}) +Y ($\sim$ 150 kms^{-1}) direction, i.e. Earthwards and duskwards. The deflection in B_X (positive) and B_Y (negative) indicates a strong core field in the +X and -Y direction. The bipolar signature is not symmetric which is the result of a core field contribution in B_Z (positive), i.e. the axis is aligned (+X, -Y, +Z) (see below).

A minimum variance analysis was carried out on high resolution FGM data. Fig. 3.6 shows the orientation of the variance directions determined from Cluster 1 with respect to the GSM axes. This figure is a 3D view of the GSM system (unit vectors used) where the minimum variance direction is coloured black, intermediate variance direction is coloured red and maximum variance direction is coloured blue. Thin tracer lines show the projections of each vector onto the unit GSM axes. The direction of maximum variance is determined with a larger confidence than are the directions of minimum and intermediate variance since the minimum:intermediate eigenvalue ratio is smaller than the intermediate:maximum eigenvalue ratio for all spacecraft. The frame with the largest eigenvalue separation was selected, which in this case was that returned from analysis of Cluster 1 data, where the minimum:intermediate:maximum eigenvalue ratios were 1:3.2:17.9. The

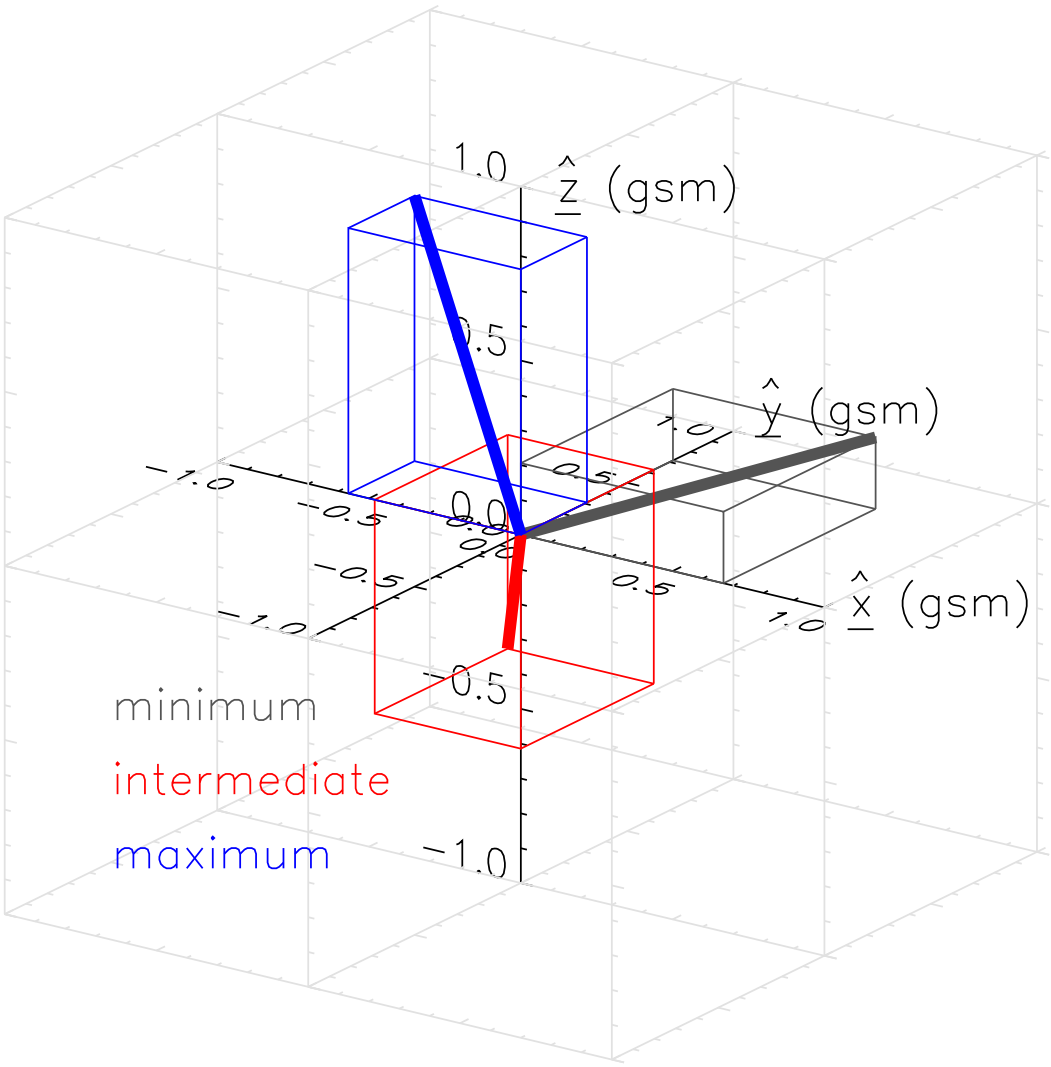

Figure 3.6: A 3D view of the variance system in GSM unit space from Cluster 1 for the 2ndOctober 2003 event. The minimum variance direction is coloured black, intermediate variance direction is coloured red and maximum variance direction is coloured blue. Thin tracer lines are plotted giving the projections onto the GSM unit axes as a guide to the direction of the vectors.

minimum variance direction is mostly in the +X +Y direction. The intermediate variance direction is highly inclined to the XY plane. If, as would be expected for a constant α force-free flux rope, this direction corresponds to the flux rope axis, the axis would be in the (-X, +Y, -Z) direction consistent with the opposite direction of the core field in the magnetic field measurements. The core field should therefore be negative along the intermediate variance direction.

The magnetic field observations are plotted in the minimum variance frame in Fig. 3.7. This figure shows four panels; the magnetic field in the minimum, inter-

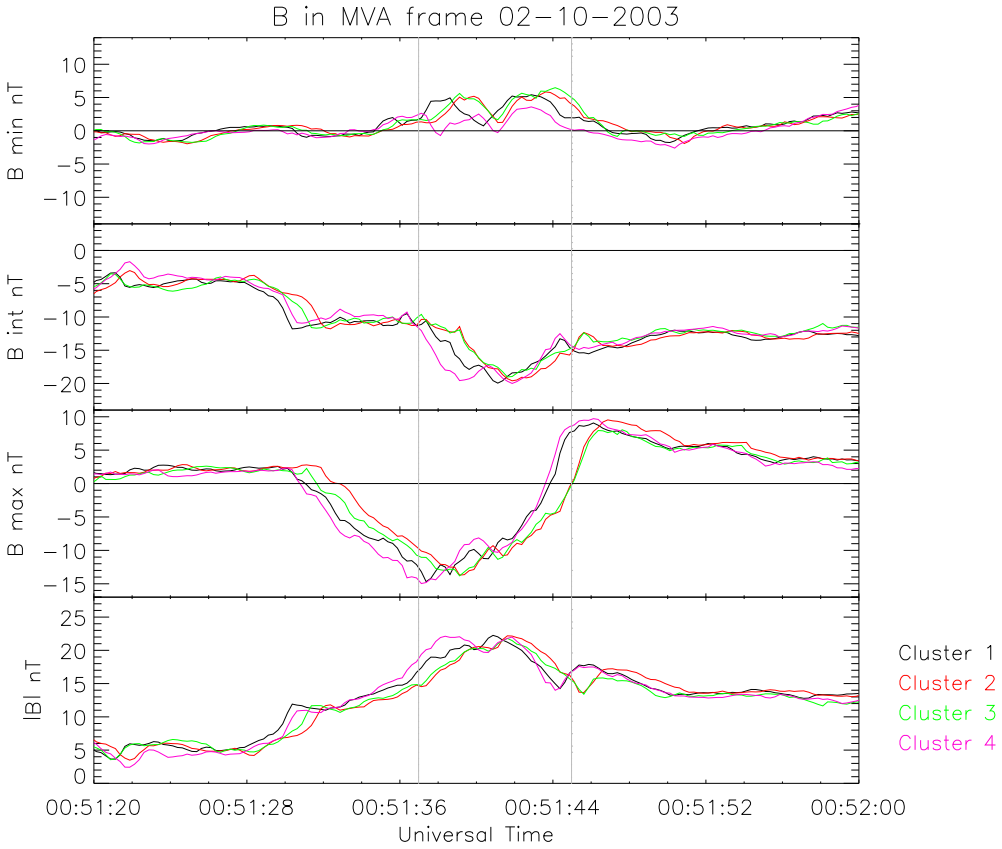

Figure 3.7: Magnetic field observations from 2ndOctober event transformed into the variance frame of Cluster 1; the magnetic field in the minimum, intermediate and maximum variance directions (Fig. 3.6) and the magnitude from all spacecraft. Cluster colours are in the same format as those in Fig. 3.5. The approximate boundaries of the flux ropes, located at the inflection points, are marked by grey lines.

mediate and maximum variance directions and the magnitude from all spacecraft, with spacecraft colours in the same format as those in Fig. 3.5. Grey lines mark the approximate boundaries of the flux rope, identified in this chapter as the locations of the inflection points of the bipolar signature and the central core magnetic field. The magnetic fields in both the minimum and intermediate variance directions are peaked. The larger negative peak in the intermediate variance direction represents the core field. The bipolar signature appears in the maximum variance direction (a rotation of the magnetic field between $\sim$ -15 nT and 9nT for Cluster 1). This is consistent with expectations from the simple constant α force-free flux rope. The enhancement in $|\mathbf{B}|$ suggests a spacecraft closest approach time of 00:51:41 UT. As

described above, 4SCT provides a test of the minimum variance analysis results. This analysis was performed on levels of constant magnetic field magnitude for both the inbound (20 nT) and outbound (18 nT) parts of the encounter and the $\mathbf{V}_{\text{timg}}$ vectors produced can be seen in Fig. 3.8 in the variance frame of Cluster 1. This figure is a 3D view of the variance analysis axes (unit vectors used). The first $\mathbf{V}_{\text{timg}}$ is coloured red, the second coloured blue. Thin tracer lines show the projections of each vector onto the unit variance axes.

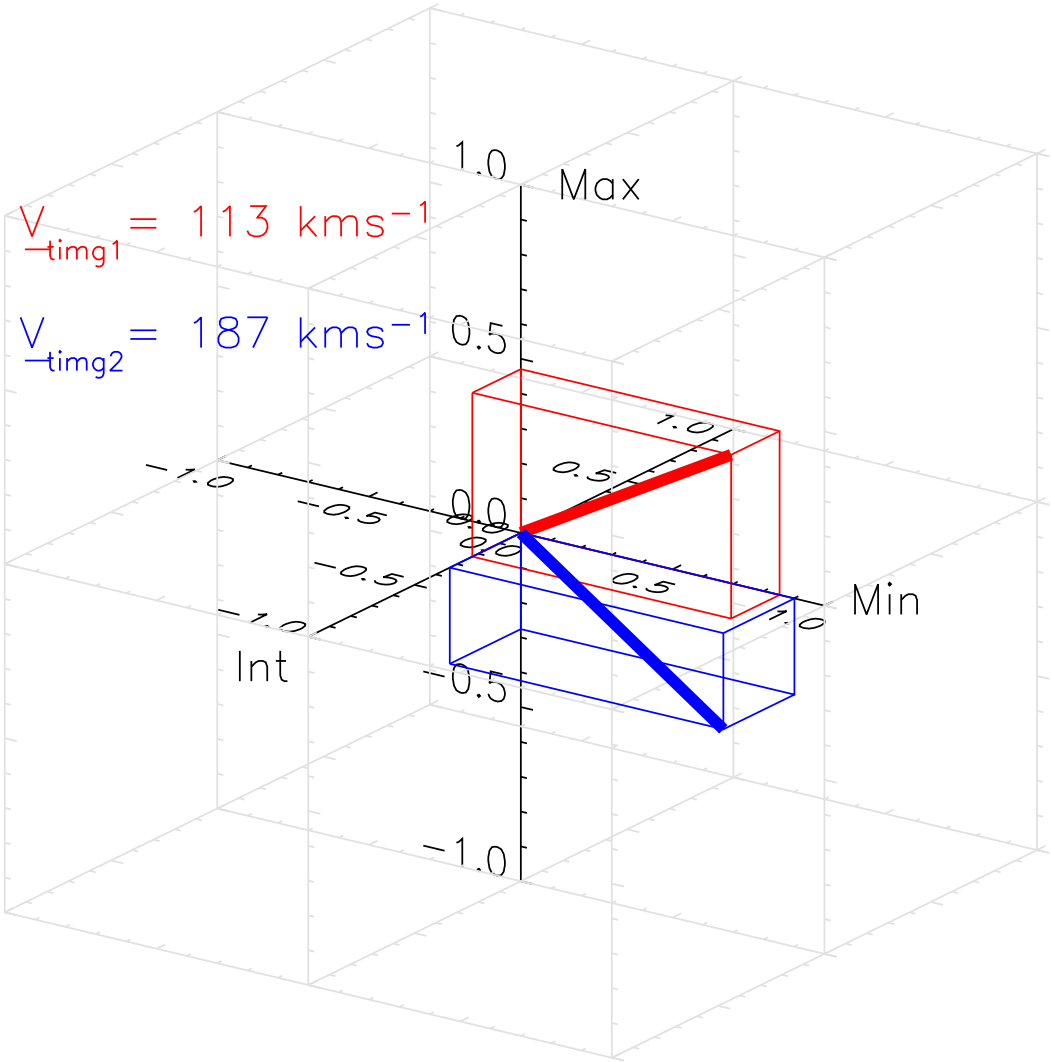

Figure 3.8: A 3D view of the variance frame with $\mathbf{V}_{\text{timg}}$ vectors produced from constant flux surfaces on 2$^{\text{nd}}$October event. The directions 'Min', 'Int' and 'Max' correspond to the minimum, intermediate and maximum variance directions plotted in GSM unit space in Fig. 3.6.

It can be seen that both inbound and outbound timing vectors lie close to the

minimum-maximum variance plane and define a plane whose normal is close to the intermediate variance direction (see Eqn. 3.1). This result suggests that the intermediate variance direction is indeed close to the axis of the flux rope and that the variance analysis is returning a system that is consistent with a natural 'flux rope frame'.

4SCT can also be used to compute a velocity of the flux rope over the spacecraft. Fig. 3.9 shows a schematic of the velocities involved. In this figure the surface being investigated is moving along $\mathbf{V}$, while the normal to the surface is $\hat{\mathbf{n}}$. The velocity $\mathbf{V}_{\text{timg}}$ returned by 4SCT is the velocity of the surface along the normal, $|\mathbf{V}_{\text{timg}}|= \mathbf{V}.\hat{\mathbf{n}}$, where $\mathbf{V}$ is the velocity of the flux rope. If the minimum variance direction can be assumed to be along or close to the trajectory, then the velocity $\mathbf{V}$ along this direction can be calculated by $|\mathbf{V}|= |\mathbf{V}_{\text{timg}}|/cos(\theta)$ where θ is the angle between $\mathbf{V}$ and $\mathbf{V}_{\text{timg}}$. This was calculated on both inbound ($\sim$ 130 kms^{-1}) and outbound ($\sim$ 190 kms^{-1}) vectors and an average taken. A resultant velocity of 160 kms^{-1} corresponds to a size of $\sim 0.3\text{R}_E$ (taking the time between the inflection points of $\sim$ 10s) for this flux rope. This is a lower estimate of the diameter of the flux rope, $\sim 0.3\text{R}_E$ representing the distance between the boundaries of the flux rope at this particular impact parameter, which is here defined as the relative distance from the centre of the flux rope. The velocity of the flux rope determined by 4SCT is so directed that the flux rope is travelling Earthward, in agreement with the south-then-north polarity of the B_Z signature and CIS ion velocities. CIS ion velocities rotated into the minimum variance frame (not shown) give a velocity along the minimum variance direction of $\sim$ 190 kms^{-1} in approximate agreement with the velocities derived from 4SCT, with smaller velocities along the intermediate and maximum variance directions of $\sim$ 40 kms^{-1} and $\sim$ -60 kms^{-1} respectively.

Note that 4SCT assumes that the size of the flux rope is large enough that the surface encountered can be considered planar. As the size of the tetrahedron is $\sim$ 0.03 R_E, ten times smaller than the inferred size of the flux rope, this assumption

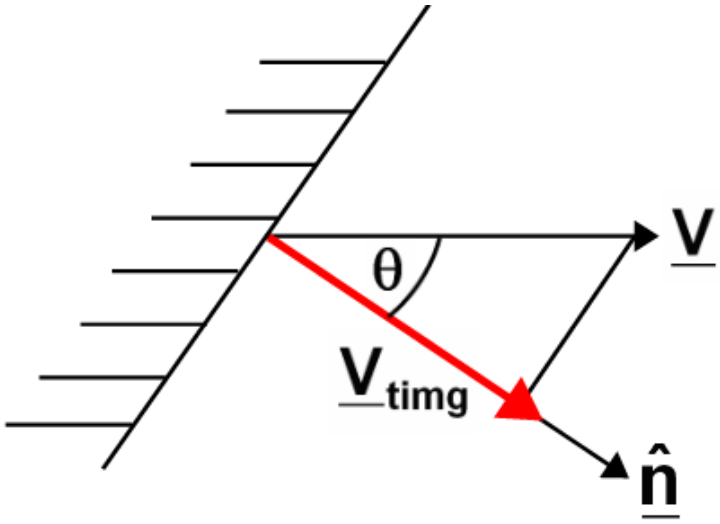

Figure 3.9: Schematic of the velocities computed in 4SCT. The velocity $\mathbf{V}_{\text{timg}}$ returned by 4SCT is the velocity of the surface along the normal.

should be valid in this case.

The Curlometer technique described above was applied to this period of data and the results are shown in Fig. 3.10. Panel 1 shows the current parallel to the magnetic field (black) and the magnitude of the current perpendicular to the magnetic field (red). Note that the barycentric magnetic field is used; i.e. the predicted magnetic field at the geometric centroid of the Cluster tetrahedron. Panel 2 shows the current projected into the minimum (black), intermediate (red) and maximum (blue) variance directions of the magnetic field from Cluster 1 (Fig. 3.6) respectively. Panel 3 shows the magnitude of the current. Panel 4 shows the relative error in the Curlometer current, χ (Eqn. 2.26). For this event E = 0.21, P = 0.30 giving a $\sqrt{E^2 + P^2}$ of 0.37. The tetrahedron is therefore a good example of a pseudo-sphere and χ, identified as the relative error, should give a good measure of the quality of the Curlometer result. Panels 5 to 8 show the magnetic force (black, barycentric magnetic field used), the magnetic pressure force (red, see Eqn. 1.25) and the magnetic tension force (blue, calculated from $\mathbf{j} \times \mathbf{B} - \nabla\left(\frac{B^2}{2\mu_0}\right)$) transformed into the minimum, intermediate and maximum variance directions of the magnetic field of Cluster 1, and their magnitudes. Panels 9 and 10 show the electron and ion pressure derived from PEACE and CIS data respectively. The final two panels again show

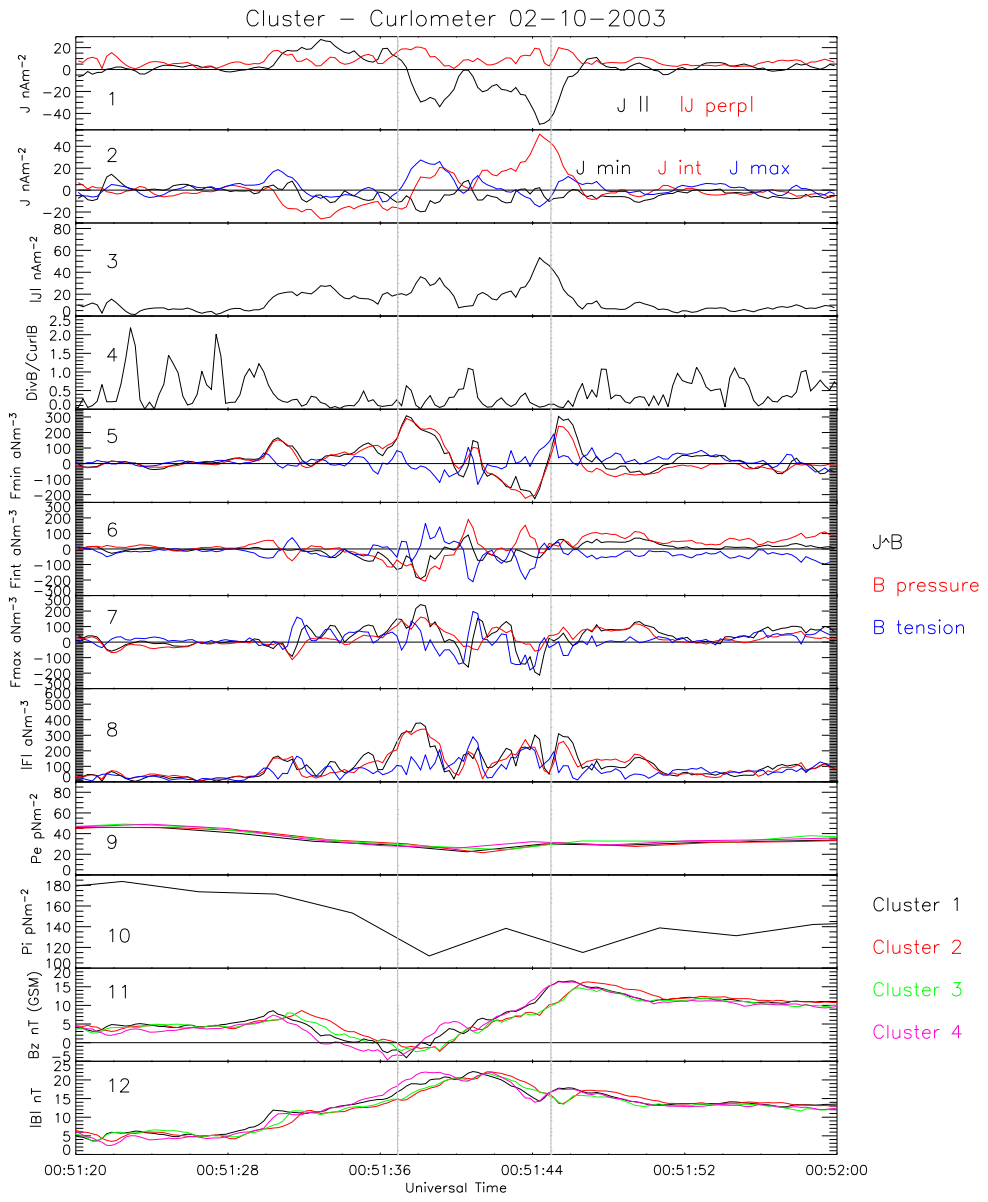

Figure 3.10: Cluster Curlometer observations of 2ndOctober 2003. Panel 1 shows the current parallel (black) and the magnitude of the current perpendicular (red) to the magnetic field. Panel 2 shows the current projected into the minimum (black), intermediate (red) and maximum (blue) variance directions respectively. Panels 3 and 4 show the magnitude of the current and the fractional error in the Curlometer result respectively. Panels 5 to 7 show $\mathbf{j}\times\mathbf{B}$ (black), magnetic pressure (red) and magnetic tension (blue) projected onto the minimum, intermediate and maximum variance directions of Cluster 1 respectively. Panel 8 shows $|\mathbf{j}\times\mathbf{B}|$ and the magnitudes of the magnetic pressure and tension forces. Panels 9 and 10 show the electron and ion pressure respectively, with the final two panels showing the B_Z and $|\mathbf{B}|$ observations.

the B_Z component and $|\mathbf{B}|$ from each spacecraft for reference.

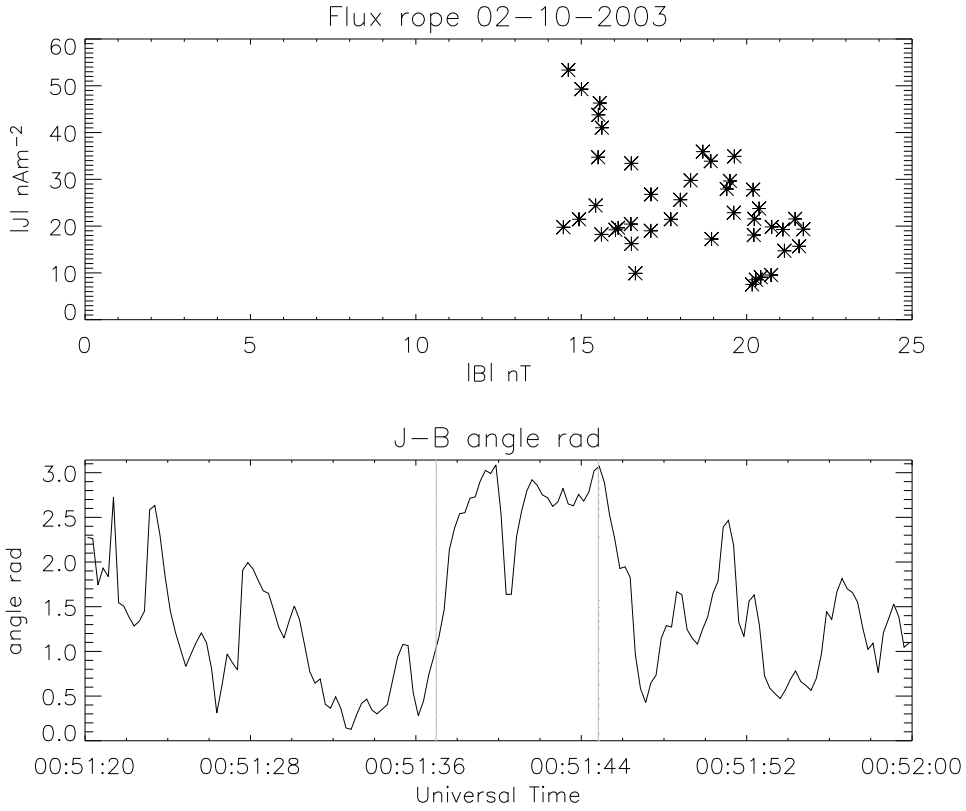

Figure 3.11: $|\mathbf{j}|$ versus $|\mathbf{B}|$ and the angle (in radians) between the magnetic field and current density vectors for the 2ndOctober 2003 flux rope. For a constant α force-free flux rope $|\mathbf{j}|$ would be proportional to $|\mathbf{B}|$ and the magnetic field and current density vectors would be parallel.

Panels 1 and 3 show that there are three large current enhancements around the time of the flux rope encounter and that the first enhancement (00:51:33 UT) is largely directed parallel, the second two enhancements (00:51:38 and 00:51:44 UT) are directed anti-parallel (but with a small perpendicular component) to the magnetic field direction. As the boundary of the flux rope is identified as being between the two inflection points of the bipolar signature ($\sim$ grey vertical lines), the first current enhancement (parallel to the magnetic field) is outside the flux rope by this definition (i.e. just Earthward of the flux rope), while the second two current enhancements are inside the structure. Also, the current is smaller in the centre of the

flux rope than near the edges. It can be seen from panel 2 that the smaller first current enhancement inside the flux rope (00:51:38 UT) is in the intermediate (red) and maximum (blue) variance directions, whereas the larger second current enhancement (00:51:44 UT) is in the intermediate variance direction (red). This current would therefore seem to be mainly axially directed, but not located in the centre of the flux rope. The smaller currents in the maximum variance direction (blue) show a reversal during the flux rope encounter, first positive along the maximum variance direction (00:51:38 UT) changing to negative (00:51:44 UT). χ (panel 4) is small, being generally less than 0.5 over the whole of the flux rope, apart from one small section close to the centre (00:51:41 UT) where the error becomes ~ 1. In this region the current is small, meaning that a large χ will have an insignificant result on the overall current. Panel 5, the magnetic force along the minimum variance direction (assumed to be the trajectory), shows two direction reversals, or a tripolar signature. The force along this direction is first positive (00:51:37 UT), turning negative (00:51:44 UT), then quickly turning positive again very close to the trailing edge of the flux rope (00:51:46 UT). The direction reversal over the flux rope (i.e. between vertical grey lines) suggests that the magnetic force is acting to expand the flux rope, i.e. acting away from the flux rope centre, consistent with the magnetic pressure dominance of the total magnetic force. The total magnetic force along the axis (panel 6) is generally smaller than that of any other component. The magnetic pressure and tension forces generally have opposite signs along all directions, but are not balanced. Note that a force-free flux rope will have an exact magnetic pressure-tension force balance in the absence of a plasma pressure gradient. The electron and ion pressures (panels 9 and 10) are reduced inside the flux rope.

In order to compute the total sum of forces acting on this flux rope, the spatial gradient of plasma pressure must be compared to the magnetic forces. The gradient in the pressure cannot here be calculated because CIS aboard Cluster 2 is not op-

erational and the pressure gradient structure cannot be compared to the small scale magnetic force structure because of the low time resolution of the plasma instruments. In order to make an estimate of the total force acting on the flux rope the change in plasma pressure recorded at a point just before (or after) and inside the flux rope is compared to the magnetic pressure (calculated by $|\mathbf{B}|^2/2\mu_0$) change measured on the same spacecraft over the same time range. Assuming most of the magnetic force comes from the magnetic pressure force (as it does in this case) a useful estimate of the balance of forces (both plasma and magnetic) can be made across the flux rope. Over the first half of the flux rope (Cluster 1 ion and magnetic pressure evaluated at 00:51:31 UT and 00:51:39 UT with the Cluster 1 electron pressure evaluated at 00:51:33 and 00:51:41 UT) a simple comparison shows that the change in magnetic pressure is a factor of ~ 1.4 larger than that of the plasma pressure. Over the second half of the flux rope (ion and magnetic pressure evaluated at 00:51:39 UT and 00:51:51 UT, electron pressure evaluated at 00:51:41 and 00:51:53 UT) the comparison again suggests that the change in magnetic pressure is larger than that of the plasma pressure, but this time by a factor of ~ 2.3. This would seem to suggest that the flux rope is experiencing an expansive total force.

Fig. 3.11 shows a scatter plot of the magnitudes of the current density and magnetic field, along with the angle (in radians) between the current density and magnetic field vectors. In a constant α force-free flux rope $|\mathbf{j}|$ is proportional to $|\mathbf{B}|$, and the current density and magnetic field vectors would be parallel. $|\mathbf{j}|$ versus $|\mathbf{B}|$ for this event yields no clear proportionality and there exists a non-constant non-zero angle between the current density and magnetic field vectors. These results are inconsistent with the flux rope being in a constant α force-free configuration.

If the magnetic force can be assumed to be acting only radially, finding the direction along which the magnetic force is minimal can give another estimate of the axial direction. A minimum variance analysis carried out on $\mathbf{j} \times \mathbf{B}$ gives the minimum variance direction to be (-0.759, 0.613, -0.219) with a minimum:intermediate

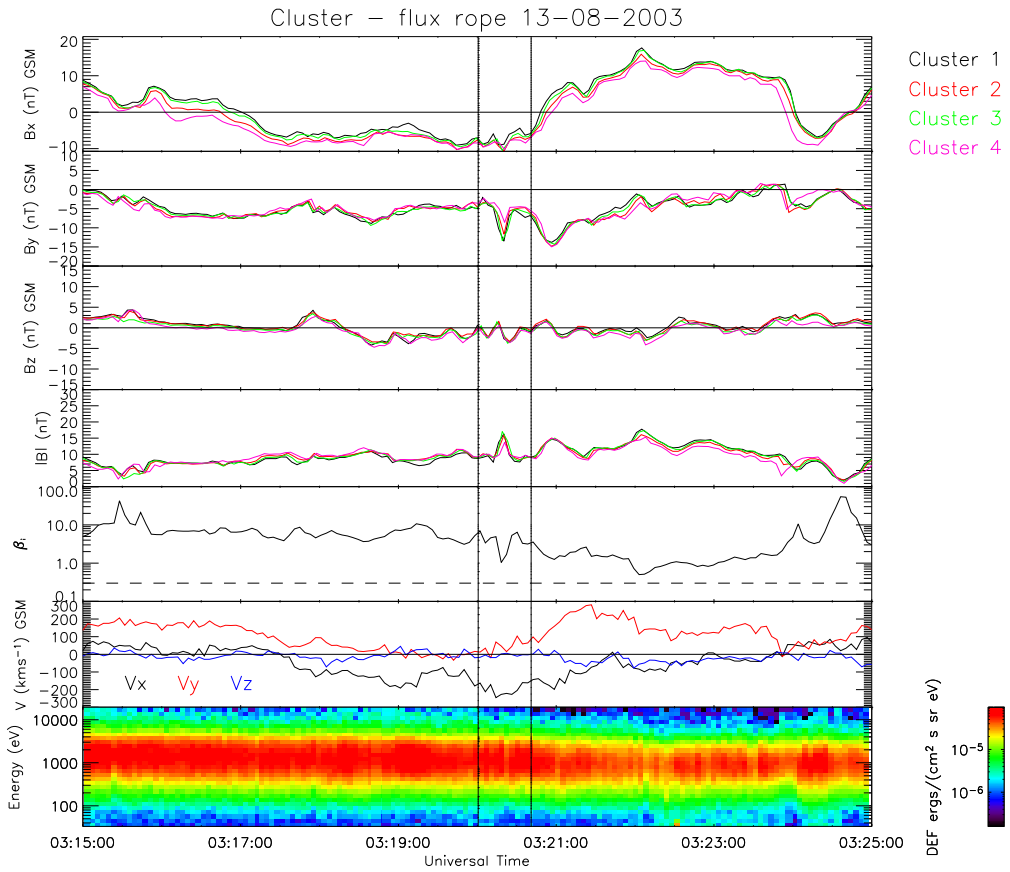

Figure 3.12: Cluster observations of 13$^{\text{th}}$August 2003 in the same format as Fig. 3.5.

eigenvalue ratio of 5.0. This direction makes an angle of 28° to the intermediate variance direction of the magnetic field, the assumed axis: (-0.481, 0.625, -0.614). The maximum variance direction of the current density is (-0.026, -0.442, 0.897) with an intermediate:maximum eigenvalue ratio of 3.0. This makes an angle of 35° to the assumed axis and confirms that the current is not simply axial.

3.5 Case study two - 13$^{\text{th}}$August 2003 (B)

On the 13$^{\text{th}}$of August at approximately 03:00 UT, all four Cluster spacecraft were located at $\sim$ (- 18, - 7, 0) R_E. Fig. 3.12 shows the components of the magnetic field, CIS β_i (using 'corrected' on-board density moments) and velocity from Cluster 1, and the PEACE electron spectrogram in the same format at Fig. 3.5.

Again the PEACE electron spectrogram together with B_X $\sim$ -7 nT, $|\mathbf{B}|$ $\sim$ 7

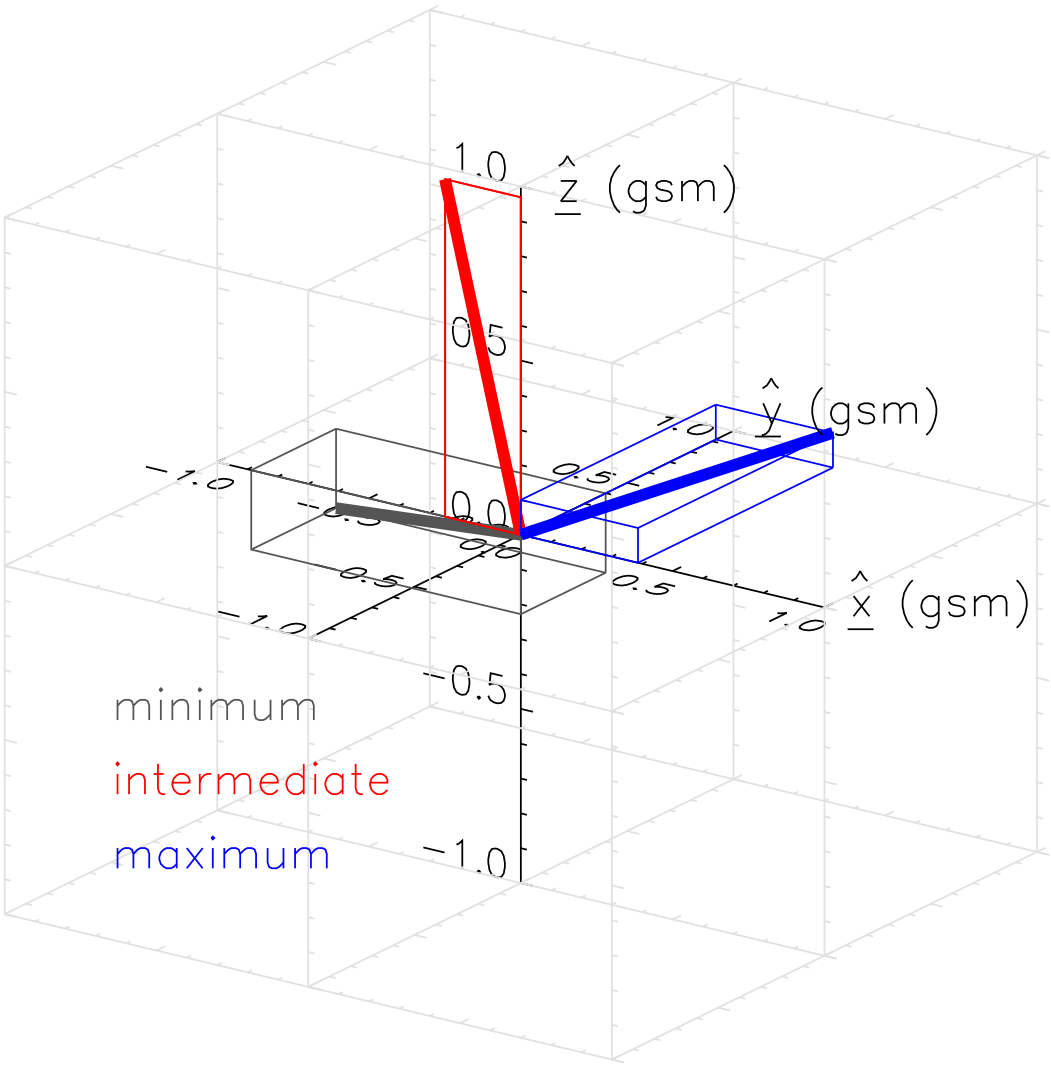

Figure 3.13: The variance system in GSM unit space from Cluster 1 for the 13thAugust event in the same format as Fig. 3.6

nT and β_i ranging from $\sim$ 1 to 10 confirms that the Cluster spacecraft were in the plasma sheet throughout this period. At approximately 03:20:30 UT a large enhancement in $|\mathbf{B}|$ (to $\sim$ 17 nT) is concurrent with a small north-then-south bipolar B_Z signature. The AE index for this time indicates that the magnetosphere was in the expansion phase of a large substorm. The polarity of the bipolar signature suggests a flux rope moving tailward. The flux rope is embedded in a fast tailward flow, with $V_X \sim$ -250 kms^{-1}. The core field deflection is in (negative) B_Y (from $\sim$ -3 nT to $\sim$ -15 nT), with very little variation in B_X, indicating that the strong core field was in the -Y direction.

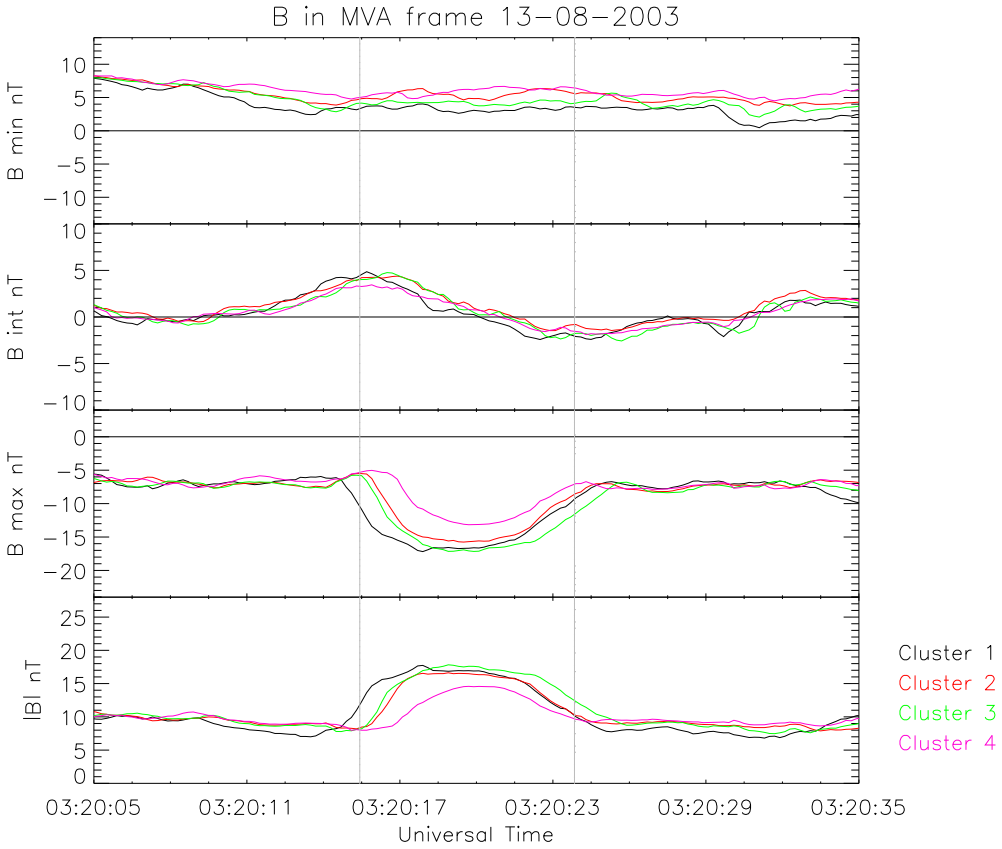

Figure 3.14: Magnetic field observations from 13thAugust event transformed into the variance frame of Cluster 1 in the same format as Fig. 3.7.

A minimum variance analysis was carried out on high resolution magnetic field data for this period and Fig. 3.13 shows the variance directions determined from Cluster 1 with respect to the GSM axes in the same format as Fig. 3.6. This spacecraft again returned the largest separation of eigenvalues. However, the ratio of eigenvalues for this event is 1:41.4:149, suggesting that the minimum variance direction is determined rather better than the intermediate and maximum variance direction. The minimum variance direction is mainly in the -X direction. The intermediate variance direction is close to the +Z direction. In this case it is the maximum variance direction which lies almost along the +Y direction, most consistent with the direction of the core magnetic field. This flux rope is therefore not-consistent with the expectations of the constant α force-free flux rope discussed in section 3.2.

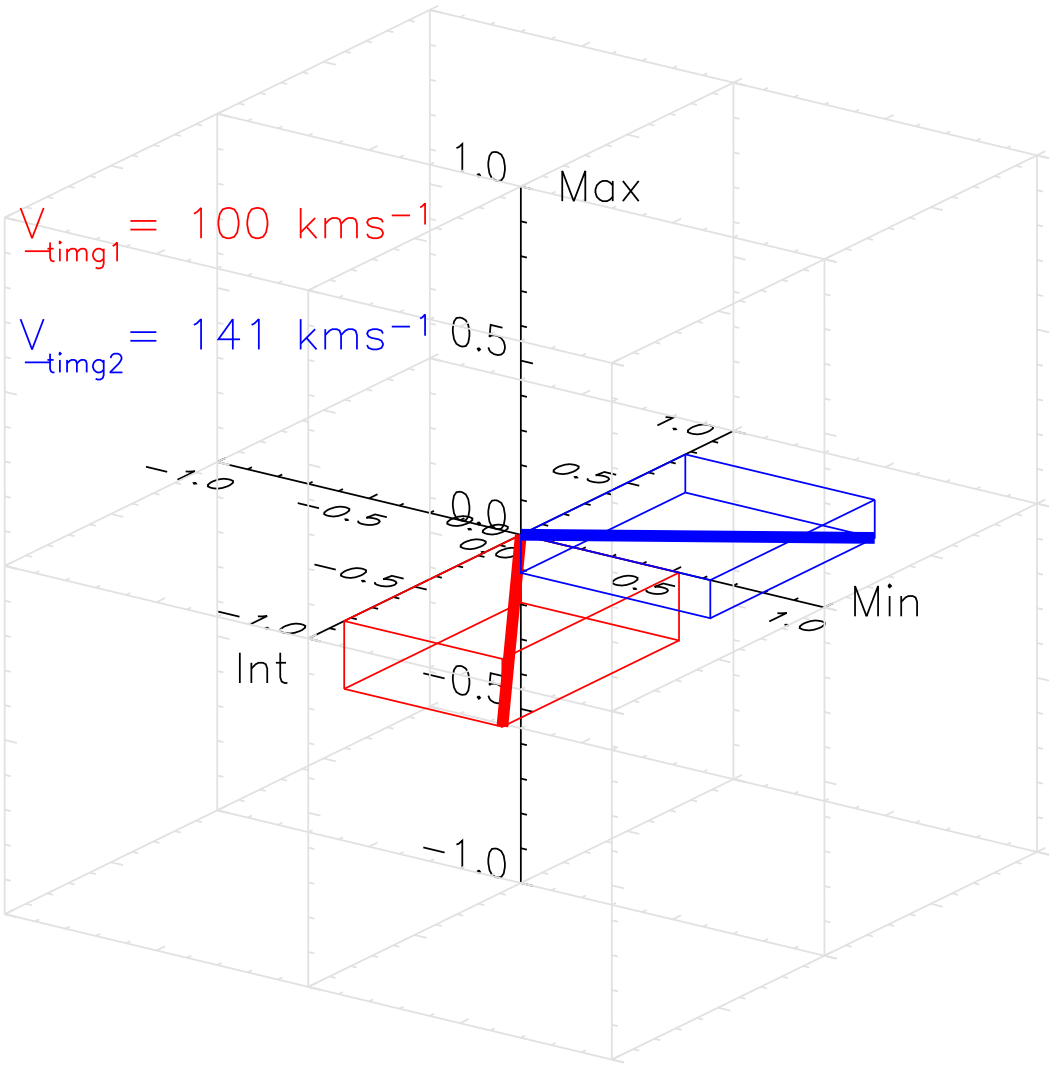

Figure 3.15: $\mathbf{V}_{\text{timg}}$ vectors produced from constant flux surfaces on 13$^{\text{th}}$August event in the unit variance frame in the same format as Fig. 3.8. The directions 'Min', 'Int' and 'Max' correspond to the minimum, intermediate and maximum variance directions plotted in GSM unit space in Fig. 3.13.

Fig. 3.14 shows the magnetic field plotted in the variance frame in the same format as Fig. 3.7. The small bipolar signature observed in Fig. 3.12 becomes clear in the intermediate variance direction, while the unipolar core field appears in the maximum variance direction. It is therefore expected that the maximum variance direction should closely correspond to the axis in agreement with the magnetic field observations. The $|\mathbf{B}|$ signature suggests a closest approach time of 03:20:20 UT. 4SCT can be used to provide an independent test of the interpretation of this result and was performed on surfaces of constant magnetic flux magnitude. The $\mathbf{V}_{\text{timg}}$

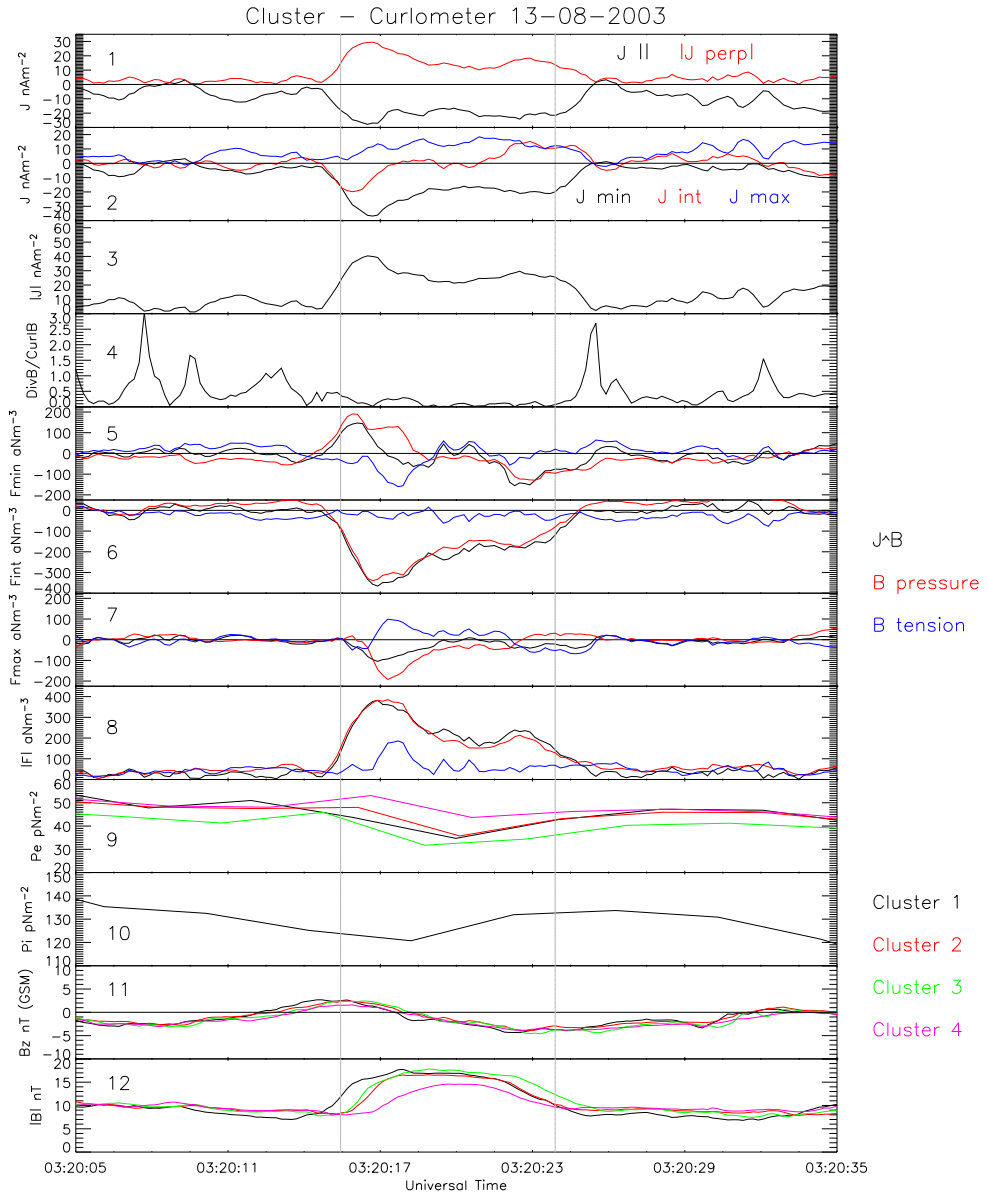

Figure 3.16: Curlometer results from 13thAugust event in the same format as Fig. 3.10.

vectors produced from 4SCT of inbound (9 nT) and outbound (10.5 nT) surfaces in the variance frame of Cluster 1 can be seen in Fig. 3.15, in the same format as Fig. 3.8. In this figure both vectors lie close to the minimum-intermediate plane and thus define a plane whose normal is close to the maximum variance direction, indeed consistent with the axis of this flux rope being directed along the maximum variance direction (see Eqn. 3.1). This result confirms that the variance analysis has successfully determined a good approximation to a 'flux rope frame'. However, in contrast to the previous case, the maximum variance direction is the appropriate flux rope axis. By finding the appropriate velocity along the minimum variance direction (assumed to be approximately the same direction as the flux rope trajectory) for both inbound (180 kms^{-1}) and outbound (220 kms^{-1}) vectors and taking an average, a velocity of 200 kms^{-1} is resultant. This velocity again corresponds to a size of $\sim$ $0.3R_E$ (taking the time between the inflection points of $\sim$ 10s) for this flux rope. Again this is a lower estimate for the size of the structure. The velocity of this flux rope shows that it is travelling tailwards, consistent with the north-then-south polarisation of the bipolar signature. CIS ion velocities rotated into the minimum variance frame (not shown) give a velocity along the minimum variance direction of $\sim$ 200 kms^{-1} in good agreement with the velocities derived from 4SCT, and along the intermediate variance direction of $\sim$ 50 kms^{-1} and maximum variance direction of $\sim$ -50 kms^{-1}.

The Curlometer technique described above was applied to this period of data and can be seen in Fig. 3.16, in the same format as Fig. 3.10. At the beginning of the encounter the magnitude of the perpendicular current (red) is approximately the same as the parallel current (black). In the middle of the flux rope (03:20:20 UT) however, the perpendicular current falls to a level below the parallel current and then climbs again to the level of the parallel current at the end of the encounter. The parallel current stays almost steady throughout the flux rope encounter, with the change in the magnitude of the current being due to the change in the perpen-

dicular component. It can be seen that the current is unidirectional in the minimum (black) and maximum (blue) variance directions and that it undergoes a direction reversal in the intermediate variance direction (red). It would appear therefore that the current circulates around the axis as well as having an axial component. For this event E = 0.21, P = 0.27 giving a $\sqrt{E^2 + P^2}$ of 0.34. The tetrahedron is again a good pseudo-sphere and χ (Eqn. 2.26) is identified with the relative error in the Curlometer current. χ (panel 4) is less than 0.3 throughout the flux rope, meaning the quality of the Curlometer result should be high. Panels 5 to 12 show the components of the magnetic forces (barycentric magnetic field used) transformed into the variance frame of Cluster 1, their magnitudes, the electron and ion pressure from PEACE and CIS, the B_Z component and $|\mathbf{B}|$. The magnetic forces along the minimum variance direction (assumed to be the trajectory) shown in panel 5 exhibit direction reversals in both total and magnetic pressure force (positive at 03:20:16 UT, negative at 03:20:23 UT). The direction reversals and the pressure dominance of the magnetic force suggests that the magnetic force is acting to expand the flux rope. A comparison across panels 5 to 7 shows that most of the magnetic force is in the plane perpendicular to the axis. The domination of the magnetic pressure force over the magnetic tension force over the flux rope agrees with the observed large core field and small bipolar magnetic field. The non-constant α force-free nature of the flux rope is confirmed in panel 8, showing a large increase in the magnitude of $\mathbf{j} \times \mathbf{B}$ inside the flux rope. However, this force is again weaker in the centre than in the outer sections. The electron pressure from PEACE (panel 9) is reduced inside the flux rope as is the ion pressure (panel 10).

A simple comparison of the change in plasma pressure and magnetic pressure over the first (Cluster 1 ion and magnetic pressure evaluated at 03:20:10 and 03:20:18 UT, Cluster 1 electron pressure evaluated at 03:20:12 and 03:20:20 UT) and second halves of the flux rope (ion and magnetic pressure evaluated at 03:20:18 and 03:20:26 UT, electron pressure evaluated at 03:20:20 and 03:20:28 UT) show

that the change in magnetic pressure is larger than the change in plasma pressure by a factor of ~ 3.1 and ~ 3.6 respectively. It is possible therefore that this flux rope was under a large expansive magnetic pressure dominated total force.

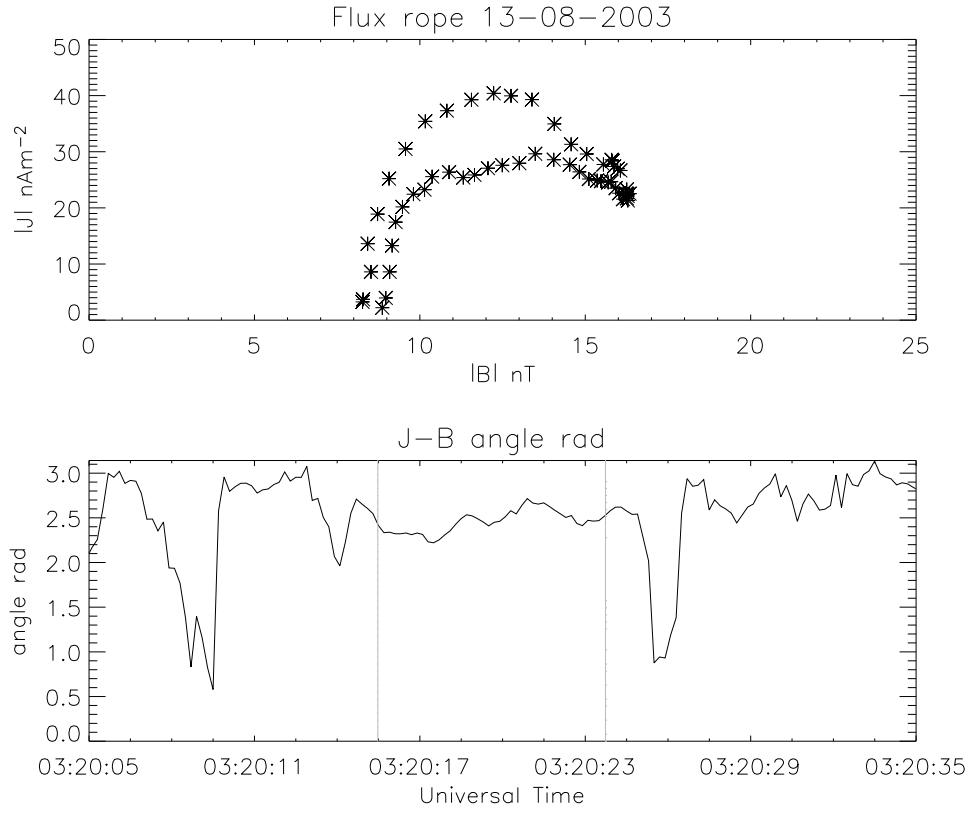

Figure 3.17: $|\mathbf{j}|$ versus $|\mathbf{B}|$ and the angle (in radians) between the magnetic field and current density vectors for the 13$^{\text{th}}$August 2003 flux rope.

Fig. 3.17 shows a scatter plot of the magnitudes of the current density and magnetic field, along with the angle (in radians) between the current density and magnetic field vectors. Again, $|\mathbf{j}|$ versus $|\mathbf{B}|$ yields no clear proportionality and there exists a quasi-constant but non-zero angle between the current density and magnetic field vectors. These results are inconsistent with the flux rope being in a constant α force-free configuration.

Again, an independent estimate of the axis direction can be made if the magnetic force is assumed to be only radially acting. A minimum variance analysis carried

out on $\mathbf{j} \times \mathbf{B}$ gives the minimum variance direction to be (0.514, 0.858, -0.056) with a minimum:intermediate eigenvalue ratio of 11.9. This makes an angle of 12° to the maximum variance direction of the magnetic field: (0.386, 0.917, 0.100).The non-axial nature of the current is confirmed from the maximum variance direction of the current density; (-0.993, 0.063, -0.099). This makes an angle of 109° to the assumed axis.

3.6 Discussion

The event observed by the Cluster spacecraft on the 2nd October 2003 was moving Earthward. From a trivial investigation of the magnetic field components, the flux rope axis was not expected to be simply aligned in the $\pm$Y direction nor moving solely in the $\pm$X direction. The evidence for this came from the core field being in the (+X, -Y, +Z) direction. This direction was found to be close to the negative intermediate variance direction of the magnetic field, the direction along which the smallest component of the magnetic force was directed, as well as being the direction along which the majority of the derived current was directed. The current was not maximum in the centre of the flux rope. The $\mathbf{V}_{\text{timg}}$ produced in 4SCT also defined a plane whose normal was close to the intermediate variance direction, which thus can be safely concluded to be the axis of the flux rope in this case. It has been noted in previous studies (Moldwin and Hughes, 1991; Slavin et al., 2003b) that minimum variance analysis does not always satisfactorily define a flux rope frame. The multi-spacecraft timing method employed here is thus a useful test of the derived variance frame. In this case the test verified that the minimum variance analysis technique did indeed provide a good approximation to the 'flux rope frame'. The duration of the flux rope bipolar signature corresponds to a size of $\sim$ 0.3 R_E and a velocity of $\sim$ 160 kms^{-1}, in approximate agreement with CIS velocity moments. The size of the flux rope quoted here is a lower estimate of the diameter, 0.3 R_E corresponding to the distance between the boundaries of the flux rope at

this impact parameter. The larger speed of the outbound $\mathbf{V}_{\text{timg}}$ vector compared to the inbound vector shows that the constant flux surfaces are either closer together on the tailward side than on the Earthward side of the flux rope, that the flux rope is accelerating or that the flux rope is being compressed during the time that it is observed.

Fig. 3.18 shows a summary of these interpretations in the form of two schematics. The first schematic shows the flux rope with the magnetic field (Fig. 3.7), 4SCT vectors (Fig. 3.8) and current (Fig. 3.10) marked. The magnetic pressure (red) and tension forces (blue, Fig. 3.10) are marked on the second schematic. Both of these schematics are in the variance analysis frame. The magnetic force along the minimum variance direction exhibits a tripolar signature (Fig. 3.10). This signature can be thought of as two bipolar signatures, one centred around the flux rope closest approach time and one observed either outside, or on the outer boundary of the flux rope. The magnetic tension and pressure forces in this flux rope appear to be unbalanced (Figs. 3.10 and 3.18). Throughout the duration of the first bipolar signature in the force along the minimum variance direction, the magnetic pressure force is acting away from the flux rope centre (Fig. 3.18), whilst the magnetic tension force is acting towards the flux rope centre. In the maximum variance direction, the magnetic tension force is generally acting towards the flux rope centre, with the magnetic pressure force acting somewhat away from the flux rope centre (Fig. 3.18). The resolution of these forces, $\mathbf{j} \times \mathbf{B}$, is generally acting away from the flux rope centre, i.e. acting to expand the flux rope. The magnetic force along the intermediate variance direction is generally smaller than any other component, showing that the force is mainly acting radially. The magnetic force which comprises the second bipolar signature along the minimum variance direction, the large positive pressure dominated enhancement in $\mathbf{j} \times \mathbf{B}$ as the spacecraft leaves the flux rope, is most likely acting to push the flux rope Earthward. This could be caused by effects outside the flux rope such as a compression of the flux rope caused by the

outflow from a nearby X-line, in agreement with the increased velocity of constant flux surfaces measured on the outbound part of the flux rope (Fig. 3.8). The magnetic pressure dominance in this flux rope describes a strong core magnetic field and a circulating current. A simple comparison of the changes of plasma and magnetic pressure over the flux rope suggested that the flux rope was experiencing an expansive total force.

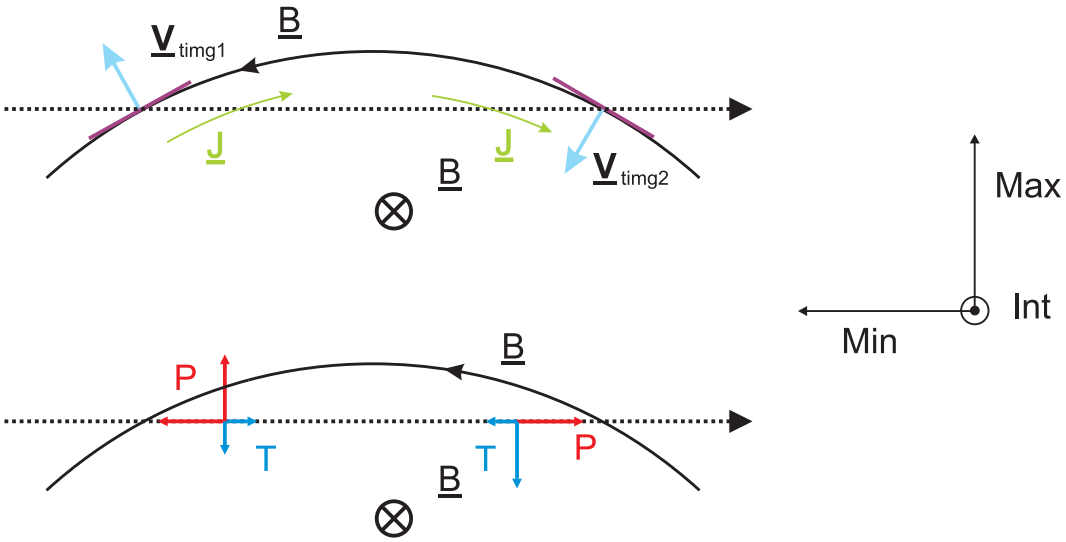

Figure 3.18: Schematics of the main results of the 2nd October 2003 flux rope. The magnetic field (Fig. 3.7), 4SCT vectors (Fig. 3.8) and current (Fig. 3.10) marked on one schematic, the magnetic pressure (red) and tension (blue, Fig. 3.10) marked on the other in the variance analysis frame. The relative trajectory of the spacecraft through the flux rope is marked by a dotted line.

The event observed by the Cluster spacecraft on the 13thAugust 2003 was moving tailward. The flux rope, expected to be aligned to the $\pm$Y direction and travelling in the $\pm$X direction from trivial investigations of the magnetic field, was not expected to be in a constant α force-free configuration. The evidence for this came from the observation of a large core field in the -Y direction, this direction being close to the maximum variance direction of the magnetic field and the direction along which the least of the magnetic force was directed. This was confirmed by the $\mathbf{V}_{\text{timg}}$ produced in 4SCT which defined a plane whose normal was close to the maximum variance direction, again confirming that the minimum variance analysis returned a good approximation to a 'flux rope frame'. The flux rope bipolar

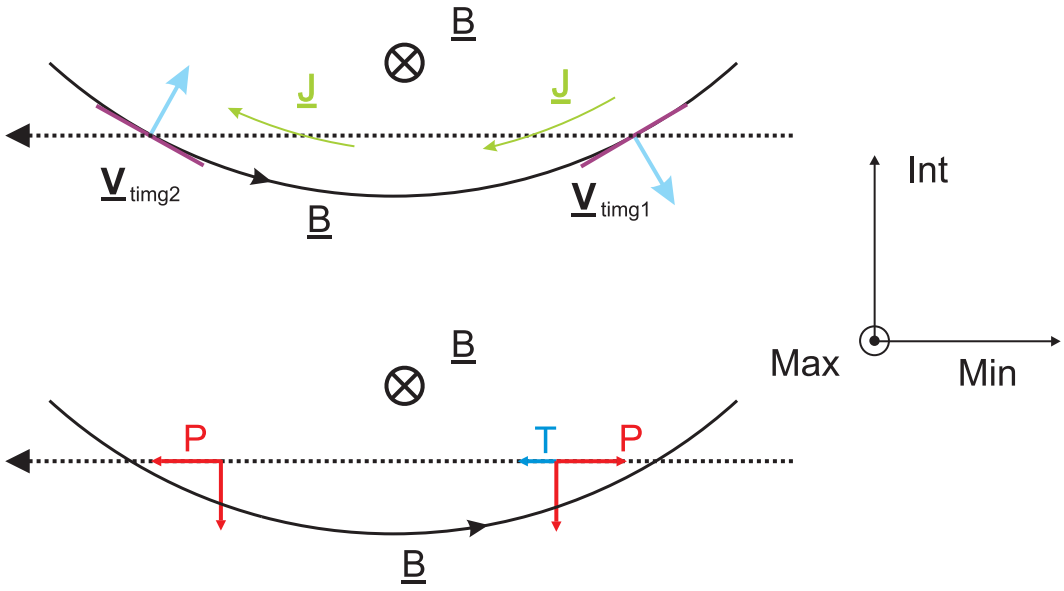

Figure 3.19: Schematic of the main results of the 13thAugust 2003 flux rope in the same format as Fig. 3.18

signature duration corresponded to a size of 0.3 R_E, the flux rope was travelling at $\sim$ 200 kms^{-1}, in agreement with CIS velocity moments. The current was not mainly directed along the maximum variance direction and was therefore not only axial. The current had significant components along the minimum variance direction (trajectory) and maximum variance direction (axis) and showed a reversal in the intermediate variance direction. It therefore appears that the current was circulating in a plane whose normal was the axis.

Fig. 3.19 shows two schematics of the 13thAugust 2003 flux rope in the same format as Fig. 3.18. The magnetic force is again unbalanced with the magnetic pressure force along the minimum variance direction being bipolar (Fig. 3.16), acting away from the flux rope centre (Fig. 3.19). The magnetic tension force along this direction opposes the magnetic pressure force over the first half of the flux rope, i.e. toward the flux rope centre, falling to zero over the second half of the flux rope. Along the intermediate variance direction, the magnetic pressure is acting away from the flux rope centre, acting to expand the flux rope. The force along the maximum variance direction is small, showing that the force is mainly radial. Thus, the total force is magnetic pressure dominated, and is acting to radially

expand the flux rope. This flux rope is dominated by a core magnetic field with a weakly circulating magnetic field, agreeing with the weak bipolar signature in the intermediate variance direction (Fig. 3.14). The current is mainly circulating around the axis (Fig. 3.16). The lack of magnetic tension as the spacecraft left the flux rope suggests that the spacecraft flew through a region where the magnetic field lines are weakly curved on the scale of the spacecraft separation. A simple comparison of the plasma and magnetic pressure changes over the flux rope was consistent with the flux rope experiencing a large net outward directed force.

The mechanism for the creation of these structures is important for the study of the break-up of current sheets near substorm onset. The flux ropes reported here are not force-free, indeed tending to be less force-free in the outer sections of the flux rope than in the centre. The cores of these flux ropes would perhaps be expected to relax in time into the constant α force-free flux rope state, the lowest energy state of a helical magnetic field, as is the case for those seen in the distant tail. If the process responsible for the creation of these flux ropes is MXR and if it is occurring close to the point where the flux ropes are observed, the flux ropes might not have had time to fully relax into this force-free state. However, as the flux in the centre of the flux ropes would have reconnected before that in the outer sections, the central flux would have had more time to begin the evolution towards a force-free configuration. The outer sections would therefore be expected to less force-free than the centre, as observed in both flux ropes reported here.

The lower estimate sizes of these flux ropes are consistent with previous studies of the near-tail plasma sheet. Although Slavin et al. (2003a) estimates flux rope diameters of $\sim$ 2 to 5 R_E at X $\sim$ -15 to -30 R_E using Geotail, a number of flux ropes had estimated radii in the region $\sim$ 0 to 1 R_E. In addition, Walsh et al. (2007) reported flux ropes sizes of between 0.2 and 0.4 R_E, approximately the same size as those reported here. Due to the small sample of flux ropes reported here (and previous studies), this study is unable to determine whether flux ropes at X $\sim$ -20

R_E are generally smaller than those observed out to X $\sim$ -30 R_E.

Slavin et al. (2003a) found a large range of orientations of flux ropes; the highly inclined orientation of the 2nd October 2003 flux rope reported here may not be particularly unusual. The reason for deviation of the flux ropes' orientation away from the GSM axes remains unclear, but could be due to tilted X-lines or the effects of shear in the plasma sheet flows in which the flux ropes are embedded (Winglee, 2004).

Eastwood et al. (2005) recently reported on the motion of two X lines in the tail and an associated flux rope. The flux rope reported by Eastwood et al. (2005) was observed 5 minutes before the 2nd October 2003 flux rope reported in this chapter. Eastwood et al. (2005) identifies, using different multi-spacecraft timing methods, a flux rope moving at $\sim$ 140 kms^{-1} in the direction (0.778, 0.595, 0.158). This direction is approximately the same as the minimum variance direction reported here and the velocity is approximately the same as reported using 4SCT rotations here. This could suggest that these two flux ropes could be from the same MXR event.

In Slavin et al. (2003b), the current in the presented flux rope is calculated and is found to be not always parallel to the magnetic field. Fig. 3 in their paper shows that at some points the magnitude of the current perpendicular to the magnetic field exceeds the magnitude of the current parallel to the magnetic field. This again shows that near-Earth flux ropes seem not to exhibit the characteristics of a constant α class of force-free flux ropes.

Slavin et al. (2003a) find that approximately 60% of the flux ropes found between X $\sim$ -15 to -30 R_E were a good fit to a force-free model and were generally larger than those reported here. One interpretation of the tailward moving flux ropes observed at the distances that Slavin et al. (2003a) investigated is a sample of 'older' and larger tailward moving flux ropes than the 13thAugust event reported in this chapter. The fact that not all flux ropes reported in Slavin et al. (2003a) seem to

be force-free could be explained if some are evolving away from the form detailed here to a more force-free configuration.

In Slavin et al. (2003a) the plasma beta is reduced during a flux rope encounter (their Fig. 7). The authors note that without the benefit of high resolution plasma instruments to resolve inside the flux rope, this reduction could simply be caused by an increase in the magnetic field rather than by any reduction in plasma pressure. Figs. 3.10 and 3.16 of this chapter would suggest that the reduction could be due a combination of both factors.

There is a build up of plasma pressure on the Earthward side of the 2nd October 2003 Earthward-moving flux rope (not shown). This, along with a large enhancement of current just before the flux rope core (Fig. 3.10), could be explained if the flux rope was pushing up against oppositely directed terrestrial closed magnetic field lines. There would be a 'snow plough' effect as the plasma and magnetic field Earthward of this flux rope was compressed by the flux rope. As the flux rope magnetic field lines and the closed field lines have opposite polarity, re-reconnection could take place, essentially stripping away the outer layers of the flux rope as it travelled further Earthward. If this were the case a small current sheet would be formed with opposite polarity to that inside the flux rope. Indeed, Fig. 3.10 shows that the current enhancement is mainly in the intermediate variance direction of the magnetic field, i.e. in the axial direction, but directed oppositely to the current inside the flux rope.

Both of the flux ropes reported here are under expansive magnetic forces in their outer sections. These observations could be due to their evolution towards the force-free configuration seen further down the tail after formation in MXR. If this is the case and the 13thAugust event is a young flux rope, multiple X point reconnection must have happened shortly Earthward of $\sim$ 18 R_E down the tail.

3.7 Conclusions

Few well-formed flux ropes were found in the 2003 Cluster tail season, but two have been investigated in detail in this chapter. Neither flux rope was found to be in a magnetic force free configuration, demonstrated by the computation of the $\mathbf{j} \times \mathbf{B}$ forces inside the flux ropes. The magnetic force was smaller in the centre than in the outer sections of the flux ropes and was generally small along the axis. The magnetic force was magnetic pressure dominated and generally acted away from the flux rope centres, i.e. acting to make the flux ropes radially expand. In one case the axis of the flux rope was in the intermediate variance direction, in the other the axis was in the maximum variance direction. The axis directions were confirmed using multi-spacecraft timings, and were consistent with trivial observations of the magnetic field. The flux ropes were small and slow moving, derived from multi-spacecraft timings, consistent with CIS ion moments. Plasma pressure (both electron and ion) was reduced inside the flux ropes. Both flux ropes were under net expansive total forces, this force imbalance being larger in the 13$^{\text{th}}$August 2003 (tailward moving) flux rope.

These flux ropes have been interpreted as evidence for multiple X-line reconnection in the near-tail close to Cluster apogee (X $\sim$ -20 R_E). If the flux ropes are newly formed their centres may have had more time to relax towards the force-free state observed further down the tail, consistent with observations of smaller magnetic forces in the centres of the flux ropes. These more distant-tail flux ropes are generally much larger than those observed here, possibly consistent with the expansive magnetic pressure dominance of the $\mathbf{j} \times \mathbf{B}$ force and overall force imbalance in the 13$^{\text{th}}$August 2003 flux rope. The observation of a tailward moving flux rope suggests that this flux rope was created Earthward of X $\sim$ -18 R_E.

Chapter 4

Ohm's law near an X-line

4.1 Introduction

The large and small scale behaviour of the magnetosphere is governed by electric fields. The flow of magnetic field and plasma from the solar wind gives rise to the convection electric field that permeates the magnetosphere. On smaller scales, electric fields are thought to play a vital role in the microphysics of reconnection.

Electric fields are governed by the generalised Ohm's law (Eqn. 1.19):

$$\mathbf{E} = -\mathbf{v}_i \times \mathbf{B} + \frac{\mathbf{j} \times \mathbf{B}}{en_e} - \frac{\nabla . \mathsf{P}_e}{en_e} - \frac{m_e}{e}\frac{d\mathbf{v}_e}{dt} + \eta \mathbf{j} \tag{4.1}$$

Here, **E**, **v**, n and P are electric field, velocity, density and pressure tensor respectively (subscripts e and i denote the species). **B**, **j** and η are the magnetic field, current density and the resistivity respectively and e is the electronic charge.

The first term on the RHS is the ideal MHD term expressing frozen-in convection of magnetic field and plasma. The second term is the Hall term and becomes important when the scale size of the system approaches the ion inertial length. At this scale size the ions become demagnetised and no longer move with the magnetic field. The electrons remain magnetised until the electron inertial length where they too become demagnetised. The third and fourth terms are the divergence of

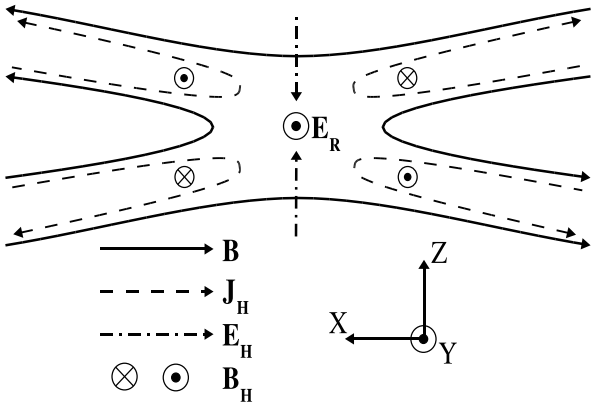

Figure 4.1: Magnetic field, electric field and current topology around an X-line. The field-aligned current system ($\mathbf{J_H}$) associated with the Hall current system and quadrupolar magnetic field system ($\mathbf{B_H}$) are marked. Previous observations and simulations show that the Hall electric field normal to the current sheet ($\mathbf{E_H}$) points towards the current sheet. The reconnection electric field ($\mathbf{E_R}$) points across the magnetotail.

the electron pressure tensor ($\nabla . \mathsf{P}_e$) and electron inertia terms. Attempts have been made to estimate the $\nabla . \mathsf{P}_e$ term (e.g. André et al., 2004) and empirically argue its role in parallel electric field generation (e.g. Scudder et al., 2002). However, neither the $\nabla . \mathsf{P}_e$ or the electron inertia terms have, to date, been properly determined in previous observational studies. In the absence of anomalous resistivity caused by, for example, wave-particle interactions (Labelle and Treumann, 1988; Schmitz and Grauer, 2006), the last term can be normally considered negligible in collisionless space plasmas.

The plasma sheet is a prime location for magnetic reconnection (Vasyliunas, 1979) to occur and create one or more X-lines (Fig. 3.1). The reconnection itself is believed to occur within an extremely localised region of the magnetotail called the 'diffusion region'. This surrounds the X-line and comprises two distinct parts, the ion and electron diffusion regions (Sonnerup, 1979). These regions are on the scales of the ion and electron inertial lengths (Eqn. 1.27), which, in the plasma sheet, are on scales of a few hundred km and a few km respectively.

As was discussed in section 1.5, reconnection can occur when two anti-parallel magnetic field lines come into contact. In the GSM coordinate system these field

lines would be in the positive and negative X direction. Figure 4.1 shows the magnetic topology of an X-line in the GSM coordinate system. The reconnection electric field would be in the same direction (+Y) as the cross tail current and cause an $\mathbf{E} \times \mathbf{B}$ drift of plasma and magnetic field towards the X-line from above and below the neutral sheet.

Assuming there is no guide magnetic field in the Y direction, the magnetic field at the X-line vanishes. Thus, the Hall and ideal MHD terms cannot support the reconnection electric field at this point. The electron terms must therefore play a significant role at the X-line. Theory (Vasyliunas, 1979) and simulations (Hesse et al., 1999; Kuznetsova et al., 2001; Yin et al., 2001a; Yin et al., 2001b; Yin and Winske, 2003) suggest that the spatial derivatives of the off-diagonal components of P_e support the reconnection electric field in a small region around, and at, the X-line. Outside this small region, the reconnection electric field is supported by the Hall term, then the ideal MHD term at larger distances.

The measurement of the $\nabla . \mathsf{P}_e$ term is therefore very important for both the understanding of the general properties of the plasma sheet and the reconnection process.

Equation 4.1 can also be used to investigate the general electric field properties of the plasma sheet. As the electrons continue to move towards the X-line with the magnetic field, a charge separation is set up by the ions, no longer moving with the magnetic field. This occurs when the scale size of the system is reduced to the ion inertial length. In this way a Hall electric field pointing towards the neutral sheet on both sides appears (Figure 4.1) (Nagai et al., 2001, Borg et al., 2005, Wygant et al., 2005).

Additionally, the electron pressure would be expected to be larger towards the centre than the edges do to the convective nature of the reconnection electric field. This simple effect will lead to an electric field pointing away from the neutral sheet from the $\nabla . \mathsf{P}_e$ term in the normal (Z) direction.

Hall-MHD simulations by Yin et al. (2001), which include the full electron pressure tensor to initiate reconnection, find that in the X direction the contributions are generally towards (away from) the X-line for the $\nabla . \mathsf{P}_e$ (Hall) term. The electric field contributions normal to the neutral sheet (Z) from the Hall ($\nabla . \mathsf{P}_e$) term points towards (away from) the neutral sheet and is largest at the X-line. The contributions normal to the neutral sheet were found to be more spatially extensive and larger than those in the plane of the neutral sheet. In order to observe this field, it can be seen that a spacecraft would have to approach very close to the X-line.

As well as the creation of a neutral sheet directed electric field, the differential motion of ions and electrons within the ion diffusion region creates Hall currents directly related to reconnection. These in turn drive a system of field aligned currents outside the ion diffusion region, which act to close the Hall currents and also create the quadrupolar magnetic field structure previously reported (Nagai et al., 2001, Runov et al., 2003, Asano et al., 2004, Borg et al., 2005, Alexeev et al., 2005). These systems are illustrated in Fig. 4.1.

The four-spacecraft nature of the Cluster mission can be used to directly determine both the Hall and $\nabla . \mathsf{P}_e$ terms using the multi-point observations.

In this chapter, section 2 will give an overview of the period of data selected for this study. In the section 3 the contributions to the electric field, as well as the currents and magnetic field will be investigated in a region close to an active X-line. Hall signatures of reconnection are also investigated. In the section 4 the data comes from a region very close to an active X-line. The results will then be discussed in section 5 and conclusions drawn in section 6. These investigations include the first calculations of the full $\nabla . \mathsf{P}_e$ term calculated from 3D electron phase space distributions as first described in Henderson et al. (2006b).

4.2 Data Overview - 17thAugust 2003

At 16:00 UT on the 17thAugust 2003 the Cluster spacecraft were located at (-16.6, -5.3, 4.1) R_E (GSM coordinates will be used throughout section 4.2), near apogee in the magnetotail. As discussed in section 2.1, the average separation of the Cluster tetrahedron in this tail season was only 200 km. The multi-spacecraft methods described in section 2.6 assume that the measured quantity varies linearly over the tetrahedron. This assumption will be most valid at time when the spacecraft separation is small, ideally smaller than the structure being observed. The spacecraft were in burst mode (see section 2.2.3) which meant that 3D data from the PEACE instruments on board all four Cluster spacecraft, as well as CIS on Cluster 4, was sent to the ground. As usual for burst mode events in the magnetotail, Clusters 1 and 3 provide 3DR (LEEA) and 3DX1P (HEEA), with Clusters 2 and 4 providing 3DX1P (LEEA) and 3DX2P (HEEA). It is noted that Cluster 4 CIS CODIF was the only CIS instrument functioning. The fact that the spacecraft were in burst mode allows one to derive the divergence of the electron pressure tensor (as described in section 2.6.2). This divergence appears in the generalised Ohm's law (Eqn. 4.1) and can be compared to the Hall term. This latter term can be determined after measuring the current via the Curlometer technique (as described in section 2.6.2). These two derived quantities are in some sense averages through the tetrahedron which should be applied at the barycentre of the tetrahedron. Great care and effort has been made to verify the calibration of the four PEACE data sets in order to support differencing of the data from different spacecraft to produce valid gradients required here. Section 2.2.6 briefly describes this correction of the electron moments due to the V_Z problem. It is important to note that all the plasma data were interpolated onto the time stamps of Cluster 4 PEACE, while high time resolution FGM data, and the current density derived from this data, were averaged onto these time stamps.

Figure 4.2 shows data from the 17thAugust 2003 between 15:55 and 17:35 UT. Panels 1 to 4 show the magnetic field components, B_X, B_Y, B_Z and $|\mathbf{B}|$, with Cluster

1 in black, Cluster 2 in red, Cluster 3 in green and Cluster 4 in magenta. This colour scheme will be used throughout this chapter. As the magnetic field lines are stretched into the magnetotail and point towards Earth above the neutral sheet and away from the Earth below the neutral sheet, B_X can often be taken as a proxy for the position of the spacecraft relative to the neutral sheet. It is important to note that the velocity of Cluster is generally much less than the velocity associated with the motion of the plasma sheet. In this way, it is most often the plasma sheet which moves over the stationary spacecraft rather than the spacecraft moving over the stationary plasma sheet. According to panel 1, the spacecraft were initially north of the neutral sheet (15:55 UT) and slowly crossed to the south of the neutral sheet at approximately 16:05 UT.

There were a number of quicker crossings at approximately 16:30 and 16:40 UT. This behaviour could be indicative of the plasma sheet flapping as geomagnetic activity increased (this behaviour was statistically shown in Sergeev et al. (2006)).

The spacecraft moved away from the plasma sheet (B_X becoming increasingly negative) between approximately 16:40 and 16:55 UT. At 16:55 UT the spacecraft moved back towards the neutral sheet, and with the exception of one crossing at $\sim$ 17:00 UT, remained south of it. At the end of the period presented here the spacecraft remained close to, but south of, the neutral sheet.

The AE index for this time (panel 5) shows an enhancement from approximately 16:30 UT. It is noted that the AE index starts to decrease from its peak at approximately 17:10 UT. At the peak, AE index reaches $\sim$ 800 nT, indicative of strong substorm activity and reconnection in the tail.

If one assumes a simplified pressure balance across the tail, in which the total pressure is constant over the tail (Baumjohann et al., 1990b), then the pressures in the lobes and plasma sheet can be described thus:

$$\frac{B_L^2}{2\mu_0} + \left(n_i k_b T_i + n_e k_b T_e\right)_L = \frac{B_{PS}^2}{2\mu_0} + \left(n_i k_b T_i + n_e k_b T_e\right)_{PS} \tag{4.2}$$

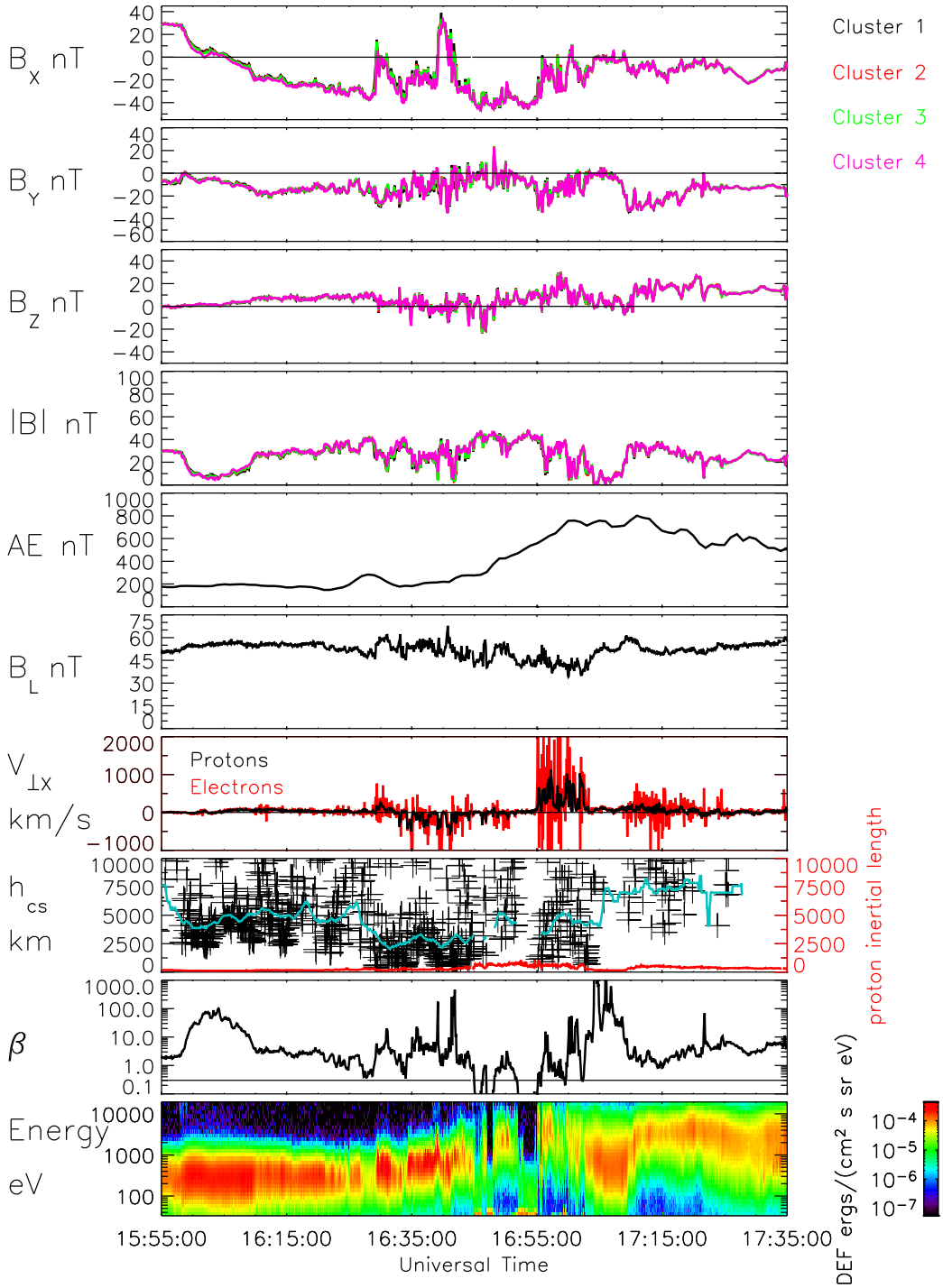

Figure 4.2: Panels 1 to 4 show the magnetic field from all spacecraft (Cluster 1 - black, Cluster 2 - red, Cluster 3 - green, Cluster 4 - magenta). Panel 5 shows the AE index. Panels 6 and 7 show the estimated lobe magnetic field strength (Equation 4.3) and the X component of velocity for protons (black) and electrons (red) from Cluster 4. Panel 8 shows the estimated current sheet half thickness (black crosses, Eqn. 4.7, Green; boxcar average) and the proton inertial length (red). The final two panels show the full plasma beta and an energy time spectrogram of electrons in the energy range 30 eV to 26 keV from Cluster 4.

Where B, n and T are the magnetic field, number density and temperature respectively. The subscripts PS, L, i and e denote the contributions from the plasma sheet, lobes, ions and electrons respectively.

If the plasma pressure in the lobes is negligible (a working definition of the lobes) and one can measure the magnetic field and plasma parameters in the plasma sheet, it is possible to estimate the magnetic field in the lobes (B_L):

$$B_L = \left[B^2 + 2\mu_0 k_b \left(n_i T_i + n_e T_e\right)\right]^{\frac{1}{2}} \tag{4.3}$$

B_L (Eqn. 4.3) is shown in panel 6 of Fig. 4.2. It can be seen that B_L was $\sim$ 55 nT until approximately 16:30 UT. At this point the field strength became smaller, reaching $\sim$ 40 nT at approximately 17:00 UT. If B_L can be identified as a measure of the amount of magnetic flux stored in the tail, the overall trend during this time (ignoring high frequency variations) suggests that flux was being removed from the tail in the locality of Cluster.

Panel 7 shows the X component of velocity from protons (black) and electrons (red). This panel shows fast flows in the negative X direction for both protons and electrons ($\sim$ 500 kms^{-1}) between approximately 16:30 and 16:55 UT. After 16:55 UT however, the flow reversed to the positive X direction for both protons electrons $\sim$ 1000 kms^{-1}).

This signature is consistent with the tailward retreat of an X-line. Under this interpretation, the X-line crossed over the Cluster spacecraft at approximately 16:55 UT. Indeed reconnection at an X-line would act to remove open flux in the tail, consistent with the inferred reduction in B_L (panel 5).

If one assumes a magnetic field profile is of a Harris (1962) type, then the half thickness of the current sheet can be derived. A Harris (1962) magnetic field profile is a one dimensional current sheet, where all magnetic field is assumed to be in the X direction and is a function of Z only:

$$\mathbf{B}(z) \equiv B_L \tanh\left(\frac{z}{h}\right)\ \hat{\mathbf{x}} \tag{4.4}$$

Differentiating **B** with respect to z gives:

$$\nabla_z B_x = \frac{d\mathbf{B}(z)}{dz} = \frac{B_L}{h}\,\mathrm{sech}^2\left(\frac{z}{h}\right) \tag{4.5}$$

or:

$$\nabla_z B_x = \frac{B_L}{h}\ \left[1 - \left(\frac{B_x}{B_L}\right)^2\right] \tag{4.6}$$

Therefore, by measuring the spatial gradient of the magnetic field ($\nabla_z B_x$) and by knowing the magnetic field in the lobes (B_L), the half thickness h_{cs} can be estimated (Runov et al., 2005b):

$$h_{cs} = \frac{B_L}{\nabla_z B_x}\ \left[1 - \left(\frac{B_x}{B_L}\right)^2\right] \tag{4.7}$$

Equation 4.7 is an estimate of the half-thickness of the current sheet. h_{cs} is plotted in panel 8 as black crosses. Overplotted in green is a boxcar average of these points (between 0 and 10000 km) to show the general trend throughout the period.

It can be seen that at the beginning of the encounter, the boxcar average lies near 5000 km. Towards 16:35 and 17:00 UT this is reduced closer to 2000 km but with many points measured in hundreds of km. This suggests that the current sheet thinned as the spacecraft moved closer to the reconnection site (e.g. Hones et al., 1967, Hones et al., 1984, Dewhurst et al., 2004). The scale length of the proton diffusion region (the proton inertial length) is also plotted (red, Eqn. 1.27). It can be seen that during the removal of flux, where B_L is reduced between 16:30 and 17:00 UT, the half thickness of the current sheet approached the proton inertial length. At this scale non-ideal-MHD processes become important and may play a role here.

Panel 9 shows the full plasma β (Eqn. 1.26), with $\beta = 0.3$ marked. $\beta = 0.3$ is here identified with the boundary between the plasma sheet and lobes. It can be seen that at the beginning of this interval (from 15:55 to 16:30 UT) β remained above $\sim$ 1, showing that Cluster remained inside the plasma sheet. Indeed, during the first crossing of the neutral sheet (16:05 UT), β approached 100, consistent with a very low magnetic field (panel 4). During the second and third crossings of the neutral sheet (16:30 and 16:40 UT) β began to fluctuate, at points being reduced to $\sim$ 0.3, indicating that the spacecraft moved towards the edges of the plasma sheet. This movement away from the centre of the plasma sheet is concurrent with the current sheet half thickness decreasing and could be indicative of the thinning of the plasma sheet.

Panel 10 shows an energy-time spectrogram of electrons with energies between approximately 30 eV and 26 keV. The Z axis is the differential energy flux. The thinning of the current sheet is dramatically shown in panels 8 and 9 between 16:40 and 16:55 UT. β dropped below 0.3 and the differential energy flux of electrons was dramatically reduced. This is consistent with the plasma sheet thinning, resulting in the spacecraft moving out into the lobes.

The energy of the peak differential energy flux in the spectrogram is at approximately 300 eV at 16:00 UT. Throughout the period between 16:30 and 16:55 UT the plasma sampled as the spacecraft encountered the plasma sheet or PSBL had a higher energy peak, reaching approximately 6 keV at 16:55 UT, consistent with an energisation of the plasma sheet. The plasma sheet enveloped the spacecraft after approximately 16:55 UT, with the peak energy of the surrounding plasma $\sim$ 1 keV at 17:00 to 17:10 UT. At approximately 17:10 UT the spacecraft entered a region in which it observed increasingly hotter plasma until the end of the encounter.

It can be seen that during the period shown in Fig 4.2 the magnetosphere was very dynamic. During this period flux was removed from the tail and bipolar signatures were observed in the X component of plasma flow, consistent with the tailward

retreat of an active X-line. A large enhancement in the AE index was also observed. The plasma sheet thinned to scales approaching the proton inertial length and the spacecraft encountered regions containing increasingly hotter plasma. These signatures are all consistent with the occurrence of a substorm (section 1.6) during this period.

The following case studies will detail the observations of two sets of crossings from this day.

4.3 Case study one - Remote sensing of the X-line

Fig. 4.3 shows observations from a 5-minute period between 16:38 and 16:43 UT, containing a number of neutral sheet crossings in the same format as Fig. 4.2. It can be seen that all B_X were initially negative, indicating that all spacecraft were nominally south of the neutral sheet, but became positive as the spacecraft crossed the neutral sheet at approximately 16:39:20 UT. After several more crossings between 16:41 and 16:42 UT the spacecraft moved south of the neutral sheet at approximately 16:42:30 UT. B_Y was negative throughout most of this time and B_Z was small. The magnitude of the magnetic field observed at high resolution (10 vectors per second, not shown) is small ($\sim$ 2 nT) at all spacecraft when $B_X = 0$, suggesting there was little or no guide field.

It has been assumed that GSM satisfactorily approximated the current sheet frame (with magnetic field reversal in the X direction, cross tail current in the Y direction and neutral sheet normal in the Z direction). In some cases this approximation can be invalid, leading to significant deviations from GSM (Zhang et al., 2002, Sergeev et al., 2003). A minimum variance analysis (Sonnerup and Cahill, 1967) is therefore performed on this period of data and suggests the neutral sheet normal, identified with the minimum variance direction, was in the (-0.037, 0.088, -0.995) direction, with a minimum:intermediate eigenvalue ratio of 3.7. The GSM system should therefore satisfactorily represent a natural neutral sheet frame at this

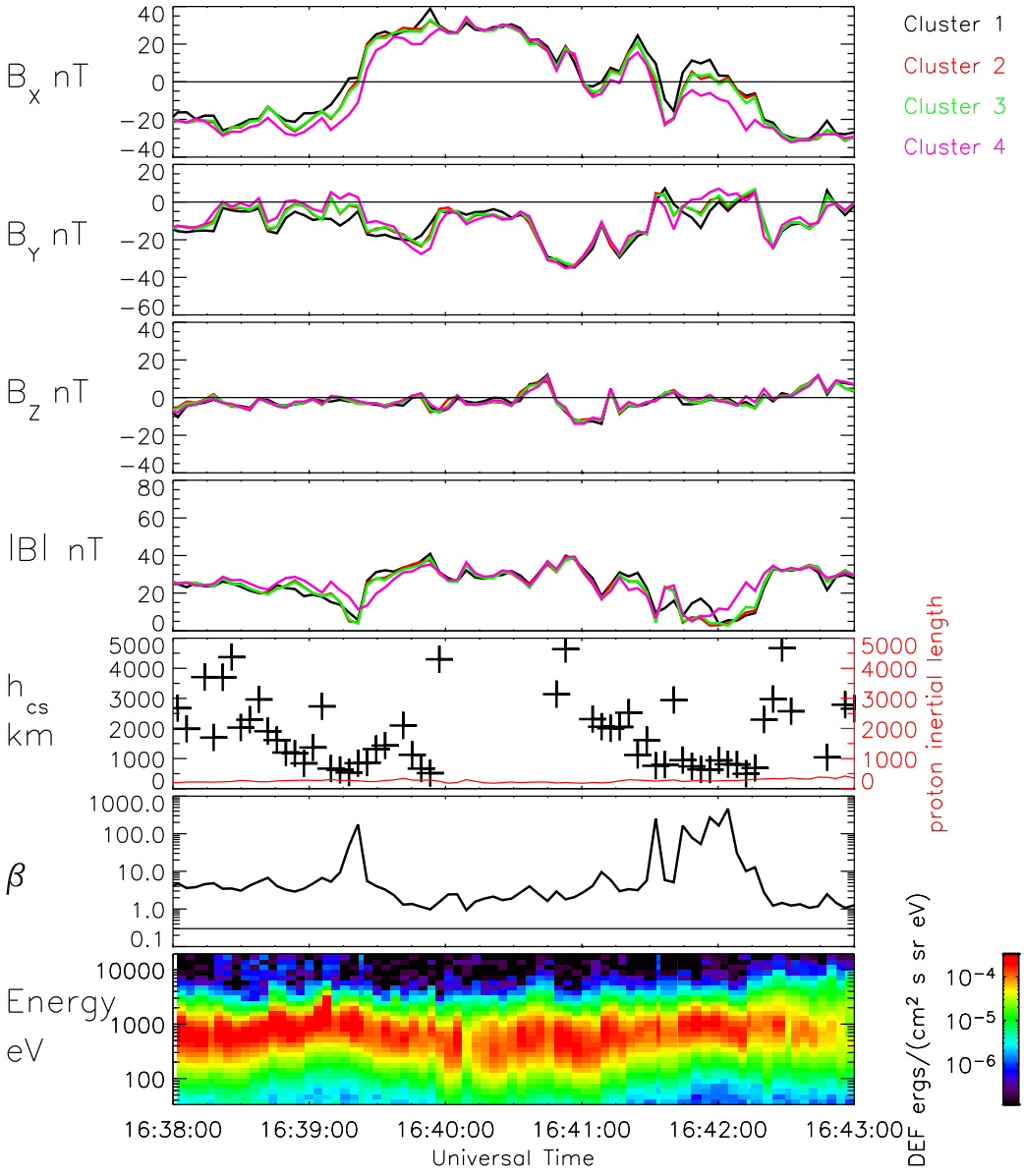

Figure 4.3: Data from case study two in the same format as Fig. 4.2.

time, with GSM Z corresponding to the neutral sheet normal direction. GSM will therefore be used throughout this section.

The current sheet thickness (panel 5) was thin, approximately 500 km. Plasma β remained above 1 (panel 6) and a clear signature of $\sim$ 1 keV electrons indicates that the spacecraft were in the plasma sheet throughout this period (panel 7).

Note that these spacecraft were separated by only $\sim$ 220 km in the Z direction at this time. At a neutral sheet crossing location (16:39:49 UT) the plasma density was $\sim$ 0.8 cm^{-3}, giving a proton (electron) inertial length $\sim$ 255 km ($\sim$ 6 km), which defines the scale length of any proton (electron) diffusion region. The flows in the period shown here were in the tailward direction (Fig. 4.2), which suggests that the active X-line was located Earthwards of the spacecraft.

Figure 4.4 shows the magnetic and electric field observations for this time period. Panels 1 to 4 show the four components of the magnetic field measured on each spacecraft. Panel 5 shows $\frac{1}{3}Tr\mathsf{P}_e$, an indication of the total electron pressure observed at each spacecraft. Panels 6 to 9 show the electric field contributions parallel to, and the three components perpendicular to the magnetic field respectively from the Hall and $\nabla.\mathsf{P}_e$ terms in Ohm's law. In these panels the electric field contribution from the Hall term is in red, whereas the electric field contribution from the $\nabla.\mathsf{P}_e$ term is in black. Note that as the Hall term is always perpendicular to the magnetic field no red trace can be seen on panel 6. The magnetic field used in the derivation of the contributions parallel and perpendicular to the magnetic field is the barycentric magnetic field, the predicted magnetic field at the centroid of the Cluster tetrahedron.

Panel 5, the magnitude of the electron pressure ($\frac{1}{3}Tr\mathsf{P}_e$) from each spacecraft, shows that the electron pressure was generally higher when the spacecraft were closer to the neutral sheet.

Panels 6 to 9 in Fig. 4.4 show the full components of the electric field arising from the $\nabla.\mathsf{P}_e$ term (black) and the Hall term (red) in the generalised Ohm's law

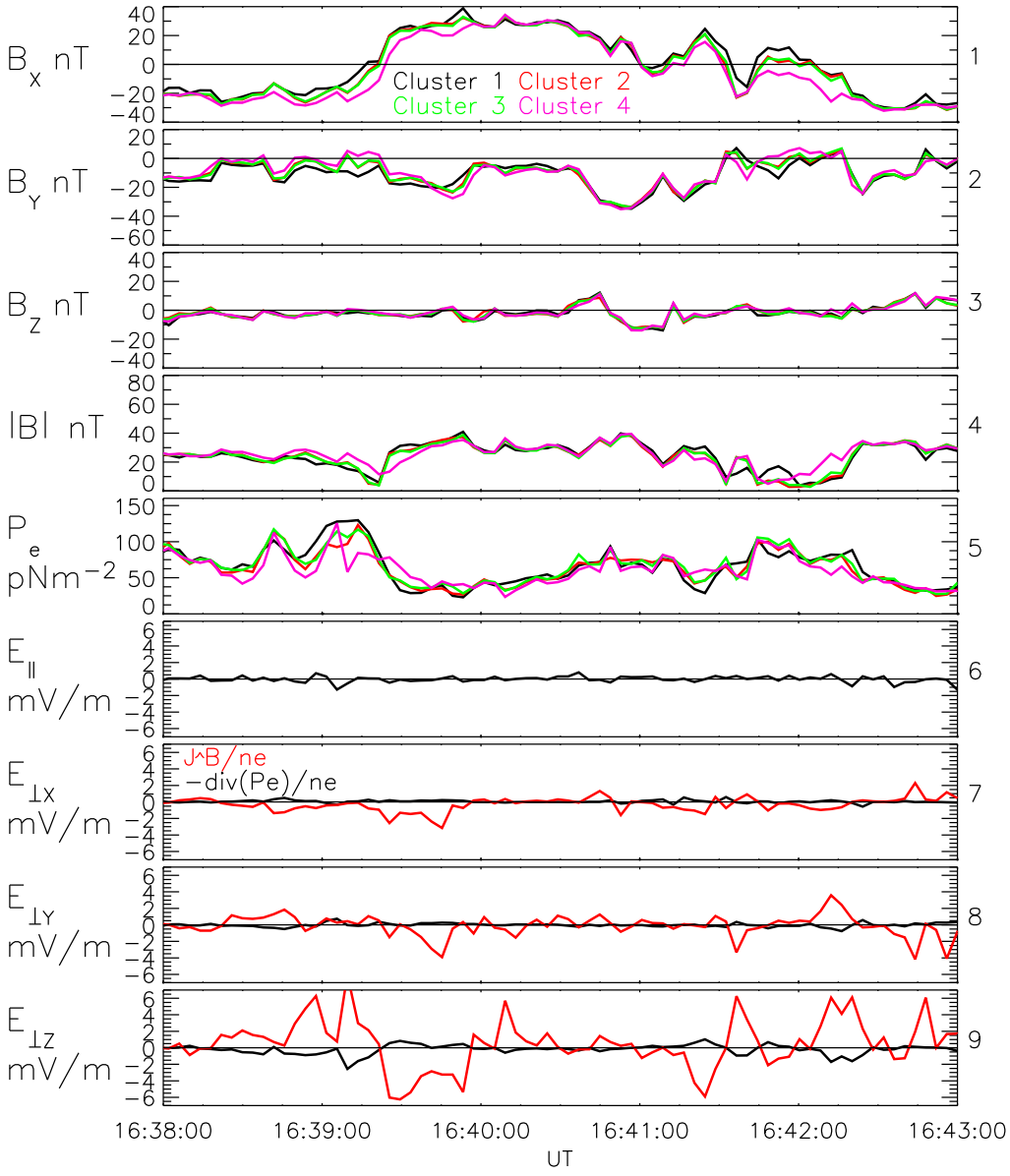

Figure 4.4: Panels 1 to 4 show the B_X, B_Y and B_Z components and $|B|$ from all spacecraft (Cluster 1 - black, Cluster 2 - red, Cluster 3 - green, Cluster 4 - magenta) for the first crossing investigated in detail in this chapter. Panel 5 shows $\frac{1}{3}Tr\mathsf{P}_e$. Panel 6 shows the parallel component of the electric field from $\nabla.\mathsf{P}_e$ at the barycentre. Panels 7 to 9 show the perpendicular components of the electric field from the Hall term (red) and $\nabla.\mathsf{P}_e$ (black) terms.

(Eq. 4.1). These are derived from the gradients between each of the 4 Cluster spacecraft and are the first such calculation performed (Henderson et al., 2006b).

There was little electric field contribution parallel to the magnetic field from the $\nabla . \mathsf{P}_e$. If the other terms in Ohm's law that could produce a parallel electric field are negligible at this time then the lack of parallel electric field would suggest that $\mathbf{E}.\mathbf{B}$ is close to zero, in turn suggesting that MHD is valid. At 16:39:30 UT, the X and Y components of the perpendicular electric field from the Hall term (red trace) are both negative. As at this time $B_X \sim B_Y$, this electric field would seem to the directed across the tail, but could in some part be associated with the Hall term pointing away from the X-line in agreement with Yin et al. (2001). Moreover, no clear sustained signature of a reconnection electric field in the (positive) Y direction supported by the $\nabla . \mathsf{P}_e$ term can be seen (panel 8). A number of peaks in the (positive) Y direction can be seen in the contribution from the Hall term and these could be supporting (part of) the reconnection electric field away from the X-line. Panel 9 shows the Z component of the perpendicular electric field (i.e. the component normal to the nominal neutral sheet). Where the spacecraft were close to the neutral sheet (i.e. around the $B_X = 0$ crossings) it can be seen that the Hall term pointed towards the neutral sheet while the $\nabla . \mathsf{P}_e$ term pointed away from it. The bipolar signatures in this component are thus caused by the spacecraft barycentre crossing the neutral sheet.

Between 16:41:44 and 16:42:10 UT the 4 second averaged magnetic field data shows that Cluster 1 was north of the neutral sheet ($B_X \sim +10$ nT), whereas Cluster 4 was south of the neutral sheet ($B_X \sim -10$ nT). The same data suggest that the spacecraft concurrently observed significantly different B_Y (Cluster 1 observed $B_Y \sim -5$ nT, Cluster 4 observed $B_Y \sim +5$ nT). The high time resolution magnetic field data show some high frequency fluctuations, but generally reflect the behaviour seen in the 4 second averaged data. For example, at 16:41:49 UT Cluster 1 observed $B_X = +10$ nT and $B_Y = -6$ nT, whereas Cluster 4 observed $B_X = -8$ nT and $B_Y =$

+6 nT. At 16:41:55 UT Cluster 1 observed B_X = +11 nT and B_Y = -8 nT, whereas Cluster 4 observed B_X = -12 nT and B_Y = +4 nT.

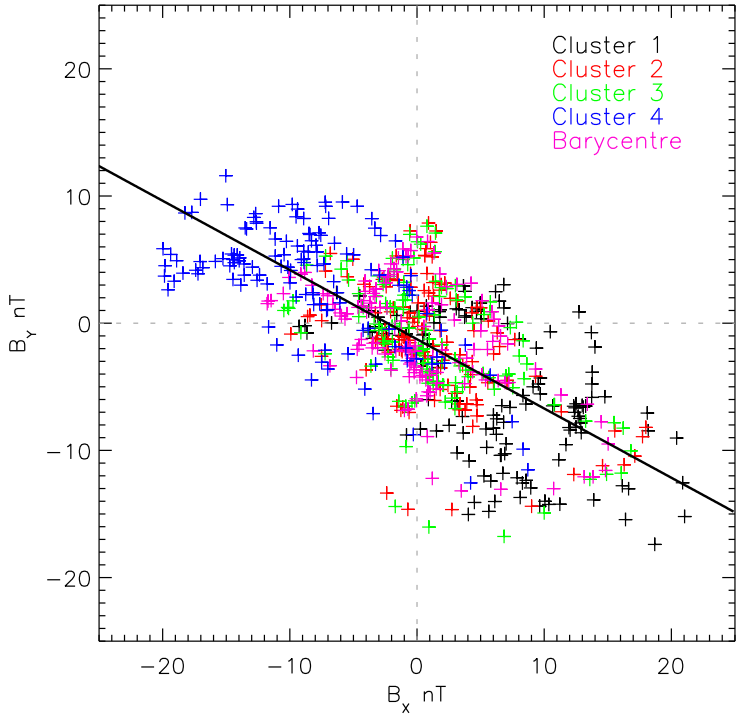

Figure 4.5: A scatter plot of the magnetic field observed on all spacecraft and the barycentre between 16:41:44 and 16:42:10 UT.

Fig. 4.5 is a scatter plot of the B_X and B_Y components of the high time resolution magnetic field from this period. It can be seen that the B_X and B_Y are anti-correlated, in agreement with the expected polarity from observations of the tailward part of the Hall quadrupolar magnetic field system (Fig. 4.1). A best fit line is plotted with a gradient of -0.55 and an intercept at B_X = 0 of B_Y = -1.2 nT, again showing that there was little or no guide field at this time. The correlation coefficient is -0.67 (statistical significance $> 99\%$) and shows that the data from all spacecraft and the barycentre are well correlated.

Figure 4.6 shows the spatial derivatives of all the elements of the electron pressure tensor that comprise the contribution to the electric field from the $\nabla . \mathsf{P}_e$ term. The contribution to the electric field in the X direction comes from the sum of the first three panels, the contribution to the Y direction comes from the sum of the

second three panels with the contribution to the Z direction coming from the sum of the final three panels.

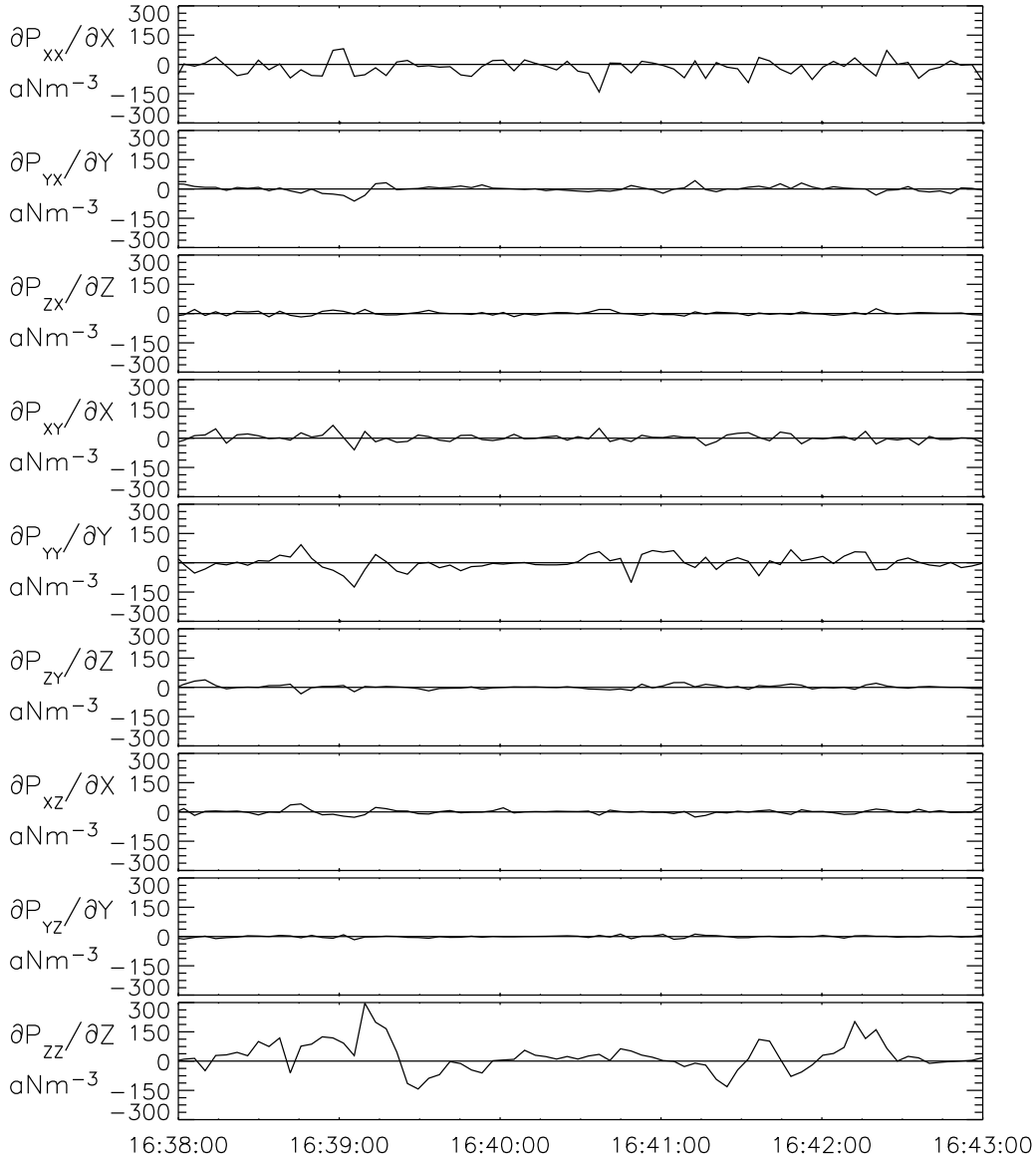

Figure 4.6: Plot showing the spatial derivatives of all elements of the electron pressure tensor. Note that the electric field contribution from the $\nabla . \mathsf{P}_e$ term in the X direction consists of the sum of the first three panels, the Y component consists of the second three panels and the Z component consists of the sum of the final three panels.

The contributions from the spatial gradients of the off-diagonal components of the electron pressure tensor to the $\nabla . \mathsf{P}_e$ term are generally smaller than those of the diagonal terms. However, this is not always the case (Fig. 4.6). For example, some

of the off-diagonal components become significant around 16:39 UT, becoming comparable in size to those from the diagonal components.

Fig. 4.7 shows a scatter-plot of the Hall and $\nabla.\mathsf{P}_e$ contributions to the perpendicular Z direction electric field measured between 16:38:30 and 16:42:30 UT. A best fit straight-line shows that the Hall term was well anti-correlated (correlation coefficient = -0.91, statistical significance $> 99\%$) with the $\nabla.\mathsf{P}_e$ term and is on average $\sim$ 5.3 times stronger during this period.

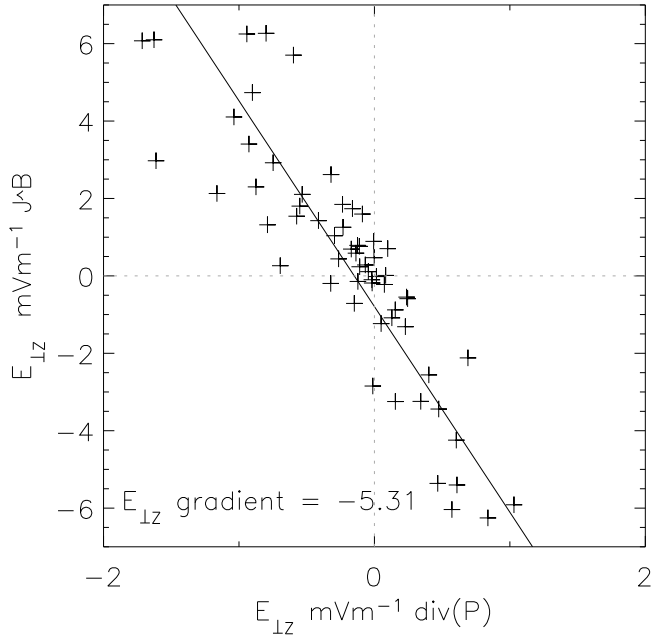

Figure 4.7: Scatter-plot showing the contributions to the perpendicular Z direction electric field from the Hall term and $\nabla.\mathsf{P}_e$ terms in Ohm's law. The coordinate system in this Figure is GSM.

As detailed in section 2.5, if it can be assumed that the parallel electric field is negligeable (i.e. $\mathbf{E}.\mathbf{B} = 0$), then the two-component electric field measured by the EFW instrument can be reconstructed to a three component electric field. As shown in Eqn. 4.1, the only terms that can produce a breakdown of $\mathbf{E}.\mathbf{B} = 0$ are $-\nabla.\mathsf{P}_e/en_e$, $-(m_e/e)(d\mathbf{v}_e/dt)$ and $\eta\mathbf{j}$. As stated earlier, the last term is normally considered negligeable in space plasmas. The other terms in Ohm's law terms are all by definition perpendicular to the magnetic field. Therefore, if it assumed that

the electron inertia is smaller than the $\nabla.\mathsf{P}_e$ term (e.g. Schmitz and Grauer, 2006), then Fig. 4.4 shows that $\mathbf{E}.\mathbf{B} = 0$, and that the reconstruction of the full electric field should be valid. The thresholds used for reconstruction (see section 2.5) were $B_Z > 1$ nT and $|(B_X/B_Z)| < 10$ nT.

Figure 4.8 shows the full electric field as measured by the EFW probe on Cluster 4 (black), $-\mathbf{v}_i \times \mathbf{B}$ (red) as measured by CIS and FGM on Cluster 4, $\mathbf{j} \times \mathbf{B}/en_e$ (green) as measured by the FGM instrument and $-\nabla.\mathsf{P}_e/en_e$ (blue) as measured by the PEACE instruments. In addition, the pink line shows the total of the contributions measured in the red, green and blue traces and, if these are the only terms that contribute to $\mathbf{E}$, should be the same as the black trace. However, note that while $\mathbf{j} \times \mathbf{B}/en_e$ and $-\nabla.\mathsf{P}_e/en_e$ are measured at the barycentre, $\mathbf{E}$ and $-\mathbf{v}_i \times \mathbf{B}$ are measured at Cluster 4.

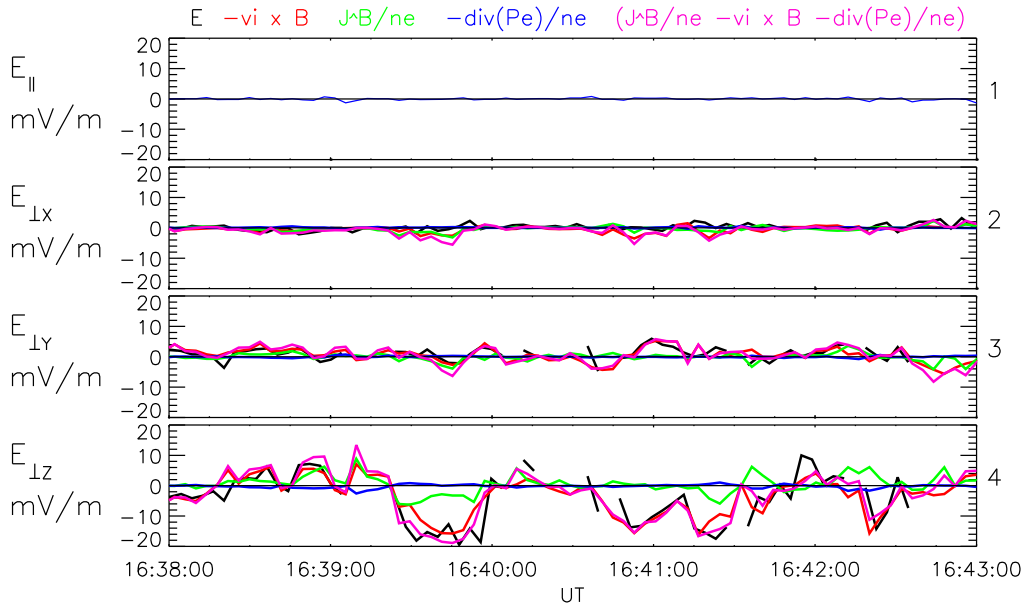

Figure 4.8: The full electric field as measured by the EFW probe on Cluster 4 (black), $-\mathbf{v}_i \times \mathbf{B}$ (red) as measured by CIS and FGM on Cluster 4, $\mathbf{j} \times \mathbf{B}/en_e$ (green) as measured by the FGM instrument and $-\nabla.\mathsf{P}_e/en_e$ (blue) as measured by the PEACE instruments. In addition, the pink line shows the total of the contributions measured in the red, green and blue traces, and should be the same as the black trace.

It can be seen that the electric field in the X and Y directions are small ($\mathbf{E}_Y$ being positive on average) and mostly supported by the ideal MHD term ($-\mathbf{v}_i \times \mathbf{B}$). In

the Z direction, the electric field is again supported by the MHD term, however the Hall term makes significant contributions in some places (eg 16:39:30 to 16:40:00 UT, 16:41:25 to 16:41:45 UT). At these points, the closer correspondence between the sum of the measured components of electric field (pink) and the electric field (black), than simply the MHD (red) and electric field (black) is clear. The contribution from the $\nabla . \mathsf{P}_e$ term is relatively small.

The electric field here is dominated by the ideal MHD term, with an appreciable contribution from the Hall term. However, it is important to note here that the electron inertia and the anomalous resistivity have been neglected. This assumption is probably valid in this case if these factors is assumed to be on the same order as, or smaller than, the $\nabla . \mathsf{P}_e$ term.

Figure 4.9 shows the currents and associated velocities for electrons and protons during this period. Panels 1 to 4 show the current parallel and perpendicular to the barycentric magnetic field derived from the Curlometer method (black). Panel 5 shows the relative error, χ (Eqn. 2.26). Panels 6 to 9 show the velocity of electrons (black) and protons (red) parallel and perpendicular to the magnetic field on Cluster 4. Data from this spacecraft are used to calculate the particle velocities from the moments of the distributions of the phase space density from the PEACE and CIS instruments respectively.

Magnetic field data are used to transform these data into field aligned coordinates. As the magnetic field inferred at the barycentre may be different to that measured at Cluster 4, panel 10 shows a comparison of these two measurements.

Panel 1 shows that the majority of the Curlometer-derived current was aligned to the magnetic field. The main perpendicular component was in the Y direction and can be identified with the cross tail current. Three enhanced current contributions parallel to the magnetic field are highlighted and labelled A to C. On the basis of concurrent magnetic field strength, A is observed when the spacecraft were located close to, but south of, the neutral sheet whereas B and C were related to

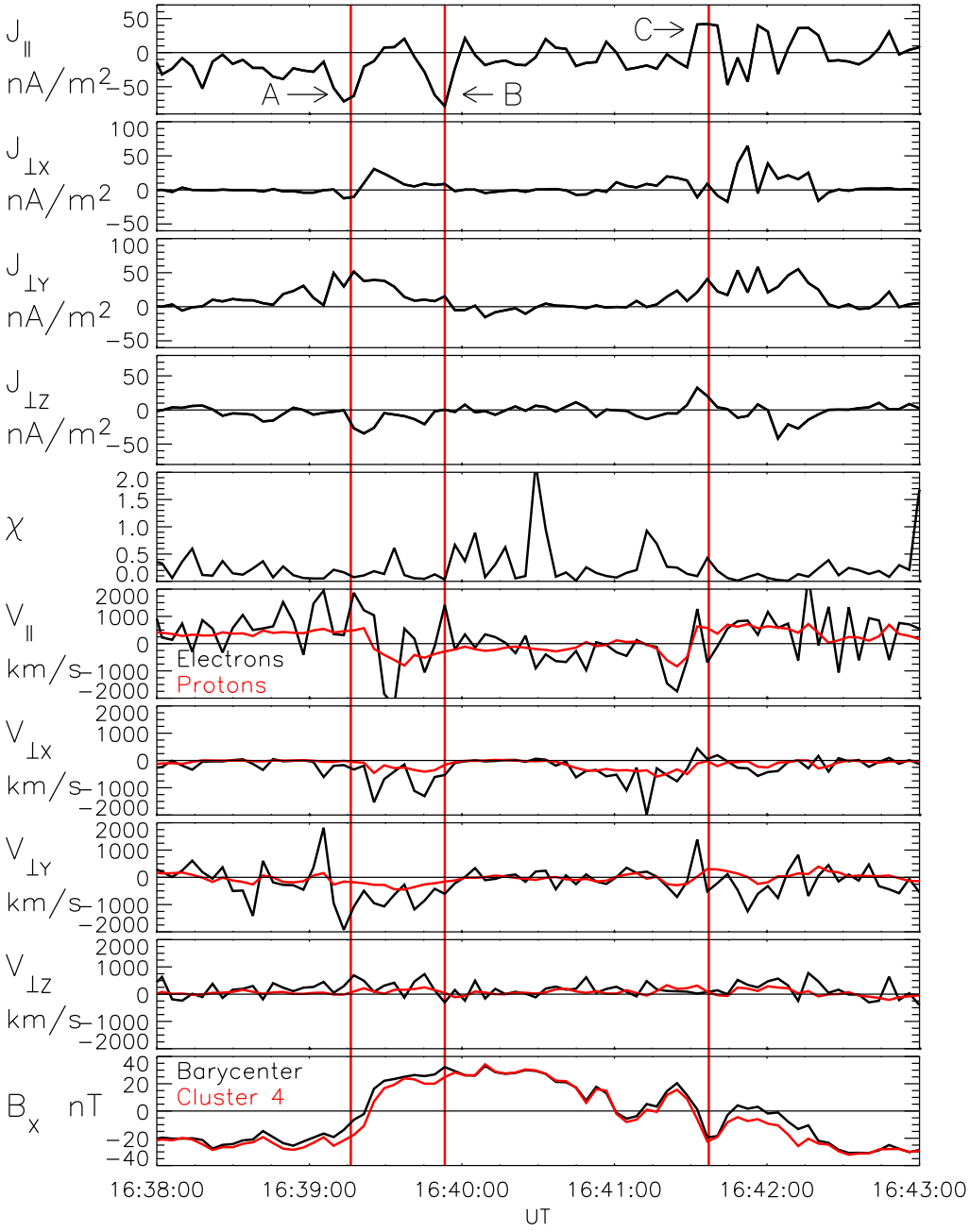

Figure 4.9: Panels 1 to 4 show the parallel and three perpendicular components of the current density derived from the Curlometer technique (at barycentre). Panel 5 shows the relative error, χ (Eqn. 2.26). Panels 6 to 9 show the parallel and three perpendicular components of velocity from electrons (black) and protons (red). The particle measurements are from Cluster 4. The bottom panel shows B_X at the barycentre and at Cluster 4.

currents nearer the boundaries of the plasma sheet (north and south of the neutral sheet respectively). Current A was directed anti-parallel (i.e. in the + X direction, towards the X-line), B was in the anti-parallel direction (in the - X direction, away from the X-line) whereas current C was in the parallel direction (again in the - X direction). The relative error in the curlometer current is small throughout this period, only becoming large when the current is close to zero (16:40:30 UT). At this time (16:40:30 UT) E = 0.22 and P = 0.25, giving a $\sqrt{E^2 + P^2}$ of 0.33. The tetrahedron is therefore a good example of a pseudo-sphere and χ, identified as the relative error, should give a good measure of the quality of the Curlometer result. Panels 6 to 9 suggest that the electrons generally carry the current. The highlighted Curlometer current signatures are consistent with enhancements of electron velocity during periods of constant proton velocity at Cluster 4. Signature B (C) is consistent with the movement of protons (electrons) anti-parallel to the magnetic field and electrons (protons) parallel to the magnetic field.

It is again noted that the magnetic field used to derive field-aligned coordinates for the Curlometer was that inferred at the barycentre, whereas that used to derive coordinates for the particles came from Cluster 4. A comparison of the X components of the magnetic fields at these two points is given in the final panel of Fig. 4.9. At some points the traces can be different by some nT (e.g. during current enhancement A). In these places care must therefore be taken when comparing results from the Curlometer and particles. For example, a spacecraft may observe locally perpendicular current that could be in the same direction as the barycentric magnetic field, perhaps giving misleading results.

During current enhancement A, all spacecraft see similar parallel electron flows to those observed on Cluster 4 (not shown). However, as Cluster 1 approaches the neutral sheet and B_X is close to zero, its local magnetic field becomes almost perpendicular to the mainly -X directed barycentric magnetic field. At this point (16:39:15 UT) Cluster 1 sees large negative perpendicular X directed electron flows

(not shown).

4.4 Case study two - In the vicinity of the X-line

Figure 4.10 shows a plot of the magnetic field from the period 16:54 to 17:04 UT, as well as the estimated current sheet half thickness (Eqn. 4.7), full plasma β (Eqn. 1.26) and an electron energy time spectrogram in the same format as Fig. 4.2. Panel 1 shows B_X and suggests that the spacecraft generally stayed south of the neutral sheet for the majority of the encounter, with one excursion of all spacecraft north of the neutral sheet at approximately 17:01 UT. However, individual spacecraft did briefly cross the neutral sheet (16:56, 16:59 UT). B_Y was generally negative and B_Z was positive. As can be seen from panels 6 and 7, the spacecraft started in the lobe and entered the plasma sheet boundary layer (PSBL) at 16:55 UT. The PSBL plasma was hot, around 6 keV, when first observed. If GSM is assumed to be a good approximation to the neutral sheet frame, it can be seen from panels 6 and 7 that the spacecraft moved towards the neutral sheet between 16:56:00 and 16:58:30 UT and moved away from the neutral sheet to the PSBL between 16:58 and 17:00 UT. At 17:00 UT the spacecraft entered the cooler central plasma sheet again and remained there until the end of the time period shown here, apart from one excursion into the plasma sheet boundary layer at 17:02 UT.

A minimum variance analysis was carried out on this period of data in an attempt to determine whether the GSM coordinate system approximates the neutral sheet frame during this period. A variance analysis on the period 16:59:30 and 17:02 UT provided the best separation of eigenvalues which were stable to small changes in the time interval chosen. The minimum variance direction was derived as being in the (0.39,0.56,0.73) GSM direction, with an intermediate:minimum eigenvalue separation of 4.5. It can be seen that the neutral sheet is therefore somewhat tilted away from the natural GSM frame, which was considered a good approximation only 20 minutes before this period. The system used in the remainder of this section

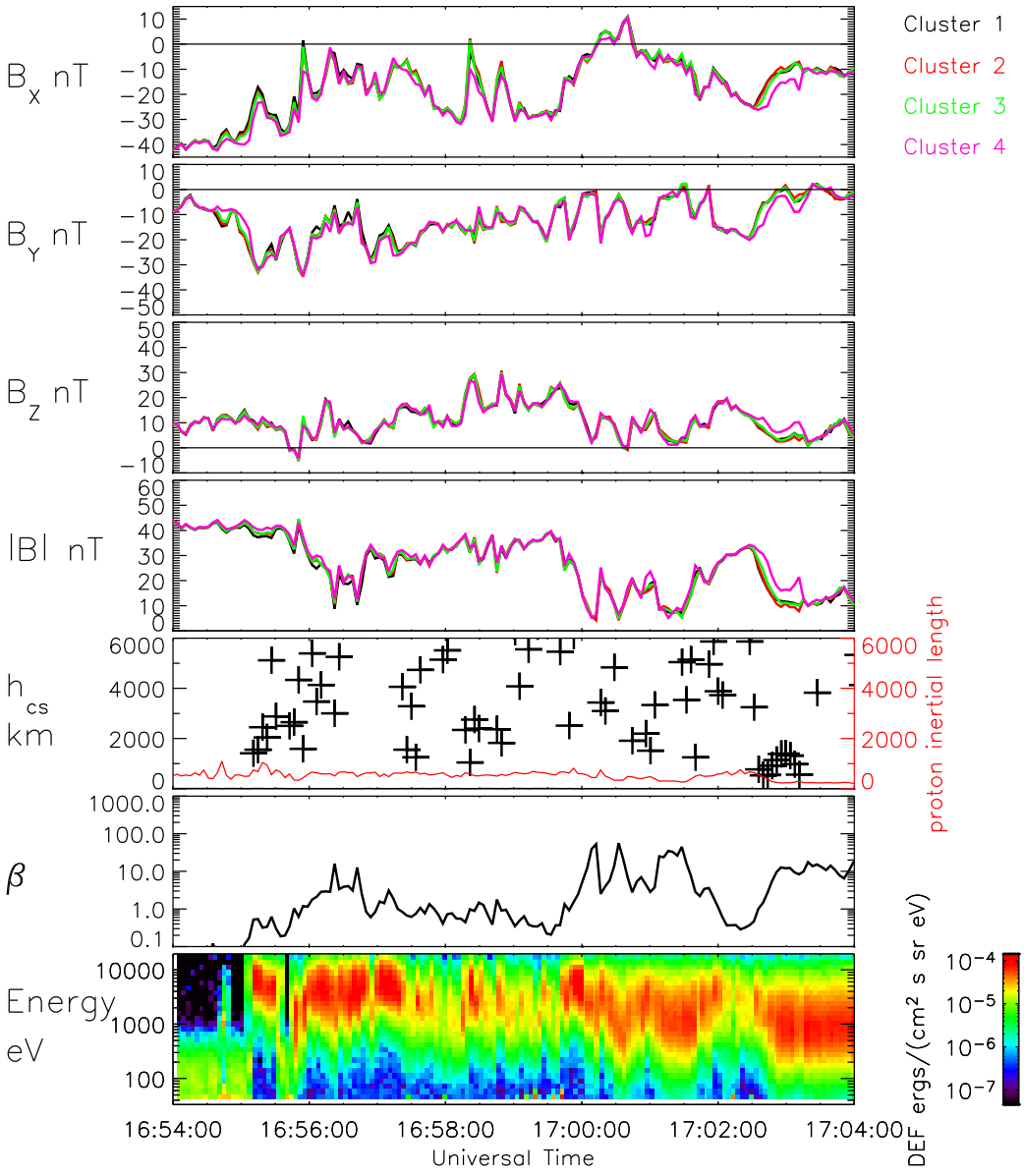

Figure 4.10: Data from case study three in the same format as Fig. 4.2.

will be this variance analysis frame. Note that the current sheet thickness in panel 5 of Fig. 4.10 was estimated using the current system in this variance frame.

During 16:59:30 to 17:02 UT, the spacecraft observed the largest change in $|\mathbf{B}|$ and should therefore give the largest cross-sectional sampling of the plasma sheet. Indeed, this is also the period of the largest change in B_X, which is close to the maximum variance direction in GSM. The plasma (probably plasma sheet plasma) observed in this short time period is at a somewhat different energy than that observed previously (e.g. around 16:56 UT, probably PSBL). It is possible that the orientation of the neutral sheet may have changed due to the rapid flapping motions.

Figure 4.11 shows the magnetic field (in the variance analysis frame), $\frac{1}{3}Tr\mathsf{P}_e$ and electric field contributions from the Hall and $\nabla.\,\mathsf{P}_e$ terms (in the variance analysis frame) in the same format as Fig. 4.4. In the variance analysis frame it can be seen that the spacecraft cross briefly the neutral sheet on only one occasion (17:00:30 UT), at all other times the spacecraft staying south the neutral sheet (note that B_{MAX} being positive is very approximately a proxy for being on the southern lobe side of the neutral sheet). As is expected, the electron pressure is generally higher towards the neutral sheet, however, it is highest towards the beginning of the encounter. This again suggests that there could be two separate plasma populations, a high pressure high energy plasma sheet between the start of the encounter and 17:00 UT and the other, a lower energy, plasma sheet population from 17:00 UT to the end of the encounter. This could be a temporal or spatial effect, the separation of the Cluster tetrahedron is not large enough to differentiate between these effects.

There is a guide field fluctuating around -10 to -20 nT in the intermediate variance direction and the magnetic field in the minimum variance direction is generally small, except for a large value towards the start of the interval. Again, the large magnetic field in the minimum variance direction is suggestive of a lack of applicability of the minimum variance frame, derived from data between 16:59:30 and 17:02 UT,

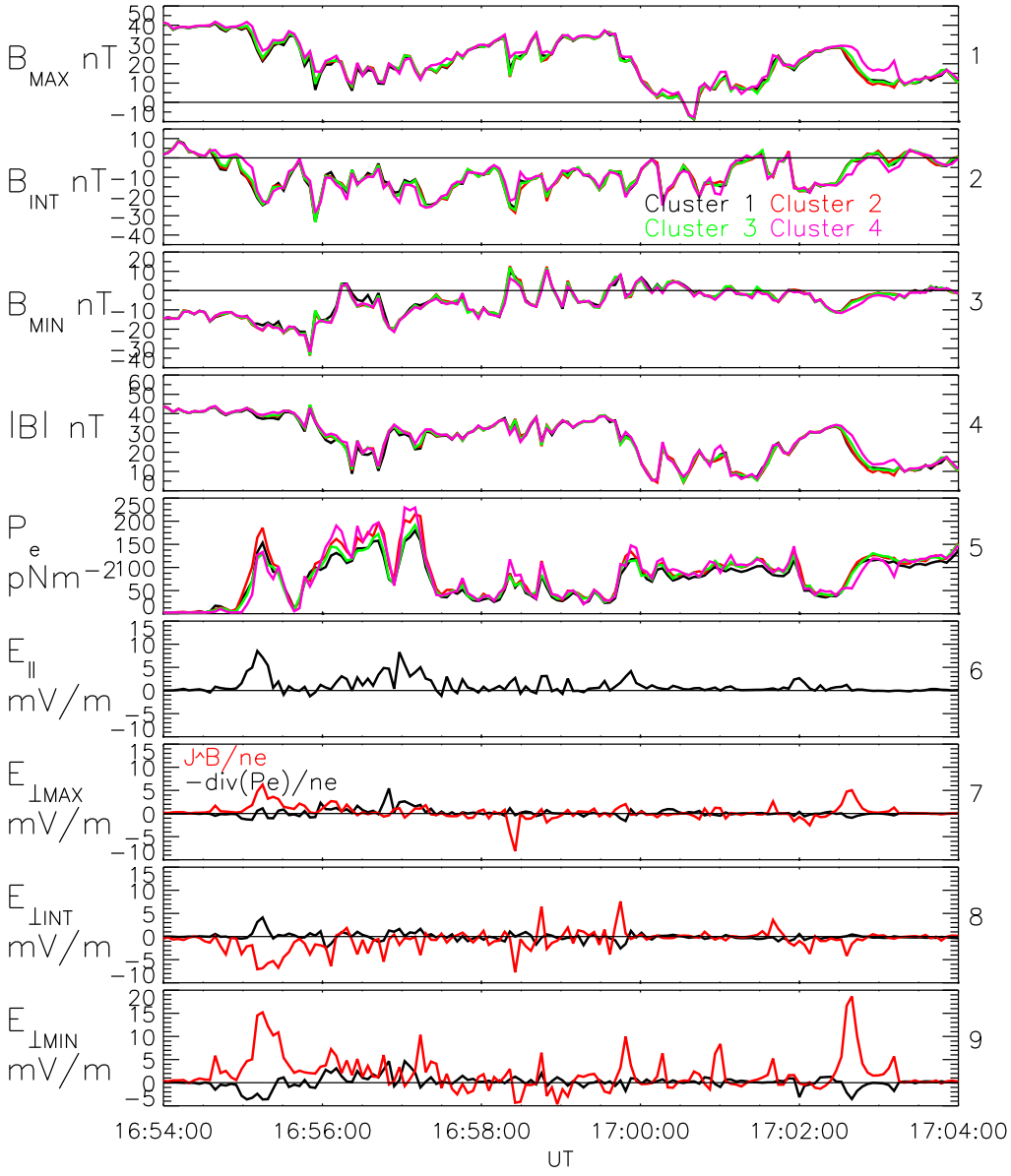

Figure 4.11: Magnetic and electric field data from case study three in the same format as Fig. 4.4.

to the beginning for this period. It is again noted that no minimum variance frame could be derived for this earlier time that was consistent when small changes in the start and end times of the analysis period were made.

A parallel electric field arising from the $\nabla . \mathsf{P}_e$ term can be seen in panel 6. The largest parallel electric field contribution from this term came at the beginning of the interval in the PSBL (16:55 to 16:56 UT) and the plasma sheet (16:56 to 16:58 UT). Further away from the beginning of the interval (and therefore the X-line) the parallel electric field became smaller, falling to negligeable levels at the end of the interval. Note that all spacecraft see similar plasma here, suggesting that this is not an edge effect.

The perpendicular electric field contributions from the Hall and $\nabla . \mathsf{P}_e$ terms are not anti-correlated between 16:54 and 16:57 UT, where the contributions are sometimes in the same direction (for example in the minimum and maximum variance directions at 16:56 to 16:57). After 16:57 UT the behaviour reverts to the familiar anti-correlated pattern, again suggestive of two separate plasma populations and the inapplicability of one minimum variance frame to the whole of the period. It is interesting to consider whether if the correct frame in which to view this initial period of data (16:55 to 16:57 UT) could be found, whether the component that contains the correlated electric field contributions might be in the reconnection field direction.

During this interval, the full 3D electric field from EFW cannot be reconstructed as the reconstruction process assumes no parallel electric field is present, which is not true here. However, the effects of the parallel electric field can be observed by analysing the two components that EFW does measure in the spin plane (a few degrees from GSE). Note that from Fig. 4.10 it can be seen that the magnetic field is also mainly in the X and Y (GSM) directions.

Panels 1 and 2 of Fig. 4.12 show the contribution to the electric field from the $\nabla . \mathsf{P}_e$ term in the full GSE X and Y (black, i.e. with the parallel electric field

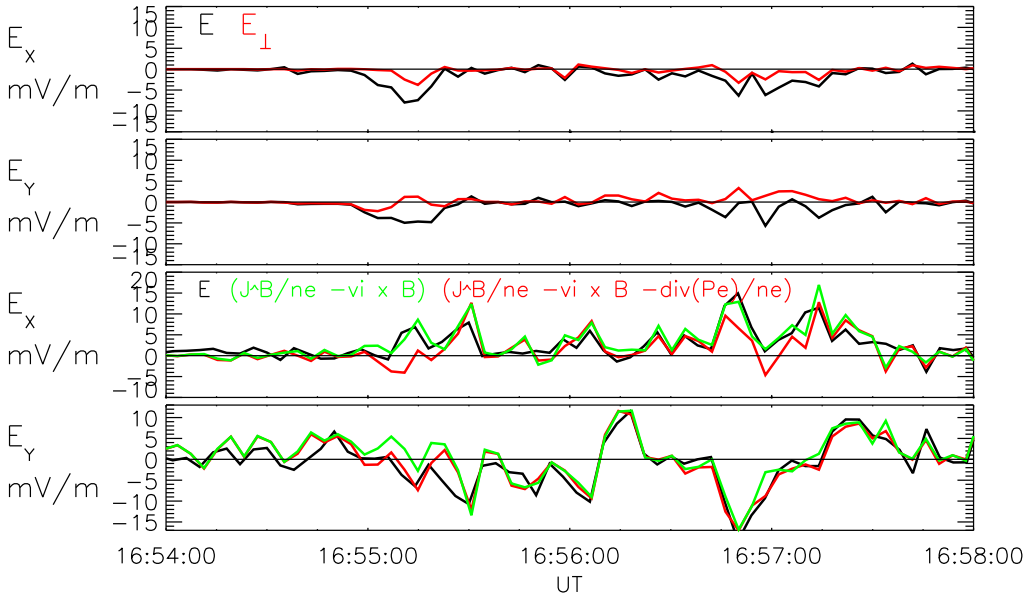

Figure 4.12: Panels 1 and 2 show the contribution to the electric field from the $\nabla . \mathsf{P}_e$ term in the X and Y (black) and perpendicular X and Y (red) directions. Panels 3 and 4 show the X and Y directed electric field as measured by EFW (black), the sum of the Hall and ideal MHD terms (green) and the sum of the Hall, ideal MHD and $\nabla . \mathsf{P}_e$ terms (red).

included) and perpendicular GSE X and Y (red, i.e. without the parallel electric field included) directions in the time during which the parallel electric field is observed. The black trace includes the contribution from the parallel electric field in these directions.

The differences in the traces in panels 1 and 2 show that the parallel electric field makes a large contribution in both directions between 16:55:00 and 16:55:15 UT, and between 16:56:45 and 16:57:15 UT. In the X (Y) direction, the parallel electric field acts in the same (opposite) direction as the perpendicular X (Y) directed electric field

Panels 3 and 4 of Fig. 4.10 show the electric field measured by EFW (black, measured at C4 and in a coordinate system a few degrees from GSE), the sum of the Hall and ideal MHD terms (green, the Hall term estimated at the barycentre and the MHD term measured at Cluster 4, both in GSE) and the sum of the Hall, ideal MHD and $\nabla . \mathsf{P}_e$ terms (red, with the $\nabla . \mathsf{P}_e$ term estimated at the barycentre, again all in GSE).

Panel 3 shows that the electric field (black) is poorly approximated in the X direction by the sum of the three terms (red). Indeed, the inclusion of the $\nabla . \mathsf{P}_e$ makes the fit worse between 16:55:00 and 16:55:15 UT, and between 16:56:45 and 16:57:15 UT. However, in the Y direction the approximation is very good, the inclusion of the $\nabla . \mathsf{P}_e$ term making the fit significantly better. It would appear that it is the parallel electric field projection in the Y direction that supports the electric field observed by EFW.

It is important to realise that no attempt has been made here to estimate the electron inertia, or any effects from anomalous resistivity. In addition, the electric field and MHD terms are point sources with the Hall and $\nabla . \mathsf{P}_e$ terms being estimated at the barycentre. Due to these factors, there may be uncertainty in the comparison performed here of the electric field measured by EFW and any summation of the measurable terms in Ohm's law.

Fig. 4.13 shows the components that make up the divergence of the electron pressure tensor. As not to clutter the figure, the minimum variance direction is signified by X, intermediate by Y and maximum by Z. Again the largest contributions come from the spatial derivatives of the diagonal components, with the spatial derivatives of the off-diagonal components contributing significantly in some places.

Fig. 4.14 shows the Curlometer current and proton and electron velocity for this period in the same format as Fig. 4.9. The Curlometer current was mainly parallel or anti-parallel to the magnetic field, possibly with the cross tail current appearing in the intermediate variance direction as expected (17:03 UT). The error in the curlometer current was small, with enhancements up to $\chi \sim 1$ when the current was small.

In panel 7 it can be seen that the particles moved in the negative maximum variance direction. This is approximately the positive X direction and suggests that their source is now tailwards of the spacecraft. Between the start of the encounter

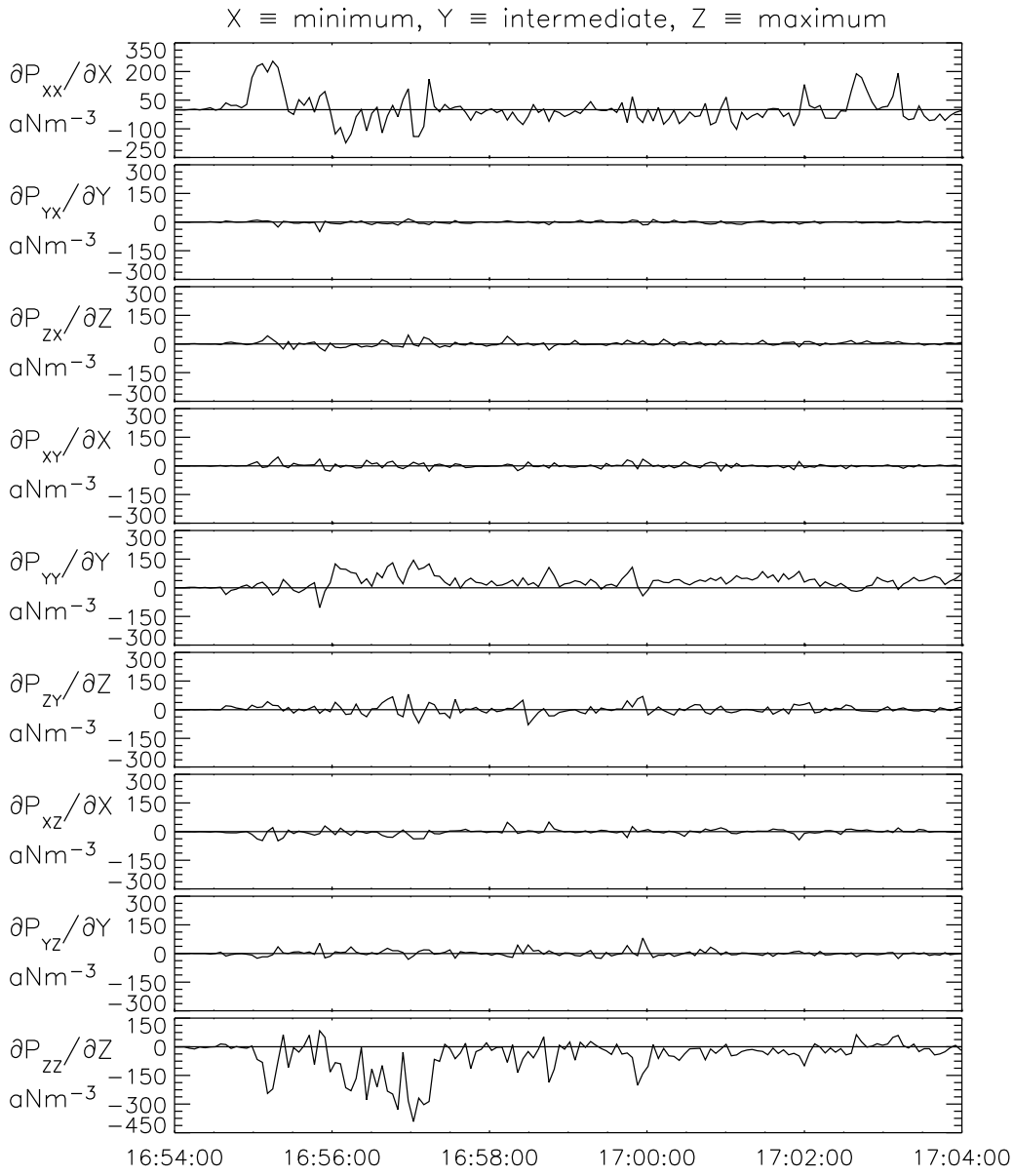

Figure 4.13: Plot showing the spatial derivatives of all elements of the electron pressure tensor in the same format as Fig. 4.6. the coordinate system used here is the variance analysis frame.

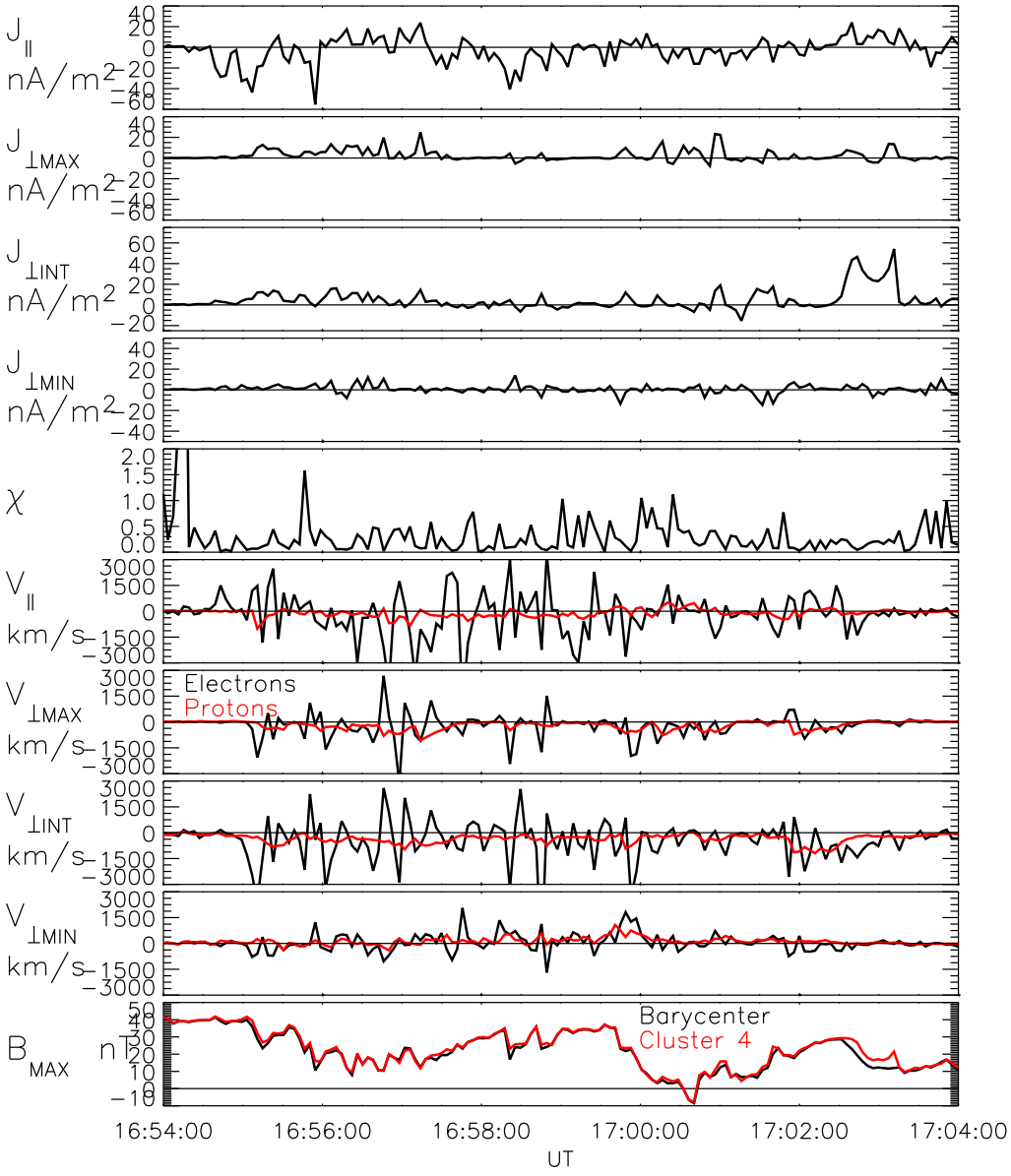

Figure 4.14: Plot showing the current and velocity measurements from this period in the same format as Fig. 4.9

and 16:57 UT the parallel Curlometer current was first anti-parallel then parallel, consistent with anti-parallel electrons followed by parallel electrons. Again based on concurrent magnetic field strength, this time simply taking the magnitude of the magnetic field as a proxy for the distance to the neutral sheet, the anti-parallel current was observed close to the outer boundary of the plasma sheet whereas the parallel current was observed closer towards the centre of the plasma sheet. It is noted that these directions are opposite to those observed in the previous case study. These currents are consistent with the field aligned current system acting to close the Hall current system predicted in the plasma sheet on the Earthward side of an X-line (Fig. 4.1), again consistent with the retreating X-line picture.

4.5 Discussion

Between 15:55 and 17:35 UT on the 17thAugust 2003, Cluster was often located in the plasma sheet. A reversal of the GSM X velocity, for both electrons and protons, was observed at approximately 17:00 UT. The estimated amount of open flux in the lobe was reduced between 16:30 and 17:00 UT. A simple estimate of the current sheet half thickness showed that the current sheet thinned significantly between 15:55 and 17:00 UT. The motion of the plasma sheet as a whole was initially slow, evolving to a flapping motion at 17:00 UT. The AE index was 200 nT at 15:55 UT, increasing to 800 nT at 17:00 UT. This evidence suggests that the data were recorded during the build up to a substorm and that an X-line was initially Earthwards of the spacecraft, this X-line subsequently retreating tailwards past the spacecraft. The closest point Cluster came to observing the X-line was at approximately 17:00 UT, near the reversal of the velocity reversal.

Two sets of crossings of the neutral sheet were investigated in this chapter. During the first case study, whose results were first reported in Henderson et al. (2006b), the electric field properties of the plasma sheet, as well as some Hall signatures were investigated. It was suggested that the region investigated was magnetically

connected to a diffusion region, i.e. on magnetic field lines that mapped close to the X-line. In the final set of crossings, near the X-line, the electric field and some more general properties of the plasma sheet were investigated.

In the first crossing investigated, which was in the vicinity of the X-line, the electric field from the Hall term pointed towards the neutral sheet whilst the electric field from the $\nabla . \mathsf{P}_e$ term pointed away from the neutral sheet. This latter observation is consistent with the observation that the electron pressure is largest at the neutral sheet (Harris, 1962). However, this quantitative result was achieved by directly calculating the divergence of the full electron pressure tensor using multi-spacecraft methods. The PEACE and FGM instruments, used to derive the $\nabla . \mathsf{P}_e$ and Hall terms respectively, are independent, measure physically different parameters and are non-cross-calibrated. The high correlation coefficient in the scatter plots of the contributions to the electric field from these terms gives confidence that the data is not instrument error dominated. A large dispersion of these points might be expected if the errors were large.

These two contributions to the electric field were anti-correlated and a linear best-fit showed that the electric field contribution from the Hall term was ~ 5.3 times stronger during this period.

The contributions to the electric field from the spatial derivatives of the off-diagonal components of the pressure tensor were sometimes significant.

At times during this period Clusters 1 and 4, having the largest separation in Z, were on either side of the neutral sheet. This allowed the spacecraft to observe simultaneously magnetic fields either side of the neutral sheet. In addition, field-aligned current systems were observed with both magnetometer and particle data.

In the second case study in this chapter, the spacecraft observe the plasma sheet very close to the inferred passage of the active X-line. Initially, the magnetic field was very turbulent and meant that a clear determination of the correct frame in which to view the data was difficult, the frame being determined from the less tur-

bulent second half on the encounter. The plasma sheet was hot, thin and dynamic at the beginning of the encounter and meant that the spacecraft often left the central plasma sheet and moved out into the lobes or the PSBL. As the X-line moved away from the spacecraft a cooler, thicker and less dynamic plasma sheet was observed in which a neutral sheet frame could be determined. A large parallel electric field contribution from the $\nabla . \mathsf{P}_e$ term was observed in the first half of the encounter, pointing towards the X-line. In the second part of the encounter the anti-correlation of the Hall and $\nabla . \mathsf{P}_e$ was again observed.

In the first case study, between 16:41:45 and 16:42:00 UT Clusters 1 and 4 were either side of the neutral sheet (Cluster 1-4 B_X separation $\sim$ 20 nT). These spacecraft simultaneously detect B_Y with opposing signs (Cluster 1-4 B_Y separation $\sim$ 12 nT). This behaviour can be observed in both the high time resolution and 4 second averaged magnetic field data. This could be interpreted as an observation of tailward half of the Hall quadrupolar system (Figs. 4.5 and 4.1). There is little or no guide field at this time and the out-of-plane quadrupolar magnetic field is smaller than that observed before. Borg et al. (2005) noted that the quadrupolar magnetic field contributed up to 50 to 75% of the total magnetic field. In the example investigated in this chapter the quadrupolar magnetic field was approximately half the strength of the B_X field. As the B_Z field was weak at this time it can be estimated that not more than 30% of the magnitude of the magnetic field originated from the quadrupolar B_Y magnetic field.

Nagai et al. (2001) observed that the B_Y perturbations were less than 20% of the lobe field, whereas Mozer et al. (2002) reported approximately 55% of the lobe field. Simulations by Hesse et al. (2001) and Pritchett (2001) show that the quadrupolar perturbations reached a peak of 40% and 20 % of the value of the lobe magnetic field respectively.

The quadrupolar perturbation in the second set of crossings was at least 15 nT (as the spacecraft may not sample the peak of the B_Y field), and that the lobe field

was approximately 50 nT (panel 5 of Fig. 4.2). Hence in this example it can be concluded that the perturbations were at least 30% of the lobe field, inconsistent with the Nagai et al. (2001) and Pritchett (2001) studies, but consistent with the Mozer et al. (2002) and Hesse et al. (2001) studies. It would seem therefore that the observational constraints on the quadrupolar magnetic field system are not fine enough to limit the predictions of theory at this stage.

Current density derived from the Curlometer technique showed a number of enhancements in the component parallel to the magnetic field. Towards the centre of the current sheet, the current is directed towards the X-line, whereas towards the boundary of the plasma sheet the currents are directed away from the X-line. These currents are consistent with the field-aligned current system acting to close the Hall current system (Fig. 4.1). When these current enhancements are compared with particle velocity moments it can be seen that electrons dominate the currents.

It is noted that other small currents parallel and antiparallel to the magnetic field can be observed when the Curlometer current is examined at higher resolution (e.g. 16:40:47 UT, 16:42:40 UT, 16:42:47 UT, 16:35:30 UT, 16:48:00 UT). These currents are also observed at concurrent magnetic field strengths and in directions such that they are consistent with the field-aligned current systems that act to close the Hall current system. The short time periods over which the spacecraft observe these field aligned currents may explain why they are not easily observed when the high resolution data is averaged over the spin period. The reason that the spacecraft observe certain branches of this system to have large currents and some to have small currents is not clear. However, this may be due to the spatial size of the individual branches; only if the spacecraft are very close to the branches will their effects be observed.

The contributions to the $\nabla . \mathsf{P}_e$ term mainly originated from the spatial gradients of the diagonal components of the electron pressure tensor, with the contribution of the off-diagonal components sometimes being non-negligible.

Simulations predict that the region in which the reconnection electric field is supported by the $\nabla . \mathsf{P}_e$ term alone, although extended across the tail, is very localised around the X-line. It is unlikely that Cluster sampled this region as the electron inertial length is on the order of a few km. The reconnection electric field from the Hall term is more spatially extended in simulations (the ion diffusion region, which is on the order of the ion inertial length). As no strong reconnection electric field contribution from the Hall or $\nabla . \mathsf{P}_e$ term was seen during the first and second case studies in this chapter, it is suggested that the spacecraft do not sample directly either diffusion region. The electric field system normal to the neutral sheet as well as the system of field aligned currents that close the Hall currents and the associated magnetic field deflections are expected to exist in regions extending away from the diffusion regions. The observation of a B_X separation of $\sim$ 20 nT in spacecraft separated by $\sim$ 220 km (Clusters 1 and 4) suggests that the current sheet was thin at this time. This, along with the observation of field-aligned current system associated with the Hall current system, suggests that the Cluster spacecraft were at least magnetically connected to an ion diffusion region during the first case study, i.e. on magnetic field lines that map to the vicinity of the diffusion region.

It is noted that the particle velocities from Cluster 4 are point measurements and are therefore not expected to correspond exactly with all the current signatures determined by the Curlometer, which in some sense is an average current density through the tetrahedron. For example, at 16:42 UT the parallel current derived from the Curlometer is enhanced. However, no anti-parallel electron or parallel proton flows that could cause this signature are observed at Cluster 4. It is noted that at this time Clusters 1, 2 and 3 do observe fast ($\sim$ 1000 kms^{-1}) anti-parallel electron flows (not shown) giving confidence in the particle moments. This result also suggests that the parallel current signatures are spatially thin.

In the second case study in this chapter, the spacecraft observe the plasma sheet very close to the active X-line. The spacecraft initially observed $\sim$ 6 keV elec-

trons, the energy of observed electrons not falling to below $\sim$ 1 keV during the entire period. The period seemed to be separable into two distinct sections. The first, here denoted as period A, lasted from approximately 16:54 to 17:00 UT, was characterised by magnetic fields with high frequency fluctuations in all GSM directions. The magnitude of the magnetic field was high (always above 10 nT), and the plasma was hot. β was high and suggests that Cluster was embedded in the plasma sheet for most of the period. The first plasma that Cluster observed (16:55 UT) was extremely hot, around 6 keV with a magnetic field magnitude of approximately 40 nT. Towards the end of the section (towards 17:00 UT) β reduced to PSBL levels. During this time identification of a natural current sheet frame was difficult due to the large variations in the magnetic field, as well as the fact that the spacecraft did not make a clear crossing of the neutral sheet. After this very energetic section, between 17:00 and 17:04 the spacecraft moved into a region containing cooler plasma (period B), but still above 1 keV. β increased and showed that the spacecraft were generally in the plasma sheet. During this time the spacecraft did make a crossing of the neutral sheet (GSM B_X = 0) and the fluctuations in the magnetic field were reduced. This allowed the derivation of an approximation to a natural current sheet frame via the use of the minimum variance technique. The frame derived from this section of data was applied to the entire period. It was therefore assumed that the frame of the current sheet did not change throughout the period discussed.

During period A a large parallel electric field was observed that pointed towards the X-line. This parallel electric field is independent of the choice of frame in which to observe the perpendicular components and could suggest that during this time Cluster is on magnetic field lines that map close to the diffusion regions. When the perpendicular components are observed in the minimum variance frame from the analysis carried out in period B, it can be seen that the components appear to be anti-correlated in all directions.

When compared to the electric field measured from EFW, the parallel electric

field contributed significantly to the total electric field, indeed occasionally supporting a large proportion of the electric field in the Y direction. The electric field in the X direction appeared to be poorly approximated by these terms. The reasons for the good correspondence in one direction only are not clear, but could be associated with the lack of applicability of a comparison of point measurements to average estimates at the barycentre or the fact that the coordinate systems are slightly different. A 3D measurement of the electric field, and four point ion velocity moment observations, would allow the electric field, both parallel and perpendicular components, to be compared directly with the sum of the ideal MHD, Hall and $\nabla . \mathsf{P}_e$ terms.

Parallel electric fields have been observed previously in this context. The Polar spacecraft has a three axis electric field instrument and can therefore directly measure all components of the electric field (Cluster can measure only two directions and certain assumptions are used to reconstruct the third direction, such as $\mathbf{E} \cdot \mathbf{B} = 0$ which defines that there is no parallel electric field). Mozer et al. (2002) reported a large parallel electric field at the magnetopause, directed towards the X-line lasting for approximately three seconds.

Fig. 4.15 is taken from Mozer et al. (2002) and shows the topology around the X-line as well as direction and location of the large parallel electric field reported in that paper. It can be seen that if this figure were to be rotated through 90 degrees clockwise then the magnetic topology would match that expected in the tail. The large parallel electric field (marked red at bottom right) is in the same approximate location and in the same direction as the parallel electric field reported in this chapter. Mozer et al. (2002) argue that the electric field is caused by the divergence of the electron pressure tensor as the parallel electric fields were measured in the vicinity of the largest changes in the plasma density. In this chapter it is indeed the electric field contribution from the $\nabla . \mathsf{P}_e$ term that causes a similar parallel electric field.

Scudder et al. (2002) also reported parallel electric field measurements at the

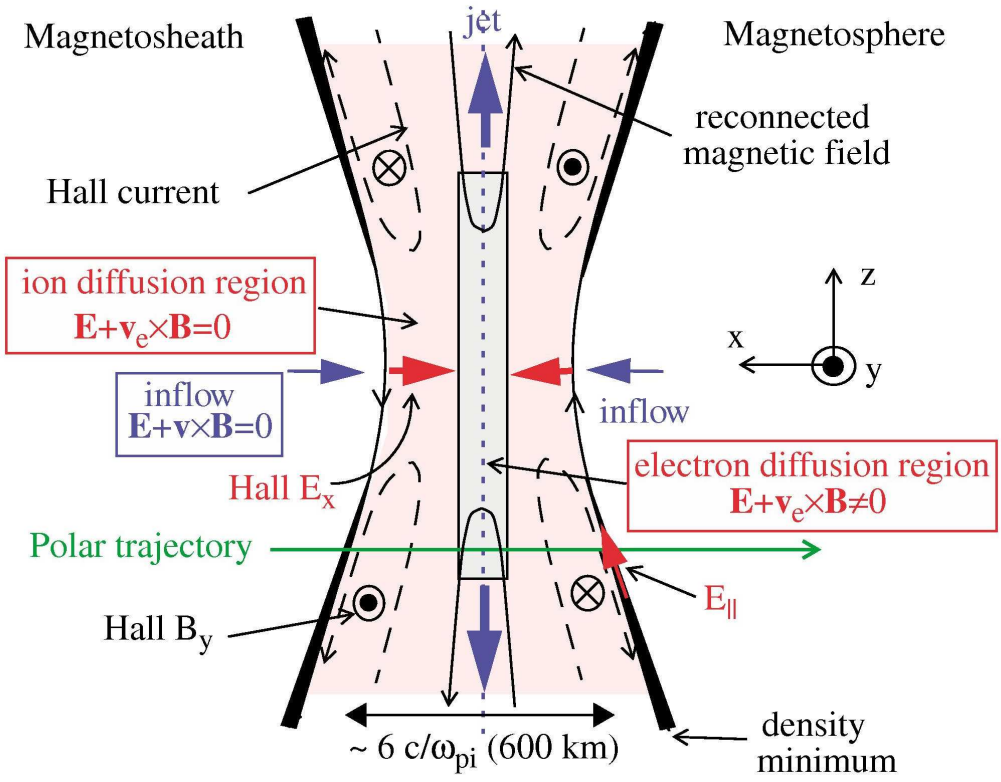

Figure 4.15: The geometry of the reconnection region with the parallel electric field marked. This figure is adapted from Mozer et al. (2002).

magnetopause and empirically argued that the fields arose from the divergence of the electron pressure tensor. Mozer et al. (2003) and Mozer (2005) reported parallel electric fields in yet more examples, again arguing that the fields originated from the divergence of the electron pressure tensor. Seventy five apparent electron diffusion regions in Mozer et al. (2003) and 117 in Mozer (2005) were recorded by observing that $\mathbf{E} + \mathbf{v}_e \times \mathbf{B} \neq 0$ with Cluster and directly observing parallel electric fields with Polar respectively. Mozer (2005) argued that parallel electric fields are required for reconnection, and the breakdown of MHD in the electron diffusion region. It was suggested that the divergence of the electron pressure caused the breaking of this condition. Indeed Mozer et al. (2003) and Mozer (2005) argue that it is sufficient to observe a divergence of the electron pressure to conclude that an electron diffusion region has been observed. This chapter would suggest that a divergence of the

electron pressure is almost ubiquitous in the plasma sheet (as a simple Harris sheet would suggest), calling into question their criteria.

The parallel electric field reported here came mainly from the spatial derivatives of the diagonal terms of the electron pressure tensor as opposed to the contributions from the off-diagonal. However, there was some non-negligible contributions from the spatial derivatives of the off-diagonal components (Fig. 4.13). The parallel electric field is independent of the frame in which the data is viewed. However, as the pressure tensor is in the minimum variance analysis frame, a poorly determined minimum variance analysis frame can still lead to mixing of the pressure tensor components. This effect could in turn lead to some uncertainty of the origin (either off-diagonal or diagonal) of the parallel electric field.

Fig. 4.11 shows that in period B that the parallel electric field is greatly reduced. All components now return to the familiar anti-correlated behaviour observed in the previous crossings. This suggests that the two periods, A and B, are different in some way. This may be a simple difference in appropriate frame (which may explain the different in correlative behaviour, but not the reduction in parallel electric field), or that period B is far enough away from the X-line to observe behaviour similar to that in the first crossing discussed in this chapter and period A is close enough to the X-line to observe reconnection characteristics similar to those reported in the numerical simulations of Yin et al. (2001). Indeed, the parallel electric field in period A would suggest the second scenario.

For this crossing the contributions of the spatial derivatives of the diagonal components of the pressure tensor contribute the most to the electric field. However, it is again noted that during the first half of the period discussed the frame in which the electric (and magnetic) field are viewed may not be the most appropriate.

The current (Fig. 4.14) is again mainly in the direction parallel to the magnetic field. Between 16:54 and 16:58 UT the magnetic field in the maximum variance direction and the magnitude of the magnetic field is reduced. This can be taken as

an indication that the spacecraft move closer to the neutral sheet during this period. The bipolar nature of the parallel (Curlometer) currents may therefore yield another observation of the field-aligned current system that acts to close the Hall current system in the ion diffusion region. In the boundary of the current sheet the current is mainly anti-parallel, whereas towards the centre of the current sheet the current is parallel. If it is noted that the spacecraft are approaching the neutral sheet from the south, and that the X-line is tailwards of the spacecraft at this time, the currents described above are consistent with the field aligned system in Fig. 4.1. It would appear that the electrons carry the current.

4.6 Conclusions

On the 17thAugust 2003 Cluster sampled the plasma sheet over many hours. During this period a number of crossings of the neutral sheet were made. A reversal of the velocity of both electrons and protons in the GSM X direction, as well as an increase in AE index, thinning plasma sheet, and reduction in open flux in the tail suggested that a large substorm occurred during this period. An X-line was initially Earthwards of the Cluster spacecraft, moving past the spacecraft during this period. Two period were investigated on either side of the X-line, and allowed the Cluster spacecraft to sample the plasma sheet near (both spatially and temporally) and close to an X-line.

As the spacecraft were in burst mode (a relatively rare phenomenon) these observations of the plasma and neutral sheet allowed, after considerable efforts by the PEACE team to perfect the PEACE calibration, the derivation of the first measurements of the divergence of the full electron pressure tensor.

During the first crossing the spacecraft crossed the neutral sheet and observed a field-aligned current system (with both particle and field experiments) consistent with the system that would act to close the Hall currents in the diffusion region. The spacecraft also made a simultaneous observation of a magnetic field system that is

interpreted as two branches of the associated quadrupolar magnetic field system.

The contributions of the Hall and $\nabla . \mathsf{P}_e$ terms to the electric field in the generalised Ohm's law were anti-correlated in the direction normal to the neutral sheet, with the contribution of the Hall term being approximately five times stronger than the contribution from the $\nabla . \mathsf{P}_e$ term. The Hall term pointed towards the neutral sheet, whereas the $\nabla . \mathsf{P}_e$ term pointed away from the neutral sheet.

In the second period discussed, the spacecraft came very close to the X-line as the plasma sheet thinned and flapped about the position of the spacecraft. The orientation of the current sheet was very variable and not aligned to the GSM direction. A parallel electric field arising from the $\nabla . \mathsf{P}_e$ term in Ohm's law was observed, consistent with a previous observation and could be a acceleration mechanism for electrons away from a diffusion region. Again, the spacecraft observed a field-aligned current system consistent with the system that would act to close the Hall currents in the diffusion region, and the anti-correlation in the Hall and $\nabla . \mathsf{P}_e$ contributions to the electric field.

Chapter 5

The relationship between j $\times$ B and $\nabla . \mathbf{P}_e$

5.1 Introduction

In chapter 4, an anti-correlation was reported between the contributions to the perpendicular electric field from the Hall and $\nabla . \mathsf{P}_e$ terms in the direction normal to the neural sheet.

The Hall term may have a component that points towards the neutral sheet (a nominal cross tail current will produce an electric field towards the neutral sheet) and the $\nabla . \mathsf{P}_e$ term may point away from the neutral sheet (electron pressure normally increases in the centre of the plasma sheet). However, the scientific reasons why there is such a good anti-correlation in this case, appearing to be linear, as well at the ratio (~ 5), remain unclear.

Many further questions exist regarding this result, such as; is this anti-correlation a general result, is it directionally organised (i.e. in one direction - towards and away from the neutral sheet - only), is it generally linear, and if so, is the gradient of the anti-correlation also general. In addition, the dependence on the conditions of the magnetosphere - the result reported in chapter 4 was close to a reconnection X-line - should be investigated.

The simulations of Yin et al. (2001) can be examined in further detail in order to uncover any corresponding behaviour.

Fig. 5.1 (L. Yin, private communication, 2007) shows (left) the contribution to the electric field in the direction normal to the neutral sheet from the divergence of the electron pressure tensor. Note that the coordinate system used here is different to the GSM system. The x direction corresponds to the GSM Z direction, the y direction to GSM -X, and the z direction (into the page) to -Y GSM. Red indicates a positive electric field contribution in the x (Z GSM) direction, whilst blue indicates a negative electric field contribution in the x (Z GSM) direction. In addition this figure shows the x (GSM Z) electric field contribution at the centre of the y (GSM X) domain (right). The maximum and minimum values of the electric field (normalised to $V_A B_o/c$ where V_A is the lobe Alfvén speed) in this line plot correspond to the maximum (red, 0.030) and minimum (blue, -0.031) values in the left hand plot.

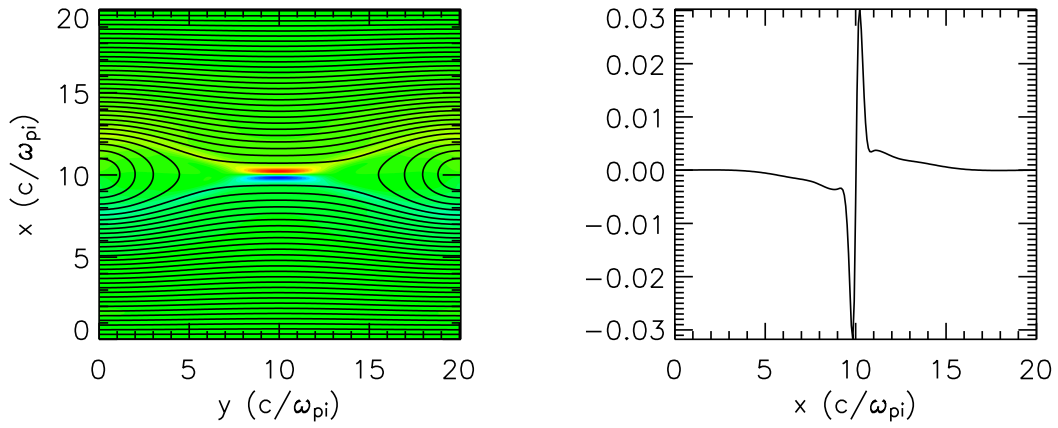

Figure 5.1: Two part plot showing the simulated contribution to the electric field in the neutral sheet normal direction from the $\nabla . \mathsf{P}_e$ term in Ohm's law (L. Yin, private communication, 2007). The left hand panel shows a 2D map of the electric field contribution. Note that in the coordinate system used here, the x direction corresponds to GSM Z, the y direction to GSM -X, and the z direction to -Y GSM. Red indicates a positive electric field contribution in the x (Z GSM) direction, whilst blue indicates a negative electric field contribution in the x (Z GSM) direction. In this way the electric field contributions from the $\nabla . \mathsf{P}_e$ term point away from the neutral sheet. The right hand panel shows the x (GSM Z) electric field contribution at the centre of the y (GSM X) domain. The maximum and minimum values of this panel (corresponding to red and blue respectively in the left hand plot) are 0.030 and -0.031 respectively.

In addition, the Yin simulation (L. Yin, private communication 2007) provides

electric field contribution due to the Hall term in Ohm's Law (Fig. 5.2). In addition, a contribution to the electric field from the MHD term does exist, and is in the same direction as the $\nabla . \mathsf{P}_e$ term with maximum and minimum of ± 0.07.

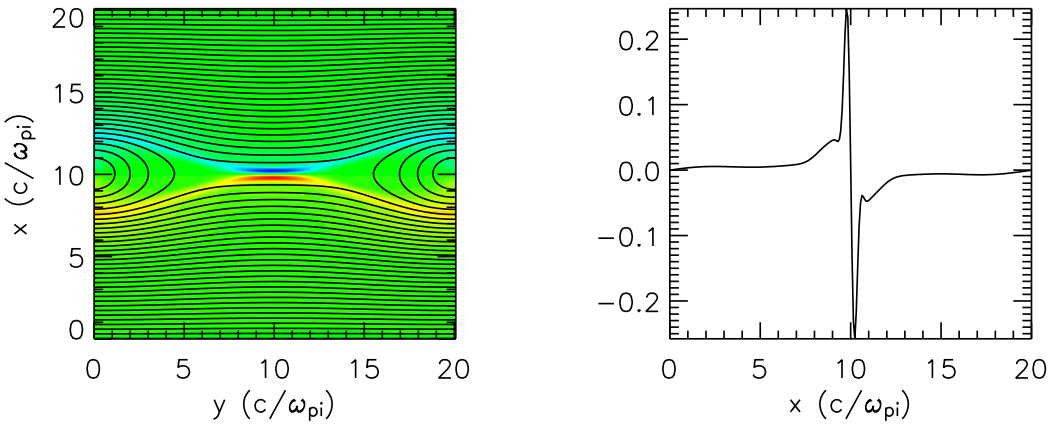

Figure 5.2: Plots showing the contribution to the electric field in the neutral sheet normal direction from the Hall term in Ohm's law from the simulations of L. Yin (private communication 2007). The coordinate system is the same as Fig. 5.1. In this way the electric field contributions from the Hall term point towards the neutral sheet. The maximum and minimum values of both panels are 0.25 and -0.25 respectively.

It can be seen from Figs. 5.1 and 5.2 that the directions of the contributions to the electric fields are in the correct sense to match the observations in chapter 4. Note that the regions of positive (red) and negative (blue) electric field are extended away from the X-line and are symmetrical about the neutral sheet in both cases.

The maximum and minimum values of the electric field contribution from the $\nabla . \mathsf{P}_e$ (Hall) term are 0.032 (0.26). It can be seen from these figures that the form of the curves look almost identical, suggesting that the anti-correlation may be general in this direction at least. The ratio of the maximum values of the electric field contributions is $\sim$ -8, close to, but not the same as that reported in chapter 4.

This chapter focusses on the anti-correlation observed in chapter 4 in an attempt to answer some of the questions presented above. In an attempt to explain the anti-correlation, the theoretical background will be considered using a simple magnetohydrostatic treatment in the next section. The observations of Henderson et al. (2006b) are investigated further in section 3. In section 4 an additional time period on 17$^{\text{th}}$August 2003 will be discussed. This event occurs away, both spatially

and temporally, from the passage of the reconnection X-line and can be used to establish if this phenomena is reconnection or substorm-phase related. In section 5, an additional period of data will be discussed in an attempt to verify the generality of the result. Further discussions and conclusions are given in sections 6 and 7.

5.2 A simple magnetohydrostatic treatment

In an attempt to explain the properties of the anti-correlation between the contribution to the electric field from the Hall and $\nabla . \mathsf{P}_e$ terms in Ohm's law, the force balance in the plasma sheet will now be considered.

Starting with the momentum equation:

$$\rho \left[\frac{\partial \mathbf{v}}{\partial t} + (\mathbf{v} . \nabla) \mathbf{v} \right] = \mathbf{j} \times \mathbf{B} + \nabla . (\mathsf{P}_e + \mathsf{P}_i) \tag{5.1}$$

Looking for static equilibrium solutions, i.e. where the total derivative is equal to zero, shows that the magnetic and plasma forces are equal and opposite:

$$\mathbf{j} \times \mathbf{B} = -\nabla . (\mathsf{P}_e + \mathsf{P}_i) \tag{5.2}$$

The ratio of the Hall term to the $\nabla . \mathsf{P}_e$ term in Ohm's law (here denoted as R) is therefore:

$$R = \frac{\mathbf{j} \times \mathbf{B}}{\nabla . \mathsf{P}_e} = -\frac{\nabla . (\mathsf{P}_e + \mathsf{P}_i)}{\nabla . \mathsf{P}_e} \tag{5.3}$$

If, as in case study one of chapter 4, it is assumed that the parallel contribution to the electric field from the $\nabla . \mathsf{P}_e$ term is negligeable away from the X-line, then R should be a negative number. By ignoring the off-diagonal terms in the pressures (which are generally a few percent of the diagonal terms), therefore writing that $\mathsf{P}_s = \frac{1}{3} Tr (\mathsf{T}_s) n_s k_b$ where s is the particle species, this equation becomes:

$$R = -\frac{\nabla \frac{1}{3} Tr\left(\mathsf{T}_e\right) n_e k_b + \nabla \frac{1}{3} Tr\left(\mathsf{T}_i\right) n_i k_b}{\nabla \frac{1}{3} Tr\left(\mathsf{T}_e\right) n_e k_b} \tag{5.4}$$

In addition to assuming isotropy, i.e. writing that $\frac{1}{3} Tr\left(\mathsf{T}_s\right) = T_s$, if the temperature for each species drops off over the length l_s then $\nabla \frac{1}{3} Tr\left(\mathsf{T}_s\right) n_s \rightarrow \left(T_s n_s\right) / l_s$, then Eqn. 5.4 is further reduced to:

$$R = -\frac{\nabla\left(T_e n_e\right) + \nabla\left(T_i n_e\right)}{\nabla\left(T_e n_e\right)} \approx -\frac{T_e n_e / l_e + T_i n_i / l_i}{T_e n_e / l_e} \tag{5.5}$$

If it is further assumed that these length scales are similar, and that quasi-neutrality is valid then this further reduces to:

$$R = -\frac{T_e + T_i}{T_e} \tag{5.6}$$

Therefore, when the only forces acting in the plasma sheet are those arising from the balance of magnetic field forces and plasma pressure gradients, the ratio of the Hall to $\nabla . \mathsf{P}_e$ terms should be equivalent to the ratio of ion to electron temperatures, $(T_i + T_e)/T_e$.

The above simple treatment suggests that the anti-correlation should be general, but the gradient should not be. The relation is linear and appears not to be directionally organised, i.e. the anti-correlation should appear in all directions. Further periods will now be investigated to test this simple treatment, and to consider why the anti-correlation reported in chapter 4 appears to be in only one direction.

5.3 17$^{\text{th}}$August 2003, further investigations

In section 4.3 an anti-correlation was observed between the contributions to the perpendicular electric field from the Hall and $\nabla . \mathsf{P}_e$ terms, in the direction normal to the neutral sheet. This behaviour was observed for five minutes between 16:38 and 16:43 UT on the 17$^{\text{th}}$August 2003. Figure 5.3 shows the data contained in

panels 6 to 9 of Fig. 4.4, the electric field contributions parallel and components perpendicular (in GSM) to the magnetic field from the Hall (red) and $\nabla . \mathsf{P}_e$ (black) terms in Ohm's law. The perpendicular Z direction (panel 4) is approximately the same as the neutral sheet normal direction, and the anti-correlation is most obvious in this component.

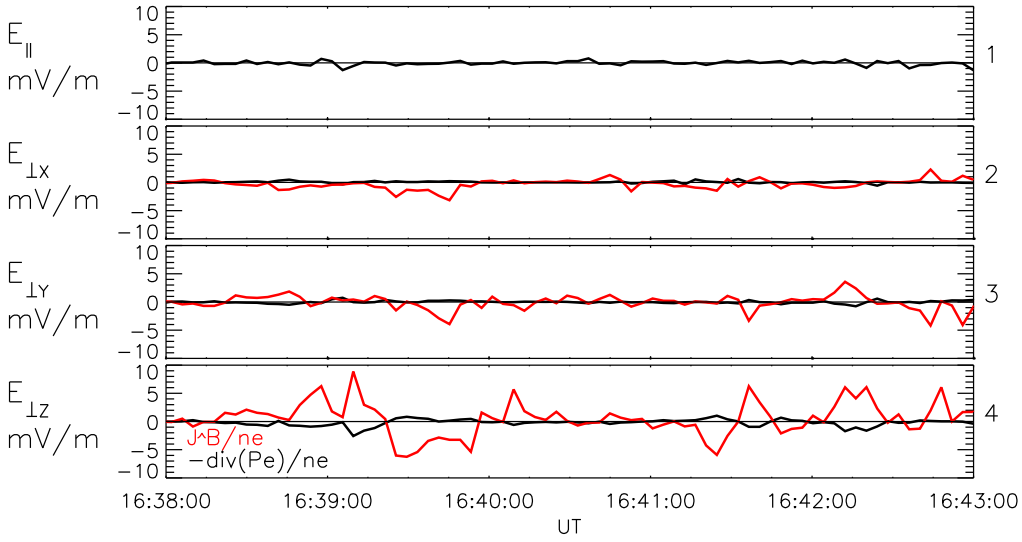

Figure 5.3: Electric field contributions from the $\nabla . \mathsf{P}_e$ (black) and Hall (red) terms parallel and three directions perpendicular to the magnetic field. This data is reproduced from chapter 4. The perpendicular Z direction is approximately in the neutral sheet normal direction.

In the electric field contributions in the perpendicular Y direction, a similar anti-correlation can be observed between these terms at 16:42:15 UT. In addition, anti-correlations can be observed in the electric field in the perpendicular X direction at 16:41:30 UT. It may be, therefore, that this anti-correlation appears in all components of the electric field. Figure 5.4 is analogous to Fig. 4.7, but shows the results for all components of the contributions to the perpendicular electric field. The gradient of the anti-correlation is marked above each figure.

Figure 5.4 shows that the anti-correlation does seem to appear in all components, however it is significantly less clear in the components in the plane of the neutral sheet (perpendicular X and Y). The correlation coefficients for these results are: X direction = -0.53, Y direction = -0.44, Z direction = -0.91. The statistical significances for these anti-correlations are all high ($> 99\%$).

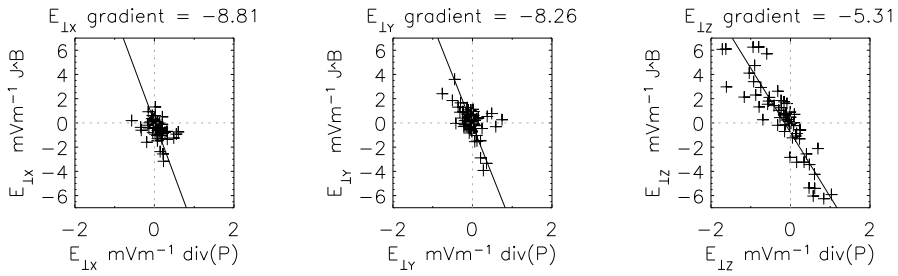

Figure 5.4: Scatter-plot showing the contributions to all components of the perpendicular electric field from the Hall term and $\nabla.\mathsf{P}_e$ terms in Ohm's law from the period discussed in chapter 4.

In addition, it is noted that if the anti-correlation was in one direction only, such as the neutral sheet normal direction, and the frame in which the data is viewed is not the accurate neutral sheet frame (note that a minimum variance analysis of the magnetic field data returned a frame that was close to, but not exactly, the GSM frame), then the anti-correlation may appear in all components of this 'erroneous rotated frame'. For this reason, the data are transformed into a frame derived from a minimum variance analysis on the Hall term data (i.e. the $\mathbf{j} \times \mathbf{B}/en_e$ data). In this way, if the anti-correlations appear only in the direction normal to the neutral sheet, they should appear only in the maximum variance analysis (of the Hall term) direction (e.g. Sonnerup et al., 1990). Sonnerup and Scheible (1998) review the applicability of the minimum variance technique to electric field data, and how the maximum variance direction can give a good estimate of the normal if the electric field in the normal direction undergoes a large change. However, to date the minimum variance technique has only been used on the electric field from $-\mathbf{v}_i \times \mathbf{B}$.

The direction of maximum variance of the Hall term (0.121, 0.104, 0.967 GSM) is close to the GSM Z direction, with a maximum:intermediate eigenvalue ratio of 6.0, showing that this direction determined with a high degree of certainty. The intermediate:minimum eigenvalue ratio was smaller, 2.4, showing that these directions were less well determined. Note that the minimum variance direction of the magnetic field was (-0.037, 0.088, -0.995) GSM. These two directions are within 17° of each other and show that the maximum variance direction of the Hall term at

this point appears to be a good estimate of the neutral sheet normal direction.

Figure 5.5 shows the same data as Fig. 5.4, but in the frame derived from that of the minimum variance analysis of the Hall term data. The plot also includes the temperature ratio, R discussed above. Note that the temperature of ions T_i is calculated as the number density weighted average of the temperature of protons (H^+), He^+, He^{++} and O^+, all measured from Cluster 4 CIS-CODIF.

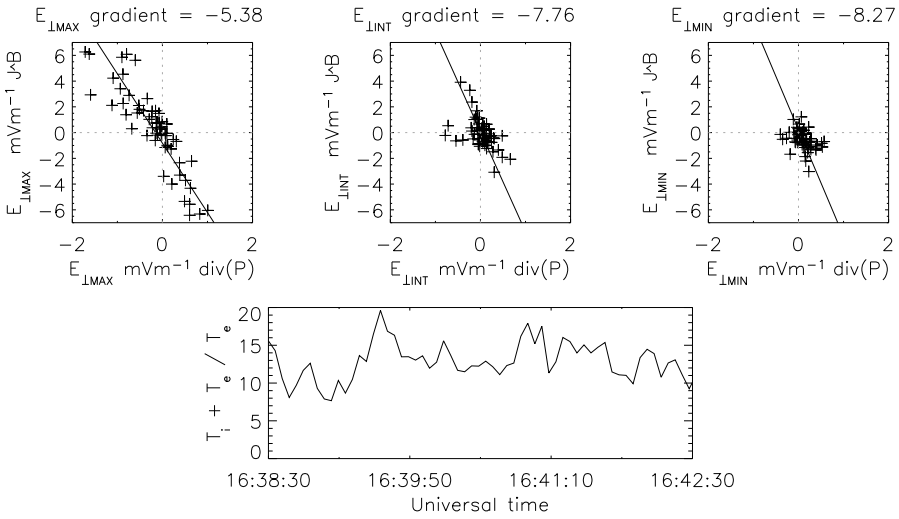

Figure 5.5: Scatter-plot showing the contributions to all components of the perpendicular electric field from the Hall term and $\nabla . \mathsf{P}_e$ terms in Ohm's law for the period discussed in chapter 4. The temperature ratio ($(T_i + T_e)/T_e$) is also plotted. The frame of reference is that resultant from a variance analysis on the Hall data.

Figure 5.5 shows that the anti-correlation is mainly in the maximum variance direction of the Hall term (correlation coefficient = -0.92). In the other components, however, there is still a small anti-correlation (minimum variance direction corelation coefficient = -0.46, intermediate variance direction corelation coefficient = -0.52). The statistical significances of these anti-correlations remain high ($> 99\%$).

As the correlation coefficients for the direction normal to the neutral sheet (GSM Z in Fig. 5.4 and the maximum variance direction in Fig. 5.5) are large, it is assumed that $\sim$5.4 is the correct gradient. The temperature ratio, R, is quite variable at this time, ranging from 8 to 20, with an average of 12.7, approximately two times larger than the gradient of the anti-correlation (5.4).

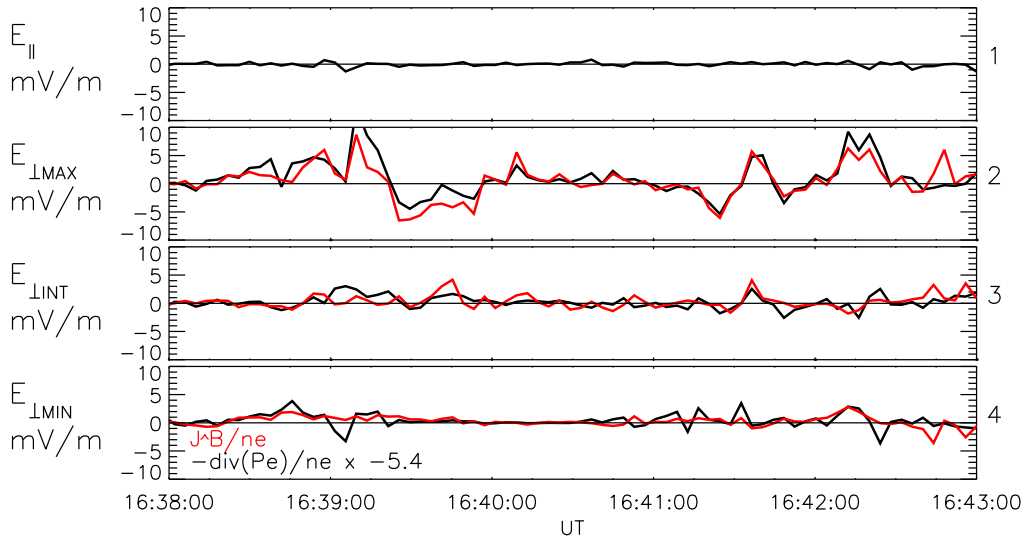

Figure 5.6: Electric field contributions from the $\nabla . \mathsf{P}_e$ (black) and Hall (red) terms parallel and three directions perpendicular to the magnetic field. The contribution from the $\nabla . \mathsf{P}_e$ term is multiplied by -5.4. The frame of reference is the frame derived from a minimum variance analysis on the Hall electric field data.

In order to show the anti-correlation clearly, Fig. 5.6 shows the same data as in Fig. 5.3 but with the electric field contribution from the $\nabla . \mathsf{P}_e$ term multiplied by -5.4. It can be seen from Fig. 5.6 that the two traces are generally similar, sometimes matching very well (e.g. perpendicular Z direction at 16:41:30 UT), and sometimes not so well (e.g. perpendicular maximum variance direction at 16:39:30 UT).

In order to test any relationship to the temperature ratio, a floating multiplier is constructed, where each $\nabla . \mathsf{P}_e$ data point is multiplied by a temperature ratio dependent value. The floating multiplier for any point is equal to the temperature ratio for that point, multiplied by the average Hall to $\nabla . \mathsf{P}_e$ ratio and divided by the average temperature ratio. Figure 5.7 shows this the same data as Fig 5.6 but with the $\nabla . \mathsf{P}_e$ data multiplied by this floating multiplier.

It can be seen from this figure that the fit is improved throughout the period. Indeed, at approximately 16:39:30 UT identified above as being a poor fit, the floating multiplier significantly improves the similarity of the two traces. Some of the spread in the points in Fig. 4.7 of chapter 4 appears to be therefore from a varying temperature ratio, not instrumental errors.

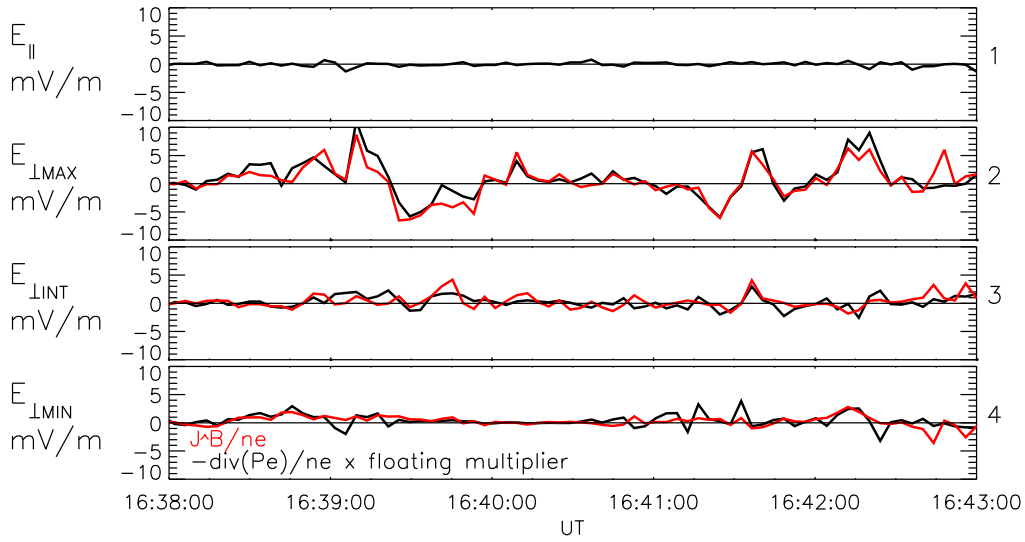

Figure 5.7: Electric field contributions from the $\nabla . \mathsf{P}_e$ (black) and Hall (red) terms parallel and three directions perpendicular to the magnetic field. The contribution from the $\nabla . \mathsf{P}_e$ term is multiplied by a floating multiplier based on the temperature ratio, where the average temperature ratio is normalised to -5.4.

It would appear from this crossing that the observed anti-correlation is mainly confined to the direction normal to the neutral sheet, and is somewhat dependent on the temperature ratio. The temperature dependence is presumably responsible for some of the scatter of points away from the $\sim$ -5.3 gradient in Fig. 4.7.

5.4 Case study one - 17$^{\text{th}}$August 2003

Fig. 5.8 shows observations between 15:55 and 16:15 UT on the 17$^{\text{th}}$August 2003, containing one crossing of the neutral sheet, in the same format as Fig. 4.2. These data are taken from a period that contains no obvious signs of any reconnection activity: Referring back to Fig. 4.2 it can be seen that the AE index is small ($\sim$ 200 nT) and the estimated magnetic field in the lobe is approximately constant ($\sim$ 55 nT), only starting to change at approximately 16:30 UT. In addition, the flow of particles in the X direction is small, the current sheet is thick ($\sim$ 5000 km) and the plasma sheet contains cool electrons ($\sim$ 300 eV) before their acceleration begins at 16:30 UT.

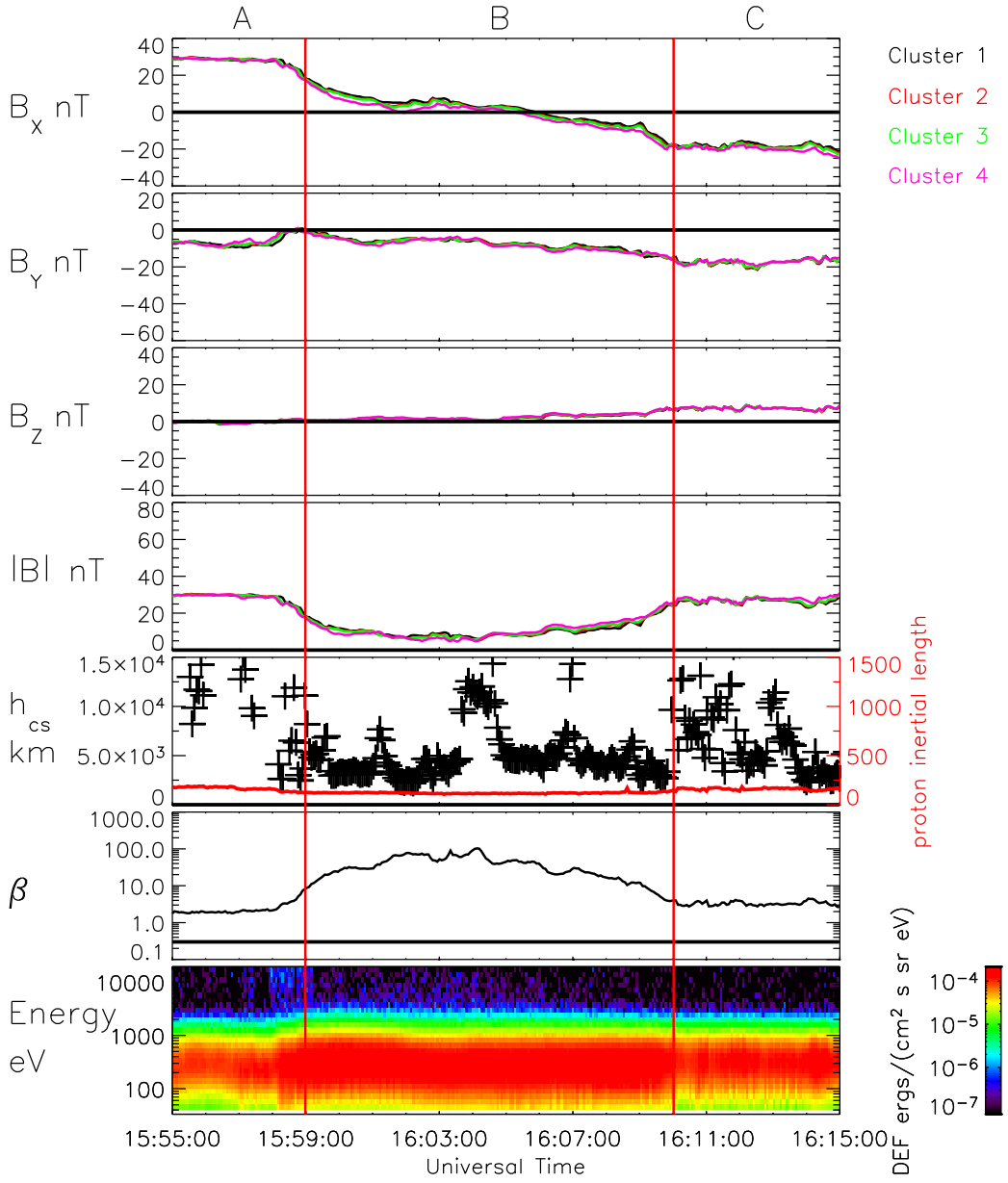

Figure 5.8: Three components (GSM) and the magnitude of the magnetic field, current sheet half thickness, plasma beta and an energy time spectrogram showing the differential energy flux of electrons. Three periods A to C are separated by red vertical lines. Note that the axis labels on the current sheet thickness and proton inertial length are different.

Panels 1 to 4 contain the magnetic field data and show that the spacecraft were initially north of the neutral sheet and crossed to the south at approximately 16:05 UT. B_Y was generally negative and B_Z was small, becoming slightly positive towards the end of the encounter.

Panel 5 shows the current sheet half thickness estimated from Eqn. 4.7 and the proton inertial length. Note that the axis labels on the current sheet thickness and proton inertial length are different. The data points group around a half thickness of 4000 to 5000 km. Panel 6 shows the full plasma β (Eqn. 1.26) and an electron spectrogram is shown in panel 7. These last two panels indicate that the spacecraft were in the plasma sheet throughout the period shown. Between 15:59 and 16:10 UT the spacecraft enter deep into the central plasma sheet, which will be here called the inner central plasma sheet. Outside this period, between 15:55 and 15:59 UT and 16:10 and 16:15 UT the spacecraft are still in the plasma sheet but nearer the outer boundary. This part of the plasma sheet will be here called the outer central plasma sheet (the boundary of the plasma sheet is identified as $\beta = 0.3$). For ease of description later in this section, the first period from 15:55 to 15:59 will be referred to as period A. Periods 15:59 to 16:10 UT and 16:10 to 16:15 UT will be referred to as periods B and C respectively. These boundaries are marked on plots in section 5.4.

The minimum variance direction of the magnetic field, identified with the neutral sheet normal, is in the (0.090, 0.242, 0.966) GSM direction, with a minimum:intermediate eigenvalue ratio of 17.5. The large separation between these two eigenvalues gives confidence in the minimum variance analysis. The maximum (intermediate) variance direction is close to the X (Y) GSM direction. In this case the GSM frame should give a good approximation to the current sheet frame and is used here.

Fig. 5.9 shows the magnetic field and Hall and $\nabla . \mathsf{P}_e$ contributions to the electric field observations between 15:55 and 16:15 UT, containing one crossing of the

neutral sheet, in the same format as Fig. 4.4.

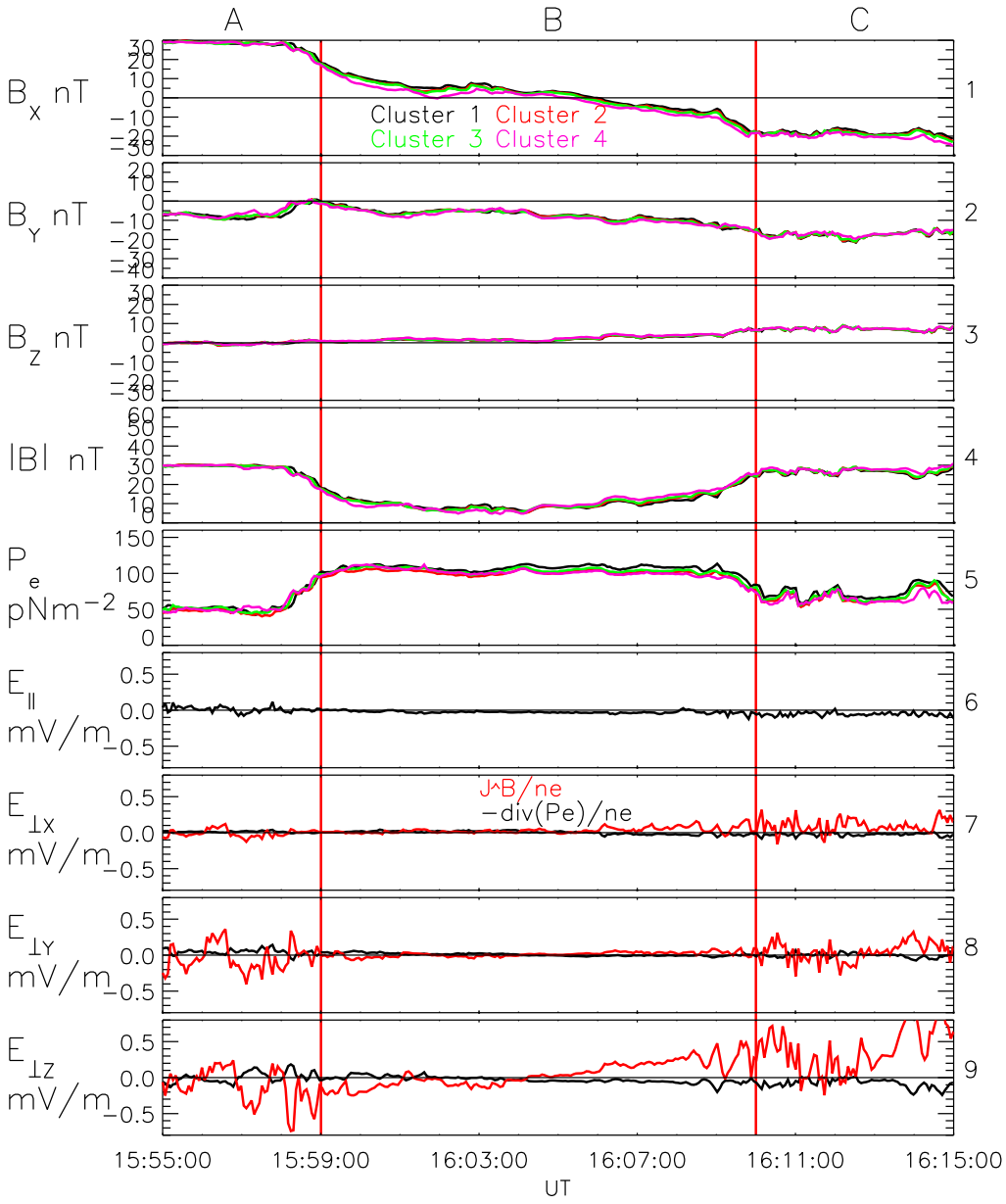

Figure 5.9: Magnetic field components and magnitude in GSM and electric field parallel to, and three directions perpendicular to the magnetic field. In these panels the electric field contribution from the Hall term is in red, with the electric field contribution from the $\nabla . \mathsf{P}_e$ term in black.

There was little electric field contribution parallel to the magnetic field from the $\nabla . \mathsf{P}_e$. In sections A and C there were fluctuations in all of the components of the electric field perpendicular to the magnetic field from both the Hall and $\nabla . \mathsf{P}_e$ terms. These two contributions appear to be anti-correlated in all perpendicular

components. During the crossing of the central plasma sheet (period B) the fluctuations appear mainly in the Z direction (normal to the neutral sheet). Throughout period B, the electric field arising from the Hall term pointed towards the neutral sheet whereas the contribution from the $\nabla . \mathsf{P}_e$ term pointed away from the neutral sheet on both sides.

A minimum variance analysis performed on the Hall data during the whole period gives a maximum variance direction of (-0.137, -0.208, -0.968) GSM with a maximum-intermediate eigenvalue ratio of 9.2. The similarity to the minimum variance direction from an analysis of the magnetic field (0.090, 0.242, 0.966) is noted. Indeed, these directions are within 4° of each other.

Figure 5.10 shows three scatter plots of the electric field contributions perpendicular to the magnetic field from the Hall and $\nabla . \mathsf{P}_e$ terms from 15:55 to 16:15 UT as well as the temperature ratio. The data are displayed in the frame derived from the variance analysis performed on the Hall data.

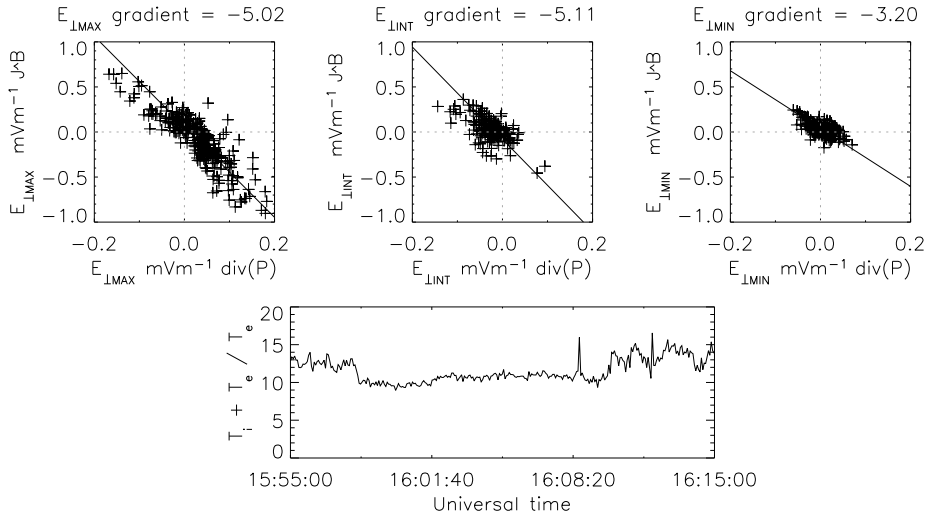

Figure 5.10: Scatter-plot showing the contributions to the components of the perpendicular electric field from the Hall term and $\nabla . \mathsf{P}_e$ terms in Ohm's law between 15:55 to 16:15 UT, as well as $(T_i + T_e)/T_e$. The frame of reference is that resultant from a variance analysis on the Hall data.

The gradient (correlation coefficient) in the minimum variance direction (of the Hall data) is -3.20 (-0.45), intermediate variance direction -5.11 (-0.48) and maximum variance direction -5.02 (-0.87).

The anti-correlations appear in all directions, suggesting that the anti-correlations are not confined to the direction normal to the neutral sheet as seen the previous example. Note however that the gradients in each component are slightly different, and the correlation coefficients in the minimum and intermediate variance directions are low. The significance of the anti-correlation in the minimum variance direction is somewhat smaller (although still $> 99\%$) than that in the maximum and intermediate variance directions.

It can be seen from this figure that the temperature ratio at this time is quite variable. Anticipating that a steady temperature ratio may lead to a steady and better defined gradient, the data is replotted for periods B and C. During period B the temperature ratio is approximately 10, whereas in period C the temperature ratio is variable, but approximately 13.

Figure 5.11 shows the same data as Fig. 5.10 but from period B, the inner central plasma sheet, where the anti-correlation is strongly directionally organised. In the maximum variance direction the anti-correlation is clear with a gradient of -4.49 (correlation coefficient = -0.87). This is approximately half the temperature ratio of 10.5, which is steady throughout the period shown. In the other variance directions there is very little anti-correlation, and it is therefore assumed that the maximum variance direction of the Hall data (-0.179, -0.135, -0.974 GSM) should be a good estimate of the neutral sheet normal. The maximum:intermediate eigenvalue separation is 38.1 and shows that this direction is defined to a high accuracy.

A minimum variance analysis of the magnetic field data, the usual means of determining the neutral sheet normal, in period B only, gives the minimum variance direction in the (0.072, 0.258, 0.964 GSM). However, the minimum:intermediate eigenvalue separation is only ~ 3 which shows that this direction is not well defined. This angle is 9° from the maximum variance direction of the Hall data in period B.

Figure 5.12 is in the same format at Fig. 5.11 and shows data for period C, the outer central plasma sheet. It can be seen that the anti-correlations appear in

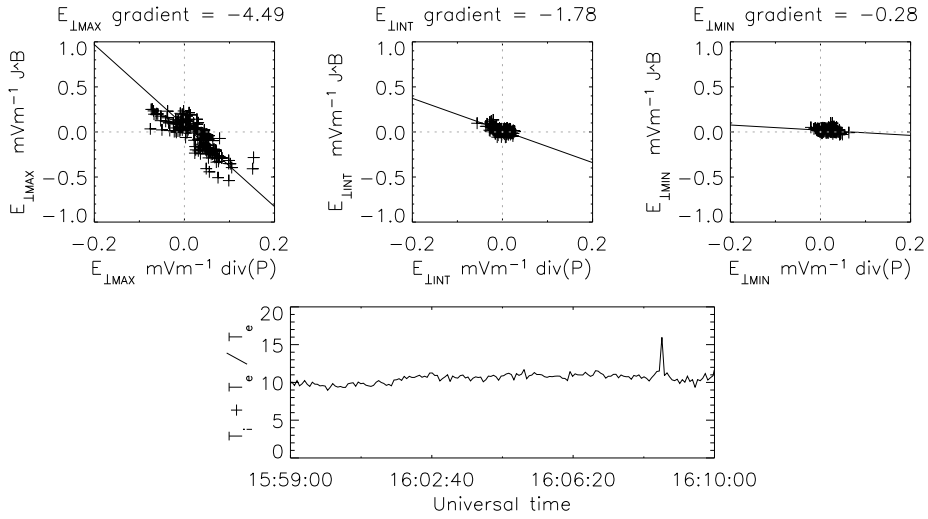

Figure 5.11: Scatter-plot showing the contributions to the perpendicular electric field from the Hall term and $\nabla . \mathsf{P}_e$ terms in Ohm's law for period B of the first crossing, in the same format as Fig. 5.10.

all variance directions (note the small scale in the right hand panel). The gradients (correlation coefficients) for the maximum, intermediate and minimum variance directions are -5.09 (-0.79), -6.06 (-0.61) and -4.20 (-0.91). The average gradient of the anti-correlation is -5.1. The statistical significances of these results are again high.

The maximum variance direction of the Hall data (0.034, 0.332, 0.943 GSM) gives a poorer determination of the current sheet frame than the results for period B as the separation of eigenvalues is smaller (5.8). The angular separation between the maximum variance directions of the Hall data from periods B and C is 14°.

The temperature ratio is approximately 11 to 14 throughout this period and averages to 13.4. It would appear that the temperature ratio increases as the spacecraft moves from the central plasma sheet towards the PSBL. The temperature ratios do not equal the gradients of the anti-correlations, being a factor of approximately 2 larger.

Panels 1 to 4 of Fig. 5.13 show the parallel and perpendicular components of the Curlometer current derived from FGM data in the barycentre (black), as well as the current calculated from the particles ($q(n_p p - n_e e)$ from Cluster 4, blue) for

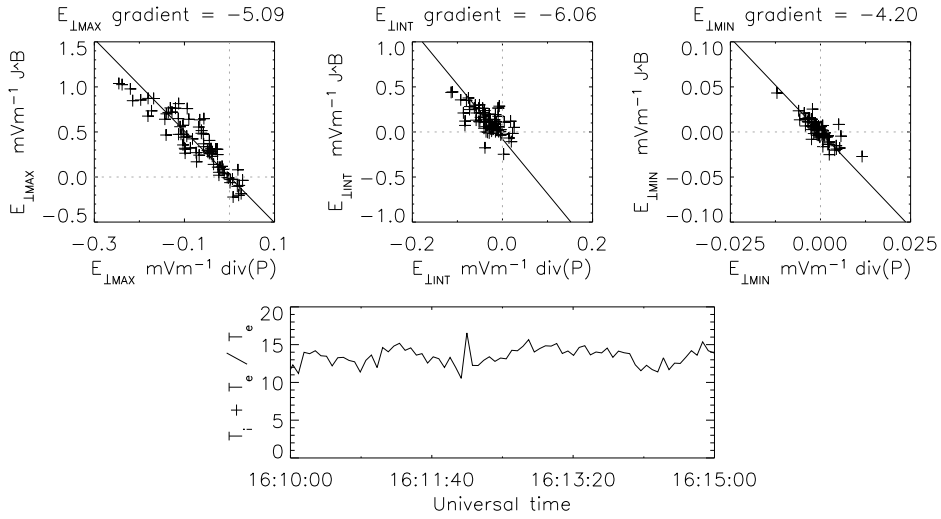

Figure 5.12: Scatter-plot showing the contributions to the perpendicular electric field from the Hall term and $\nabla . \mathsf{P}_e$ terms in Ohm's law for period C of the first crossing, in the same format as Fig. 5.10.

periods A, B and C. Panels 5 to 8 show the electron and proton velocity moments derived from PEACE and CIS-CODIF data on Cluster 4. The final panel shows a comparison of the magnetic field in the X direction from the barycentre (from where the spatial gradient estimates are made) and Cluster 4 (from where particle measurements are made).

It can be seen that the majority of the current measured by the Curlometer (black trace, panels 1 to 4) was anti-parallel or parallel to the magnetic field. The Curlometer current in the perpendicular X and Z directions (panels 2 and 4 respectively) was generally smaller, with the current in the perpendicular X direction sometimes becoming significant (for example at 16:08 UT). The cross tail current can be seen in the perpendicular Y direction, approximately the intermediate variance direction for this current sheet orientation. This is generally smaller than the parallel current but again can have a significant contribution to the overall current (for example at 16:00 and 16:08 UT). The current sheet appears to be bifurcated (Nakamura et al., 2002; Runov et al., 2003; Thompson et al., 2006), as at 16:05 UT where B_X drops to zero, identified as the neutral sheet, the perpendicular current drops to zero.

The particle current (blue, panels 1 to 4) has high frequency fluctuations but

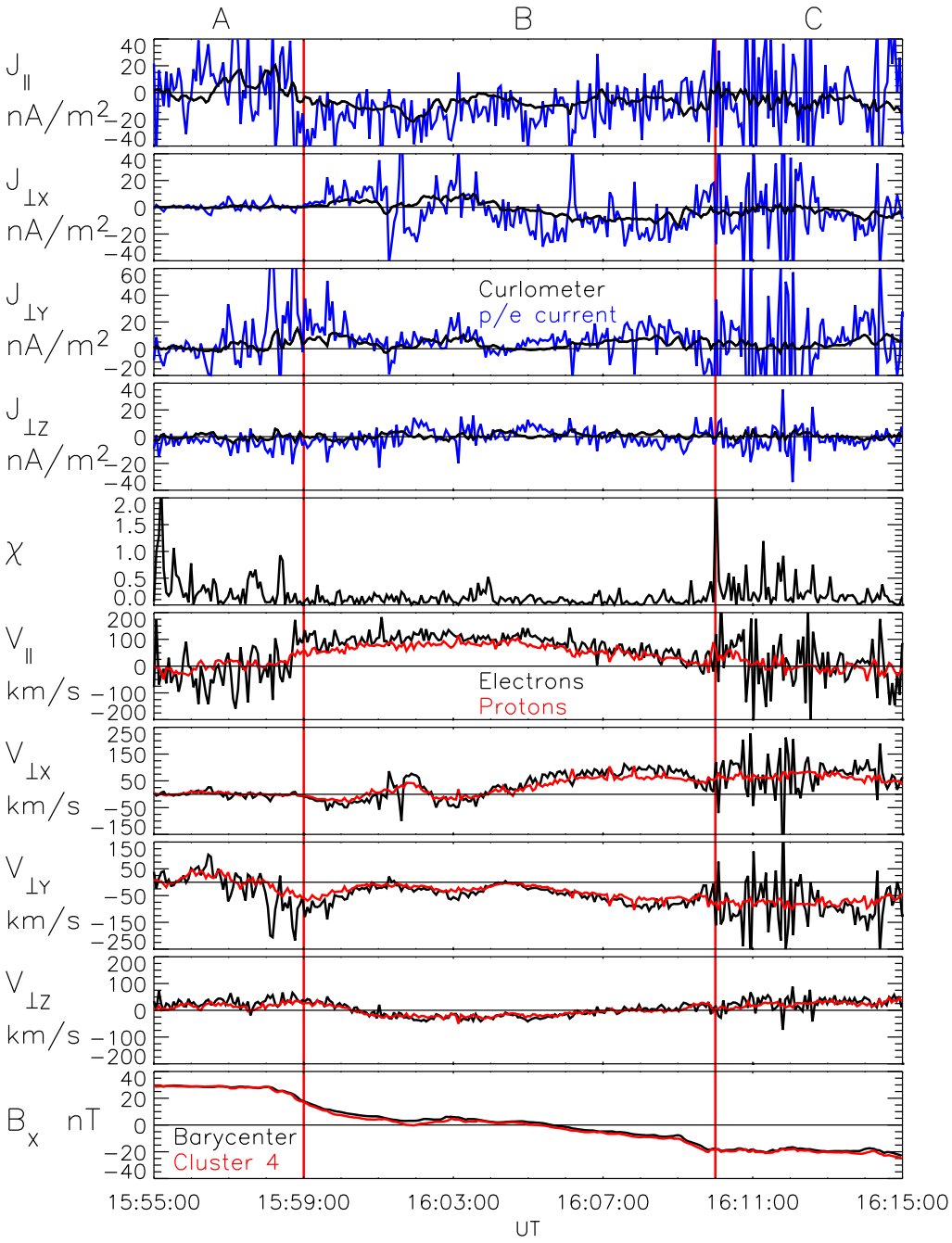

Figure 5.13: Panels 1 to 4 show the parallel and three perpendicular components of the current density derived from the Curlometer technique (at barycentre) and particle current. Panel 5 shows the relative error, χ (Eqn. 2.26). Panels 6 to 9 show the parallel and three perpendicular components of velocity from electrons (black) and protons (red). The particle measurements are from Cluster 4. The bottom panel shows B_X at the barycentre and at Cluster 4.

follows the Curlometer current on average. The two forms of current calculation generally agree well (particularly in the Y direction, panel 3) but occasionally the Curlometer underestimates the particle current (16:03 to 16:10 UT - X direction, panel 2). Generally, the Curlometer current does not overestimate the particle current. The electron current is very variable on small spatial scales (Alexeev et al., 2005) and the Curlometer technique would average out a large local current. The bifurcation of the current sheet can also be observed in the particle current. The relative error in the curlometer current is generally small.

Panels 6 to 9 show that both species of particles seem to move together, with the currents measured by the Curlometer generally coming from electrons moving slightly faster than the protons. The bifurcation of the cross tail current can be seen in the particle velocities as both cross tail particle velocities fall to zero at the neutral sheet (16:05 UT) rather than having equal electron-proton cross tail velocity. The velocities observed were generally no larger than 200 kms^{-1}. Fast flows, indicative of reconnection activity, do not occur at this time.

The large fluctuations in the Hall contribution to the electric field (Fig. 5.9) in periods A and C in the Y and Z directions are caused by the fluctuations in the current in the Y and Z direction and the large magnetic field in the X direction. The fluctuations in the Hall contribution to the electric field in the X direction are caused by the small current fluctuations in the Z direction and the smaller magnetic field in the Y direction. The electric field contribution fluctuations in periods A and C are sometimes larger than those in period B due to the smaller electron density in periods A and C (not shown).

In period B the electric field contribution from Hall and $\nabla.\mathsf{P}_e$ terms become more directionally organised (i.e. the electric field contributions are mainly in one direction). The contribution in the Z direction is clearly anti-correlated, with the anti-correlations in the other directions being less clear. It can be seen from this figure that the reversing sign of B_X and a quasi-constant cross tail current give rise

to this directionally organised anti-correlation. The contribution to the electric field from the Hall term again pointed towards the neutral sheet whereas that from the $\nabla . \mathsf{P}_e$ term pointed away from the neutral sheet.

5.4.1 A Harris current sheet?

In the derivation of the current sheet half thickness, a Harris type magnetic profile was assumed (Eqn. 5.7).

$$\mathbf{B}(z) = B_L \tanh\left(\frac{z}{h}\right) \hat{\mathbf{x}} \tag{5.7}$$

However, it has been shown that the actual current sheet appears bifurcated. This bifurcation can be demonstrated in the present crossing event discussed here as the spacecraft makes a relatively slow crossing through a large proportion of the plasma sheet. In a treatment similar to Runov et al. (2005b), the spatial profile is reconstructed with use of the linear estimator method (section 2.6.2). As the spacecraft cross the plasma sheet, slowly enough to enable a satisfactorily large data set and fast enough to assume that the plasma conditions do not change during the traversal (i.e. assuming that the observed variation in structure is purely spatial), the spatial profile can be reconstructed by computing the following integral to obtain an effective vertical scale, Z^*:

$$Z^* = \int_{t_0}^{t_1} \frac{\partial B_{max}}{\partial t} \left[\frac{\partial B_{max}}{\partial n}\right]^{-1} \mathrm{d}t \tag{5.8}$$

Where B_{max} is the magnetic field in the maximum variance direction and n is the direction normal to the neutral sheet. In this example the maximum variance direction is close to the X direction, and the normal direction is close to the Z direction. The integration was carried out with $\mathrm{d}t = 0.2$s, using 'trapezium rule' numerical integration. Z^* is defined as zero at $B_X = 0$.

The first panel of figure 5.14 shows the current profile as measured by the Cur-

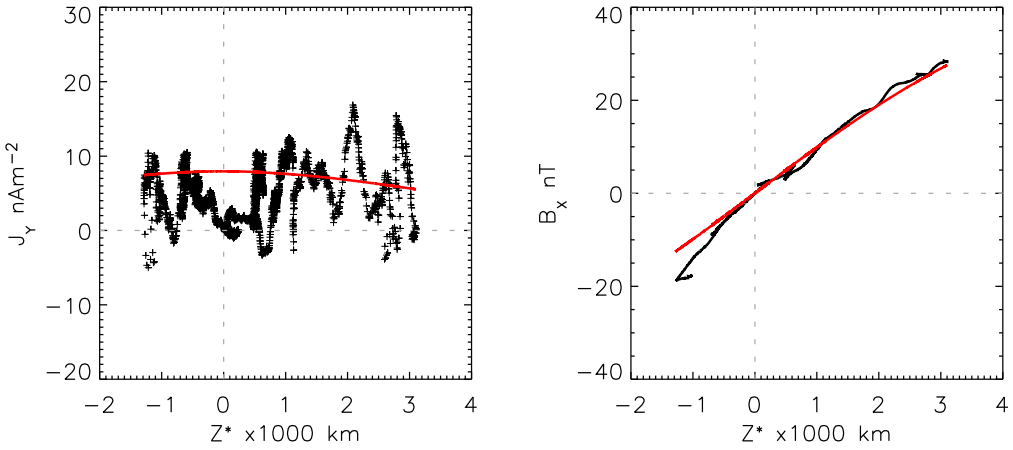

Figure 5.14: In the left hand plot, black crosses show the current density in the perpendicular Y direction, as measured by the Curlometer (Fig. 5.13), against reconstructed distance Z^* (Eqn. 5.8). Overplotted in red is the model Harris current, using $B_L = 50$ nT and h_{cs} = 5000 km. The right hand plot shows the profile of the measured B_X (black) and the Harris model B_X.

lometer (also shown in panel 3 of Fig. 5.13) against reconstructed distance Z^* (Eqn. 5.8) as black crosses. Overplotted is the current profile from the Harris model (red). The second panel shows the B_X (barycentre black, Harris model red) profile against Z^*. In the model profiles above, the values $B_L = 50$ nT and h_{cs} = 5000 km have been used, and have been taken from panels 8 and 5 in Figs. 4.2 and 5.8 respectively.

As mentioned before, the current is bifurcated with the current density being clearly zero in the centre of the plasma sheet. The structure away from the centre of the plasma sheet is highly complex, with large current enhancements present. These small scale structures, embedded in the current sheet, appear not to be symmetric about the neutral sheet. There exists no region at the extremum of the Z^* range where the current drops to zero, which suggests that the spacecraft do not sample the edges of the current sheet during this period. Indeed, β is high and suggests that the spacecraft do not come close to the boundaries of the plasma sheet.

In the right hand panel it can be seen that the magnetic field profile follows closely the Harris model profile, with Z^* being approximately linearly related to B_X. This is again indicative of the spacecraft being in the centre of the plasma

sheet.

It would appear therefore that the structure of the current sheet at this time is not like that of the Harris model. The direct applicability of the current sheet half thickness estimate in Fig. 5.8 may be in question, but it would appear from Fig. 5.14 that the overall current sheet is thicker than 4000 km, and is composed of a number of smaller scale current sheets.

5.5 Case study two - 25thOctober 2003

In order to verify and investigate the generality of the existence of the anti-correlations, a second, distinct, period was found on the 25thOctober 2003 where the spacecraft were in burst mode. This again enabled the derivation of both the Hall term and $\nabla.\mathsf{P}_e$ terms in Ohm's law. In the next section, an overview of a period within this day will be given followed by an investigation of the relative contributions to the electric field.

The Cluster spacecraft were located (-15.9,-4.9,4.9) R_E GSM, separated by $\sim$ 200 km, and crossed the GSM neutral sheet a number of times. Figure 5.15 shows the magnetic field, electron pressure, estimated current sheet half thickness, plasma β and electron spectrogram in the same format as Fig. 5.8. The spacecraft are initially north of the neutral sheet and cross to the south at $\sim$ 11:10 UT, returning to the north of the neutral sheet at $\sim$ 11:13 UT. B_Y and B_Z are quite variable at this time, with B_Y changing sign at approximately the same time as B_X. B_Z is positive throughout the period shown, and is generally the largest component of the magnetic field. The current sheet thickness (panel 5) is large, $\sim$ 5000 to 10000 km. The spacecraft are deep inside the plasma sheet, shown by a large β and large differential energy flux of electrons at $\sim$ 500 eV. The particle flows are small, being smaller than 200 kms^{-1} (not shown). AE index at this time is small (< 100 nT), consistent with there being no substorm or reconnection activity in the magnetotail.

In order to determine the correct frame in which to view this crossing, a mini-

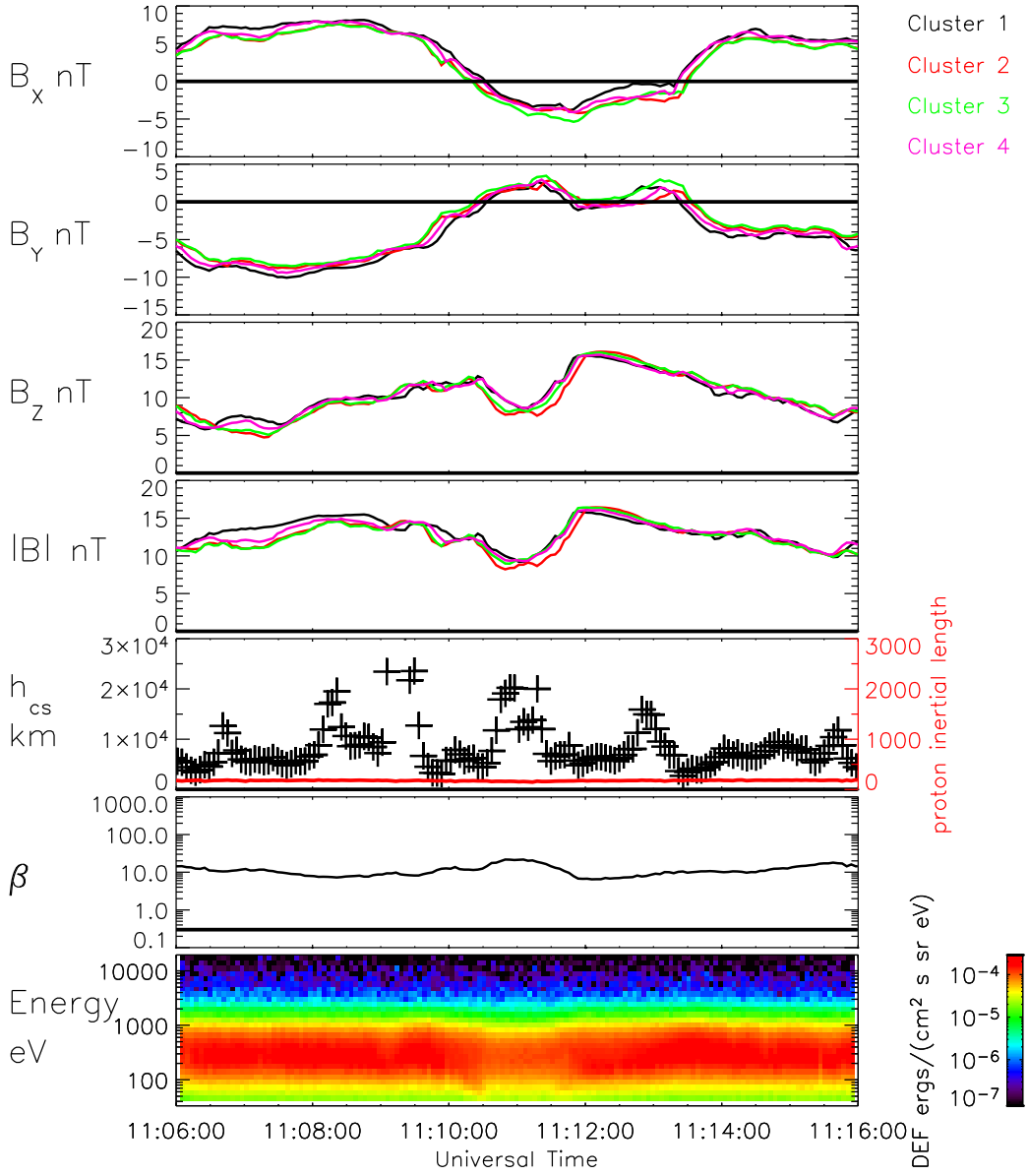

Figure 5.15: Magnetic field, current sheet half thickness, plasma beta and an energy time spectrogram of electrons in the same format as Fig. 5.8.

mum variance analysis was carried out on the period 11:08:00 to 11:11:00 UT. The minimum variance direction was in the (-0.678, -0.699, 0.227) GSM direction, with an intermediate:minimum eigenvalue ratio of ~ 24. This direction is far from the GSM Z direction and, if a good approximation to the neutral sheet normal direction, shows that the current sheet at this time was highly tilted.

In this frame the current, determined from the Curlometer technique (not shown) is small (< 10 nAm^{-2}) in all components perpendicular to the magnetic field. There is no clear cross tail current. Note that it is the current in this frame that is used to calculate the current sheet half thickness in Fig. 5.15.

Fig. 5.16 shows the contributions to the electric field from the Hall and $\nabla . \mathsf{P}_e$ terms during this period, as well as the magnetic field measurements and $\frac{1}{3}Tr\mathsf{P}_e$ in the same format as Fig. 5.9. These data are in the frame returned from the minimum variance analysis on the magnetic field discussed above. The type of data products used to derive the $\nabla . \mathsf{P}_e$ is the same as in the 17$^{\text{th}}$August event.

In the variance frame, the spacecraft cross the neutral sheet at approximately 11:10 and 11:13 UT. The largest magnetic field component was in the intermediate variance direction, varying between 5 and 15 nT (note that the maximum:intermediate eigenvalue separation is ~ 20, showing that these directions are well determined). The magnetic field in the minimum variance direction was small throughout this period.

It can be seen from Fig. 5.16 that the electric field contribution from the $\nabla . \mathsf{P}_e$ term parallel to the magnetic field is small. The contributions perpendicular to the magnetic field are larger and again appear anti-correlated. The electric field contributions are of equivalent magnitude in all components, and no clear bipolar signatures can be observed as the spacecraft cross the neutral sheet (i.e. no directional organisation with respect to the neutral sheet).

The anti-correlative behaviour is clearly reproduced in Fig. 5.17, which shows a scatter plot of the contributions to the electric field from the Hall term and $\nabla . \mathsf{P}_e$

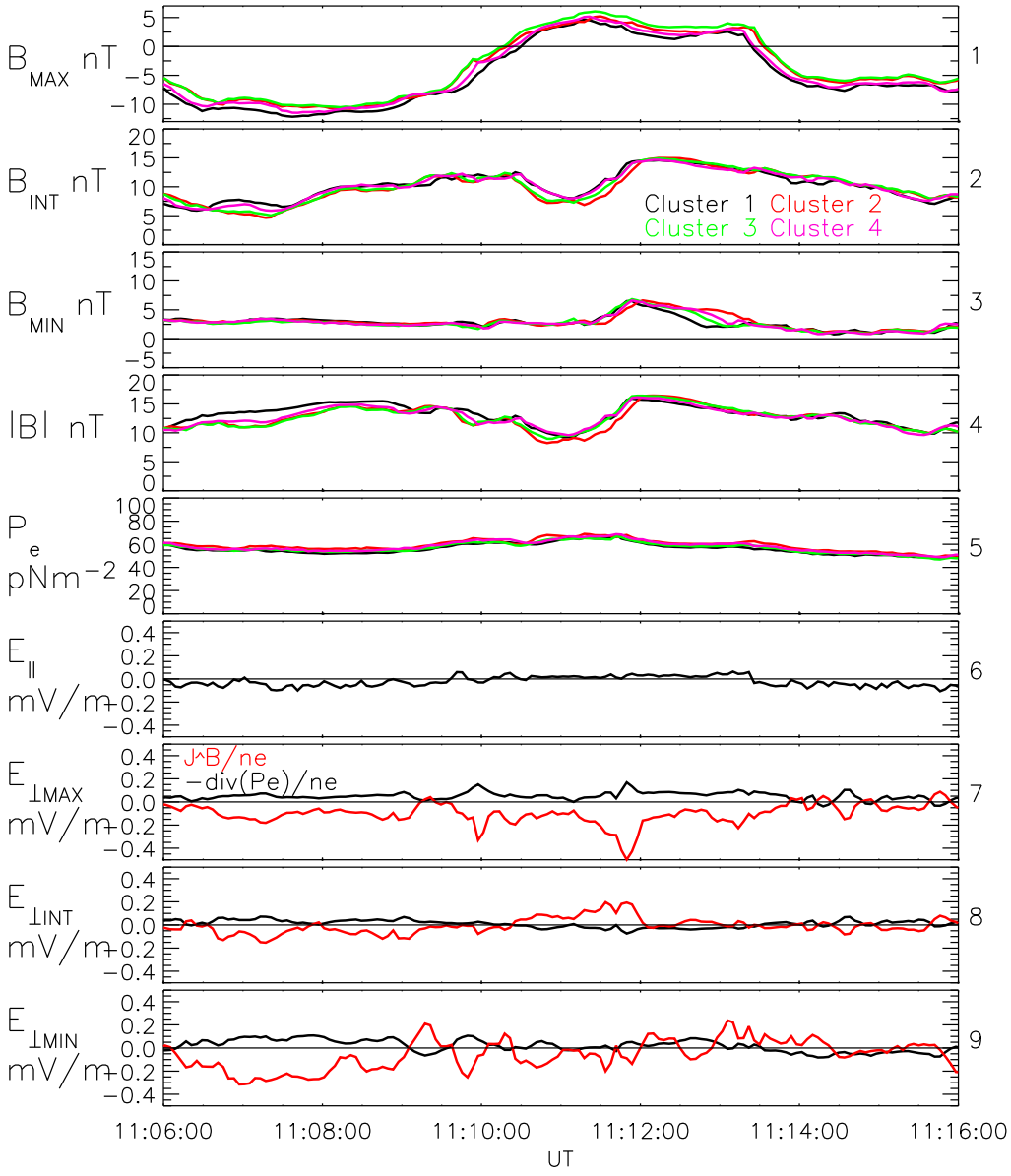

Figure 5.16: Magnetic field and electric field contributions from the $\nabla . \mathsf{P}_e$ and Hall terms from case study two, in the same format at Fig. 5.9.

terms, as well as the temperature ratio in the same format at Fig. 5.10. The frame of reference is now that returned from a variance analysis of the Hall term data.

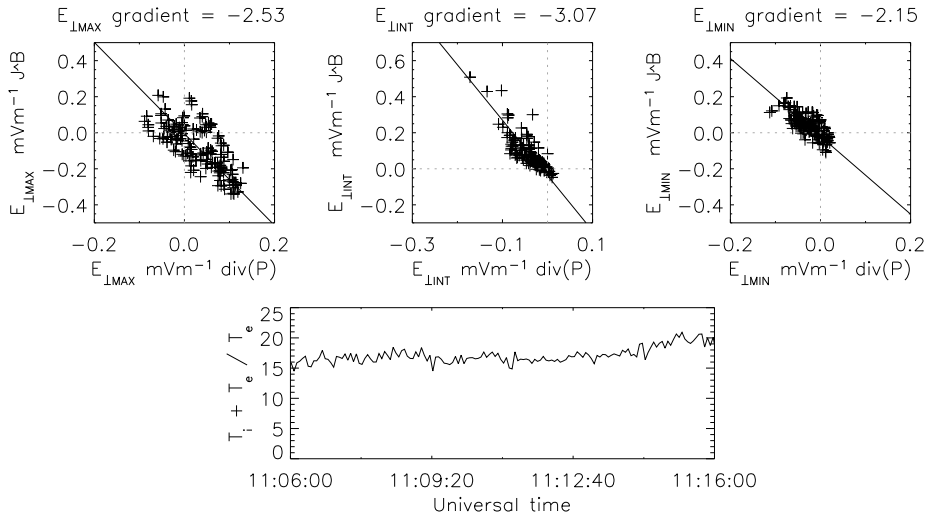

Figure 5.17: Scatter-plot showing the contributions to the perpendicular electric field from the Hall term and $\nabla . \mathsf{P}_e$ terms in Ohm's law in the same format at Fig. 5.10. The frame of reference is that returned from a variance analysis of the Hall term data.

The anti-correlations are clear with a consistent gradient of -2.6 on average. The correlation coefficients are high, being -0.73, 0.86 and 0.70 for the maximum, intermediate and minimum directions respectively (all with high statistical significance).

The temperature ratio varies between 15 and 20, averaging at 17.1, approximately 7 times larger than the gradient of the correlations.

The maximum variance direction of the Hall data is in the (-0.811, -0.505, 0.295) GSM direction, with a maximum:intermediate eigenvalue ratio of 2. This direction is not similar to the minimum variance direction of the magnetic field and has a low maximum-intermediate eigenvalue ratio, showing that these directions are poorly determined.

5.6 Discussion

During the selected periods on the 17th August and 25th September 2003, the Cluster spacecraft were in the plasma sheet. During these period the spacecraft sampled

various plasma sheet conditions in which the relationship between the Hall and $\nabla . \mathsf{P}_e$ terms in Ohm's law could be investigated. Periods with and without a significant cross tail current, close to and far from reconnection and close and far from substorm conditions were sampled.

Initially, a simple magnetohydrostatic treatment was proposed to explain the anti-correlation between the Hall and $\nabla . \mathsf{P}_e$ contributions to the electric field. It was assumed that in equilibrium conditions, the gradient of the anti-correlation should correspond to the ratio of temperatures of ions and electrons. The treatment suggested that the anti-correlation should be linear and appear in all components of the electric field.

The investigations performed in chapter 4 were extended to focus on the anti-correlation between the Hall and $\nabla . \mathsf{P}_e$ terms in Ohm's law in order to test the predictions of the simple treatment. This period was close, both spatially and temporally, to reconnection and was during the buildup to a large substorm. There was a large cross tail current in the centre of the plasma sheet. The anti-correlations were limited to the direction normal to the neutral sheet. Variance analysis performed on the magnetic and Hall showed that the neutral sheet normal direction could be identified from the Hall data alone. In this way, the anti-correlations appear 'directionally organised'. The ratio of the Hall term to the $\nabla . \mathsf{P}_e$ term, shown by the gradient of a linear best-fit was $\sim$ -5.4. The simple treatment put forward to explain this phenomena predicted that the ratio should be $\sim$ -13, although this prediction varied between -8 and -20.

Figure 5.6 showed a comparison of the Hall data and the $\nabla . \mathsf{P}_e$ data, with the latter term being multiplied by -5.4. The variability of the temperature ratio may explain why the multiplicative factor employed in Fig. 5.6 did not always give a good match between the two time series; the appropriate multiplicative factor may change throughout the period as the temperature ratio varies. A floating multiplier, based on the temperature ratio, was constructed to test this idea (Fig 5.7). It was

shown that the match between the two contributions to the electric field improved significantly when the temperature ratio was taken into account, but did not explain the factor of ~ 2 difference between the average temperature ratio and the gradient of the anti-correlation.

In the first full case study in this chapter, a period was investigated where there was a crossing of the central plasma sheet, encompassing regions with small and large cross tail current. When analysed separately, these different regions gave different results.

In the outer central plasma sheet, period C, the two contributions to the electric field are not directionally organised (i.e. they are anti-correlated in all components). Relatively little cross tail current was observed at this time. The ratio of temperatures was approximately 13.4, which was in turn approximately twice the gradient of the anti-correlations in all components. It is noted that the magnitude of the electric field contributions were smaller in this period than in the period discussed in chapter 4 by an order of magnitude. This corresponds with an order of magnitude increase in the current sheet thickness.

In the inner central plasma sheet, period B, the electric field contributions were again observed to be directionally organised in the neutral sheet normal direction. A relatively larger cross-tail current was observed during this period. It would appear that the appearance of a coherent cross tail current is associated with the directional organisation of the Hall term at this time. The temperature ratio in the central plasma sheet was 10.5, again approximately twice the gradient of the correlation.

In period B it was found that a variance analysis of the Hall data produced a neutral sheet normal direction close to the minimum variance direction of the magnetic field, the usual estimate of the neutral sheet normal (Sonnerup and Cahill, 1967).

It has been observed here that the direction of minimum variance of the magnetic field is approximately in the same direction as the maximum variance direction of

the Hall term, with the second direction being better determined than the first. The certainty of the direction from the Hall variance analysis, evaluated by the separation of eigenvalues, was large, indeed larger than the separation of the eigenvalues of the magnetic field variance analysis.

Previous authors (e.g. Sonnerup et al., 1990) have found that the maximum variance direction of the electric field (calculated from $-\mathbf{v}_i \times \mathbf{B}$) can provide a normal to magnetospheric boundaries, even in cases where a minimum variance analysis of the magnetic field fails to. This is the first such observation of this behaviour with the Hall term ($\mathbf{j} \times \mathbf{B}/en_e$) and shows that in certain cases, where a large cross tail current is present, it could be that a neutral sheet normal may be more confidently obtained from a variance analysis of the Hall term data than that returned from a variance analysis of the magnetic field data.

The evidence that the Hall term is directionally organised by the cross tail current supports the basic motivation of a force balance argument to explain the anti-correlation: With the Hall signature being organised into one direction, the $\nabla . \mathsf{P}_e$ term would only appear in the same component. Therefore, the current organising the Hall term contribution to the electric field also organises the $\nabla . \mathsf{P}_e$ term contribution to the electric field.

The reason for the directional organisation of the anti-correlation in the period discussed in chapter 4 would be the same, a significant cross tail current.

It would appear that as the temperature ratio increases from the inner central plasma sheet to the outer central plasma sheet, so does the ratio of the Hall term to the $\nabla . \mathsf{P}_e$ term. Indeed, the relative increase in the temperature ratios from the inner plasma sheet period to the outer plasma sheet period is approximately the same relative increase as the gradient of the Hall term to the $\nabla . \mathsf{P}_e$ term, again confirming that the gradient of the anti-correlation is related to the temperature ratio.

In the second case study, included to assess the generality of the above results, the contributions to the electric field from the Hall and $\nabla . \mathsf{P}_e$ terms were again

linearly anti-correlated. In this example anti-correlations could be seen in all components, consistent with the lack of cross-tail current at this time. The current sheet was highly tilted away from the GSM XY plane and a very high temperature ratio was observed. This period showed no signs of reconnection activity.

The gradients are approximately 2.6, this being a factor of ~ 7 times smaller than the temperature ratio. It would appear therefore that the correlations are general in the cases studied, but the link to the temperature ratio is not as simple as suggested in section 5.2.

Slavin et al. (1985) performed a statistical survey using ISEE 3 of the ion to electron temperature ratio, T_i/T_e, from 30 to 220 R_E downtail and found that the ratio varied between 4.8 and 7.8. Paterson and Frank (1994), in a survey from 10 to 210 R_E found the ratio to vary between 4.5 to 6.2. Schriver et al. (1998), in simulations, found that the ratio was between 4 to 6. Using the Geotail spacecraft during a long neutral sheet crossing, Kaufmann et al. (2001), found that T_i/T_e ranged between 5 and 10.

In the statistical study of the magnetotail from approximately X (GSM) = - 9 to - 18 R_E by Baumjohann et al. (1989), it was found that the ion and electron temperatures were highly correlated, with T_i/T_e being approximately constant over a large range of electron temperatures, $\lesssim 100$ eV to ~ 1 keV. The electron temperature of the crossings in this chapter were within this range. During the period discussed in this chapter, the Cluster spacecraft were located approximately X = - 16.6 and 15.9 R_E. The survey by Baumjohann et al. (1989) should provide results that are comparable to the results of the present chapter. In the outer plasma sheet Baumjohann et al. (1989) found that T_i/T_e = 7.2 (note that the quantity investigated in this chapter is $(T_i + T_e)/T_e$, so 1 should always be added to the results of Baumjohann et al. (1989) for comparison). Their correlation coefficient was 0.93, and more than 80% of their data points had temperature ratios between 5 and 10 (6 and 11 for comparison). In the inner plasma sheet the correlation was still clear (their correlation

coefficient 0.71) with their T_i/T_e = 7.8. Again, 80% of the their data fell inside the range of 5.5 to 11 (6.5 to 12). The authors noted that the difference in the ratios was interesting, but they suggest that this may be due to a sampling effect. They note that the ratios seemed not to have a dependence on AE index.

The temperature ratios reported in this chapter seem to be significantly larger than those reported in Baumjohann et al. (1989); Slavin et al. (1985); Paterson and Frank (1994) and Schriver et al. (1998). It is noted that even though 80% of the data reported in Baumjohann et al. (1989) fell within the limits specified above, the maximum value of the ratio is somewhat larger. It would be interesting to repeat the study of Baumjohann et al. (1989) with Cluster in order to investigate whether the ratios reported here are abnormally high for the plasma sheet observations during 2003, or whether the improved instrumentation and intercalibration of the Cluster instruments may modify the results of Baumjohann et al. (1989).

An increased temperature ratio is observed as Cluster moves from the inner to outer plasma sheet in the first crossing, opposite to the findings of Baumjohann et al. (1989). With this small sample of events, conclusions about the generality of this result cannot be made.

It may be that the basic concept of the simple treatment proposed in section 5.2 is valid as it has been observed that when the temperature ratio increases so does the gradient of the anti-correlation by approximately the same relative amount (periods B and C in section 5.4). However, the simple treatment significantly overestimates the gradient by the factors of ~ 2 and ~ 7. The assumptions made must be questioned in an attempt to further constrain the simple treatment.

It was assumed that the only forces acting in the plasma sheet were magnetic and plasma pressure divergence, and that the system was in equilibrium (i.e. no inflow or outflow from the system). While there is some inflow and outflow in the system it is not large (in sections 5.4 and 5.5 the flows are no larger than 200 kms^{-1}). Kaufmann et al. (1997) found in simulations that the $\nabla . \mathsf{P}_e$ force balanced

the $\mathbf{j} \times \mathbf{B}$ force to a good approximation in a quiet time model. Petrukovich et al. (1999) noted that pressure imbalances across the magnetotail could be compensated by the magnetic tension force. However, difficulties with measuring the $\mathbf{j} \times \mathbf{B}$ force with single spacecraft has meant, to the best of our knowledge, that no spacecraft studies of full force balance in the magnetotail have been published.

It is noted that the case studies presented here had very different magnetospheric conditions. On the 17$^{\text{th}}$August a large substorm took place whereas on the 25$^{\text{th}}$September there was no substorm activity. The implied length scale ratio is the same, however, during period B of section 5.4, during which no reconnection activity was observed, as in the period discussed in chapter 4 (both on the 17$^{\text{th}}$August), during which a large amount of reconnection activity was observed in the tail. The modifications that the substorm process makes to the system might violate the assumption of equilibrium.

It may be possible to test the assumption that the only forces acting in the plasma sheet were magnetic and plasma pressure divergence, and that the system was in equilibrium (i.e. no inflow or outflow from the system) by directly calculating Eqn. 5.2. This would require a four spacecraft measurement of the ion pressure tensor. As there is no CIS instrument functioning on Cluster 2, this is not currently possible. It is noted however that in certain situations this equation will be mainly acting in the neutral sheet normal direction (when there is a large cross tail current). It may be possible to carefully select a time period where two spacecraft are separated in GSM Z (the assumed normal) and estimate $\nabla . \mathsf{P}_i$ as $\partial P_{iZZ}/\partial Z$, assuming that there is no contribution from any other elements of the ion pressure tensor. Note that for the period discussed in chapter 4 $\nabla . \mathsf{P}_e \approx \partial P_{eZZ}/\partial Z$, however the CIS instrument aboard Cluster 4 is the only one of the four functional on this day.

It was assumed that the scales over which the gradients in ion and electron temperatures acted were equal. However, if these scales were different then Eqn. 5.6 could be modified significantly, being multiplied by some length scale multiplier,

i.e:

$$\frac{T_i}{T_e} + 1 \rightarrow \frac{T_i}{T_e}\frac{l_e}{l_i} + 1 \tag{5.9}$$

In the examples investigated in this chapter $l_e/l_i < 1$, suggesting that the length scale for the ions is larger than that of the electrons.

By taking the gradient of the anti-correlation ($(T_i/T_e) + 1$) as -4.5 (10.5), -5.1 (13.4), -5.4 (12.7), -2.6 (17.1) for periods B and C of section 5.4, the period discussed in chapter 4 and the period in section 5.5, the implied values of l_e/l_i are 0.37, 0.33, 0.38 and 0.1 respectively. These values may give information about the structure the plasma sheets in question. The appropriate scale lengths are the scales over which the ion and electron pressures change and may depend on the structure and state of the plasma sheet.

Significant deviations from simple Harris current sheet model have been observed previously, for example bifurcated current sheets (Nakamura et al., 2002; Runov et al., 2003; Thompson et al., 2006). In addition, thin embedded current sheets (McComas et al., 1986; Sergeev et al., 1993; Sanny et al., 1994, also Fig. 5.14 in this chapter) are often observed, with Asano et al. (2005) reporting that in a statistical survey of atypical current sheets that bifurcation is seen in 17% of cases, and that embedding is observed in most cases. Indeed, section 5.4 clearly shows that even in a 'quiet' plasma sheet the current can appear bifurcated (Fig. 5.14). In simulations, Schindler and Birn (2002) and Zelenyi et al. (2006) have reported that the thin embedded current sheets can be electron current sheets. Much theoretical work (e.g. Sitnov et al., 2006) is currently trying to understand these various different current sheet structures. These embedded current sheets may lead to a complex structure of the plasma sheet where different particle species have different scale lengths, as observed here.

It is worth noting that two different crossings were examined on the 17th August, one where the current sheet was clearly bifurcated (15:55 to 16:15 UT) and one

where, although the crossings were too fast to reconstruct the profile, the current sheet did not look bifurcated (Fig. 4.9). The ratio of temperatures did not change significantly from one current sheet configuration to the other, which may suggest that the length scale ratio does not depend on the structure of the plasma sheet.

A simple qualitative argument that may explain the differences in the scales over which the pressure changes can be made by considering the evolution of two field-aligned particle beams in the PSBL (for example, originating from a reconnection site), one of ions and one of electrons, each having the same initial kinetic energy.

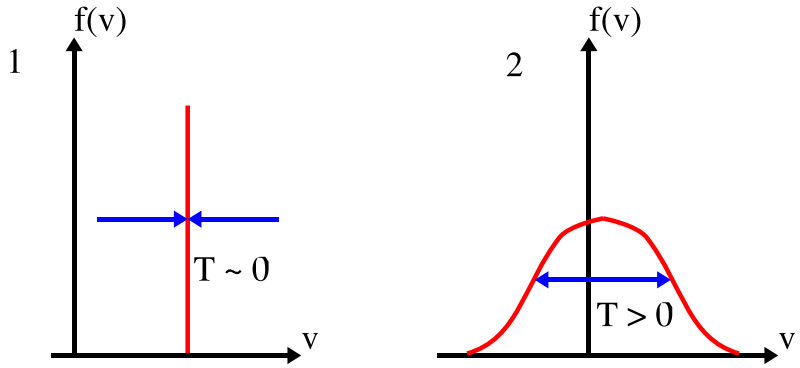

Figure 5.18: This plot shows a particle beam (1) as it thermalises (2) by (e.g.) scattering and wave particle interactions.

Figure 5.18 shows that if these distributions can initially be considered delta functions in velocity space, they have near-zero thermal energy (1). The particles in these populations slowly thermalise with the surrounding plasma via scattering and wave-particle interactions, moving to a lower bulk velocity but a higher thermal temperature state (2).

As the electrons move significantly faster than ions of similar kinetic energy, electrons will travel back and forth along the magnetic field lines many more times than the ions. Therefore, the integrated length of magnetic field line that the electrons sample will be much larger, and they will encounter many more scattering and interaction sites than the ions. Thus, the thermalisation of the electrons will occur on shorter timescales than the thermalisation of the ions.

The timescale over which the particle beams thermalise to the plasma sheet populations can be converted to a length scale normal to the neutral sheet, l, by observing that the magnetic field lines, onto which both particle populations are frozen, convect, over time, towards the centre of the plasma sheet in the reconnection scenario. As the electrons thermalise quicker, they will do this over a shorter normal length scale than the ions. Thus, the length scale over which the electron temperature changes, l_e, would be smaller than the length scale over which the ion temperature changes, l_i. For these particles, $l_e/l_i < 1$, as is observed in this thesis.

The reason why the factors are different on different days is unknown and remains a problem for theory and simulation to solve. The extension of this study to a survey of the plasma sheet would be needed to assess fully the generality of the results. This undertaking would be difficult due to the rarity of burst mode events in the 2003 Cluster tail season, as well as the effort required by the PEACE team to calibrate PEACE moments to the level where they can be used in this way. Future missions (such as MMS) may be able to overcome these issues.

5.7 Conclusions

The relationship between the Hall and $\nabla.\mathsf{P}_e$ terms in Ohm's law was investigated in further analysis of the data presented in chapter 4 as well as two separate case studies. These studies were from periods with different plasma sheet conditions, and enabled an investigation of the generality of the results.

Initially, the anti-correlation reported in chapter 4 and Henderson et al. (2006b) was investigated. It was shown that the anti-correlation was mainly in the direction normal to the neutral sheet, and this enabled a determination of the neutral sheet normal via a variance analysis of the Hall term (i.e. $\mathbf{j} \times \mathbf{B}/en_e$) data.

On the same day, during a crossing of a much thicker plasma sheet, the electric field contributions were found to be anti-correlated in all components. This anti-correlation became directionally organised during the crossing of the central

plasma sheet during which a directionally organised (i.e. cross-tail) current was also observed. The maximum variance direction of the Hall data, identified with the neutral sheet normal, was determined better than the minimum variance direction of the magnetic field data, also identified with the neutral sheet normal. This crossing enabled the profile of the current sheet against vertical distance to be reconstructed. It was found that the current sheet had a complex structure and was bifurcated.

In the final period discussed, the anti-correlations were again observed in all the components of the contributions to the electric field from the two terms. No clear cross-tail current was observed.

A simple magnetohydrostatic treatment was used to explain the correlation and directional organisation. While simple, the treatment was able to explain why the two terms may be anti-correlated, and how the gradient of the anti-correlation may be linked to the temperature ratio of the different plasma constituents as well as their spatial scales. In the examples reported here, the scale length over which the electron pressure changed l_e was smaller than the scale over which the ion pressure changed l_i, with l_e/l_i being between $\sim$0.1 and $\sim$0.4. A simple scenario was proposed to explain this effect, but further work may be needed to theoretically describe fully the relationship between these two terms.

From this small sample of plasma sheet observations, it would appear that the anti-corelation between these two terms is a general result and is linear, with the Hall term contributing more to the electric field than the $\nabla.\mathsf{P}_e$ term. The directional organisation (i.e. the electric field contributions being in one direction only) observed in chapter 4 and Henderson et al. (2006b) is not general, appearing when a large cross tail current is present. When the directional organisation is strong, a minimum variance analysis on the Hall term data can return a normal to the neutral sheet (the maximum variance direction) that is defined to a high degree of accuracy. The gradient of the anti-correlation is not general and takes on different values that may depend on the temperatures of the plasma constituents and scale lengths of the

ion and electron components of the plasma sheet.

Chapter 6

Summary, conclusions and future work

Several different objects and processes were investigated in this thesis with the use of both single and multi-spacecraft techniques. The smallest separation of the Cluster tetrahedron to data was chosen, 200 km, in order to investigate small-scale objects in the magnetotail plasma sheet.

One of the most exciting processes occurring in the magnetosphere is reconnection. The ion inertial scale, where ideal MHD breaks down for ions, is on the order of hundreds of km in the magnetotail near Cluster apogee. The fact that the Cluster separation is of this order in 2003 enables the investigation of processes directly relating to ion diffusion, such as Hall physics. In addition, flux ropes, perhaps created in reconnection, can, if observed early in their evolution, approach the length scale of thousands of km in the magnetotail near Cluster apogee. Having a Cluster separation significantly smaller than this enables the detailed reconstruction of the internal structure of these objects.

In chapter 3, also reported in Henderson et al. (2006a), two flux ropes observed in the 2003 tail season were investigated. Contrary to previous surveys at other magnetotail distances, few well-formed flux ropes were found in 2003. Neither flux rope was found to be in the classic 'force-free' configuration. Indeed, the flux ropes

were found to have more magnetic force (magnetic pressure and tension forces) in their outer sections than in the centre. The magnetic force was magnetic pressure dominated and generally acted away from the flux rope centres, i.e. acting to make the flux ropes radially expand. Large magnetic field strengths were observed in the centres of the flux ropes. By using PEACE and CIS moments it was found that the flux ropes, one moving Earthward and one moving tailward, were embedded in the ambient plasma flows, unstable, and under net expansive total forces.

A technique to determine the orientation of flux ropes was developed (and has now been formalised by Zhou et al., 2006) which utilised the ability of Cluster to derive the velocity of an assumed planar surface through the tetrahedron. This was an important advance, as it enabled this determination without the use of the popular minimum variance technique, which often provides unsatisfactory orientations.

These flux ropes have been interpreted as evidence for multiple X-line reconnection in the near-tail close to Cluster apogee (X $\sim$ -20 R_E). A scenario was envisaged where the centres of newly formed flux ropes may have had more time to relax towards the force-free state observed further down the tail, consistent with observations of smaller magnetic forces in the centres of the flux ropes. The outer sections of the flux rope would therefore be more composed of recently reconnected non-force-free flux.

In chapter 4 the contributions to the electric field from certain terms in Ohm's law were calculated. The contribution to the electric field from the divergence of the full electron pressure tensor was calculated using the moments from the PEACE detector and multi-spacecraft techniques, whereas the contribution to the electric field from the Hall term was calculated using magnetic field data and the same multi-spacecraft methods.

One day, the 17thAugust 2003, was investigated during which Cluster observed a large substorm and the passage of a large reconnection X-line in the magnetotail. During one case study, also reported in Henderson et al. (2006b), Hall sig-

natures of reconnection (Hall quadrupolar magnetic fields, field-aligned electron current systems and Hall electric fields) were observed. The currents perpendicular to the magnetic field in the ion diffusion region were closed by field-aligned electron flows, observed with the PEACE instrument. It was concluded therefore that the observations were made on magnetic field lines that mapped close to the ion diffusion region.

It was noted that the contribution to the electric field from the divergence of the electron pressure tensor ($\nabla . \mathsf{P}_e$) was anti-correlated with the contribution of the Hall term in Ohm's law. The contribution from the $\nabla . \mathsf{P}_e$ pointed away from the neutral sheet on both sides of it whereas the contribution from the Hall term pointed towards it from both sides. The calculation of the $\nabla . \mathsf{P}_e$ term reported in Henderson et al. (2006b) was the first such calculation.

In the second case study, observed soon after the passage of the X-line, a large parallel electric field was observed originating from the $\nabla . \mathsf{P}_e$ term, as well as Hall signatures of reconnection similar to those seen in the first case study. This period was very close to the reconnection site and the magnetotail was very dynamic.

In the final chapter, chapter 5, the anti-correlation between the $\nabla . \mathsf{P}_e$ and Hall terms was investigated with two further case studies.

These investigations showed that the anti-correlation appeared to be a general result throughout the plasma sheet: The two contributions to the electric field became mainly directed towards (Hall) and away from ($\nabla . \mathsf{P}_e$) the neutral sheet when a large cross-tail current was present, however, in the absence of this directionally organised current the anti-correlation appeared in all directions.

The simple theoretical background to the gradient of the anti-correlation was investigated and it was revealed that the gradient is related to the ratio of the temperatures of the plasma constituents, T_i/T_e and the ratio of the scale lengths of the electron and ion components of the plasma sheet l_e/l_i. Using a simple magnetohydrostatic treatment, it was inferred from the results of the case studies in this chapter

that the scale over which the electron pressure changed was smaller than the scale over which the ion pressure changed.

6.1 Further work

In chapter 3 it was suggested that the two flux ropes observed were under net total expansive forces, i.e. from the gradients of the magnetic field and plasma pressure. However, due to the time resolution of the plasma detectors, relatively little plasma data was collected inside the flux rope, limiting the comparisons possible with the high time resolution magnetic field data. The analysis of larger or slower moving flux ropes would give a more accurate determination of the net forces acting inside the flux rope.

In addition, a full survey of flux ropes in the Cluster data would be able to generalise the findings of this chapter. Are all flux ropes observed between -15 to -20 R_E non-force-free, indeed under expansive forces? The sizes of the flux ropes reported in chapter 3 appeared to be smaller than the 'average flux rope'found in surveys covering the same magnetospheric region (note that only an estimate of the minimum size of the flux ropes was give in chapter 3). Many flux rope models exist that do not require the structure to be force-free. These models could be used to estimate some of the observed features of the flux ropes reported in this thesis, such as their orientation and size.

If the Cluster spacecraft passed over the electron diffusion region, it may be possible to observe the spatial derivatives of the off-diagonal components of the electron pressure supporting the reconnection electric field. Theory and simulations often suggest that this is the case, but confirmation of this effect would come from observations. In the 2003 tail season, the separation of the Cluster tetrahedron was 200 km, against an electron inertial length of $\sim$ 5 km. This separation is probably too large to observe the reconnection electric field being supported by the $\nabla . \mathsf{P}_e$ term. In June 2007 however, Cluster 3 and 4 entered a new phase where their

separation is as low as 40 km in the magnetotail. Depending on the orientation of the reconnection region, it might be possible to observe this important process.

In this thesis the effects of anomalous resistivity or electron inertia have not been assessed. An observational comparison of the relative contributions to Ohm's law from all the terms in Ohm's law would be a significant addition to the literature.

The final chapter in this thesis details the investigation of three periods of data in which anti-correlations are observed between the $\nabla . \mathsf{P}_e$ and Hall terms in Ohm's law. Indeed, the gradient of the anti-correlation gives information about the length scales over which electron and ion pressure changes. It would be useful to be able to add more events to this database and learn more about these length scales and the physics associated with the $\nabla . \mathsf{P}_e$ term (indeed, the $\nabla . \mathsf{P}_e$ term has only been investigated in small periods on two days of the 2003 tail season), however this is currently prohibited by the complexity of inter-calibration between the PEACE detectors.

It was noted in the final chapter that the ratio of ion to electron temperature was significantly higher than had been observed in previous studies. A survey of this ratio throughout the plasma sheet using the Cluster spacecraft would show if the ratios reported here are abnormally high, or that the typical ratio in the plasma sheet, when measured using improved instrumentation, was generally higher than that previously reported.

An assumption made in the simple magnetostatic treatment in the final chapter was that the magnetotail was in force balance, with the forces arising from gradients in the plasma being balanced by the magnetic forces. To this date, due to the difficulty in measuring the magnetic tenson force (a multi-spacecraft mission, such as Cluster, is needed), a survey of the total balance of forces in the magnetotail has not been made.

Bibliography

Akasofu, S. I.: The development of the auroral substorm, Planet. Space. Sci, 12, 273–282, 1964.

Akasofu, S. I.: Polar and Magnetospheric Substorms, D. Reidel Publishing Co., Dordrecht, Holland; Springer-Verlag New York Inc., New York, 1968.

Alexeev, I. V., Owen, C. J., Fazakerley, A. N., Runov, A., Dewhurst, J. P., Balogh, A., Reme, H., Klecker, B., and Kistler, L.: Cluster observations of currents in the plasma sheet during reconnection, Geophys. Res. Lett., 32, L03 101, 2005.

Alfvén, H.: Existence of electromagnetic-hydrodynamic waves, Nature, 150, 405, 1942.

André, M., Vaivads, A., Buchert, S. C., Fazakerley, A. N., and Lahiff, A.: Thin electron-scale layers at the magnetopause, Geophys. Res. Lett., 31, L03 803, 2004.

Angelopoulos, V., Baumjohann, W., Kennel, C. F., Coronti, F. V., Kivelson, M. G., Pellat, R., Walker, R. J., Luehr, H., and Paschmann, G.: Bursty bulk flows in the inner central plasma sheet, J. Geophys. Res., 97, 4027–4039, 1992.

Angelopoulos, V., Kennel, C. F., Coroniti, F. V., Pellat, R., Kivelson, M. G., Walker, R. J., Russell, C. T., Baumjohann, W., Feldman, W. C., and Gosling, J. T.: Statistical characteristics of bursty bulk flow events, J. Geophys. Res., 99, 21 257–21 280, 1994.

Asano, Y., Mukai, T., Hoshino, M., Saito, Y., Hayakawa, H., and Nagai, T.: Current sheet structure around the near-earth neutral line observed by Geotail, J. Geophys. Res., 109, A02 212, 2004.

Asano, Y., Nakamura, R., Baumjohann, W., Runov, A., Vörös, Z., Volwerk, M., Zhang, T. L., Balogh, A., Klecker, B., and Rème, H.: How typical are atypical current sheets?, Geophys. Res. Lett., 32, 3108, 2005.

Aschwanden, M.: Physics of the Solar Corona, Praxis Publishing Ltd, Chichester, UK, 2005.

Aubry, M. P., Russell, C. T., and Kivelson, M. G.: Inward motion of the magnetopause before a substorm., J. Geophys. Res., 75, 7018–7031, 1970.

Baker, D. N., Pulkkinen, T. I., Angelopoulos, V., Baumjohann, W., and McPherron, R. L.: Neutral line model of substorms: Past results and present view, J. Geophys. Res., 101, 12 975–13 010, 1996.

Balogh, A., Carr, C. M., Acuna, M. H., Dunlop, M. W., Beek, T. J., Brown, P., Fornaçon, K.-H., Georgescu, E., Glassmeier, K.-H., Harris, J., Musmann, G., Oddy, T., and Schwingenschuh, K.: The Cluster Magnetic Field Investigation: overview of in-flight performance and initial results, Ann. Geophys., 19, 1207–1217, 2001.

Bame, S. J., Asbridge, J. R., Felthauser, H. E., Hones, E. W., and Strong, I. B.: Characteristics of the Plasma Sheet in the Earth's Magnetotail, J. Geophys. Res., 72, 113, 1967.

Baumjohann, W. and Treumann, R. A.: Basic space plasma physics, Imperial Collage Press, London, 1996.

Baumjohann, W., Paschmann, G., and Cattell, C. A.: Average plasma properties in the central plasma sheet, J. Geophys. Res., 94, 6597–6606, 1989.

Baumjohann, W., Paschmann, G., and Luehr, H.: Characteristics of high-speed ion flows in the plasma sheet, J. Geophys. Res., 95, 3801–3809, 1990a.

Baumjohann, W., Paschmann, G., and Luehr, H.: Pressure balance between lobe and plasma sheet, Geophys. Res. Lett., 17, 45–48, 1990b.

Birkeland, K.: The Norwegian Aurora Polaris Expedition, 1902-03. Vol. I.: On the Cause of Magnetic Storms and the Origin of Terrestrial Magnetism, Christiania, 1908.

Birn, J., Drake, J. F., Shay, M. A., Rogers, B. N., Denton, R. E., Hesse, M., Kuznetsova, M., Ma, Z. W., Bhattacharjee, A., Otto, A., and Pritchett, P. L.: Geospace Environmental Modelling (GEM) Magnetic reconnection challenge, J. Geophys. Res., 106, 3715, 2001.

Borg, A. L., Oieroset, M., Phan, T., Mozer, F., Pedersen, A., Mouikis, C., McFadden, J., Twitty, C., Balogh, A., , and Reme, H.: Cluster encounter of a magnetic reconnection diffusion region in the near-Earth magnetotail on September 19, 2003, Geophys. Res. Lett., 32, L19 105, 2005.

Cao, F. and Lee, L. C.: Plasma pressure and anisotropy inferred from the Tsyganenkomagnetic field model, Ann. Geophys., 12, 286–295, 1994.

Chapman, S. and Ferraro, V. C. A.: A new theory of magnetic storms, Part 1, The initial phase, Terrest. Magnetism and Atmospheric Elec., 36, 171–186, 1931.

Chisham, G. and Freeman, M. P.: A technique for accurately determining the cusp-region polar cap boundary using SuperDARN HF radar measurements, AG, 21, 983–996, 2003.

Cowley, S. W. H.: Plasma populations in a simple open model magnetosphere, Space Sci. Rev., 26, 21, 1980.

Cowley, S. W. H. and Lockwood, M.: Excitation and decay of solar wind-driven flows in the magnetosphere-ionosphere system, Ann. Geophys., 10, 103–115, 1992.

Deng, X. H., Matsumoto, H., Kojima, H., Mukai, T., Anderson, R., Baumjohann, W., and Nakamura, R.: Geotail encounter with reconnection diffusion region in the Earth's magnetotail: Evidence of multiple X lines collisionless reconnection?, J. Geophys. Res., 109, A05 206, 2004.

Dewhurst, J., Owen, C., Fazakerley, A., and Balogh, A.: Thinning and expansion of the substorm plasma sheet: Cluster PEACE timing analysis, Ann. Geophys., 22, 4165–4184, 2004.

Dungey, J. W.: Interplanetary Magnetic Field and the Auroral Zones, Phys. Rev. Lett., 6, 47–48, 1961.

Dunlop, M. W., Balogh, A., Glassmeier, K.-H., and Robert, P.: Four-point Cluster application of magnetic field analysis tools: The Curlometer, J. Geophys. Res., 107, 1384–1397, 2002.

Eastman, T. E., Frank, L. A., Peterson, W. K., and Lennartsson, W.: The plasma sheet boundary layer, J. Geophys. Res., 89, 1553–1572, 1984.

Eastman, T. E., Frank, L. A., and Huang, C. Y.: The boundary layers as the primary transport regions of the earth's magnetotail, J. Geophys. Res., 90, 9541–9560, 1985.

Eastwood, J. P., Balogh, A., Dunlop, M. W., and Smith, C. W.: Cluster observations of the heliospheric current sheet and an associated magnetic flux rope and comparisons with ACE, J. Geophys. Res., 107, 1365–1373, 2002.

Eastwood, J. P., Sibeck, D. G., Slavin, J. A., Goldstein, M. L., Lavraud, B., Sitnov, M., Imber, S., Balogh, A., Lucek, E. A., and Dandouras, I.: Observations of

multiple X-line structure in the Earth's magnetotail current sheet: A Cluster case study, Geophys. Res. Lett., 32, L11 105, 2005.

Elphic, R. C., Cattell, C. A., Takahashi, K., Bame, S. J., and Russell, C. T.: ISEE-1 and 2 observations of magnetic flux ropes in the magnetotail: FTEs in the plasma sheet?, Geophys. Res. Lett., 13, 648–651, 1986.

Escoubet, C. P., Fehringer, M., , and Goldstein, M.: The Cluster mission, Ann. Geophys., 19, 1197 – 1200, 2001.

Fairfield, D. H. and Ness, N. F.: Configuration of the geomagnetic tail during substorms., J. Geophys. Res., 75, 7032–7047, 1970.

Frank, L. A.: On the Extraterrestrial Ring Current during Geomagnetic Storms, J. Geophys. Res., 72, 3753, 1967.

Gowen, R. A. and Birdseye, M. A.: Extracting Bulk Parameters of a Particle Distribution, Tech. rep., Mullard Space Science Laboratory, 1988.

Hapgood, M. A.: Space physics coordinate transformations - A user guide, PSS, 40, 711–717, 1992.

Harris, E. G.: On a plasma sheet separating regions of oppositely directed magnetic field, Nuovo Cim., 23, 1962.

Harvey, C. C.: Spatial Gradients and the Volumetric Tensor, in Paschmann and Daly (1998), pp. 303–322, 1998.

Henderson, P. D., Owen, C. J., Alexeev, I. V., Slavin, J., Fazakerley, A. N., Lucek, E., and Reme, H.: Cluster observations of flux rope structures in the near tail, Ann. Geophys., 24, 651–666, 2006a.

Henderson, P. D., Owen, C. J., Lahiff, A. D., Alexeev, I. V., Fazakerley, A. N., Lucek, E., and Reme, H.: Cluster PEACE observations of electron pressure tensor divergence in the magnetotail, Geophys. Res. Lett., 33, L22 106, 2006b.

Hesse, M., Schindler, K., Birn, J., and Kuznetsova, M.: The diffusion region in collisionless magnetic reconnection, Phys. Plasmas, 6, 1781–1795, 1999.

Hesse, M., Birn, J., and Kuznetsova, M.: Collisionless magnetic reconnection: Electron processes and transport modelling, J. Geophys. Res., 106, 3721–3736, 2001.

Hones, Jr., E. W., Asbridge, J. R., Bame, S. J., and Strong, I. B.: Outward Flow of Plasma in the Magnetotail Following Geomagnetic Bays, J. Geophys. Res., 72, 5879, 1967.

Hones, Jr., E. W., Pytte, T., and West, Jr., H. I.: Associations of geomagnetic activity with plasma sheet thinning and expansion - A statistical study, J. Geophys. Res., 89, 5471–5478, 1984.

Hughes, W. J. and Sibeck, D. G.: On the 3-dimensional structure of plasmoids, Geophys. Res. Lett., 14, 636–639, 1987.

Johnstone, A. D., Alsop, C., Burdge, S., Carter, P. J., Coates, A. J., Coker, A. J., Fazakerley, A. N., Grande, M., Gowen, R. A., Gurgiolo, C., Hancock, B. K., Narheim, B., Preece, A., Sheather, P. H., Winningham, J. D., and Woodcliffe, R. D.: PEACE, A Plasma Electron and Current Experiment, Space Sci. Rev, 79, 351–398, 1997.

Kaufmann, R. L., Larson, D. J., Kontodinas, I. D., and Ball, B. M.: Force balance and substorm effects in the magnetotail, J. Geophys. Res., 102, 22 141–22 154, 1997.

Kaufmann, R. L., Ball, B. M., Paterson, W. R., and Frank, L. A.: Plasma sheet thickness and electric currents, J. Geophys. Res., 106, 6179–6194, 2001.

Kivelson, M. G. and Russell, C. T., eds.: Introduction to Space Physics, Cambridge University Press, Cambridge, 1995.

Kuznetsova, M., Hesse, M., , and Winske, D.: Collisionless reconnection supported by nongyrotropic pressure effects in hybrid and particle simulations, J. Geophys. Res., 106, 3799–3810, 2001.

Labelle, J. and Treumann, R. A.: Plasma waves at the dayside magnetopause, SSR, pp. 175–202, 1988.

Lee, L. C.: A Review of Magnetic Reconnection: MHD Models, p. 139, Physics of the Magnetopause, 1995.

Lepping, R. P., Jones, J. A., and Burlaga, L. F.: Magnetic Field Structure of Interplanetary Magnetic Clouds at 1 AU, J. Geophys. Res., 95, 11 957–11 965, 1990.

Lighthill, M. J.: Studies on Magnetohydrodynamic Waves and Other Anisotropic Wave Motions, Royal Society of London Philosophical Transactions Series A, 252, 397–430, 1960.

Liu, Z. X., Escoubet, C. P., Pu, Z., Laakso, H., Shi, J. K., Shen, C., and Hapgood, M.: The Double Star mission, Ann. Geophys., 23, 2707–2712, 2005.

Lui, A. T. Y.: Current disruption in the Earth's magnetosphere: Observations and models, J. Geophys. Res., 101, 13 067–13 088, 1996.

Lui, A. T. Y., Dunlop, M. W., Rème, H., Kistler, L. M., Gustafsson, G., and Zong, Q.-G.: Internal structure of a magnetic flux rope from Cluster observations, GRL, 34, 7102, 2007.

Lyons, L. R. and Pridmore-Brown, D. C.: Force balance near an X line in a collisionless plasma, J. Geophys. Res., 95, 20 903–20 909, 1990.

Lyons, L. R. and Pridmore-Brown, D. C.: Force balance near an X line along which E x J is less than 0, J. Geophys. Res., 97, 2955–2960, 1992.

Manapat, M., ieroset, M., Phan, T. D., Lin, R. P., , and Fujimoto, M.: Field-aligned electrons at the lobe/plasma sheet boundary in the mid-to-distant magnetotail and their association with reconnection, Geophys. Res. Lett., 33, L05 101, 2006.

McComas, D. J., Bame, S. J., Russell, C. T., and Elphic, R. C.: The near-earth cross-tail current sheet - Detailed ISEE 1 and 2 case studies, J. Geophys. Res., 91, 4287–4301, 1986.

McComas, D. J., Barraclough, B. L., Gosling, J. T., Hammond, C. M., Phillips, J. L., Neugebauer, M., Balogh, A., and Forsyth, R. J.: Structures in the polar solar wind: Plasma and field observations from Ulysses, J. Geophys. Res., 100, 19 893–19 902, 1995.

McPherron, R. L.: Growth phase of magnetospheric substorms, J. Geophys. Res., 75, 5592–5599, 1970.

McPherron, R. L., Aubry, M. P., Russell, C. T., and Coleman, Jr., P. J.: Satellite studies of magnetospheric substorms on August 15, 1968. 4. Ogo 5 magnetic field observations., J. Geophys. Res., 78, 3068–3078, 1973a.

McPherron, R. L., Russell, C. T., and Aubry, M. P.: Satellite studies of magnetospheric substorms on August 15, 1968. 9. Phenomenological model for substorms, J. Geophys. Res., 78, 3131–3149, 1973b.

Moldwin, M. B. and Hughes, W. J.: Plasmoids as Magnetic Flux Ropes, J. Geophys. Res., 96, 14 051–14 064, 1991.

Moldwin, M. B. and Hughes, W. J.: Observations of Earthward and tailward propagating flux rope plasmoids: Expanding the plasmoid model of geomagnetic substorms, J. Geophys. Res., 99, 183–198, 1994.

Mozer, F. S.: Criteria for and statistics of electron diffusion regions associated with subsolar magnetic field reconnection, J. Geophys. Res., 110, 12 222, 2005.

Mozer, F. S., Bale, S. D., and Phan, T. D.: Evidence of Diffusion Regions at a Subsolar Magnetopause Crossing, Phys. Rev. Lett., 89, 015 002, 2002.

Mozer, F. S., Bale, S. D., Phan, T. D., and Osborne, J. A.: Observations of Electron Diffusion Regions at the Subsolar Magnetopause, Phys. Rev. Lett., 91, 245 002, 2003.

Nagai, T., Nakamura, R., Mukai, T., Yamamoto, T., Nishida, A., and Kokubun, S.: Substorms, tail flows and plasmoids, Advances in Space Research, 20, 961–971, 1997.

Nagai, T., Shinohara, I., Fujimoto, M., Hoshino, M., Saito, Y., Machida, S., and Mukai, T.: Geotail observations of the Hall current system: Evidence of magnetic reconnection in the magnetotail, J. Geophys. Res., 106, 25 929–25 950, 2001.

Nakamura, R., Baumjohann, W., Runov, A., Volwerk, M., Zhang, T. L., Klecker, B., Bogdanova, Y., Roux, A., Balogh, A., Rème, H., Sauvaud, J. A., and Frey, H. U.: Fast flow during current sheet thinning, Geophys. Res. Lett., 29, 55–1, 2002.

Ness, N. F.: The Earth's Magnetic Tail, J. Geophys. Res., 70, 2989, 1965.

Ness, N. F.: The geomagnetic tail., Reviews of Geophysics, 7, 97–127, 1969.

Owen, C. J., Slavin, J. A., Fazakerley, A. N., Dunlop, M. W., and Balogh, A.: Cluster electron observations of the separatrix layer during traveling compression regions, Geophys. Res. Lett., 32, L03 104, 2005.

Parker, E. N.: Sweet's Mechanism for Merging Magnetic Fields in Conducting Fluids, J. Geophys. Res., 62, 509–520, 1957.

Parker, E. N.: Dynamics of the Interplanetary Gas and Magnetic Fields., APJ, 128, 664, 1958.

Parker, E. N.: The Solar-Flare Phenomenon and the Theory of Reconnection and Annihiliation of Magnetic Fields., Astrophys J. Suppl., 8, 177, 1963.

Parks, G., Chen, L. J., McCarthy, M., Larson, D., Lin, R. P., Phan, T., Reme, H., and Sanderson, T.: New observations of ion beams in the plasma sheet boundary layer, Geophys. Res. Lett., 25, 3285–3288, 1998.

Paschmann, G. and Daly, P.: Eds. Analysis Methods for Multi-Spacecraft Data, ISSI Science Report, SR-001, 1998.

Paschmann, G., Baumjohann, W., Sckopke, N., Papamastorakis, I., and Carlson, C. W.: The magnetopause for large magnetic shear - AMPTE/IRM observations, J. Geophys. Res., 91, 11 099–11 115, 1986.

Paschmann, G., Fazakerley, A. N., and Schwartz, S. J.: Moments of plasma velocity distributions, in Paschmann and Daly (1998), pp. 125 – 158, 1998.

Paterson, W. R. and Frank, L. A.: Survey of plasma parameters in Earth's distant magnetotail with the Geotail spacecraft, Geophys. Res. Lett., 21, 2971–2974, 1994.

Pedersen, A.: Solar wind and magnetosphere plasma diagnostics by spacecraft electrostatic potential measurements, Ann. Geophys., 13, 118–129, 1995.

Petkaki, P., Watt, C. E. J., Horne, R. B., and Freeman, M. P.: Anomalous resistivity in non-Maxwellian plasmas, J. Geophys. Res., 108, 14–1, 2003.

Petkaki, P., Freeman, M. P., Kirk, T., Watt, C. E. J., and Horne, R. B.: Anomalous resistivity and the nonlinear evolution of the ion-acoustic instability, J. Geophys. Res., 111, 1205, 2006.

Petrukovich, A. A., Mukai, T., Kokubun, S., Romanov, S. A., Saito, Y., Yamamoto, T., and Zelenyi, L. M.: Substorm-associated pressure variations in the magnetotail plasma sheet and lobe, J. Geophys. Res., 104, 4501–4514, 1999.

Petschek, H. E.: Magnetic Field Annihilation, in The Physics of Solar Flares, edited by W. N. Hess, p. 425, 1964.

Pritchett, P. L.: Geospace Environment Modelling magnetic reconnection challenge: Simulations with a full particle electromagnetic code, J. Geophys. Res., 106, 3783–3798, 2001.

Reme, H., Aoustin, C., Bosqued, J. M., Dandouras, I., Lavraud, B., Sauvaud, J. A., Barthe, A., Bouyssou, J., Camus, T., Coeur-Joly, O., Cros, A., Cuvilo, J., Ducay, F., Garbarowitz, Y., Medale, J. L., Penou, E., Perrier, H., Romefort, D., Rouzaud, J., Vallat, C., Alcayd, D., Jacquey, C., Mazelle, C., d'Uston, C., Mobius, E., Kistler, L. M., Crocker, K., Granoff, M., Mouikis, C., Popecki, M., Vosbury, M., Klecker, B., Hovestadt, D., Kucharek, H., Kuenneth, E., Paschmann, G., Scholer, M., Sckopke, N., Seidenschwang, E., Carlson, C. W., Curtis, D. W., Ingraham, C., Lin, R. P., McFadden, J. P., Parks, G. K., Phan, T., Formisano, V., Amata, E., Bavassano-Cattaneo, M. B., Baldetti, P., Bruno, R., Chionchio, G., Lellis, A. D., Marcucci, M. F., Pallocchia, G., Korth, A., Daly, P. W., Graeve, B., Rosenbauer, H., Vasyliunas, V., McCarthy, M., Wilber, M., Eliasson, L., Lundin, R., Olsen, S., Shelley, E. G., Fuselier, S., Ghielmetti, A. G., Lennartsson, W., Escoubet, C. P., Balsiger, H., Friedel, R., Cao, J.-B., Kovrazhkin, R. A., Papamastorakis, I., Pellat, R., Scudder, J., and et al, B. S.: First multispacecraft ion measurements in and near the Earth's magnetosphere with the identical Cluster ion spectrometry (CIS) experiment, Ann. Geophys., 19, 1303–1354, 2001.

Riley, P., Linker, J. A., Lionello, R., Mikic, Z., Odstrcil, D., Hidalgo, M. A., Cid, C., Hu, Q., Lepping, R. P., Lynch, B. J., and Rees, A.: Fitting flux ropes to a global MHD solution: a comparison of techniques, Journal of Atmospheric and Solar-Terrestrial Physics, 66, 1321–1331, 2004.

Robert, P., Dunlop, M. W., Roux, A., and Chanteur, G.: Accuracy of Current Density Determination, in Paschmann and Daly (1998), pp. 395–418, 1998.

Runov, A., Nakamura, R., Baumjohann, W., Treumann, R. A., Zhang, T. L., Volwerk, M., Voros, Z., Balogh, A., Glasmeier, K.-H., Klecker, B., Reme, H., and Kistler, L.: Current sheet structure near magnetic X-line observed by Cluster, Geophys. Res. Lett., 30, 1579–1582, 2003.

Runov, A., Nakamura, R., Baumjohann, W., Zhang, T. L., Volwerk, M., Eichelberger, H.-U., and Balogh, A.: Cluster observation of a bifurcated current sheet, Geophys. Res. Lett., 30, 8–1, 2003.

Runov, A., Sergeev, V. A., Baumjohann, W., Nakamura, R., Apatenkov, S., Asano, Y., Volwerk, M., Vörös, Z., Zhang, T. L., Petrukovich, A., Balogh, A., Sauvaud, J.-A., Klecker, B., and Rème, H.: Electric current and magnetic field geometry in flapping magnetotail current sheets, Ann. Geophys., 23, 1391–1403, 2005a.

Runov, A., Sergeev, V. A., Nakamura, R., Baumjohann, W., Zhang, T. L., Asano, Y., Volwerk, M., Vörös, Z., Balogh, A., and Rème, H.: Reconstruction of the magnetotail current sheet structure using multi-point Cluster measurements, Plan. Space, Sci., 53, 237–243, 2005b.

Russell, C. T.: The Configuration of the Magnetosphere, in Critical Problems of Magnetospheric Physics, edited by E. R. Dyer, 1972.

Sanny, J., McPherron, R. L., Russell, C. T., Baker, D. N., Pulkkinen, T. I., and Nishida, A.: Growth-phase thinning of the near-Earth current sheet during the CDAW 6 substorm, J. Geophys. Res., 99, 5805–5816, 1994.

Schindler, K.: A Theory of the Substorm Mechanism, J. Geophys. Res., 79, 2803–2810, 1974.

Schindler, K. and Birn, J.: Models of two-dimensional embedded thin current sheets from Vlasov theory, Journal of Geophysical Research (Space Physics), 107, 20–1, 2002.

Schmitz, H. and Grauer, R.: Kinetic Vlasov simulations of collisionless magnetic reconnection, Phys. Plasmas, 13, 2309, 2006.

Schödel, R., Baumjohann, W., Nakamura, R., Sergeev, V. A., and Mukai, T.: Rapid flux transport in the central plasma sheet, J. Geophys. Res., 106, 301–314, 2001.

Schriver, D., Ashour-Abdalla, M., and Richard, R. L.: On the origin of the ion-electron temperature difference in the plasma sheet, J. Geophys. Res., 103, 14 879–14 896, 1998.

Scudder, J. D., Mozer, F. S., Maynard, N. C., and Russell, C. T.: Fingerprints of collisionless reconnection at the separator, I, Ambipolar-Hall signatures, J. Geophys. Res., 107, 1294, 2002.

Sergeev, V., Runov, A., Baumjohann, W., Nakamura, R., Zhang, T. L., Volwerk, M., Balogh, A., Rème, H., Sauvaud, J. A., André, M., and Klecker, B.: Current sheet flapping motion and structure observed by Cluster, Geophys. Res. Lett., 30, 60, 2003.

Sergeev, V. A., Mitchell, D. G., Russell, C. T., and Williams, D. J.: Structure of the tail plasma/current sheet at 11 Re and its changes in the course of a substorm, J. Geophys. Res., 98, 17 345–17 366, 1993.

Sergeev, V. A., Sormakov, D. A., Apatenkov, S. V., Baumjohan, W., Nakamura, R., Runov, A. V., Mukai, T., and Nagai, T.: Survey of large-amplitude flapping motions in the midtail current sheet, Ann. Geophys., 24, 2015–2024, 2006.

Shelley, E. G., Johnson, R. G., , and Sharp, R. D.: Satellite Observations of Energetic Heavy Ions During a Geomagnetic Storm, J. Geophys. Res., 177, 6104–6110, 1972.

Sitnov, M. I., Swisdak, M., Guzdar, P. N., and Runov, A.: Structure and dynamics of a new class of thin current sheets, J. Geophys. Res., 111, 8204, 2006.

Slavin, J. A., Smith, E. J., Sibeck, D. G., Baker, D. N., and Zwickl, R. D.: An ISEE 3 study of average and substorm conditions in the distant magnetotail, J. Geophys. Res., 90, 10 875, 1985.

Slavin, J. A., Smith, M. F., Mazur, E. L., Baker, D. N., Iyemori, T., Singer, H. J., and Greenstadt, E. W.: ISEE 3 plasmoid and TCR observations during an extended interval of substorm activity, Geophys. Res. Lett., 19, 825–828, 1992.

Slavin, J. A., Owen, C. J., Kuznetsova, M. M., and Hesse, M.: ISEE 3 observations of plasmoids with flux rope magnetic topologies, Geophys. Res. Lett., 22, 2061–2064, 1995.

Slavin, J. A., Fairfield, D. H., Lepping, R. P., Hesse, M., Ieda, A., Tanskanen, E., Østgaard, N., Mukai, T., Nagai, T., Singer, H. J., and Sutcliffe, P. R.: Simultaneous observations of earthward flow bursts and plasmoid ejection during magnetospheric substorms, J. Geophys. Res., 107, 13–1, 2002.

Slavin, J. A., Lepping, R. P., Gjerloev, J., Fairfield, D. H., Hesse, M., Owen, C. J., Moldwin, M. B., Nagai, T., Ieda, A., and Mukai, T.: Geotail observations of magnetic flux ropes in the plasma sheet, J. Geophys. Res., 108, 1015–1032, 2003a.

Slavin, J. A., Lepping, R. P., Gjerloev, J., Goldstein, M. L., Fairfield, D. H., Acuna, M. H., Balogh, A., Dunlop, M., Kivelson, M. G., Khurana, K., Fazakerley, A., Owen, C. J., Reme, H., and Bosqued, J. M.: Cluster electric current density measurements within a magnetic flux rope in the plasma sheet, Geophys. Res. Lett., 30, 1362–1365, 2003b.

Slavin, J. A., Owen, C. J., Dunlop, M. W., Boralv, E., Moldwin, M. B., Sibeck, D. G., Transkanen, E., Goldstein, M. L., Fazakerley, A., Balogh, A., Lucek, E., Richter, I., Reme, H., and Bosqued, J. M.: Cluster four spacecraft measurements of small traveling compression regions in the near-tail, Geophys. Res. Lett., 30, 2208–2211, 2003c.

Slavin, J. A., Transkanen, E. I., Hesse, M., Owen, C. J., Dunlop, M. W., Imber, S., Lucek, E. A., Balogh, A., and Glassmier, K.-H.: Cluster observations of traveling compression regions in the near-tail, J. Geophys. Res., 110, A06 207, 2005.

Sonnerup, B. and Scheible, M.: Minimum and Maximum Variance Analysis, in Paschmann and Daly (1998), pp. 185 – 220, 1998.

Sonnerup, B. U. O. and Cahill, L. J.: Magnetopause structure and attitude from Explorer 12 observations, J. Geophys. Res., 72, 171–183, 1967.

Sonnerup, B. U. O., Papamastorakis, I., Paschmann, G., and Luehr, H.: The magnetopause for large magnetic shear: Analysis of convection electric fields from AMPTE/IRM, J. Geophys. Res., 95, 10 541–10 557, 1990.

Sonnerup, U. O.: Magnetic field reconnection, Solar system plasma physics. Volume 3, A79-53667 24-46 Amsterdam, North-Holland Publishing Co., 45–108, 1979.

Szita, S., Fazakerley, A. N., Carter, P. J., James, A. M., Trávnícek, P., Watson, G., André, M., Eriksson, A., and Torkar, K.: Cluster PEACE observations of electrons of spacecraft origin, Ann. Geophys., 19, 1721–1730, 2001.

Thompson, S. M., Kivelson, M. G., El-Alaoui, M., Balogh, A., Réme, H., and Kistler, L. M.: Bifurcated current sheets: Statistics from Cluster magnetometer measurements, J. Geophys. Res., 111, 3212, 2006.

Torkar, K., Riedler, W., Escoubet, C. P., Fehringer, M., Schmidt, R., Grard, R. J. L., Arends, H., Rüdenauer, F., Steiger, W., Narheim, B. T., Svenes, K., Torbert, R., André, M., Fazakerley, A., Goldstein, R., Olsen, R. C., Pedersen, A., Whipple, E., and Zhao, H.: Active spacecraft potential control for Cluster - implementation and first results, Ann. Geophys., 19, 1289–1302, 2001.

van Allen, J. A.: Observations of high intensity radiation by satellites 1958 Alpha and 1958 Gamma, in Space Science Comes of Age: Perspectives in the History

of the Space Sciences, edited by P. A. Hanle and V. D. Chamberlain, pp. 58–73, 1981.

Vasyliunas, V. M.: Theoretical models of magnetic line merging, Rev. Geophys. Space Phys., 13, 303, 1979.

Vogt, J. and Paschmann, G.: Accuracy of Plasma Moment Derivatives, in Paschmann and Daly (1998), pp. 419 – 448, 1998.

Walsh, A. P., Fazakerley, A. N., Wilson, R. J., Alexeev, I. V., Henderson, P. D., Owen, C. J., Lucek, E., Carr, C., and Dandouras, I.: Near-simultaneous magnetotail flux rope observations with Cluster and Double Star. Submitted, Ann. Geophys., 2007.

Watt, C. E. J., Horne, R. B., and Freeman, M. P.: Ion-acoustic resistivity in plasmas with similar ion and electron temperatures, GRL, 29, 4–1, 2002.

Winglee, R. M.: Ion cyclotron and heavy ion effects on reconnection in a global magnetotail, J. Geophys. Res., 109, 9206, 2004.

Witalis, E. A.: Hall magnetohydrodynamics and its applications to laboratory and cosmic plasma, IEEE Transactions on Plasma Science, 14, 842–848, 1986.

Wygant, J. R., Cattell, C. A., Lysak, R., Song, Y., Dombeck, J., McFadden, J., Mozer, F. S., Carlson, C. W., Parks, G., Lucek, E. A., Balogh, A., Andre, M., Reme, H., Hesse, M., and Mouikis, C.: Cluster observations of an intense normal component of the electric field at a thin reconnecting current sheet in the tail and its role in the shock-like acceleration of the ion fluid into the separatrix region, J. Geophys. Res., 110, A09 206, 2005.

Xiao, C. J., Pu, Z. Y., Ma, Z. W., Fu, S. Y., Huang, Z. Y., and Zong, Q. G.: Inferring of flux rope orientation with the minimum variance analysis technique, J. Geophys. Res., 109, A11 218, 2004.

Yin, L. and Winske, D.: Plasma pressure tensor effects on reconnection: Hybrid and Hall-magnetohydrodynamics simulations, Phys. Plasmas, 10, 1595–1604, 2003.

Yin, L., Winske, D., Gary, S. P., and Birn, J.: Hybrid and Hall-MHD simulations of collisionless reconnection: Dynamics of the electron pressure tensor, J. Geophys. Res., 106, 10 761, 2001.

Yin, L., Winske, D., Gary, S. P., and Birn, J.: Hybrid and Hall-MHD simulations of collisionless reconnection: Effects of plasma pressure tensor, in Space plasma simulation: proceedings of the Sixth International School/Symposium, ISSS-6, Garching, Germany, 3-7 September, 2001. Edited by J. Büchner, C.T. Dum, and M. Scholer. Berlin: Schaltungsdienst Lange o.H.G., 2001., p.403, edited by J. Büchner, C. T. Dum, and M. Scholer, p. 403, 2001.

Zelenyi, L. M., Malova, H. V., Popov, V. Y., Delcourt, D. C., Ganushkina, N. Y., and Sharma, A. S.: "Matreshka" model of multilayered current sheet, Geophys. Res. Lett., 33, 5105, 2006.

Zhang, T. L., Baumjohann, W., Nakamura, R., Balogh, A., and Glassmeier, K.-H.: A wavy twisted neutral sheet observed by CLUSTER, Geophys. Res. Lett., 29, 5–1, 2002.

Zhou, X.-Z., Zong, Q.-G., Wang, J., Pu, Z. Y., Zhang, X. G., Shi, Q. Q., and Cao, J. B.: Multiple triangulation analysis: application to determine the velocity of 2-D structures, Ann. Geophys., 24, 3173–3177, 2006.

Zong, Q.-G., Fritz, T. A., Pu, Z. Y., Fu, S. Y., Baker, D. N., Zhang, H., Lui, A. T., Vogiatzis, I., Glassmeier, K.-H., Korth, A., Daly, P. W., Balogh, A., and Reme, H.: Cluster observations of earthward flowing plasmoid in the tail, Geophys. Res. Lett., 31, L18 803, 2004.